PLASTICITY OF NICKEL BASE SINGLE CRYSTAL SUPERALLOYS

by

Christine Dianne Allan

S.M., Massachusetts Institute of Technology, 1988
S.B., Massachusetts Institute of Technology, 1986

Submitted to the Department of Mechanical Engineering
in partial fulfillment of the requirements for the degree of

Doctor of Philosophy

at the

MASSACHUSETTS INSTITUTE OF TECHNOLOGY

February 1995

Author .....
Department of Mechanical Engineering
September 30, 1994

Certified by .....
Lallit Anand
Professor of Mechanical Engineering
Thesis Supervisor

Accepted by .....
Ain Anis Sonin
Chairman, Departmental Committee on Graduate Students

PLASTICITY OF NICKEL BASE SINGLE CRYSTAL SUPERALLOYS

by

Christine Dianne Allan

Submitted to the Department of Mechanical Engineering
on September 30, 1994, in partial fulfillment of the
requirements for the degree of
Doctor of Philosophy

Abstract

A first order capabilty for high-temperature, anisotropic, inelastic design of γ/γ' single crystal superalloy turbine blades is developed. The capability consists of a new constitutive model and a computational procedure for single crystal superalloys. These two-phase γ/γ' materials consist of more than 65% γ' precipitates with an $L1_2$ crystal structure, in an fcc matrix. The yielding behavior of the superalloys is dominated by that of the majority γ' phase. In the present study we begin by developing a crystallographic slip model for $L1_2$ intermetallics. This macroscopic model is guided by the current understanding of the micromechanics of plastic deformation at the dislocation scale level. Experimental data from the literature for single crystals of an Ni_3Al-type material in several orientations over a wide range of temperatures is used to obtain the material parameters and to test the predictive capabilities of the model. This constitutive model for single phase γ' is then extended to model the two-phase γ/γ' material. Simple tension and compression experiments are performed on the two-phase material, CMSX4, at temperatures between room temperature and 850°C to determine the additional parameters and to test the predictive capabilities of the two-phase model. The model is then verified for non-homogeneous deformations of single crystals of CMSX4 in (*i*) torsion and (*ii*) tension of a notched bar. The predictive capabilities of the model are very good.

The constitutive model is implemented in a commercial finite element code. Also, the model requires only a few material parameters which are obtained from a simple set of systematic experiments. This should allow an easy transition to actual design applications.

Thesis Supervisor: Lallit Anand
Title: Professor of Mechanical Engineering

Acknowledgments

I begin by thanking my thesis supervisor, Professor Lallit Anand, for his support over the last six years. He gave me the opportunity to work on an extremely interesting and challenging problem and to learn very many skills which will serve me well in my profession. Thanks also to Professors Sam Allen, Ali Argon and David Parks for serving on my committee. The discussions which took place at my committee meetings were always very interesting.

Thanks to Allison Gas Turbine and Cannon Muskegon for providing the material used in this study and performing the heat treatment.

It has been a great pleasure and privilege to share an office and a lab with a very interesting group of people who have been great friends as well as good sources of discussion, technical and otherwise: Ellen Arruda, Srihari Balasubramanian, Curt Bronkhorst, Brian Gally, Mehrdad Haghi, Omar Hasan, Fred Haubensak, Surya Kalidindi, Manish Kothari, Chuang-Chia Lin, Antonios Zavaliangos. Special thanks to Surya who introduced me to crystal plasticity. Thanks also to Lin whose contributions to the modeling side of this project were significant. Working with him and having someone to discuss the project with in detail was really enjoyable and productive.

Leslie Regan and the staff of the graduate office were always there with all information necessary to make things run smoothly. Most of us would not get things organized as well without their help.

Sincerest thanks are owed to my dear friend Bob Samuel, who was always very encouring, and who always had a good story to tell. Thanks too for all the help and the great ideas on how to get that especially difficult experimental setup to work on many occasions.

To my family, many, many thanks. Special mention must be made of my mom, Teresa, who stuck out the undergraduate *and* the graduate years. It's finally over! My husband, Randy, and our daughter, Margaret have really made the end much more pleasurable and more worthwhile. Randy, thanks for giving me so much time to work and doing such a fantastic job raising Margaret. Thanks too for continuing to push me to finish. I now look forward to the next phase with some anticipation.

Contents

List of Figures

List of Tables

Chapter 1

Introduction

1.1 Background

The drive to improve the efficiency of gas turbine engines has consistently led to increased demands on the materials used in the engine hot sections. The trend has been towards higher melting points, greater creep and thermal fatigue resistance and longer fatigue lives. For these applications the current expected operating range of temperatures is around 600 – 1100°C, although new developments in materials and parts design are constantly aimed at increasing the upper limit. As a result, several materials are currently being investigated for this application including intermetallic compounds, ceramics and ceramic matrix composites.

However, for some time now, turbine blades in modern gas turbine engines have been made from large, investment cast single crystals of nickel-base superalloys. Much research has been performed on the development and improvement of superalloys for this application, from chemistry modifications to the development of directionally solidified materials and single crystals, and several generations exist with minor compositional changes between them, sometimes leading to major improvements in material performance. Figure 1-1 [Molloy, 1990] shows a time line on the development of high temperature superalloys over four decades, with their approximate maximum use temperatures and year of introduction. Single crystals, more recently introduced, are an attractive option for several reasons. Since they have no grain boundaries, they are not succeptible to the common failure modes of grain boundary oxidation and grain boundary creep fracture, and the grain boundary strengthening elements which also act as melting point depressants have been removed,

improving the temperature capability. Additionally, they have lower creep rates.

The blades are investment cast in final form with the ⟨001⟩ orientation approximately aligned with the major axis. Figure 1-2 shows an investment cast single crystal, complex-cored turbine blade. Significant improvements in blade design have led to these complex cored hollow blades for air cooling, allowing the incoming hot gas temperature to be well above the alloy temperature. Additionally, making the blades hollow significantly reduces the mass, thereby decreasing the stresses due to centrifugal forces at the blade roots and making them more attractive for application in aircraft engines. The fir-tree root structure and the shape of the airfoil lead to complex stress states in the blade, rather than simple tension or compression in the ⟨001⟩ direction.

1.2 Motivation for this study

Even though single crystal blades are being used in actual applications, the mechanical aspects of the design of such blades is for the most part empirically based. This is so primarily because nonlinear structural analysis methodologies for single crystal turbine blades under complex stress states require accurate anisotropic, thermo-elastic, viscoplastic constitutive models and failure criteria for cyclic thermo-mechanical loadings, but such deformation and failure models are still in their infancy (e.g. [Sheh and Stouffer, 1990], [Stouffer *et al.*, 1990], [Méric *et al.*, 1991], [Jordan and Walker, 1992]). Much remains to be done to develop a more complete understanding of the mechanisms of deformation and failure, and to develop a useful numerical capability for analysis and design of high temperature structural components made from these materials.

The recent macroscopic consitutive models for $L1_2$ materials which incorporate considerations of the mechanics of dislocation motion during deformation of Qin and Bassani [1992] and Cuitiño and Ortiz [1993]) have some deficiencies. Qin and Bassani [1992] developed a time-independent model to explain the tension-compression asymmetry of yield strength of these materials, but did not propose a mechanism to explain the anomalous temperature dependence. Cuitiño and Ortiz [1993] proposed a rather complicated constitutive model for the anomalous behavior observed in these alloys, incorporating the contributions of the obstacles created by forest dislocations and by cross-slip pinning to the "hardening" of these materials at high offset plastic strains. In both cases, no extension

is made to the two-phase materials and any effect that that might have on the plastic deformation.

The goal of this study is to develop a physically-based, readily implementable constitutive model, guided by the operative mechanisms of inelastic deformation in these superalloys, that will accurately represent the inelastic yielding behavior of these materials under complex, thermo-mechanical loading conditions. This may then be used as a tool in the design of turbine blades made from these materials. The single crystal nature of the materials requires that the constitutive model account for anisotropic elastic and viscoplastic response.

1.3 Description of material studied

In this study we will focus on the latest generation nickel-base single crystal superalloy CMSX4[1] with composition as given in Table 1.1. This alloy is a single crystal derivative of Mar-M-247 developed by the Cannon-Muskegon Corporation. Single crystals of this alloy were kindly donated by the Allison Single Crystal Operations, 5601 Fortune Circle South Dr., Suite I, Indianapolis, IN 46241. Three orientations were available: crystals within 2-3 degrees of the $\langle 001 \rangle$ and $\langle 011 \rangle$ orientations, and crystals within 10 degrees of the $\langle 111 \rangle$ orientation. They were received in the solution treated state — 1324°C, 4 hours, gas fan cool in vacuum. Additionally, a two stage aging heat treatment is required: (*i*) 1141°C, 6 hours, air cool; (*ii*) 871°C, 20 hours, air cool. This aging was performed by Cannon-Muskegon. This aging reprecipitates the γ', giving a regular cubic array for maximum creep strength. Figure 1-3 is a transmission electron micrograph (TEM) of a fully heat-treated, undeformed CMSX4. This material consists of two coherent phases. Image analysis on a TEM micrograph gives: (*i*) about 68% of an approximately regular, periodic three-dimensional array of cuboidal precipitates of Ni_3Al (γ') having an $L1_2$ crystal structure and of average dimension 0.45μm and (*ii*) an fcc matrix (γ) of average channel width 60 nm.

The γ matrix phase is simple fcc. It is much weaker than the γ' precipitate phase and is present in narrow channels as we see in the TEM micrograph, Figure 1-3. Pollock and Argon [1988] developed a model for the infinitesmal strain *creep* deformation of two-phase

[1]The difference in composition between the earlier generation superalloy CMSX3 and CMSX4 is that 0.5% Re is added in CMSX4 and this has been shown to slow the growth of the γ' precipitates during creep.

Table 1.1: Nominal composition of CMSX4 (Wt %)

Cr	Co	W	Mo	Al	Ti	Ta	Hf	Re	Ni
8.0	4.6	8.0	0.6	5.6	1.0	6.0	0.1	0.5	Balance

CMSX3 single crystals. At low strains in the early stages of creep, only the weaker γ matrix phase undergoes plastic deformation, hence the properties of the γ phase are important. At these levels, the dislocations are concentrated in the narrow matrix channels and are forced to bow around the γ' precipitates, Figure 1-4(a) [Pollock, 1989]. At higher strains, as in the later stages of creep, or at the levels where 0.2% offset plastic strain is attained in a tension or compression strain controlled test, the γ' particles are *sheared*, Figure 1-4(b). For later use we note that since the material consists of such a high volume fraction of γ', the properties of this phase will dominate the 0.2% and higher offset yield strength of these materials.

At very high temperatures the microstructure becomes unstable and the precipitates begin to raft, joining together to form long, narrow plates. Figure 1-5 shows the microstructure of CMSX3 after very low stress ($\sim$70 MPa) creep deformation at 1050°C [Pollock, 1989]. In the present study we will restrict our attention to somewhat lower temperatures (up to 850°C), so that rafting will not be considered.

1.4 Plan of thesis

The plan of this thesis follows. In Chapter 2 the behavior of $L1_2$ intermetallics, the γ' phase, is described, and a new viscoplastic constitutive model is developed guided by the present understanding of the micromechanisms of deformation. The material parameters in the model are obtained by fitting experimental data from the literature for a single-phase γ' material which cover a wide range of temperatures and a few orientations at a single strain rate. The capabilities of the model are tested by comparing predictions of the model against experiments for other orientations. The successes and limitations of the model are summarized and discussed.

Chapter 3 shows the results of the experiments conducted in this study to determine the variations in the tension and compression yield strengths (0.2% offset) with temperature for the γ/γ' superalloy CMSX4. This alloy was tested in tension and compression in the near-

$\langle 001 \rangle$, $\langle 011 \rangle$ and $\langle 111 \rangle$ orientations at several temperatures ranging from room temperature to 850°C, and a strain rate of $\pm$ .0001/sec. The $\langle 001 \rangle$ and $\langle 111 \rangle$ results were used to determine the remaining model parameters for the two-phase material at each temperature, while the $\langle 011 \rangle$ results served as predictions. By extending the results of the model for single-phase γ' from Chapter 2, and using the γ' parameters obtained, a simple constitutive model for the two-phase γ/γ' superalloys is formulated. The implications of this extension of the constitutive model to the two-phase material and its validity are discussed.

Chapter 4 gives the results of some experiments and simulations to test the predictive capability of the present model for the single crystal superalloy. These include room temperature and higher temperature experiments on more complex geometries, leading to nonhomogeneous deformations. They were: (*i*) a $\langle 001 \rangle$-oriented thin-walled tube in torsion and (*ii*) a $\langle 001 \rangle$-oriented double-notched bar in tension to model the fir tree root structure of the turbine blade. These experiments give us an appreciation of the versatility and strength of our new constitutive model.

Chapter 5 summarizes the constitutive model and the material parameters, and describes the methodology employed to determine them.

Chapter 6 summarizes the results obtained in this thesis and gives some discussion as well as suggestions for future work.

Appendix A defines the Euler angles which are used in our model to describe the crystal orientation. Appendix B describes the effect of the non-Schmid shear stresses on the dislocation cores in these materials. Appendix C describes a simple model which incorporates the non-Schmid shear stresses in a linear form, requiring only four temperature-dependent parameters. This model is appropriate for data at a single temperature, when a quick result is required. Appendix D describes some monotonic compression and cyclic experiments which were performed on an earlier generation superalloy CMSX3 in the $\langle 001 \rangle$ orientation; this appendix also describes some micro-mechanical simulations of the two-phase γ/γ' material.

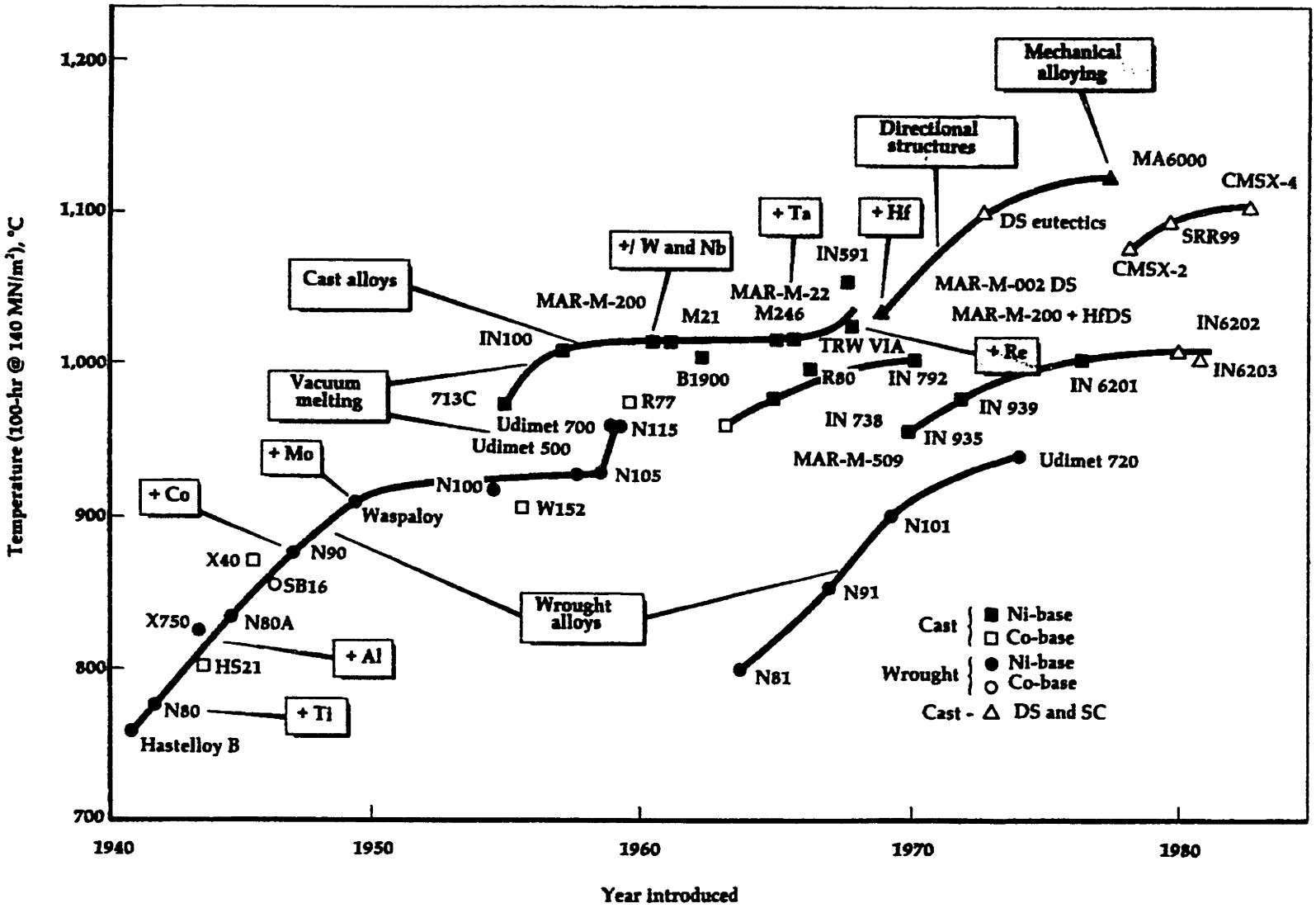

Figure 1-1: Chronological increase of temperature capability (100hr/140MPa rupture strength) of superalloys [Molloy, 1990]

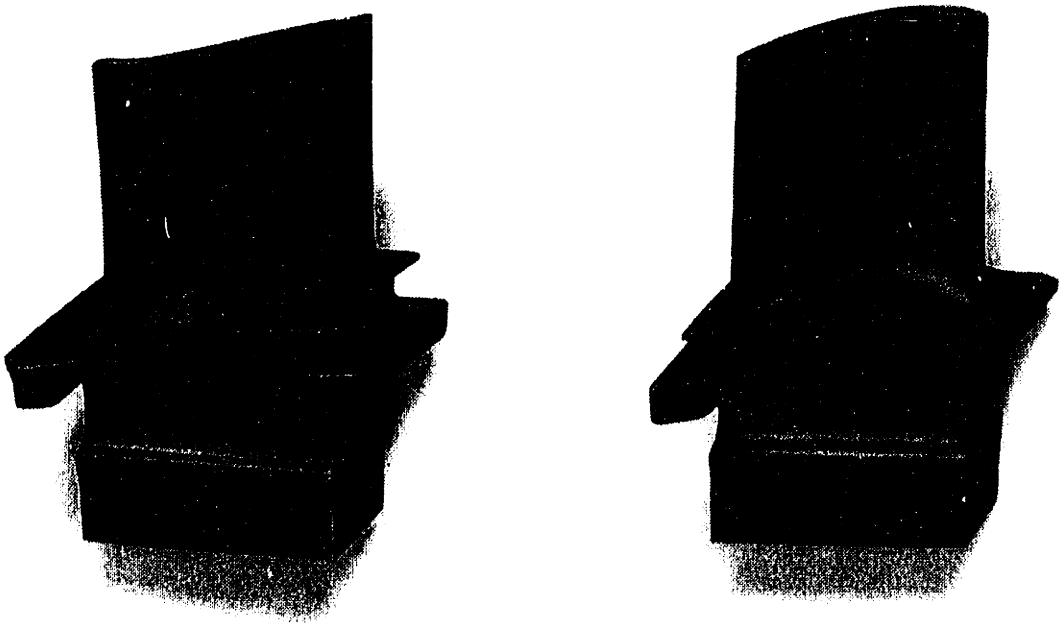

Figure 1-2: Nominally ⟨001⟩-oriented single crystal complex-cored turbine blade

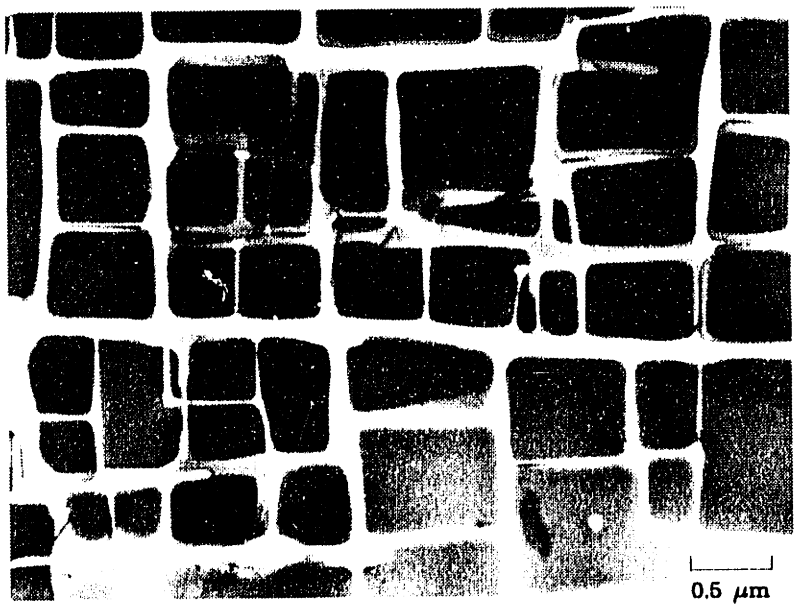

Figure 1-3: TEM micrograph of undeformed CMSX4 – ⟨001⟩ direction out of the plane

(a)

(b)

Figure 1-4: (a) Looping of dislocations in matrix around γ' precipitates during primary creep. (b) Shearing of precipitates by dislocations during compression [Pollock, 1989]

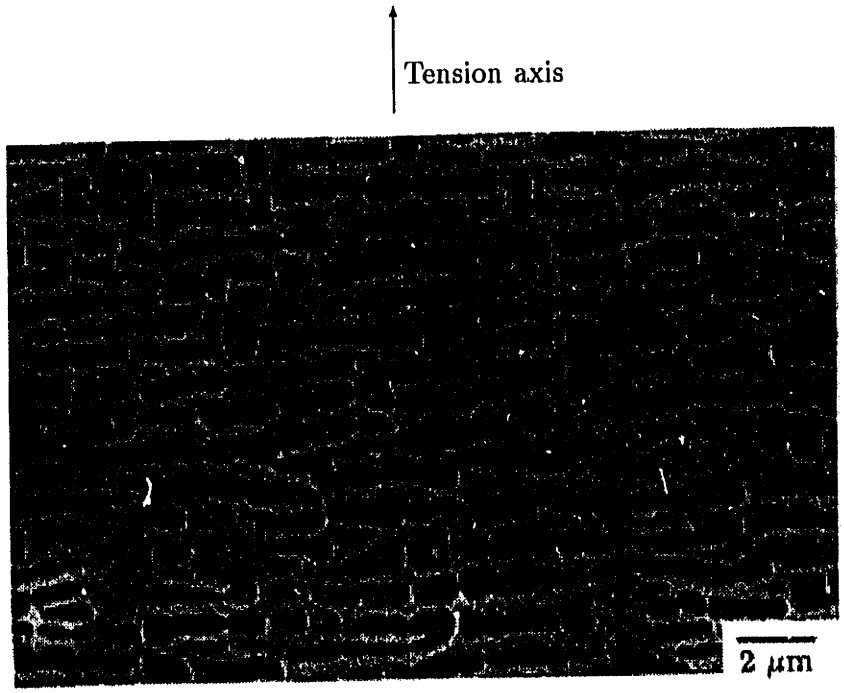

Figure 1-5: Rafting of γ' precipitates in CMSX3 due to high temperature deformation [Pollock, 1989]

Chapter 2

Modeling of $L1_2$ Intermetallics — γ' Phase

2.1 Yielding of $L1_2$ Intermetallics

2.1.1 Macroscopic Response

Yield Strength

Westbrook [1957] was the first to observe some anomalies in the hardness of $L1_2$ intermetallics. His experiments showed that the hardness of *polycrystalline* Ni_3Al (γ') increased with increasing temperature, Figure 2-1(a). A later study [Flinn, 1960] confirmed from tensile tests that the 0.01% offset yield strength of *polycrystalline* Ni_3Al also *increases* with temperature, Figure 2-1(b). This anomaly was also found in $L1_2$ compounds other than Ni_3Al and in two phase γ/γ' superalloys, and hence was attributed to the crystal structure of the γ' material.

Thornton *et al.* [1970] and Mulford and Pope [1973] observed that the extent of the anomalous increase of flow stress with temperature is dependent on the definition of yield employed. For very small[1] offset strains (10^{-6}), the flow stress is almost constant or decreases with increasing temperature over the entire temperature range, exhibiting no anomaly, Figure 2-2 [Thornton *et al.*, 1970]. This suggests that the anomalous increase with temperature may be a manifestation of some microscale strain hardening of the material.

[1]Thornton *et al.* [1970] give no details of how such microstrains at high temperatures were measured. These results seem not to have been reproduced since.

Chapter 2

Modelling of $L1_2$ Intermetallics — γ' Phase

2.1 Yielding of $L1_2$ Intermetallics

2.1.1 Macroscopic Response

Yield Strength

Westbrook [1957] was the first to observe some anomalies in the hardness of $L1_2$ intermetallics. His experiments showed that the hardness of *polycrystalline* Ni_3Al (γ') increased with increasing temperature, Figure 2-1(a). A later study [Flinn, 1960] confirmed from tensile tests that the 0.01% offset yield strength of *polycrystalline* Ni_3Al also *increases* with temperature, Figure 2-1(b). This anomaly was also found in $L1_2$ compounds other than Ni_3Al and in two phase γ/γ' superalloys, and hence was attributed to the crystal structure of the γ' material.

Thornton *et al.* [1970] and Mulford and Pope [1973] observed that the extent of the anomalous increase of flow stress with temperature is dependent on the definition of yield employed. For very small[1] offset strains (10^{-6}), the flow stress is almost constant or decreases with increasing temperature over the entire temperature range, exhibiting no anomaly, Figure 2-2 [Thornton *et al.*, 1970]. This suggests that the anomalous increase with temperature may be a manifestation of some microscale strain hardening of the material.

[1]Thornton *et al.* [1970] give no details of how such microstrains at high temperatures were measured. These results seem not to have been reproduced since.

Further studies which for the most part have concentrated on the 0.2% offset yield strength have shown several other interesting aspects of the yield behavior of these alloys. This is illustrated for single crystals of the γ' material Ni_3Al+0.2%B in Figure 2-3, plotted from the data of Heredia [1990]. The figure plots the 0.2% offset yield strength in the near-$\langle 001 \rangle$, $\langle 011 \rangle$ and $\langle 111 \rangle$ orientations and in one central orientation in the stereographic triangle as a function of temperature. Also, Figure 2-4 [Copley and Kear, 1967] plots the stress strain curves from consecutive tensile loading-unloading experiments at different temperatures. Several features are evident:

1. At temperatures below ~1000K the yield strength increases with temperature for all orientations, both in tension and compression. Above ~1000K the strength drops off significantly.

2. Schmid's law is violated: orientations with the same Schmid factor (eg. $\langle 001 \rangle$ and $\langle 011 \rangle$) have different yield strengths.

3. For the $\langle 001 \rangle$, $\langle 011 \rangle$ and $\langle 111 \rangle$ orientations, the yield strength at a given temperature differs in tension and compression over a certain temperature range; the magnitude and sense of this asymmetry depends on the temperature and the orientation. The $\langle 001 \rangle$ is stronger in tension than in compression, and the opposite is true for the $\langle 011 \rangle$ and $\langle 111 \rangle$ orientations. The tension-compression asymmetry is most pronounced between room temperature and the peak, while at lower and higher temperatures it is not significant.

4. At all temperatures the $\langle 111 \rangle$ orientation is weakest in both tension and compression (at the lowest temperature the values are all close, with the $\langle 111 \rangle$ being slightly higher than the other two), while the $\langle 001 \rangle$ orientation is stronger than the $\langle 011 \rangle$ in tension, and the reverse is true in compression. There are some orientations on the inside of the stereographic triangle, close to the $\langle 012 \rangle$ - $\langle \bar{1}13 \rangle$ great circle, where the tension-compression asymmetry is essentially zero at all temperatures.

5. Stress-strain curves show a distinct transition to plasticity, with relatively little strain hardening, especially at the highest and the lowest temperatures, Figure 2-4. The "hardening" effect on the yield strength with increasing temperature is reversible. On

unloading and reloading the specimen at a lower temperature, it is possible to attain a lower yield strength.

Slip Traces

Figure 2-5 shows slip traces for $Ni_3(Al,Nb)$ deformed over a range of temperatures in the ⟨001⟩ orientation(S), close to the ⟨011⟩ orientation(V), and close to the ⟨111⟩ orientation(W) [Lall *et al.*, 1979]. For orientation S (⟨001⟩) the resolved shear stress on the cube slip systems is always zero, so there can be no activity on any of these slip systems, as we see is the case for all temperatures in Figure 2-5(a) — slip traces corresponding only to octahedral slip are observed. For orientation V (near ⟨011⟩), slip traces corresponding to octahedral slip are observed at low temperatures, while at the two highest temperatures, 595K and 800K, slip traces corresponding to both octahedral and cube slip are observed, Figure 2-5(b). For orientation W (near ⟨11'⟩), in addition to octahedral slip at all temperatures, slip traces corresponding to cube slip start becoming apparent at temperatures as low as 300K (room temperature), Figure 2-5(c). This and other surface slip trace studies show that below the peak temperature slip occurs primarily on the octahedral slip systems ({111}⟨110⟩-type) while above the peak cube slip ({001}⟨110⟩-type) dominates for non-cube oriented samples ([Takeuchi and Kuramoto, 1973], [Lall *et al.*, 1979], [Méric *et al.*, 1991]). The exception is the ⟨111⟩ orientation where cube slip occurs at *all* temperatures.

2.1.2 Crystal Structure and Dislocations in $L1_2$ Compounds

The $L1_2$ crystal structure is a derivative of the fcc crystal structure. It is typical of compounds of composition AB_3 with the minority (A) atoms occupying the corner sites and the majority (B) atoms occupying the face centers, Figure 2-6. As a result, the lattice translation vector in $L1_2$ compounds is ⟨110⟩ as opposed to $\frac{1}{2}$⟨110⟩ in fcc materials.

Transmission electron microscopy (TEM) results show that the dislocation structure after deformation in the temperature range where the anomalies are present consists mostly of long straight screw dislocations, Figure 2-7 [Kear and Wilsdorf, 1962].

It has been suggested [Flinn, 1960] and electron microscopy evidence supports, that the ⟨110⟩ total dislocations in $L1_2$ are dissociated on the {111} planes into two $\frac{1}{2}$⟨110⟩ dislocations. Since the energy per unit length of a dislocation is proportional to μb^2 where μ is the shear modulus and b is the magnitude of the Burgers vector, this dissociation is

energetically favorable. Movement of one {111} layer relative to the other by $\frac{1}{2}\langle 110\rangle$ from position X to position Y in Figure 2-8 [Hull and Bacon, 1984] moves a B atom to an A position, leaving behind a region of disorder, or an antiphase boundary (APB). In Ni_3Al the APB energy on the {111} plane is too high to allow slip of a single $\frac{1}{2}\langle 110\rangle$ partial dislocation. Further movement of the {111} layer by another $\frac{1}{2}\langle 110\rangle$ to position Z restores order. Consequently $\frac{1}{2}\langle 110\rangle$ partials must travel in pairs separated by APBs. An example of these dissociated $\frac{1}{2}\langle 110\rangle$ dislocations, observed by TEM in the $L1_2$ compound $AuCu_3$, is shown in Figure 2-9 [Marcinkowski *et al.*, 1961].

These two $\frac{1}{2}\langle 110\rangle$ "superpartials" may in turn dissociate into $\frac{1}{6}\langle 112\rangle$ Shockley partials[2] separated by complex stacking faults (CSF). The total dislocation in $L1_2$ structures therefore consists of two pairs of Shockley partials each separated by a CSF, and separated from each other by an APB, as illustrated in Figure 2-10 [Hull and Bacon, 1984].

2.1.3 Micromechanisms for Yield Strength Anomalies

There is general agreement in the literature that the major reason for the anomalous yielding behavior of these materials is the hardening caused by the pinned segments of screw dislocations when they cross-slip from the {111} octahedral glide planes to the {001} cube planes. The driving force for this cross-slip process is the difference in APB energy on the {111} and {001} planes. Flinn [1960] performed calculations based on nearest neighbor interactions and found that the APB is a minimum on {001} and close to a maximum on {111}. When dissociation occurs on the {111} plane, cross-slip becomes more difficult since the $\frac{1}{6}\langle 112\rangle$ vector lies in only the {111} plane. Therefore an individual Shockley partial cannot cross-slip. So long as the dislocation core is extended, it is constrained to glide in the {111} plane of its fault. Although an extended screw dislocation cannot cross-slip, it may form a constriction and then be free to move in other planes ({001} or another {111}), see Figure 2-11 (reproduced from [Cuitiño and Ortiz, 1993]).

The stress which causes the Shockley partials to constrict is the shear stress resolved on the primary(p) {111} slip plane in the edge(e) direction, τ_{pe}, Figure 2-12 (adapted from [Asaro, 1983]). In one sense τ_{pe} constricts the Shockley partials, promoting cross-slip. When the sense of the stress is reversed (tension to compression, or vice versa) τ_{pe} extends the

[2] In Figure 2-9, the dissociation into Shockley partials cannot be resolved.

Shockley partials, hindering cross-slip. Therefore, in one direction the effect of τ_{pe} is to increase the yield strength and in the opposite direction, the effect is to decrease it.

For a given macroscopic uniaxial stress, the sign of τ_{pe} on the octahedral slip systems is the same for the $\langle 011 \rangle$ and $\langle 111 \rangle$ orientations, while it is reversed for the $\langle 001 \rangle$ orientation. This accounts for the difference in the sense of the asymmetry for the $\langle 001 \rangle$ orientation and the other two. Orientations in the stereographic triangle where τ_{pe} is zero for all the slip systems (along the $\langle 012 \rangle$ - $\langle \bar{1}13 \rangle$ great circle) will exhibit no tension-compresssion asymmetry. These trends are illustrated schematically in the stereographic triangle in Figure 2-3.

Takeuchi and Kuramoto [1973] suggested that cross-slip is also likely to be promoted by yet another "non-Schmid" shear stress, the stress resolved on the cube(c) cross-slip plane in the direction of the Burgers(b) vector, τ_{cb}, Figure 2-12.

According to Paidar *et al.* [1984], once the partial dislocations become constricted and cross-slip they move a short distance, on the order of $b/2$ before they redissociate on a $\{111\}$ plane, forming a sessile segment. Figure 2-11 shows the two possibilities for a [101] dislocation after cross-slip from the (111) plane. The two leading Shockley partials recombine and cross-slip to the (010) plane; they then redissociate either on the primary (111) plane or the "secondary" $(1\bar{1}1)$ plane. On this secondary plane, the resolved stress which acts on the partials, causing constriction or dissociation is τ_{se}, on the secondary(s) plane in the edge(e) direction. This resolved shear stress contributes to the tension-compression asymmetry in a way similar to τ_{pe} (see Appendix B). Note that, while the APB is on the $\{001\}$ plane, the dissociation into Shockley partials can occur only on the $\{111\}$ planes making the core of the dislocation non-planar.

The sessile cross-slipped dislocation segments act as local point obstacles to further dislocation motion. The rate of generation of these obstacles is taken to be proportional to the rate of cross-slip. The activation enthalpy for cross-slip depends on the antiphase boundary energies on the primary slip plane and the cube cross-slip plane, and on the resolved shear stresses acting on these planes. It has been estimated to be [Paidar *et al.*, 1984] (also see [Cuitiño and Ortiz, 1993]):

$$H = \frac{\mu b^3}{4\pi} \left\{ h + c + \kappa_1 (t_{pe} - \kappa_2 t_{se}) - \sqrt{\left(\frac{1}{\sqrt{3}} - \frac{\Gamma\{001\}}{\Gamma\{111\}} + |t_{cb}| \right) \frac{b}{B}} \right\} \qquad (2.1)$$

where μ is an appropriate "shear" modulus, $\Gamma^{\{001\}}$ and $\Gamma^{\{111\}}$ are the APB energies per unit area on $\{001\}$ and $\{111\}$ planes, respectively, h, c, κ_1 and κ_2 are dimensionless coefficients, $t_{xx} = \frac{\tau_{xx}}{\Gamma^{\{111\}}/b}$ are the normalized resolved shear stresses, and $B = \frac{\mu b^2}{2\pi\Gamma^{\{111\}}}$ is the equilibrium (stress-free) spacing of the superpartials on the (111) plane.

Since the formation of constrictions and subsequent cross-slip are thermally activated, the tendency to cross-slip increases with increasing temperature, causing an increase in the obstacle density, and thus the flow resistance of the material.

A competing effect which occurs simultaneously is the reduction of the strength of these obstacles with increasing temperature. In addition, for orientations other than $\langle 001 \rangle$, the resolved shear stress on the cube slip systems becomes high enough to allow slip on these slip systems. These two factors combine to cause a drop in the yield strength as temperature increases. For the $\langle 111 \rangle$ orientation, where the resolved shear stress on the cube slip systems is the highest, cube slip occurs even below the peak temperature, causing this orientation to be the weakest at all temperatures, as observed by Heredia [1990] and others.

The violation of Schmid's law may be explained as follows. The yield strength depends not only on the resolved shear stress on the slip systems, τ^α (see Figure 2-12), but also on the non-Schmid stresses τ_{pe}, τ_{se} and τ_{cb}. The shear stresses τ_{pe} and τ_{se} have been shown to contribute to the anomalous increase of yield strength with temperature, and the tension-compression asymmetry. While τ^α and τ_{pe} may be the same for two orientations, if τ_{cb} and τ_{se} are different, then the yield strength will also differ. This is the case with the $\langle 001 \rangle$ and $\langle 011 \rangle$ orientations, leading to different yield strengths in these two orientations having the same Schmid factor.

2.2 Constitutive Model

2.2.1 Crystal Plasticity Model for fcc Materials — γ phase [Kalidindi *et al.*, 1992]

Deformation in fcc materials takes place primarily by crystallographic slip on the 12 $\{111\}\langle 110 \rangle$ type (octahedral) slip systems. At a given temperature the constitutive equation for stress is given in terms of a linear elastic relation:

$$\mathbf{T}^* = \mathcal{L}[\mathbf{E}^*] \tag{2.2}$$

where

$$\mathbf{E}^* \equiv \left(\frac{1}{2}\right)\{\mathbf{F}^{*T}\mathbf{F}^* - \mathbf{1}\}, \qquad \mathbf{T}^* \equiv \mathbf{F}^{*-1}\{(\det \mathbf{F}^*)\mathbf{T}\}\mathbf{F}^{*-T} \tag{2.3}$$

are work-conjugate elastic strain and stress measures, respectively, $\mathcal{L}$ is the fourth order anisotropic elasticity tensor and $\mathbf{1}$ is the second order identity tensor. Also, $\mathbf{T}$ is the symmetric Cauchy stress tensor, $\mathbf{F}^*$ is an elastic deformation gradient defined by

$$\mathbf{F}^* \equiv \mathbf{F}\mathbf{F}^{p^{-1}}, \qquad \det \mathbf{F}^* > 0, \tag{2.4}$$

where $\mathbf{F}$ is the deformation gradient and $\mathbf{F}^p$ is a plastic deformation gradient with $\det \mathbf{F}^p = 1$. The evolution equation for the plastic deformation gradient is given by the flow rule:

$$\dot{\mathbf{F}}^p = \mathbf{L}^p\mathbf{F}^p \tag{2.5}$$

where

$$\mathbf{L}^p = \sum_\alpha \dot{\gamma}^\alpha \mathbf{S}_o^\alpha, \qquad \mathbf{S}_o^\alpha \equiv \mathbf{m}_o^\alpha \otimes \mathbf{n}_o^\alpha \tag{2.6}$$

$\mathbf{m}_o^\alpha$ and $\mathbf{n}_o^\alpha$ define the slip direction and the slip plane normal of the slip system α respectively, in a fixed reference configuration. The plastic shearing rate on the slip system α, $\dot{\gamma}^\alpha$, is given in terms of the resolved shear stress, τ^α, the temperature dependent slip system resistance on the slip system α, s^α, and the absolute temperature, θ:

$$\dot{\gamma}^\alpha = \hat{\dot{\gamma}}^\alpha(\tau^\alpha, s^\alpha(\theta), \theta) \tag{2.7}$$

The plastic stress power per unit volume in the relaxed configuration is given by [Anand, 1985]:

$$\dot{\omega} \equiv \mathbf{C}^*\mathbf{T}^* \cdot \mathbf{L}^p, \qquad \text{with} \quad \mathbf{C}^* \equiv \mathbf{F}^{*T}\mathbf{F}^*. \tag{2.8}$$

The resolved shear stress τ^α for the slip system α is then given by:

$$\dot{\omega}^p = \sum_\alpha \tau^\alpha \dot{\gamma}^\alpha \tag{2.9}$$

$$\Rightarrow \qquad \tau^\alpha \equiv (\mathbf{C}^*\mathbf{T}^*) \cdot \mathbf{S}_o^\alpha \tag{2.10}$$

For small elastic stretches, $\tau^\alpha \approx \mathbf{T}^* \cdot \mathbf{S}_o^\alpha$.

Finally, the slip system resistance may be taken to evolve as

$$\dot{s}^{\alpha} = \sum_{\beta} h^{\alpha\beta} \left| \dot{\gamma}^{\beta} \right| \tag{2.11}$$

where $h^{\alpha\beta}$ is the rate of strain hardening on slip system α due to a shearing on the slip system β.

2.2.2 Crystal Plasticity Model for Ni_3Al type $L1_2$ Alloys — γ' phase

The similarity between the $L1_2$ and fcc crystal structures and their deformation mechanisms allows us to use a similar approach to modeling this material, however, the mechanisms of dislocation dissociation which take place in the $L1_2$ crystal structure require some modifications to the constitutive model for fcc materials described above. "Non-Schmid" shear stresses, τ_{pe}^{α}, τ_{se}^{α} and τ_{cb}^{α} affect the dislocation dissociation and slip on the octahedral slip systems in $L1_2$ alloys, and so contribute to the slip resistance on these slip systems. Unlike fcc materials, the six $\{100\}\langle 110\rangle$ cube slip systems may also become active in $L1_2$ materials for orientations close to the $\langle 111\rangle$ corner of the stereographic triangle. At high temperatures these slip systems may also become active for other orientations. Table 2.1 lists and Figure 2-13 illustrates the 12 octahedral and 6 cube slip systems which are possible for these materials. For the cube slip systems, however, there are no important dislocation core effects so the "non-Schmid" terms are not necessary. The original formulation of the constitutive equations for fcc materials is therefore applicable. Equation 2.7 is accordingly modified:

$$\dot{\gamma}^{\alpha} = \begin{cases} \hat{\dot{\gamma}}^{\alpha}(\tau^{\alpha}, s^{\alpha}(\tau_{pe}^{\alpha}, \tau_{se}^{\alpha}, \tau_{cb}^{\alpha}, \theta), \theta), & \alpha = 1, \ldots, 12 \quad \text{octahedral slip systems} \\ \hat{\dot{\gamma}}^{\alpha}(\tau^{\alpha}, s^{\alpha}(\theta), \theta), & \alpha = 13, \ldots, 18 \quad \text{cube slip systems} \end{cases} \tag{2.12}$$

The slip system resistances for the octahedral systems are the ones taken to be affected by the non-Schmid shear stresses. The contribution of τ_{pe}, τ_{se} and τ_{cb} give the tension-compression asymmetry, and the relative amounts of octahedral and cube slip with varying temperature leads to the differing amount of tension-compression asymmetry with temperature. These effects are all accounted for in our formulation, to be detailed below, and make it possible to model and predict the anomalous yielding behavior of these alloys.

Table 2.1: Slip systems

Octahedral

α	$(\mathbf{n}^{\alpha})[\mathbf{m}^{\alpha}]$	$(\mathbf{n}^{\alpha}_{pe})[\mathbf{m}^{\alpha}_{pe}]$	$(\mathbf{n}^{\alpha}_{se})[\mathbf{m}^{\alpha}_{se}]$	$(\mathbf{n}^{\alpha}_{cb})[\mathbf{m}^{\alpha}_{cb}]$
1	$(111)[01\bar{1}]$	$(111)[\bar{2}11]$	$(1\bar{1}\bar{1})[\bar{2}\bar{1}\bar{1}]$	$(100)[01\bar{1}]$
2	$(111)[\bar{1}01]$	$(111)[1\bar{2}1]$	$(\bar{1}1\bar{1})[\bar{1}2\bar{1}]$	$(010)[\bar{1}01]$
3	$(111)[1\bar{1}0]$	$(111)[11\bar{2}]$	$(\bar{1}\bar{1}1)[\bar{1}\bar{1}2]$	$(001)[1\bar{1}0]$
4	$(1\bar{1}\bar{1})[0\bar{1}1]$	$(1\bar{1}\bar{1})[\bar{2}\bar{1}\bar{1}]$	$(111)[\bar{2}11]$	$(100)[0\bar{1}1]$
5	$(1\bar{1}\bar{1})[\bar{1}0\bar{1}]$	$(1\bar{1}\bar{1})[12\bar{1}]$	$(\bar{1}\bar{1}1)[\bar{1}21]$	$(0\bar{1}0)[\bar{1}0\bar{1}]$
6	$(1\bar{1}\bar{1})[110]$	$(1\bar{1}\bar{1})[1\bar{1}2]$	$(\bar{1}1\bar{1})[\bar{1}12]$	$(00\bar{1})[110]$
7	$(\bar{1}1\bar{1})[011]$	$(\bar{1}1\bar{1})[21\bar{1}]$	$(\bar{1}\bar{1}1)[2\bar{1}1]$	$(\bar{1}00)[011]$
8	$(\bar{1}1\bar{1})[10\bar{1}]$	$(\bar{1}1\bar{1})[\bar{1}2\bar{1}]$	$(111)[1\bar{2}1]$	$(010)[10\bar{1}]$
9	$(\bar{1}1\bar{1})[\bar{1}\bar{1}0]$	$(\bar{1}1\bar{1})[\bar{1}12]$	$(1\bar{1}\bar{1})[1\bar{1}2]$	$(00\bar{1})[\bar{1}\bar{1}0]$
10	$(\bar{1}\bar{1}1)[0\bar{1}\bar{1}]$	$(\bar{1}\bar{1}1)[2\bar{1}1]$	$(\bar{1}1\bar{1})[21\bar{1}]$	$(\bar{1}00)[0\bar{1}\bar{1}]$
11	$(\bar{1}\bar{1}1)[101]$	$(\bar{1}\bar{1}1)[\bar{1}21]$	$(1\bar{1}\bar{1})[12\bar{1}]$	$(0\bar{1}0)[101]$
12	$(\bar{1}\bar{1}1)[\bar{1}10]$	$(\bar{1}\bar{1}1)[\bar{1}\bar{1}2]$	$(111)[11\bar{2}]$	$(001)[\bar{1}10]$

Cube

α	$(\mathbf{n}^{\alpha})[\mathbf{m}^{\alpha}]$
13	$(100)[011]$
14	$(100)[01\bar{1}]$
15	$(010)[101]$
16	$(010)[10\bar{1}]$
17	$(001)[110]$
18	$(001)[1\bar{1}0]$

Specific Functional Form for plastic shearing rates, $\dot{\gamma}^\alpha$ for $L1_2$ alloys

For *single phase* alloys having the $L1_2$ structure, the shearing rate on slip system α is taken as follows:

$$\dot{\gamma}^\alpha = \dot{\gamma}_o \left| \frac{\tau^\alpha}{s^\alpha} \right|^{\frac{1}{m}} \text{sign}(\tau^\alpha) \qquad \alpha = 1, \ldots, 18 \tag{2.13}$$

where $\dot{\gamma}_o$ is a reference strain rate and m is a strain rate sensitivity parameter. Also,

$$s^\alpha = \begin{cases} s_o + \xi \mu b \sqrt{\psi^\alpha}, & \alpha = 1, \ldots, 12, \\ s_{oc}, & \alpha = 13, \ldots, 18. \end{cases} \tag{2.14}$$

The parameters s_o and s_{oc} are the temperature-dependent initial values of the slip system resistances, taken to be equal to s_o for all 12 octahedral slip systems and equal to s_{oc} for all 6 cube slip systems. Since we are primarily interested in the small strain regime, *i.e.* 0.2% offset yield, strain hardening has not been considered in this model: s^α is a function of temperature and not of deformation.

The shear modulus, μ, appearing in equation 2.14 is defined as follows. The Hashin-Shtrikman bounds for the isotropic shear modulus of a polycrystal material made from cubic crystals are given by [Simmons and Wang, 1971]:

$$\mu_1^* = \mu_1 + 3\left(\frac{5}{\mu_2 - \mu_1} - 4\beta_1\right)^{-1} \tag{2.15}$$

$$\mu_2^* = \mu_2 + 2\left(\frac{5}{\mu_1 - \mu_2} - 6\beta_2\right)^{-1} \tag{2.16}$$

where

$$\beta_1 = \frac{3(\kappa + 2\mu_1)}{5\mu_1(3\kappa + 4\mu_1)} \tag{2.17}$$

$$\beta_2 = \frac{3(\kappa + 2\mu_2)}{5\mu_2(3\kappa + 4\mu_2)} \tag{2.18}$$

$$\mu_1 = \frac{1}{2}(C_{11} - C_{12}) \tag{2.19}$$

$$\mu_2 = C_{44} \tag{2.20}$$

$$\kappa = \frac{1}{3}(C_{11} + 2C_{12}) \tag{2.21}$$

with κ the bulk modulus, and the C_{ij} the anisotropic elastic constants. In this study, we

take μ to be simply the average of these upper and lower bounds,

$$\mu = \frac{1}{2}(\mu_1^* + \mu_2^*) \tag{2.22}$$

The parameter b is the magnitude of the Burgers vector. The parameter ξ in equation 2.14 is a temperature-dependent parameter which is representative of the *strength* of the pinning obstacles. This strength is taken to decrease with increasing temperature according to the following simple phenomenological form,

$$\xi = \xi_o \exp\left(\frac{A}{\theta - \theta_c}\right), \qquad \theta < \theta_c \tag{2.23}$$

where ξ_o and A are positive constants, θ is the absolute temperature, and θ_c is a critical temperature, taken here to be approximately the temperature for precipitation of the γ' particles from the solutionized condition. At temperatures approaching θ_c,

$$\begin{aligned} & \theta \rightarrow \theta_c \\ \Rightarrow & \frac{A}{\theta - \theta_c} \rightarrow -\infty \\ \text{and} \quad & \xi \rightarrow 0 \end{aligned}$$

The obstacle density on slip system α, ψ^α, is taken to be given by the function,

$$\psi^\alpha = \psi_*^\alpha \exp\left(-\frac{H}{k\theta}\right) \tag{2.24}$$

where ψ_*^α is the obstacle density at gross yield, k is the Boltzmann constant, and H is the activation enthalpy for cross-slip given in equation 2.1 and repeated here for completeness.

$$H = \frac{\mu b^3}{4\pi}\left\{h + c + \kappa_1(t_{pe} - \kappa_2 t_{se}) - \sqrt{\left(\frac{1}{\sqrt{3}} - \frac{\Gamma\{001\}}{\Gamma\{111\}} + |t_{cb}|\right)\frac{b}{B}}\right\} \tag{2.25}$$

with all the terms defined previously.

The constitutive model for fcc materials has been implemented previously by Kalidindi [1992]. In the present study, the necessary modifications have been made to that model to simulate $L1_2$ and two-phase γ/γ' materials and it has been implemented in conjunction with Lin [1994] in the finite element code ABAQUS [1991].

2.3 Data for Ni_3Al (γ'-type) materials from the Literature

Heredia [1990] has performed tension and compression experiments on binary Ni_3Al and $Ni_3(Al,X)$ with several different ternary additions. His experiments were performed at a fixed strain rate of $\dot{\epsilon} = \pm 1.3 \times 10^{-3}$/sec in a few different orientations from temperatures of 77 to 1400K. Figure 2-14 shows the temperature dependence of the critical resolved shear stress (CRSS) on the octahedral slip systems for binary Ni_3Al and Ni_3Al+0.2%B in tension and compression.

In the present study simulations were performed in ABAQUS with the model developed here using a single 3-dimensional, 8-noded continuum element (ABAQUS type C3D8). The element was deformed in the 3-direction at a constant true strain rate of $\dot{\epsilon} = \pm 1.3 \times 10^{-3}$/sec just to yield. Different orientations, given by their Miller indices (hkl), were represented by a set of Euler angles, (ϕ, θ, ω) which rotate the $[hkl]$ axis of the crystal into alignment with the [001] global axis [Hirth and Lothe, 1982] (See Appendix A). The yield strength was taken as the stress corresponding to 0.2% plastic strain.

The Ni_3Al+0.2%B was simulated since the asymmetry is more pronounced than in the binary Ni_3Al and because there was data for an orientation near $\langle 111 \rangle$. The $\langle 001 \rangle$ and $\langle 111 \rangle$ data were used to fit the model parameters, while the other orientations serve as predictions. The non-temperature-dependent parameters used in these simulations are listed in Table 2.2.

Table 2.2: Model parameters

$\dot{\gamma}_o(\text{sec}^{-1})$	.001
$b(\text{m})$	2.5×10^{-10}
$\Gamma^{\{111\}}(\text{Jm}^{-2})$	0.300
$\Gamma^{\{001\}}(\text{Jm}^{-2})$	0.083
h	0.2
c	0.5
κ_1	0.282
κ_2	0.7
$\psi^{\alpha}_{*}(m^{-2})$	5.0×10^{15}
ξ_o	1.15
$A(K)$	325
$\theta_c(\text{K})$	1500

Figure 2-15(a) through (f) plots the experimental and simulated values of yield strength over the temperature range. All of the graphs are summarized in Figure 2-16 for comparison.

The fit is good, although the orientation where there is zero asymmetry in the experimental data shows some asymmetry in the simulations. No stress-strain data was available in this case.

According to Lall *et al.* [1979], however, the tension-compression asymmetry should disappear along the $\langle 012 \rangle$ - $\langle \bar{1}13 \rangle$ great circle, where τ_{pe} is zero. This is not the case with the data of Heredia [1990]. The zero-asymmetry orientation lies on the $\langle 001 \rangle$ side of the said great circle. Considering equation 2.25, we see that the shear stress τ_{se} is also included in the formulation of the activation enthalpy which controls the obstacle density. By making the term $\kappa_1(t_{pe} - \kappa_2 t_{se})$ zero, the tension-compression asymmetry disappears. This may be accomplished by setting κ_1 or the term in parentheses to zero. Adjusting κ_2, *i.e.* changing the relative weights of the τ_{pe} and the τ_{se} terms, therefore, allows us to shift the zero-asymmetry line away from the $\langle 012 \rangle$ - $\langle \bar{1}13 \rangle$ great circle in either direction: $\kappa_2 > 0$ moves the zero-asymmetry line closer to the $\langle 111 \rangle$-$\langle 011 \rangle$ great circle, while $\kappa_2 < 0$ moves closer to the $\langle 001 \rangle$ corner. Paidar *et al.* [1984] suggest a range of $0.7 \leq \kappa_2 \leq 1.0$ based on their theoretical calculations. $\kappa_2 = 1$ gives zero asymmetry along the $\langle 001 \rangle$-$\langle 111 \rangle$ boundary, since for those orientations $\tau_{pe} = \tau_{se}$ for all active slip systems. For the present case, $\kappa_2 = -0.46$ makes the zero-asymmetry orientation coincide with experiment. This value, however, causes the predictions in the $\langle 011 \rangle$ corner to be significantly degraded, Figure 2-17. Figure 2-18 shows the predictions when κ_2 is set to zero, *i.e.* no τ_{se} term; for orientations on the $\langle 001 \rangle$ side, tension is higher than compression, while on the $\langle 011 \rangle$ -$\langle 111 \rangle$ side, compression is higher than tension.

The variation of s_o and s_{oc} used in these simulations are plotted in Figure 2-19. From the above experimental data we obtained the following monotonically decreasing functions of temperature for s_o and s_{oc} (units of MPa, with the θ premultipliers in MPa/K):

$$s_o = \begin{cases} 115. - 0.144\theta, & \theta \leq 659\text{K} \\ 20., & 659\text{K} < \theta < 1000\text{K} \\ 132. - 0.1124\theta, & 1000\text{K} < \theta < 1174\text{K} \\ 0.01, & \theta \geq 1174\text{K} \end{cases} \tag{2.26}$$

$$s_{oc} = \begin{cases} 330., & \theta \leq 915\text{K} \\ 858. - 0.577\theta, & \text{otherwise} \end{cases} \tag{2.27}$$

2.3.1 Simulations over the Stereographic Triangle

A few temperatures were also selected to perform simulations over the entire stereographic triangle to study the orientation dependence of yield strength. Figure 2-20(a), (b) and (c) plots the yield strength over the entire stereographic triangle for one temperature below the peak, around the peak temperature, and one temperature above the peak, respectively, in tension and in compression. These simulations were performed with $\kappa_2 = 0.7$ as in the original simulations [Paidar *et al.*, 1984].

At the lowest temperature, the ⟨111⟩ corner of the stereographic triangle is the highest, with compression higher than tension. Similarly for the ⟨011⟩ orientation, compression is higher than tension while the opposite is true for the ⟨001⟩ orientation. The zero-asymmetry line lies somewhere in the middle of the triangle. At the peak temperature and the highest temperature, the value of the ⟨111⟩ yield strength, and to a lesser extent the ⟨011⟩ yield strength are reduced relative to that of the ⟨001⟩. This may be attributed to the activation of cube slip systems at these temperatures. This has no effect on the ⟨001⟩ orientation.

Also, at all temperatures there is practically no asymmetry in the ⟨111⟩ orientation. This is also due to the activation of cube slip at all temperatures in this orientation. Recall that the asymmetry is due to the non-Schmid shear stresses, which do not play a role on the cube slip systems. Therefore, for this orientation, since cube slip dominates, there will be very little tension-compression asymmetry.

2.4 Discussion

The micro-mechanisms believed to be operative during the plastic deformation of $L1_2$ intermetallics are accounted for in the present model for the macroscopic yielding of these alloys. The anomalous behavior of these $L1_2$ intermetallics (the increase of yield strength with increasing temperature, and the tension-compression asymmetry) are picked up by this model. Aside from the material properties which can be measured (C_{11}, C_{12}, C_{44}), and physical constants which can be calculated or estimated ($\theta_c, \psi_*^\alpha, \Gamma^{\{001\}}, \Gamma^{\{111\}}$), the major parameters are the initial slip system resistances, s_o and s_{oc}, and the parameters which determine the amount of asymmetry, κ_1 and κ_2. The determination of these latter parameters require data in only two orientations since the octahedral and cube slip systems may be decoupled to some extent: ⟨001⟩ orientation gives octahedral slip properties, while

⟨111⟩ orientation gives cube slip properties.

The literature contains a large amount of data for the variation of the yield strength of $L1_2$ intermetallics with temperature. It may be noted that the value of the yield strength and its dependence on temperature also depends on the composition of the particular alloy (see, for example, [Heredia, 1990]). The present model makes no assumptions about the contributions of different ternary additions to the level of the yield strength of Ni_3Al. Therefore, different compositions may be modelled simply by changing the values of the slip system resistances to vary the level of the yield strength. Changes in material properties such as elastic constants and antiphase boundary energies with changes in alloy content are expected to be small.

The approach used here is to keep the model as simple as possible. The major elements of the deformation mechanisms are included, while some specific microscopic details may have been overlooked. Even so, we are able to represent, both qualitatively and quantitatively, the major trends in the response of the material. We feel that with this relatively simple approach, we have captured the essential features of the material response well.

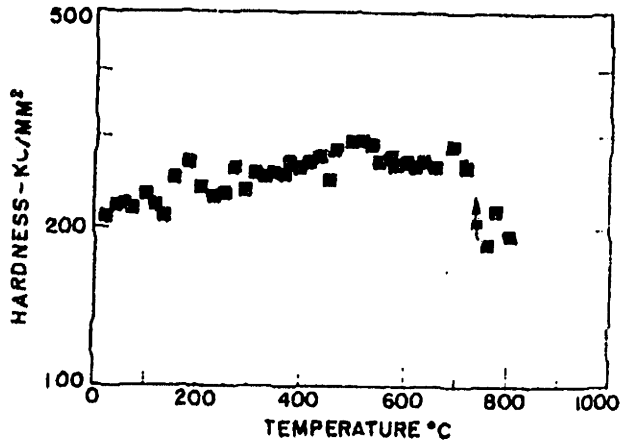

(a)

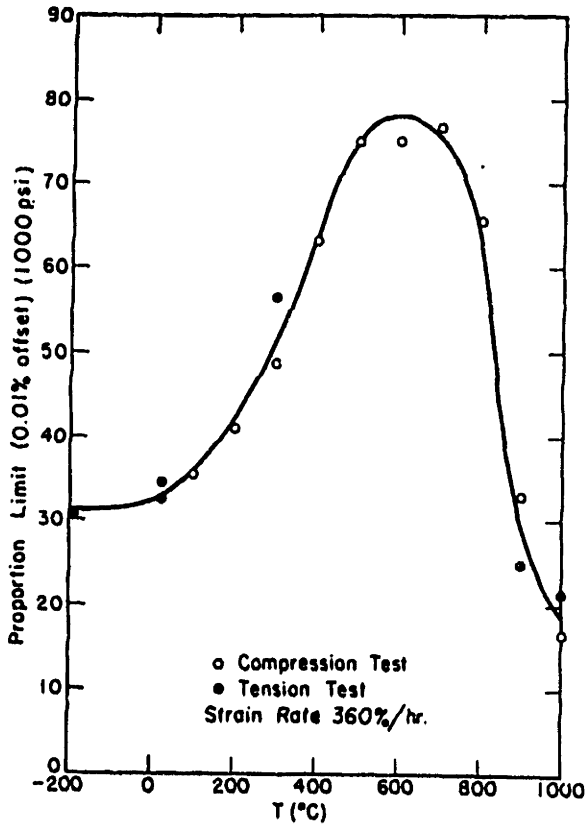

(b)

Figure 2-1: (a) Temperature dependence of the hardness of polycrystalline Ni_3Al [Westbrook, 1957] (b) Temperature dependence of yield strength of polycrystalline Ni_3Al [Flinn, 1960]

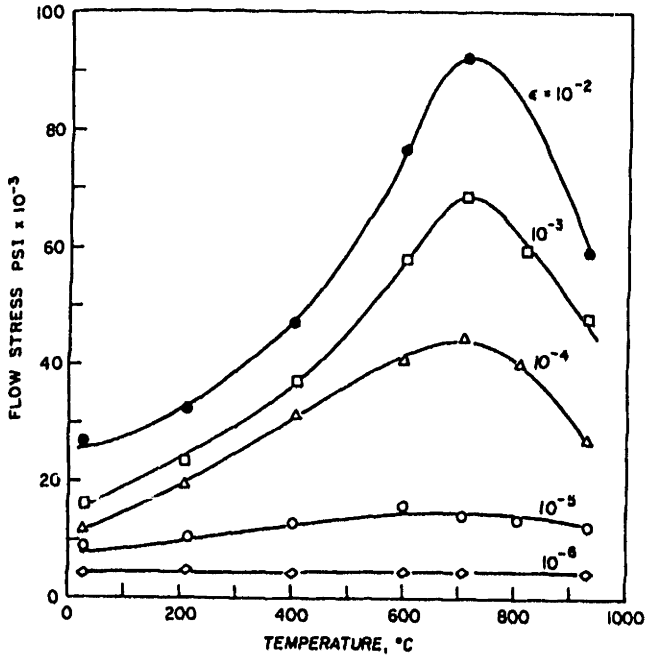

Figure 2-2: Variation of yield strength of polycrystalline Ni_3Al with temperature as a function of offset yield definition [Thornton *et al.*, 1970]

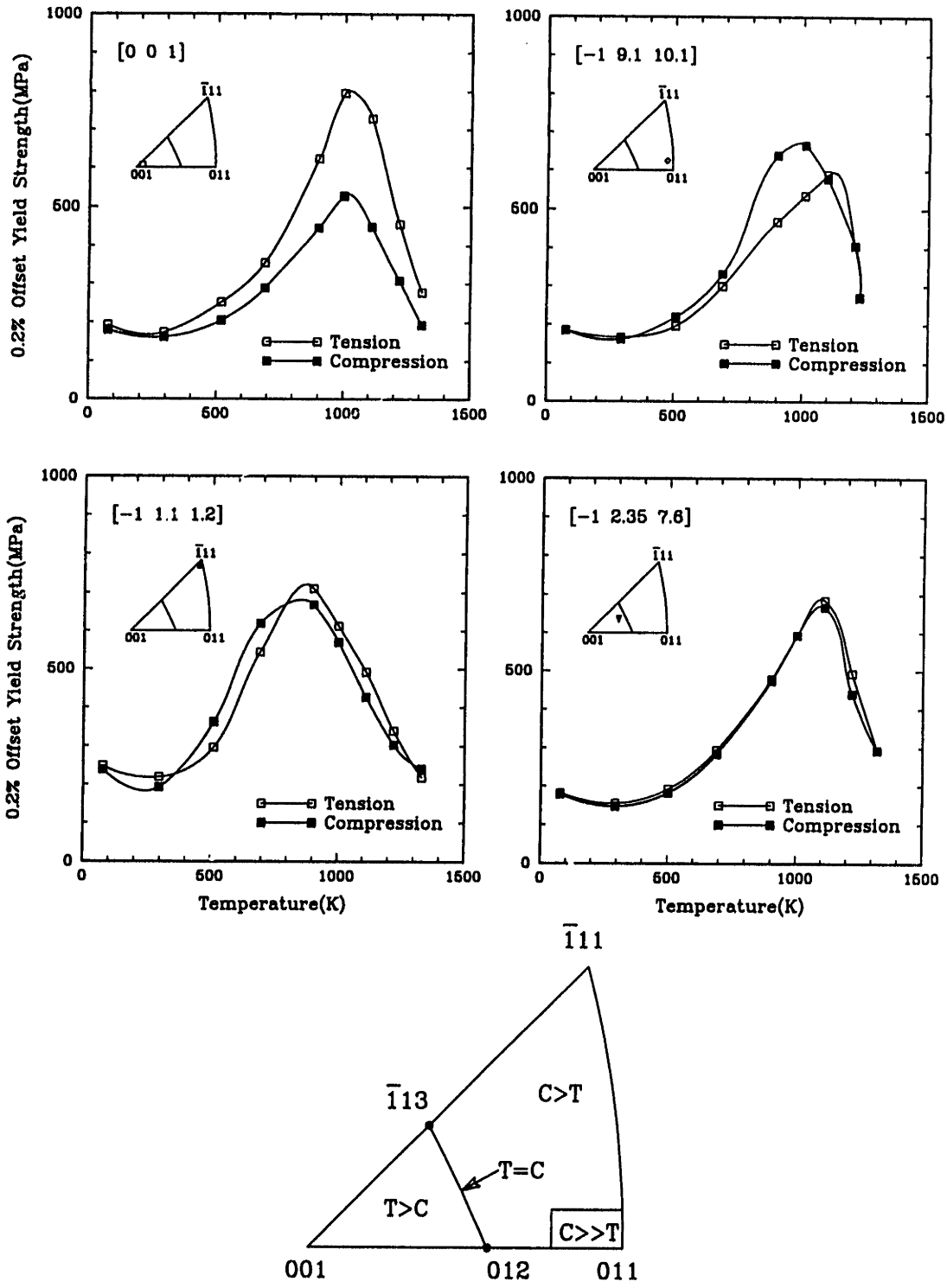

Figure 2-3: Temperature dependence of 0.2% offset yield strength for 4 orientations of Ni_3Al+0.2%B single crystals in tension and compression and expected dependence of yield strength on orientation [Heredia, 1990]

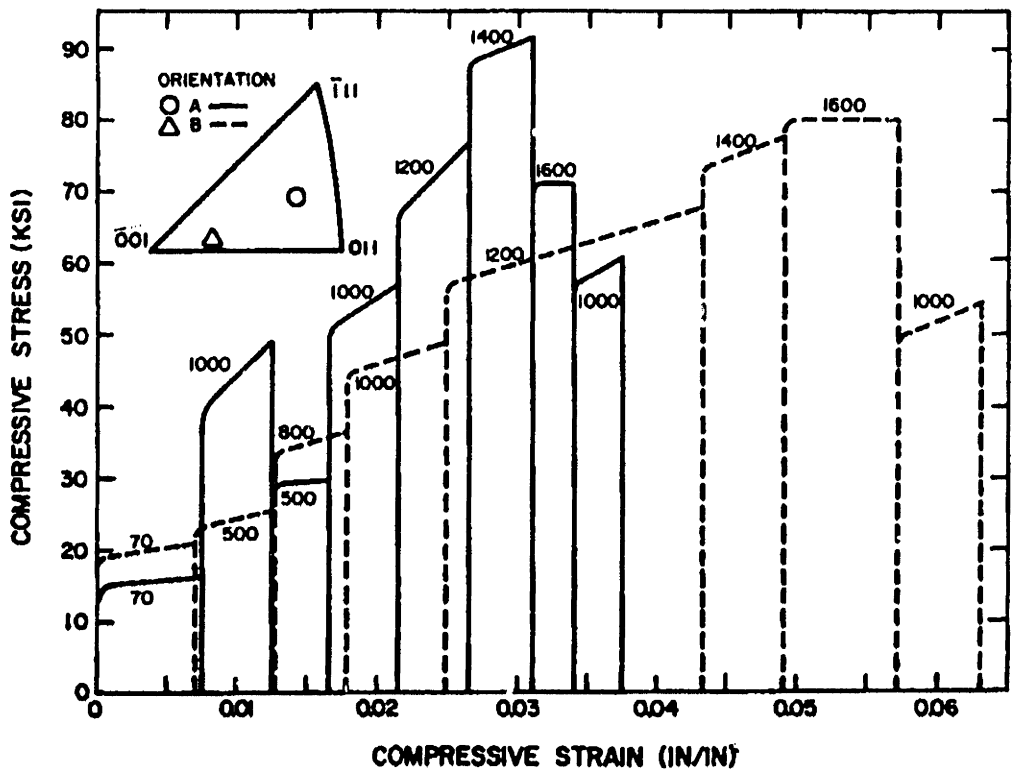

Figure 2-4: Consecutive stress-strain curves for single crystals of Ni_3Al at various temperatures in two single slip orientations. Temperature in °F [Copley and Kear, 1967]

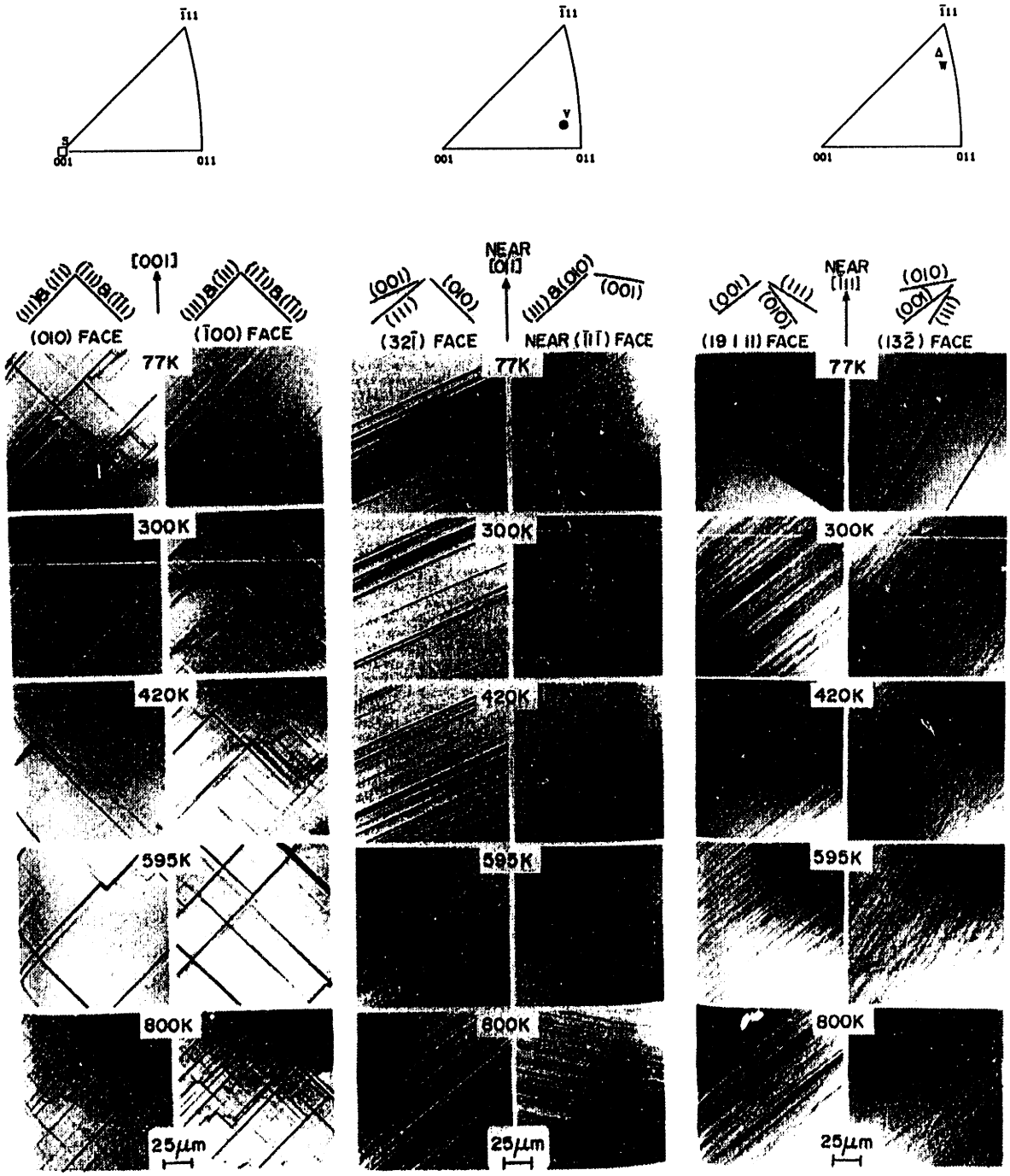

(a) (b) (c)

Figure 2-5: Slip traces on two orthogonal faces of ⟨001⟩-, near-⟨011⟩- and near-⟨111⟩-oriented samples of $Ni_3(Al,Nb)$ at various test temperatures [Lall *et al.*, 1979]

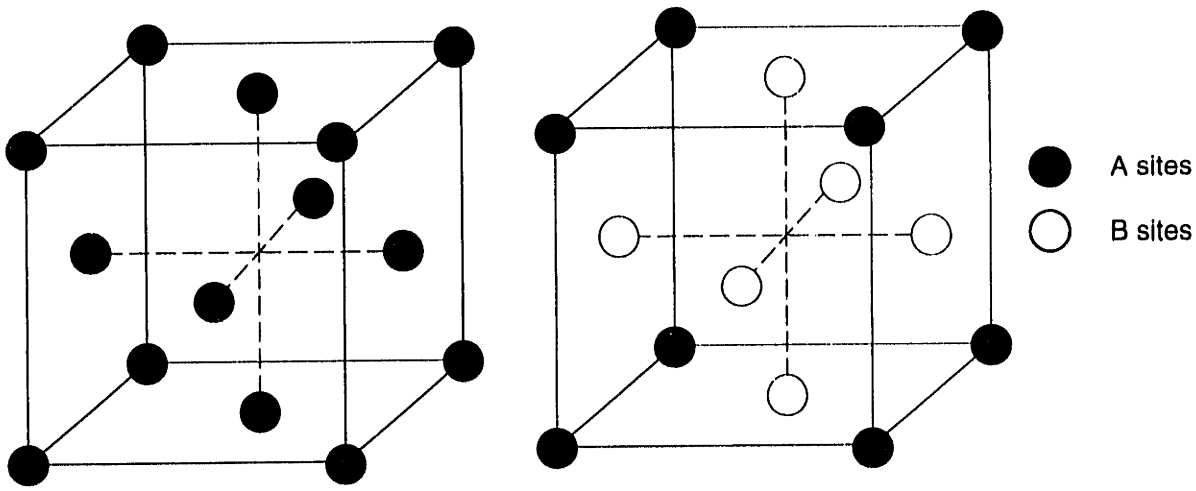

(a) (b)

Figure 2-6: (a) The fcc unit cell and (b) the $L1_2$ unit cell of AB_3 compounds

Figure 2-7: Long straight screw dislocations in $L1_2$ intermetallic, Cu_3Au, after 3% strain [Kear and Wilsdorf, 1962]

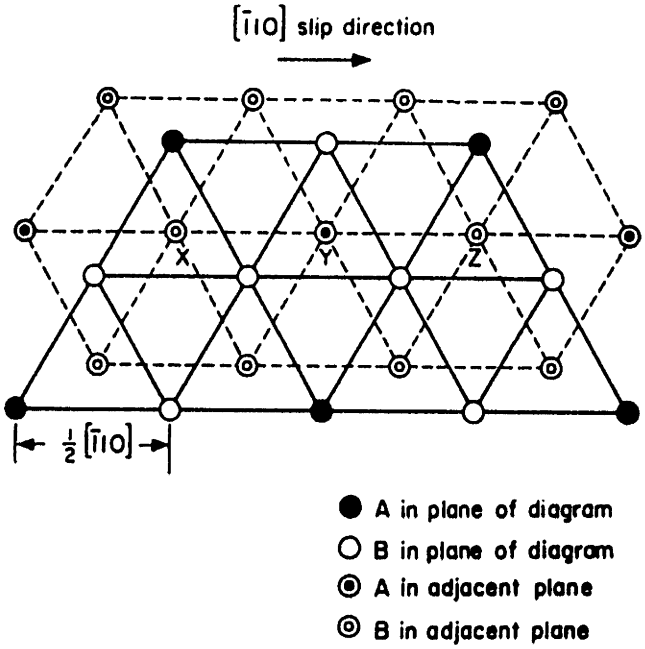

Figure 2-8: Arrangement of atoms in two adjacent (111) planes in an AB_3 superlattice [Hull and Bacon, 1984]

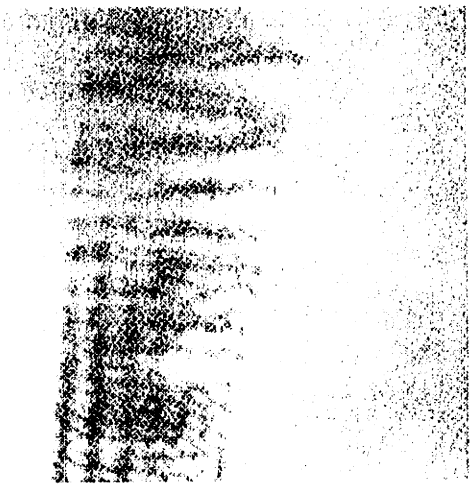

Figure 2-9: Dissociated superlattice dislocations in $AuCu_3$ [Marcinkowski *et al.*, 1961]

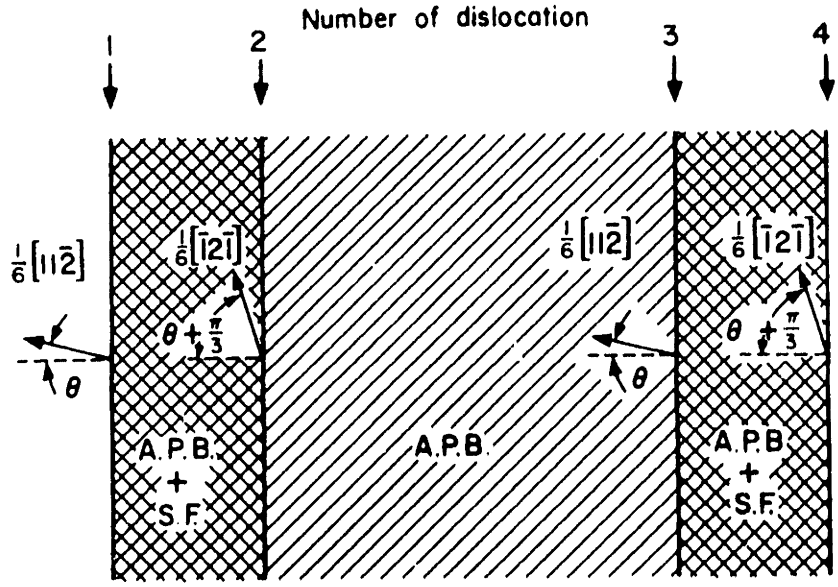

Figure 2-10: A dissociated $[01\bar{1}]$ superlattice dislocation in the AB_3 superlattice [Hull and Bacon, 1984]

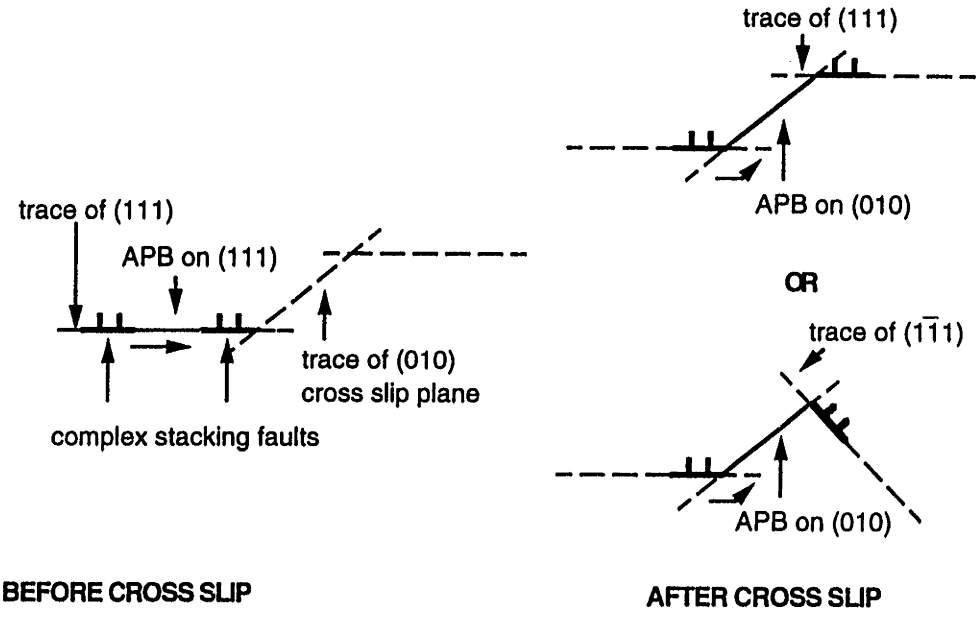

Figure 2-11: Recombination and cross-slip of Shockley partial dislocations from the (111) plane to the (010) plane followed by redissociation on either the (111) or (1$\bar{1}$1) plane [Cuitiño and Ortiz, 1993]

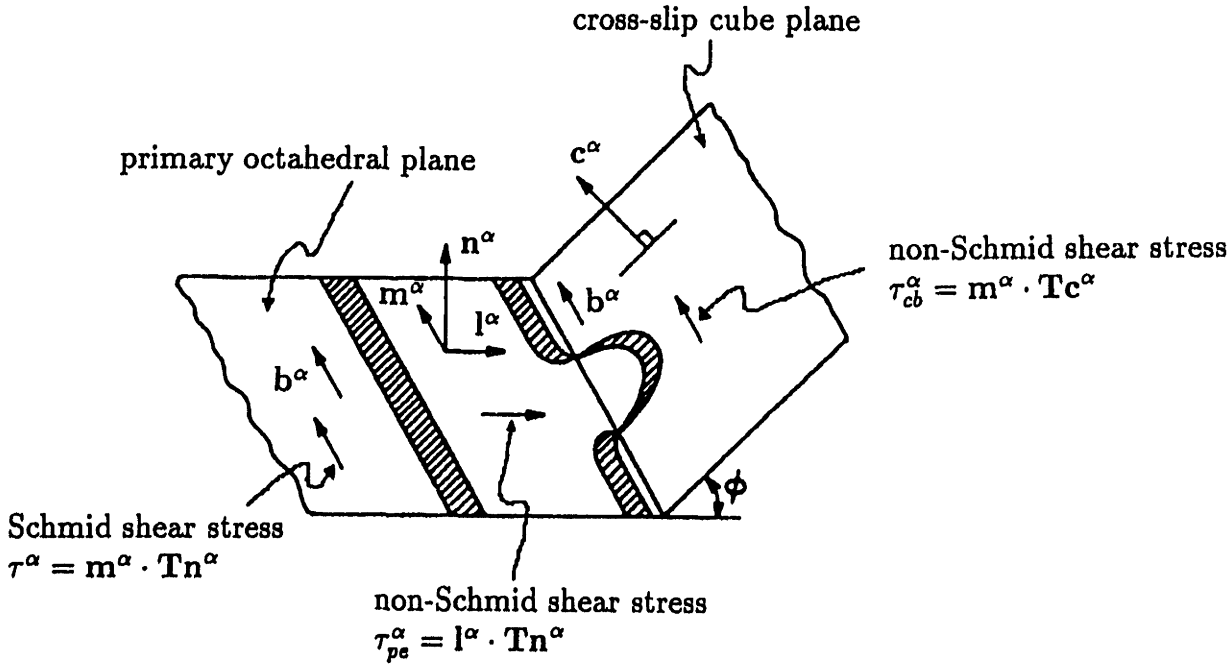

Figure 2-12: Constriction of the Shockley partial dislocations by τ_{pe}, cross-slip to the (010) plane, and definition of τ_{cb} [Asaro, 1983]

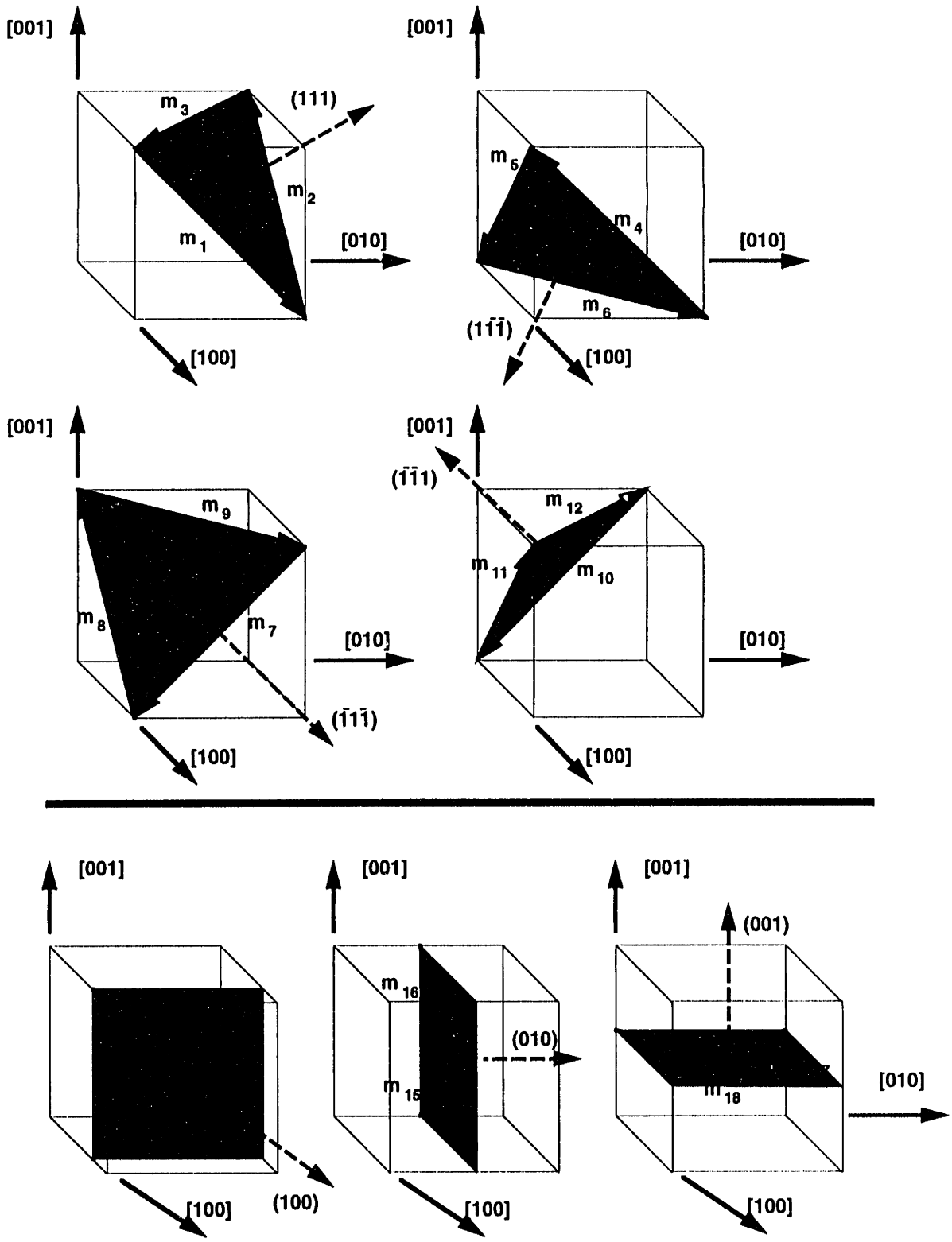

Figure 2-13: Slip systems — Octahedral and Cube

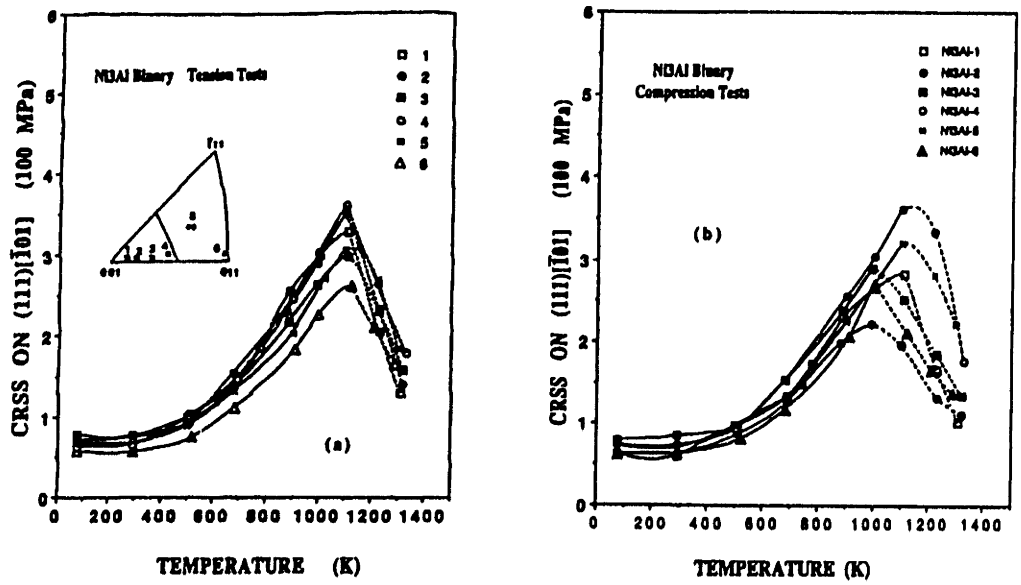

(a)

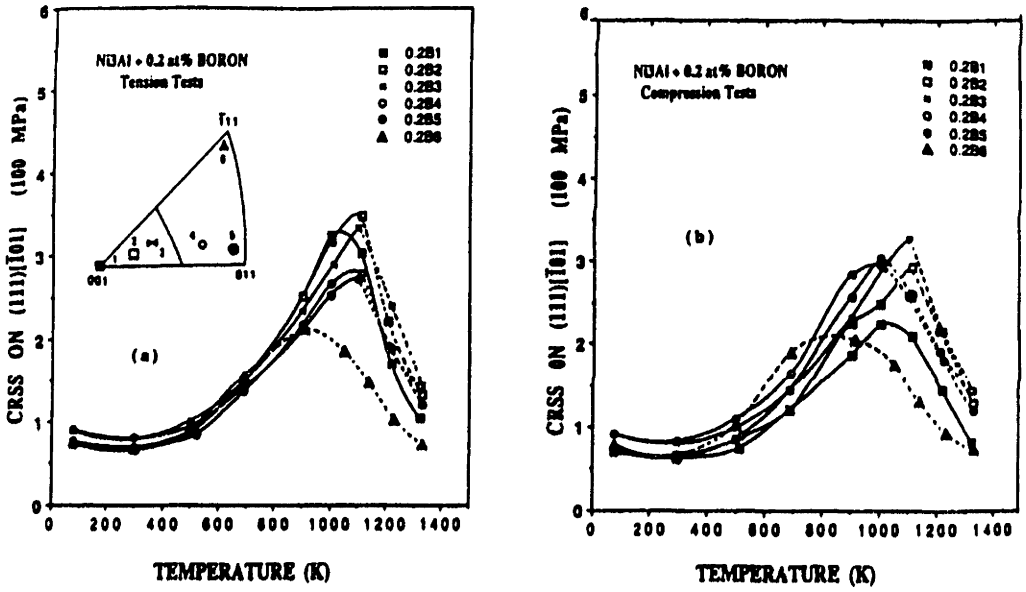

(b)

Figure 2-14: 0.2% offset yield strengths (a) Binary Ni_3Al (b) Ni_3Al+0.2%B [Heredia, 1990]

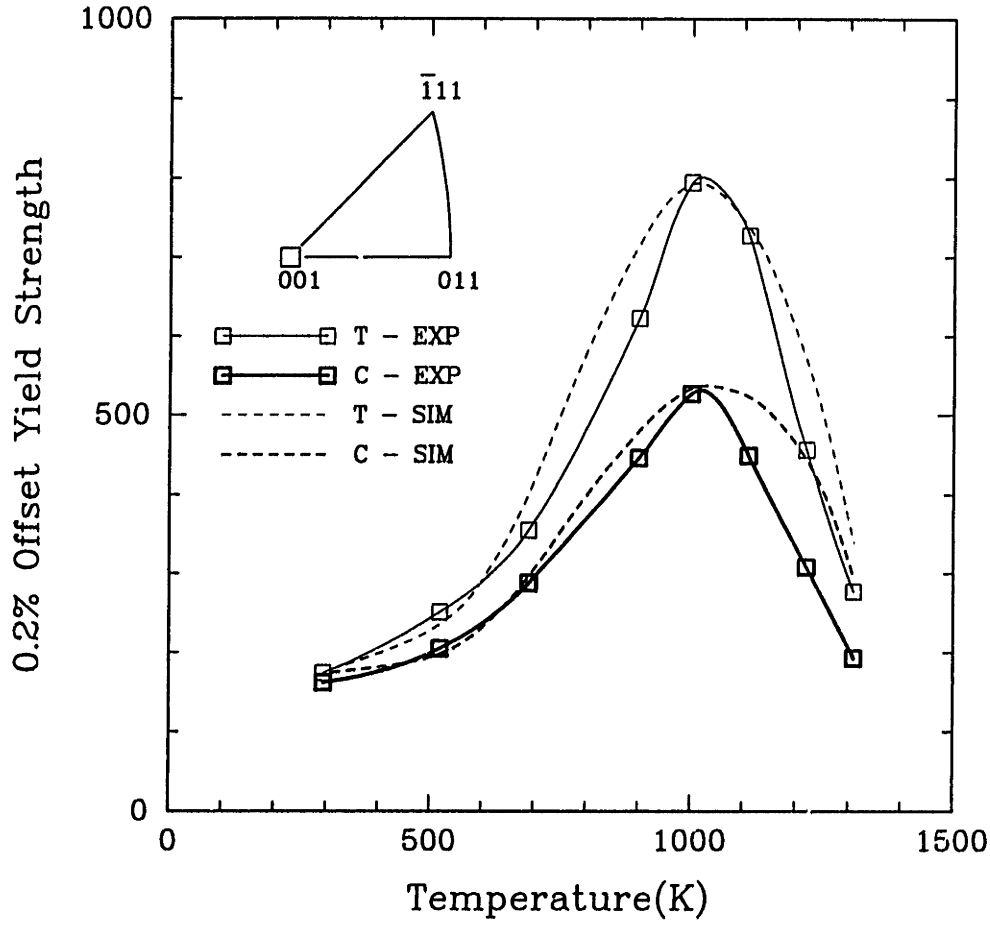

Figure 2-15: (a) Experimental and simulated yield strength vs. temperature curves for Ni_3Al+0.2%B — [001] fit

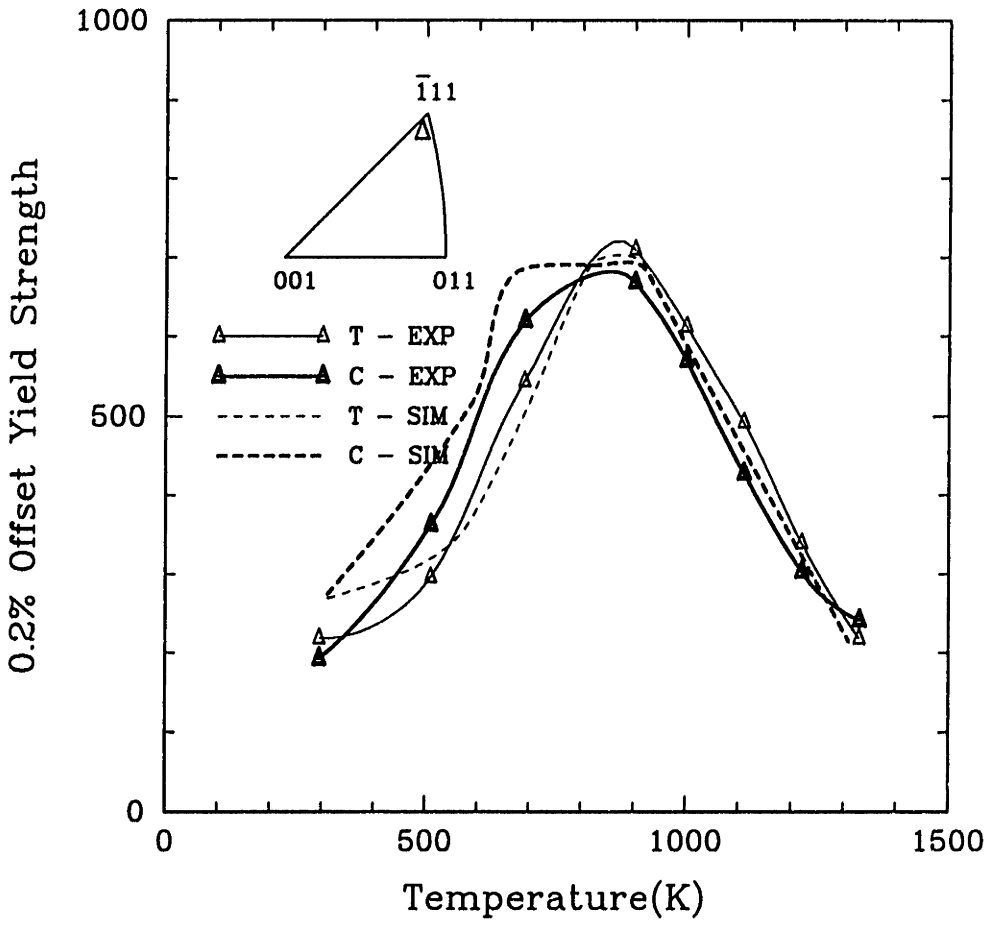

Figure 2-15: (b) Experimental and simulated yield strength vs. temperature curves for Ni_3Al+0.2%B — [-1 1.1 1.2] fit

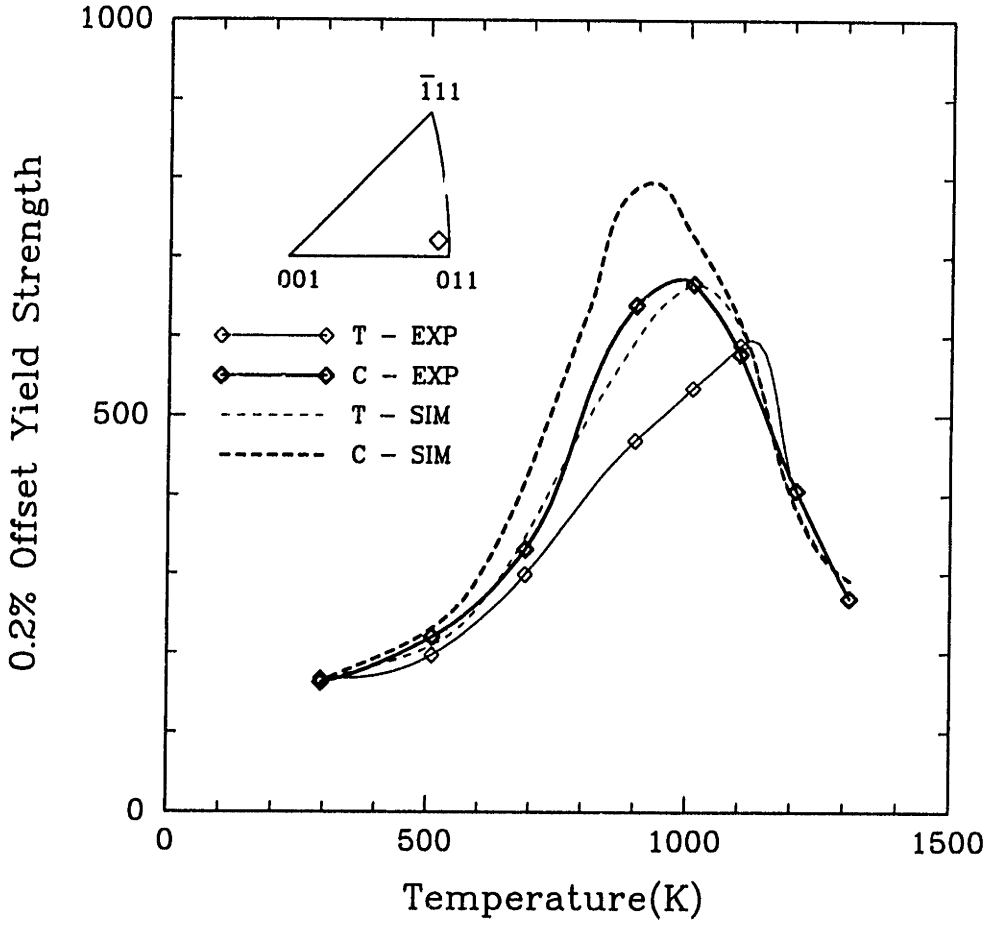

Figure 2-15: (c) Experimental and simulated yield strength vs. temperature curves for Ni_3Al+0.2%B — [-1 9.1 10.1] prediction

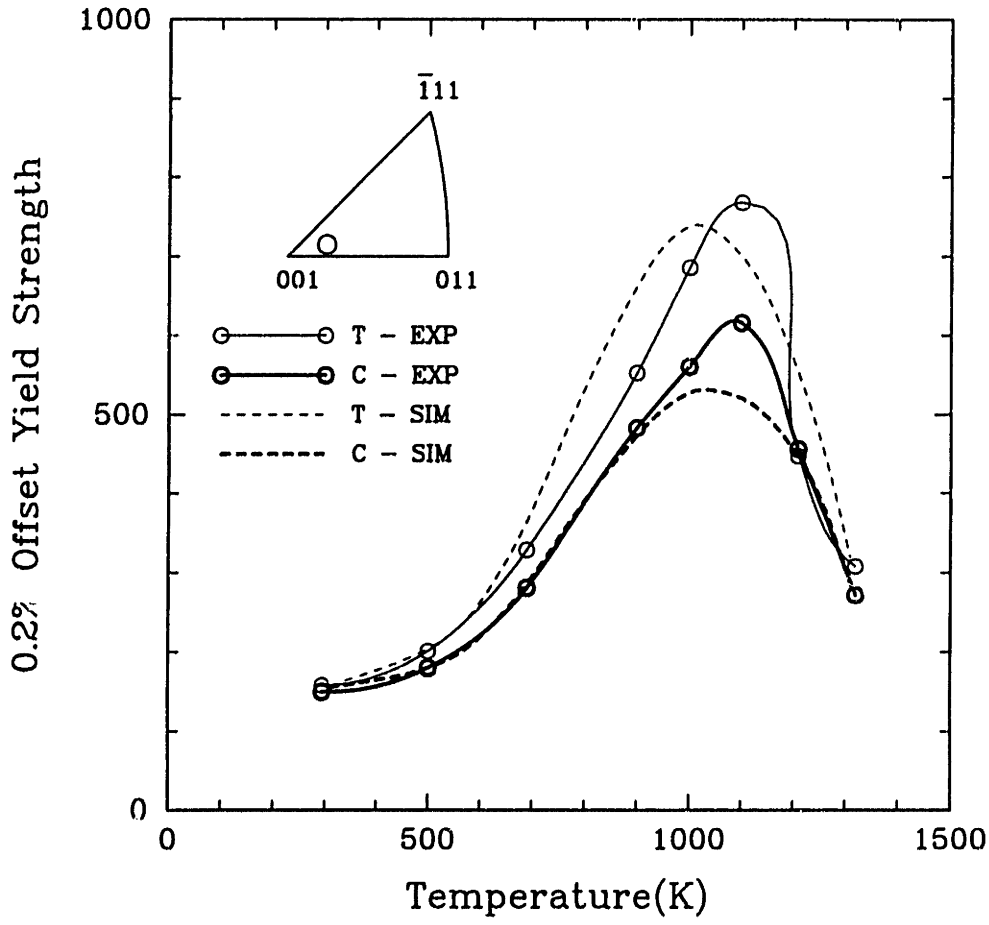

Figure 2-15: (d) Experimental and simulated yield strength vs. temperature curves for Ni_3Al+0.2%B — [-1 3.2 16] prediction

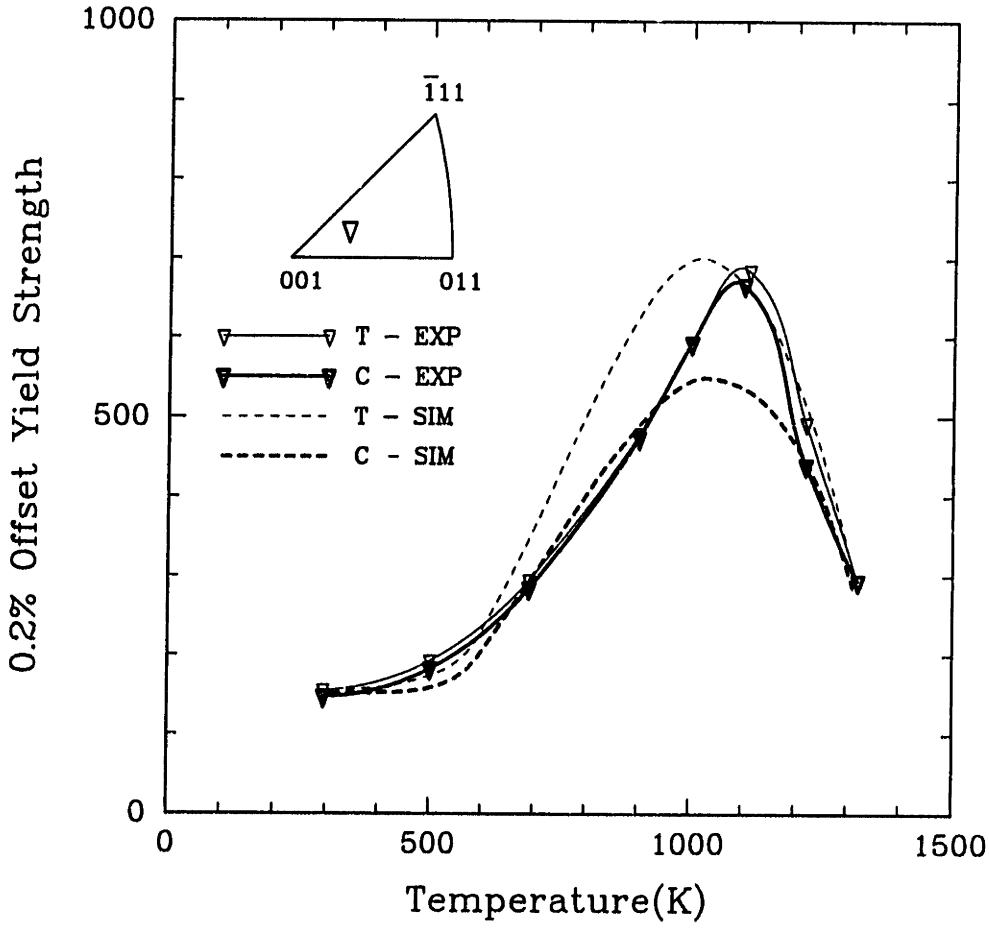

Figure 2-15: (e) Experimental and simulated yield strength vs. temperature curves for Ni_3Al+0.2%B — [-1 2.35 7.6] prediction

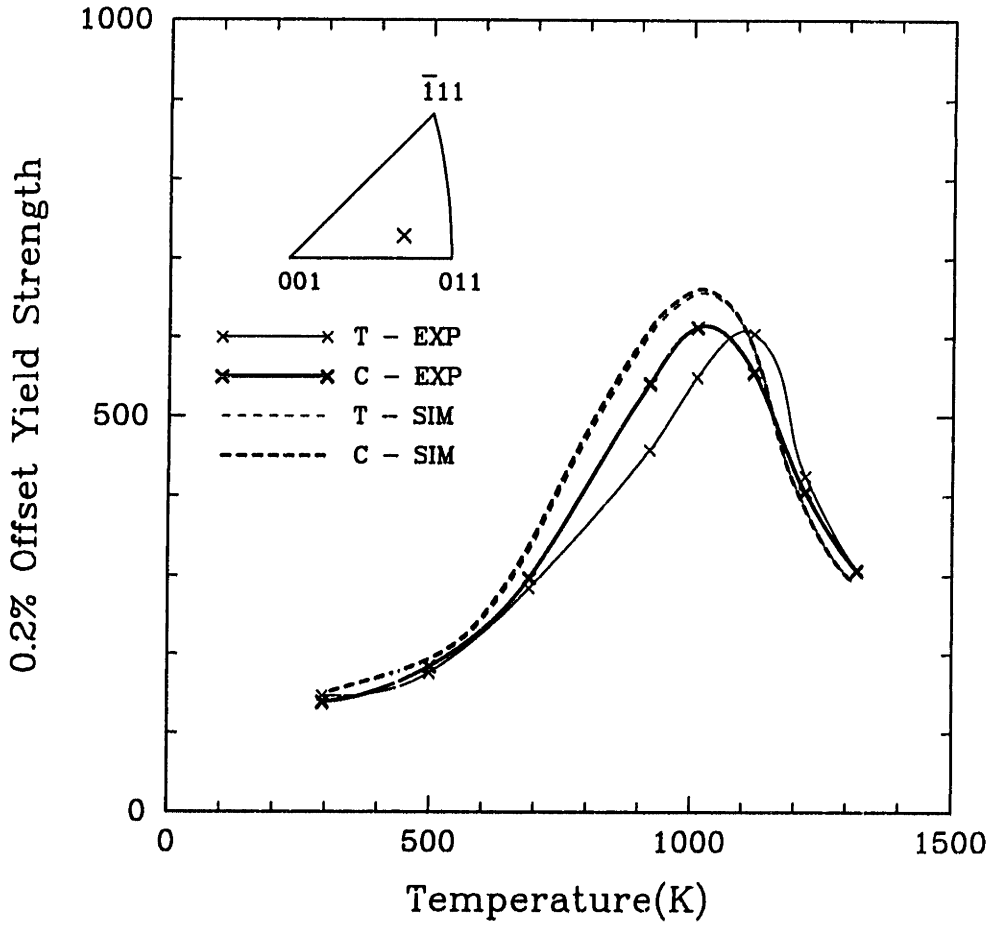

Figure 2-15: (f) Experimental and simulated yield strength vs. temperature curves for Ni_3Al+0.2%B — [-1 5 7.75] prediction

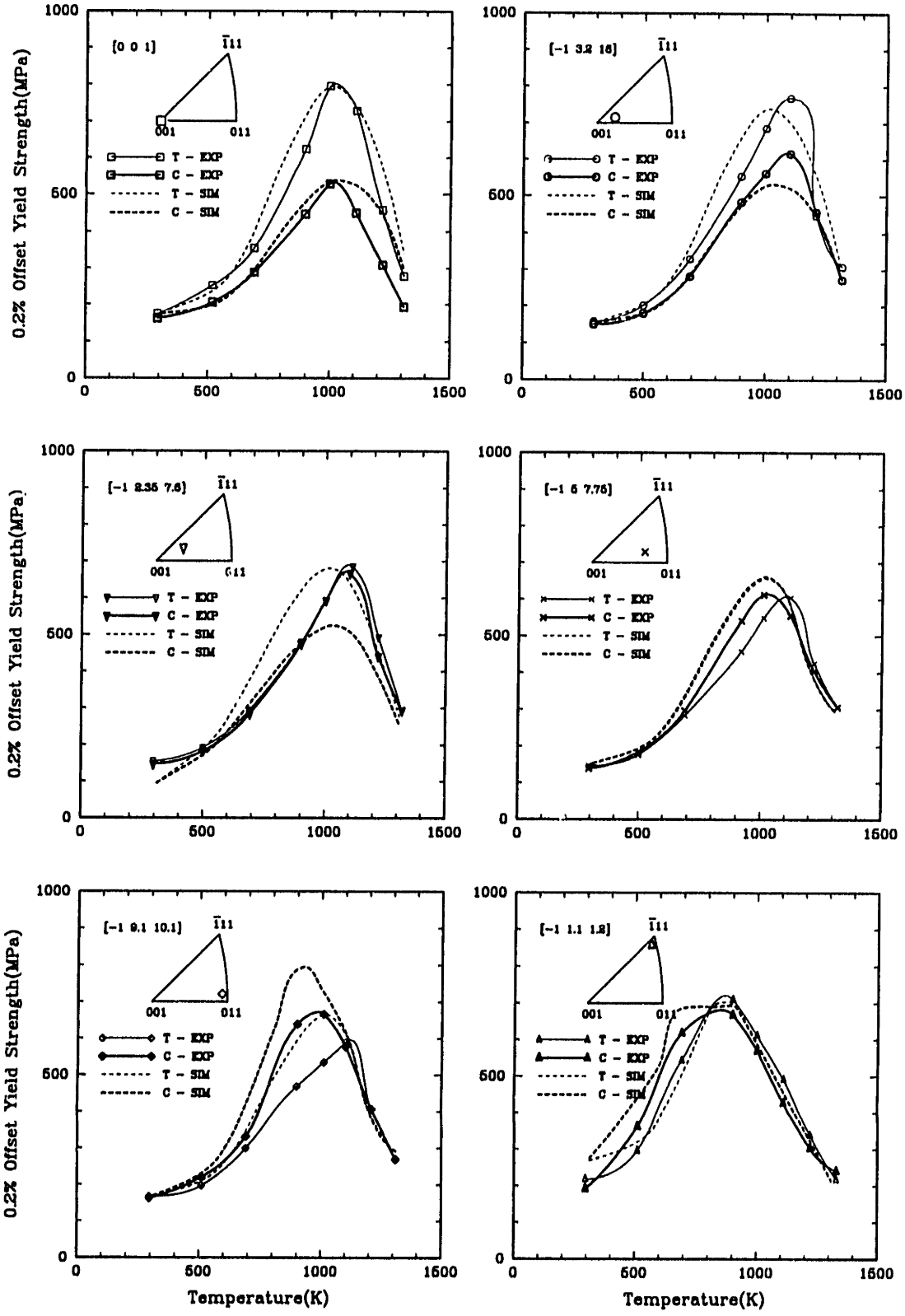

Figure 2-16: Experimental and simulated yield strength vs. temperature curves for Ni_3Al+0.2%B for six orientations

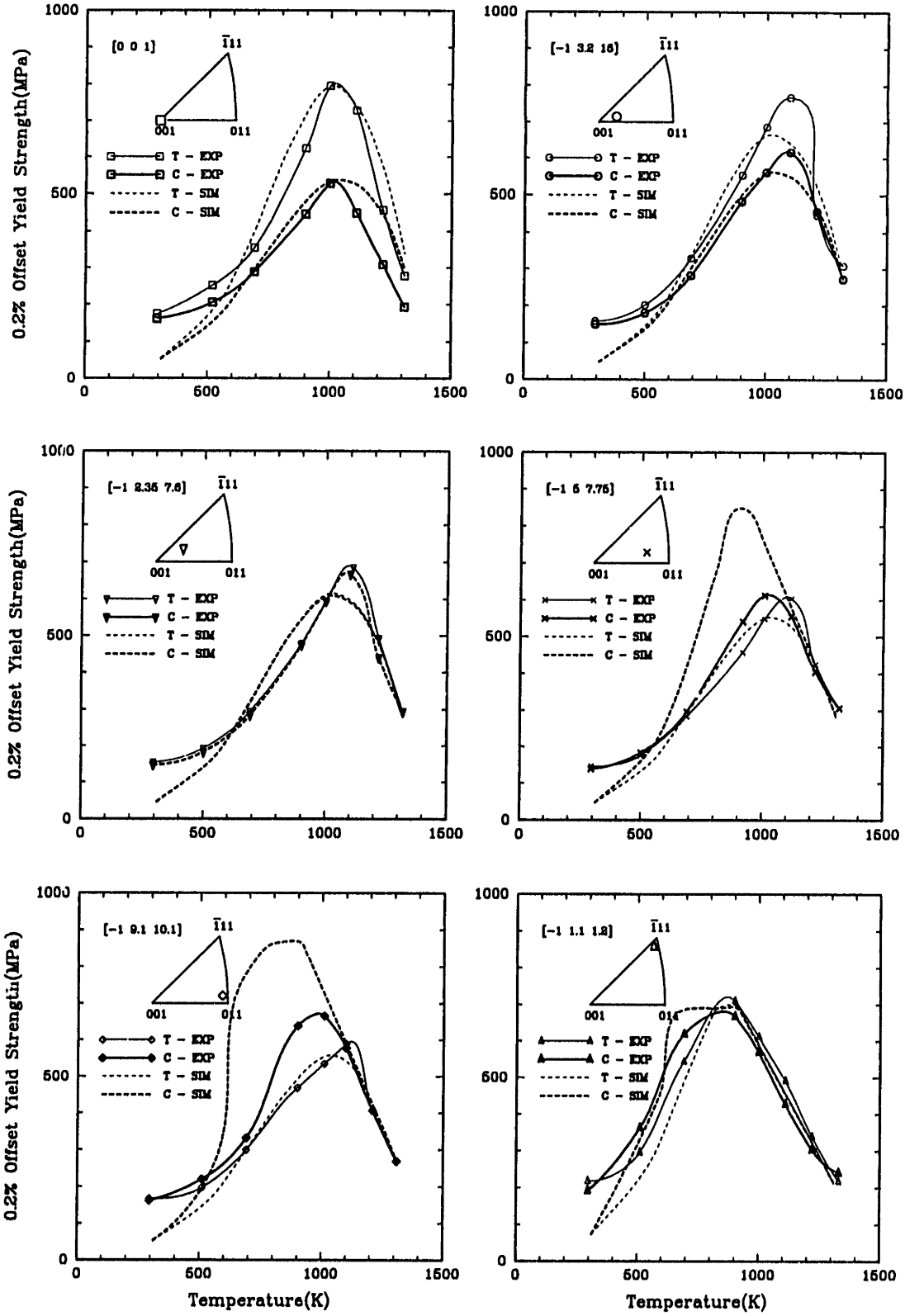

Figure 2-17: Experimental and simulated yield strength vs. temperature curves for Ni_3Al+0.2%B for six orientations – fit the zero asymmetry orientation

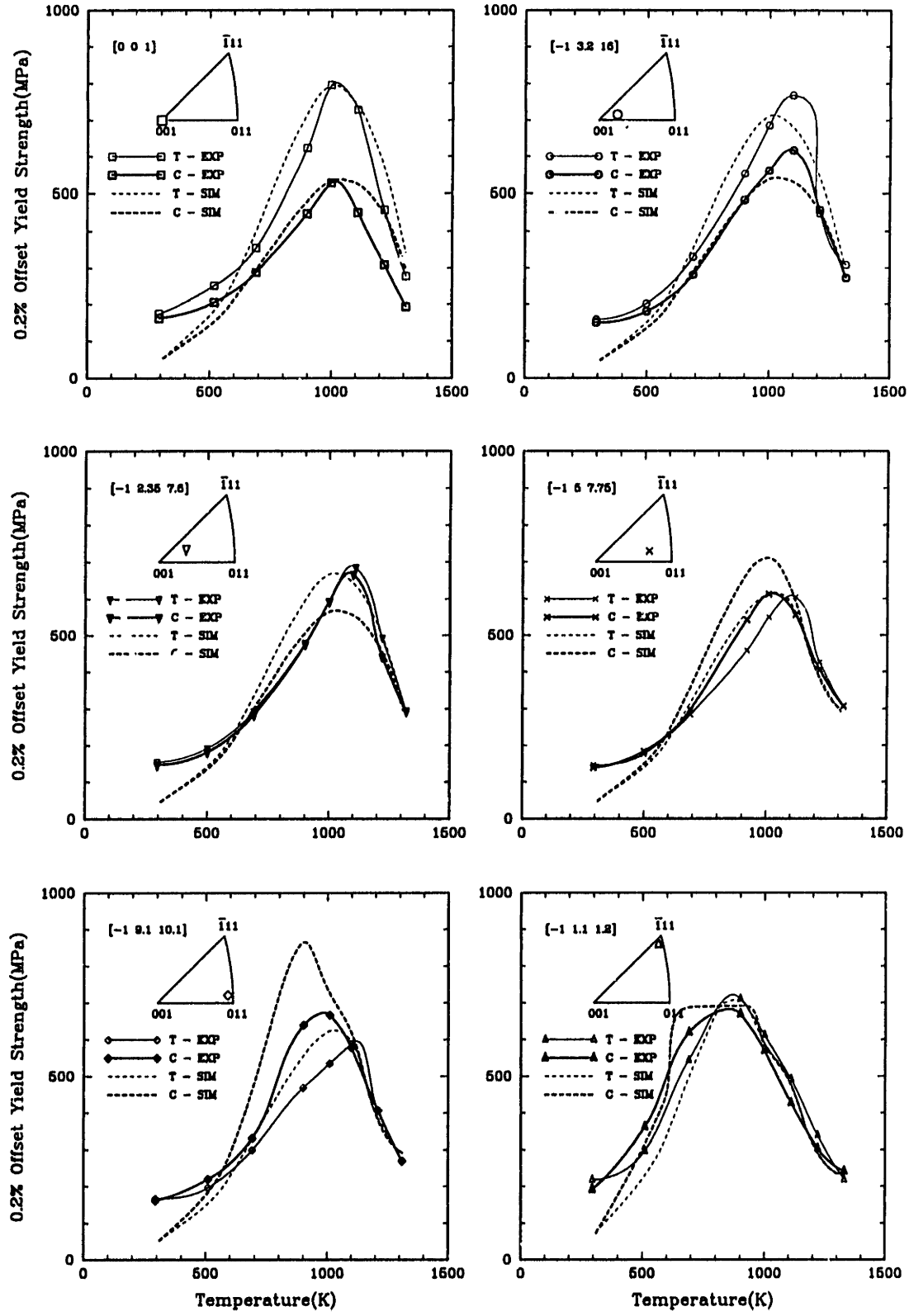

Figure 2-18: Experimental and simulated yield strength vs. temperature curves for Ni_3Al+0.2%B for six orientations – no contribution of τ_{sc}

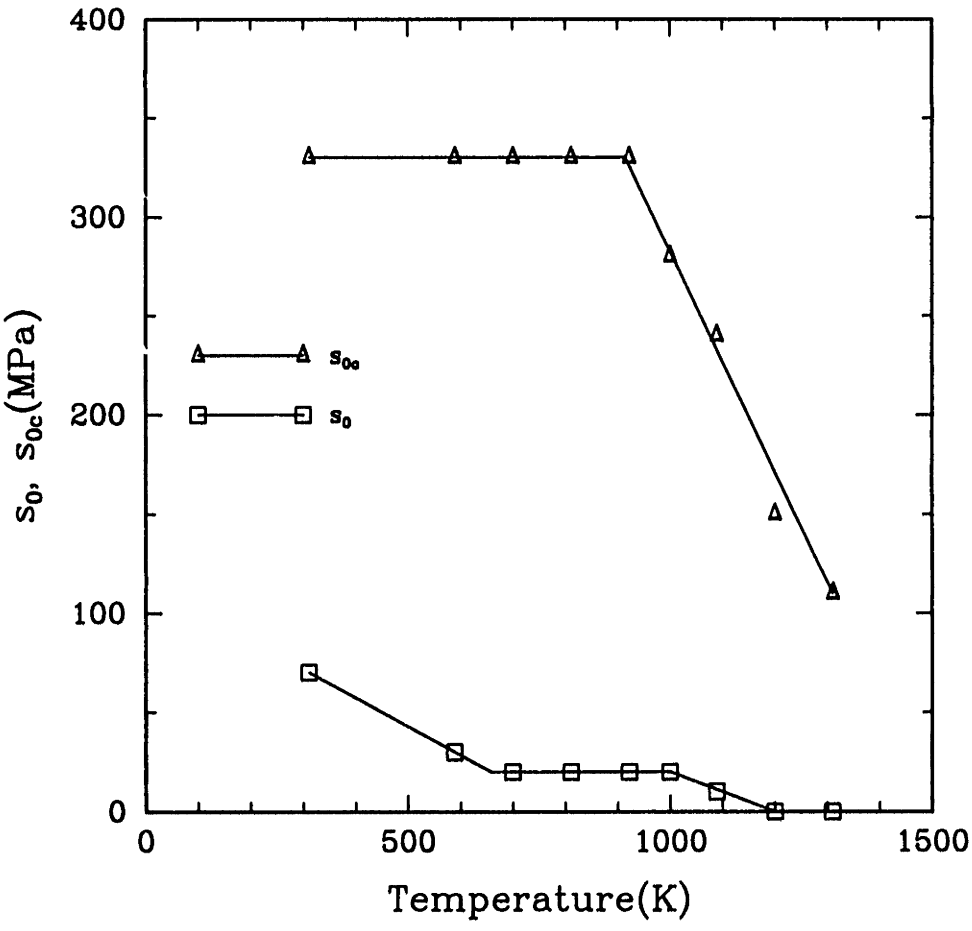

Figure 2-19: Temperature dependence of s_o and s_{oc}

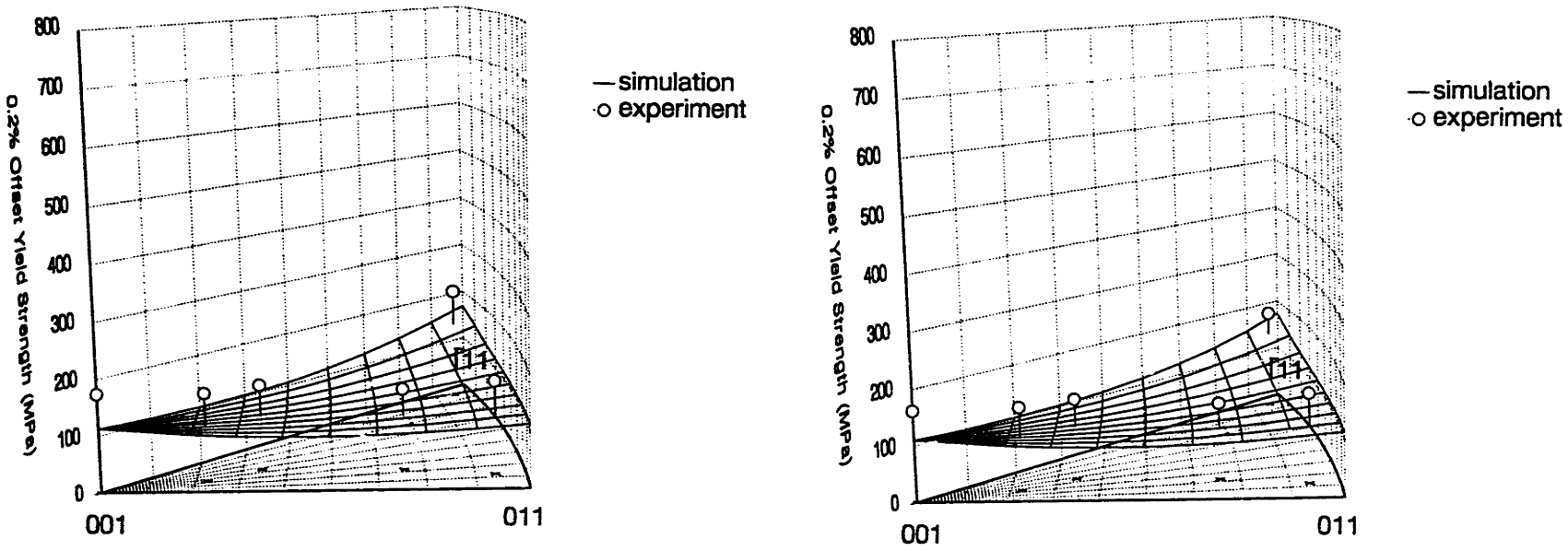

(a) (b)

Figure 2-20: Variation of yield strength with orientation at 311K (a) Tension (b) Compression

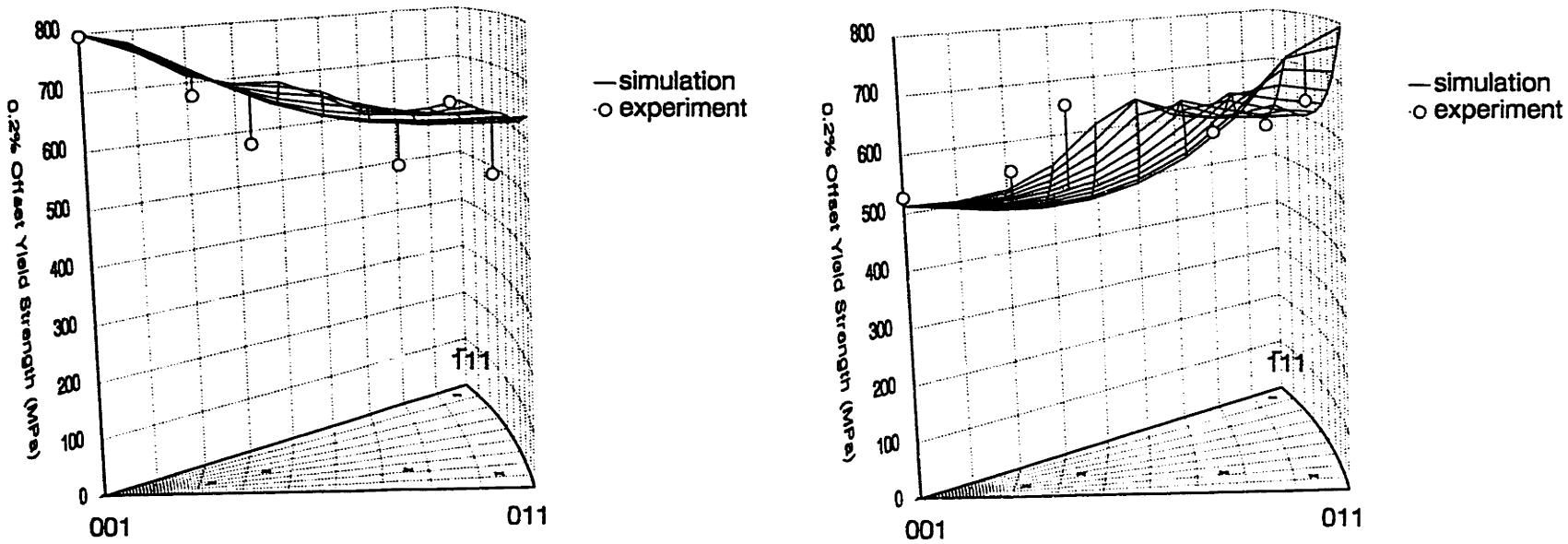

(a) (b)

Figure 2-20: Variation of yield strength with orientation at 1000K (a) Tension (b) Compression

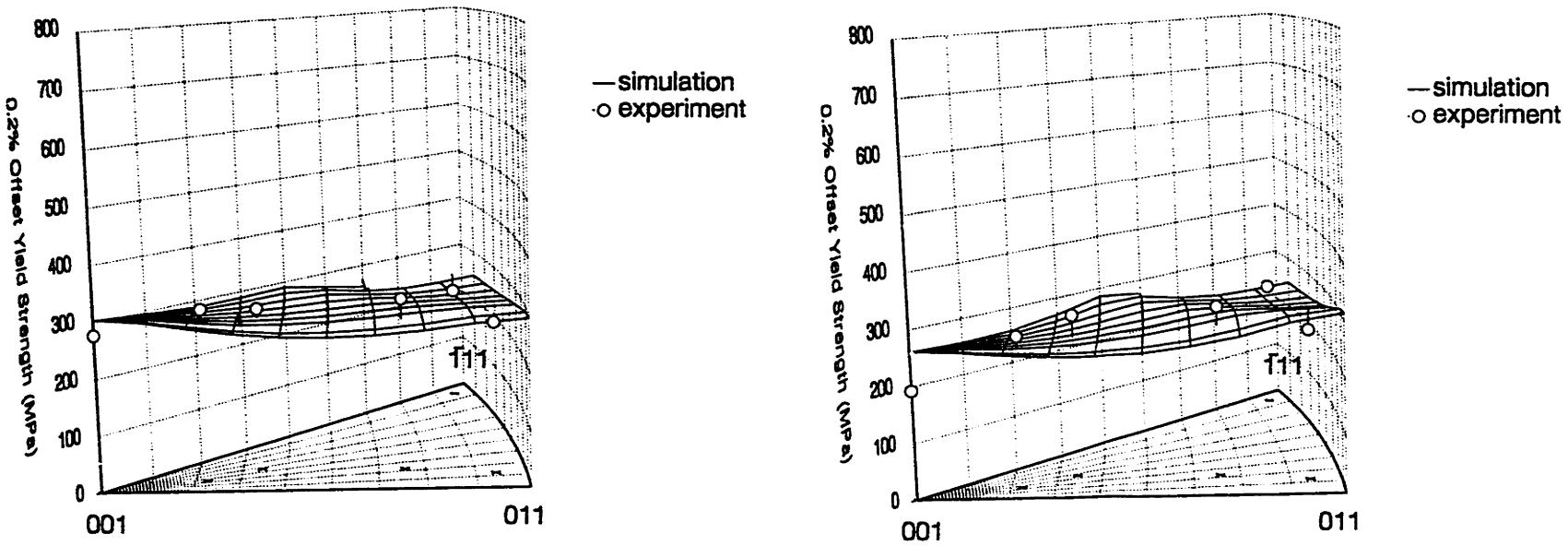

(a) (b)

Figure 2-20: Variation of yield strength with orientation at 1310K (a) Tension (b) Compression

Chapter 3

Tension and Compression Experiments and Simulations on Two-Phase CMSX4

3.1 Experimental Program

3.1.1 Material and Tests performed

Monotonic tension and compression experiments were performed on single crystal CMSX4 at various constant temperatures. The CMSX4 was kindly provided by Dr. Ken Harris of Cannon Muskegon and the Allison Gas Turbine Division of GM in 0.5 inch diameter bars of about 6 inch length in the ⟨001⟩, ⟨011⟩ and ⟨111⟩ [1] orientations. Apart from the ⟨111⟩ bars, which were off by as much as 10 degrees, all of the crystals were within 2 to 3 degrees of the true orientation. The orientations tested are shown in the stereographic triangle, Figure 3-1. Specimens were strained to a plastic strain of approximately 0.2% to obtain the offset yield strength at each temperature. Selected temperatures between 25°C to 850°C were tested in tension and compression at a constant true strain rate of ±.0001/sec. ⟨001⟩ tension tests were also performed at

In order to conserve material, each crystal was cut into three 2 inch pieces and electron-beam welded between two lengths of Inconel 718, giving an overall specimen length of

[1] These specimens were all about 10 degrees off the true ⟨111⟩ orientation. The simulations will be performed in the actual orientation, although they will be referred to as ⟨111⟩ for convenience.

6 inches(152.4 mm). The welded bars were then machined by a low stress grinding process into tension-compression specimens. The specimen geometry is shown in Figure 3-2. The length to diameter ratio was minimized to prevent buckling during the compression tests, while remaining below the breaking load of the electron beam weld and keeping the gage length long enough that the axial extensometer could be used.

3.1.2 Experimental Equipment and Procedure

Experiments were conducted on a high stiffness biaxial Instron hydraulic testing frame with a 50000lb load cell and ±0.5 inch total displacement. The experiments were performed in strain control, using a modified MTS model 632.51B-82 high temperature axial extensometer with a 0.45 inch gage length to control the actuator displacement and to measure displacement in the gage section of the specimen. The alumina extensometer rods were spring loaded on the specimen. The extensometer was protected by a water-cooled heat shield and was itself water-cooled. Computer control of the tests and data acquisition were accomplished using the data acquisition and control software Labtech Notebook, in conjunction with a Keithley Series 500 unit with analog-to-digital and digital-to-analog input and output modules.

The specimens were heated by induction heating using a coil of approximately 1 inch diameter with 5-7 turns, made of 0.125 inch diameter copper refrigeration tubing. Power was supplied by a 5KW self tuning Ameritherm Inc. generator. The temperature was controlled by a K-type thermocouple spot-welded to the specimen in the gage section using a West 2073 automatic controller made by Gulton Industries, or remotely by an optical pyrometer.

The hydraulic collet grips on the Instron machine were internally water cooled, making the ends of the specimens significantly cooler than the gage section. However, a length of 1.5 to 2 inches was heated, giving a temperature variation of no more than 2 degrees over the area of interest. During gripping the specimen and during heating, zero load was maintained so as to avoid premature plastic deformation of the specimen due to gripping and to thermal expansion. The experimental setup is shown in Figure 3-3.

After a tension or compression test, each specimen was annealed at 800°C for 1 hour in vacuum and then *reused* for a different test. Specimens for each test were selected at random, the only constraint being that, if possible, the tension and compression test

for a given orientation and temperature be performed on the same specimen or another specimen from the same bar. The annealing temperature was kept sufficiently below the final aging temperature (870°C), so that the procedure does not cause significant growth of the γ' particles which may affect the material response. The effectiveness of reusing test specimens with intermediate annealing was verified by repeating the same experiment on a sample after the heat treatment. The result was practically identical to that on the virgin specimen, Figure 3-4.

3.2 Results

3.2.1 Single Crystal Elastic Properties

Ultrasonic measurements of the anisotropic elastic constants for CMSX4 were made by Allison Turbine Division, General Motors Corporation and the data generously provided for our use here [Thomas, 1993]. The measurements were made over a range of temperatures from approximately 25°C to 1100°C. For this cubic material, there are three unique moduli, C_{11}, C_{12} and C_{44}, with the elasticity tensor $\mathcal{L}$ given by

$$\mathcal{L} = \begin{bmatrix} C_{11} & C_{12} & C_{12} & 0 & 0 & 0 \\ C_{12} & C_{11} & C_{12} & 0 & 0 & 0 \\ C_{12} & C_{12} & C_{11} & 0 & 0 & 0 \\ 0 & 0 & 0 & C_{44} & 0 & 0 \\ 0 & 0 & 0 & 0 & C_{44} & 0 \\ 0 & 0 & 0 & 0 & 0 & C_{44} \end{bmatrix} \tag{3.1}$$

Measurements are actually made of elastic compliances S_{ij} and related to the elastic moduli by the following equations

$$\begin{aligned} C_{11} &= \frac{S_{11} + S_{12}}{(S_{11} - S_{12})(S_{11} + 2S_{12})} \\ C_{12} &= \frac{-S_{12}}{(S_{11} - S_{12})(S_{11} + 2S_{12})} \\ C_{44} &= \frac{1}{S_{44}} \end{aligned} \tag{3.2}$$

The variation in the values of all C_{ij} is approximated as linear with the least squares fit

giving (units of GPa)

$$\begin{aligned} C_{11} &= 307 - 0.089\theta \\ C_{12} &= 204 - 0.052\theta \\ C_{44} &= 143 - 0.032\theta \end{aligned} \tag{3.3}$$

For a given temperature, the values of the moduli used are those which satisfy the previous equation.

In Figure 3-5, the values of the elastic moduli determined from the tension and compression experiments are compared with the values calculated from the anisotropic moduli obtained by ultrasonic measurements. They are given by the following equations [Hosford, 1990]:

$$\frac{1}{E_{\langle 001 \rangle}} = S_{11} \tag{3.4}$$

$$\frac{1}{E_{\langle 011 \rangle}} = \frac{2S_{11} + 2S_{12} + S_{44}}{4} \tag{3.5}$$

$$\frac{1}{E_{\langle 111 \rangle}} = \frac{S_{11} + 2S_{12} + S_{44}}{3} \tag{3.6}$$

Most of the experimental values are within 10% of the ultrasonic measurements.

3.2.2 Experimental Results

Figures 3-6 through 3-8 show the stress strain curves for each of the three orientations tested at each temperature in tension and compression. The $\langle 001 \rangle$ orientation is the strongest in tension and the $\langle 011 \rangle$ strongest in compression at all temperatures. Also, the $\langle 111 \rangle$ orientation is the weakest in tension and compression at all temperatures except 25°C.

The 0.2% offset yield strength is plotted as a function of temperature for the three orientations in tension and compression in Figures 3-9, 3-10 and 3-11 respectively. The curves are replotted in Figure 3-12 with the three orientations plotted together for tension and also for compression. The yield strength shows the expected rise and subsequent drop with increasing temperature for all orientations, although for the $\langle 011 \rangle$ and $\langle 111 \rangle$ orientations, there is an upturn in the curve at low temperatures.

The $\langle 001 \rangle$ orientation is stronger in tension than in compression at all temperatures

while the opposite is true for the ⟨011⟩ and ⟨111⟩ orientations, although the tension-compression asymmetry is much less pronounced for the ⟨111⟩ orientation than for the other two orientations. The peaks in these curves occur at approximately 650°C for all orientations in tension and compression. Heredia and Pope [1986] also claim that the peak temperature is dependent on the orientation and sense of applied stress. This effect was not observed here, however. The two phase material does not show such a sharp rise in the yield strength with temperature below the peak as does the single phase Ni_3Al. Below 650°C, for most orientations, the yield strength remains almost constant or decreases some, then it drops sharply with increasing temperature, in contrast to the single-phase material, which shows a sharp rise in yield strength with temperature. This is consistent with observations on other γ/γ' superalloys in the literature, Shah and Duhl [1984]. Figure 3-13 plots the 0.2% offset yield strength from these experiments on the same graph as the data for another γ/γ' superalloy, PWA1480, from various sources in the literature ([Heredia and Pope, 1986], [Shah and Duhl, 1984], [Swanson *et al.*, 1986]), at comparable strain rates.

3.3 Extension of Constitutive Model to Two-Phase Material

Recall that the two-phase γ/γ' superalloy consists of about 68% γ' precipitates interspersed in a γ matrix with which it is coherent, Figure 1-3. Since the high volume fraction γ/γ' material behaves essentially like the single phase γ', exhibiting the same trends in the variation of yield strength, we will extend the model developed for the single-phase $L1_2$ crystal structure in Chapter 2 to the two-phase CMSX4. We take a very simple first-order approach.

Experimental data shows that the yield strength[2] of the two-phase γ/γ' superalloys can greatly exceed that of the single phase γ'. This may be attributed to a combination of effects. These include:

1. In the two-phase material, it has been found that the particles of γ' are initially almost dislocation-free, as compared to the initially dislocated bulk γ' material.

2. Bowing of dislocations betwen the γ' particles, Figure 1-4(a) [Pollock, 1989]. At low

[2]In the creep regime, deformation occurs primarily in the softer γ phase. Only in the much later stages of creep do the dislocations begin to penetrate the particles.

stresses the particles are not penetrated, and plastic deformation is restricted to the softer γ phase.

3. Injection of dislocations into the γ' particles, Figure 1-4(b) [Pollock, 1989]. When the stress level is high enough it becomes possible for the γ' to undergo plastic deformation. However, moving $\frac{1}{2}\langle 110 \rangle$ dislocations from the fcc γ to the $L1_2$ γ' creates antiphase boundaries.

In our simple model, these combined effects are represented by a lumped parameter, s_{th}, a threshold strength. For a resolved shear stress below this strength level, no plastic deformation occurs in the γ'. The slip rate on slip system α is accordingly modified:

$$\dot{\gamma}^\alpha = \begin{cases} 0 & \text{if} \quad |\tau^\alpha| - s_{th} \leq 0, \\ \dot{\gamma}_o \left\{ \frac{|\tau^\alpha| - s_{th}}{s^\alpha} \right\}^{\frac{1}{m}} & \text{if} \quad |\tau^\alpha| - s_{th} > 0, \end{cases} \tag{3.7}$$

with the s^α for the octahedral and cube slip systems given in equation 2.14. Like the initial slip system resistance, s_o^α, this threshold strength is taken to have the same temperature-dependent value, s_{th}, on all 12 octahedral slip systems, and the same value, s_{thc}, on the 6 cube slip systems. However, *since this parameter lumps different effects together, it may not be interpreted directly as the stress at which any of the above phenomena begin to occur separately.*

3.4 Finite Element Simulations

Since we have no information on the true composition and yield behavior of the γ' phase of the two phase γ/γ' CMSX4 material used in this study, we will use the parameters obtained for the single phase material in Chapter 2 and use the experimental results of this study to curve-fit values for the threshold strength. It was also necessary to change the values of κ_1 and κ_2 to fit the correct amount of tension-compression for this particular two-phase material. The new values were: $\kappa_1 = 0.3, \kappa_2 = -0.333$. The value of κ_1 has not change much from the single-phase value, but the change in sign of κ_2 indicates that the zero-asymmetry orientations lie to the other side of the $\langle 012 \rangle - \langle \bar{1}13 \rangle$ great circle (on the $\langle 001 \rangle$ side).

Calculations were performed as described in Chapter 2, using a single 3-dimensional,

8-noded continuum element (ABAQUS type C3D8). Symmetry was imposed on three orthogonal faces, and a displacement was imposed at a constant true strain rate in tension or in compression.

All of the parameters for the γ' single phase material obtained in Section 2.2.2 were retained, and s_{th} values were fit to the experimental data at each temperature. The s_{th} values for the octahedral slip systems were obtained from the $\langle 001 \rangle$ experiments and these values were then used to fit the $\langle 111 \rangle$ data to obtain s_{thc} for the cube slip systems. The $\langle 011 \rangle$ experiments were then simulated using these values and serve as predictions for the model. Table 3.1 shows the experimental and simulated values for the yield strengths for the tests performed.

Figures 3-14 and 3-15 plot the experimental and fitted simulated yield strength versus temperature curves for the three orientations tested in this study. The variation of s_{th} for the octahedral and cube slip systems are plotted in Figure 3-16. The predictions for the $\langle 011 \rangle$ orientation, Figure 3-17, are good for all temperatures except room temperature where the tension-compression asymmetry completely disappears in the simulations whereas it does not in the experiments.

This may be explained by examining the slip system activity. The Schmid factors for each of the three orientations are listed in Table 3.2. Figure 3-18, 3-19 and 3-20 plot all the non-zero values of the accumulated shear strain on each slip system at 25°C, 650°C (near the peak), and 850°C. For the $\langle 001 \rangle$ orientation, as expected, there is equal activity on eight octahedral slip sytems at all temperatures.

For the $\langle 111 \rangle$ orientation, at 25°C there is equal activity on 3 cube slip systems at all temperatures. This agrees with the slip traces observed experimentally, Figure 2-5 [Lall *et al.*, 1979].

For the $\langle 011 \rangle$ orientation, however, the slip system activity is a sensitive function of temperature, and the responses in tension and compression differ. The Schmid factors for octahedral and cube slip in this orientation are sufficiently close that the choice of the values of s^α and s_{th} will very sensitively affect whether there is octahedral or cube slip occurring. At 298K, there is equal activity on two octahedral slip systems in tension and in compression: s_{oc}/s_{thc} is sufficiently higher than s_o/s_{th} to deactivate the cube slip systems. For this orientation, the Schmid factors for octahedral and cube slip are almost equal, so making one set of slip sytems significantly stronger than the other will preclude activity on

Table 3.1: Experimental and simulated yield strengths

$\dot{\epsilon} = \pm .0001/\text{sec}$

⟨001⟩	$\lvert\sigma_y\rvert_T$(MPa)		$\lvert\sigma_y\rvert_C$(MPa)	
Temp.(°C)	Expt.	Sim.	Expt.	Sim.
25	976	971	937	940
400		1028	901	891
500	1014	1063		897
600	1115	1160		963
650	1212	1213	1009	1003
700	1027	1178	978	976
750	952	953		799
850	858	824	750	707

⟨011⟩	$\lvert\sigma_y\rvert_T$(MPa)		$\lvert\sigma_y\rvert_C$(MPa)	
Temp.(°C)	Expt.	Sim.	Expt.	Sim.
25	1066	918	1187	921
400	1010	947	1228	1219
500		979		1283
600	1083	1071		1294
650	1075	1128	1218	1282
700	978	1095	1064	1174
750		904	1034	996
850	648	772	763	780

⟨111⟩	$\lvert\sigma_y\rvert_T$(MPa)		$\lvert\sigma_y\rvert_C$(MPa)	
Temp.(°C)	Expt.	Sim.	Expt.	Sim.
25	1173	1212	1240	1199
400	1021	1037	1065	1027
500	1004	982		973
600	971	981		972
650	992	971	1048	962
700	862	889	907	880
750		747		753
850	618	588	602	584

those slip systems. At 923K, however, the same two octahedral slip systems are active in compression, with much less activity on the cube slip systems. Conversely, in compression, the major activity is on four cube slip systems while the four octahedral slip systems are practically inactive. At 1123K, s_{oc}/s_{thc} and s_o/s_{th} are almost equal and there is combined activity on the octahedral and cube slip systems in tension. In compression, though, the cube slip systems are dominant.

The difference in slip system activity in tension and in compression arises from the asymmetry introduced through the octahedral slip systems. In the $\langle 011 \rangle$ orientation, compression should be higher than tension. This means that the slip system resistance on the active octahedral slip systems is higher in compression than in tension. If $s^{\alpha}_{oct,tens} < s^{\alpha}_{cube} < s^{\alpha}_{oct,comp}$, then there is the possibility that in compression cube slip will occur, while in tension octahedral slip will occur. This appears to be the case at the higher temperatures.

These results agree qualitatively with the experimental slip traces observed by Lall *et al.* [1979] for the single-phase material, Figure 2-5 although all of their experiments are compression. The differences observed here for the $\langle 011 \rangle$ orientation cannot be directly compared.

Table 3.2: Schmid factors for octahedral and cube slip systems

	[001]				[011]				[$\bar{1}$11]			
α	m^α	m^α_{pe}	m^α_{se}	m^α_{cb}	m^α	m^α_{pe}	m^α_{se}	m^α_{cb}	m^α	m^α_{pe}	m^α_{se}	m^α_{cb}
1	$-\frac{1}{\sqrt{6}}$	$\frac{1}{3\sqrt{2}}$	$\frac{1}{3\sqrt{2}}$	0	0	$\frac{2}{3\sqrt{2}}$	$\frac{2}{3\sqrt{2}}$	0	0	$\frac{4}{9\sqrt{2}}$	0	0
2	$\frac{1}{\sqrt{6}}$	$\frac{1}{3\sqrt{2}}$	$\frac{1}{3\sqrt{2}}$	0	$\frac{1}{\sqrt{6}}$	0	$-\frac{1}{3\sqrt{2}}$	$\frac{1}{2\sqrt{2}}$	$\frac{2}{3\sqrt{6}}$	$-\frac{2}{9\sqrt{2}}$	$-\frac{2}{9\sqrt{2}}$	$\frac{2}{3\sqrt{2}}$
3	0	$-\frac{2}{3\sqrt{2}}$	$-\frac{2}{3\sqrt{2}}$	0	$-\frac{1}{\sqrt{6}}$	0	$-\frac{1}{3\sqrt{2}}$	$-\frac{1}{2\sqrt{2}}$	$-\frac{2}{3\sqrt{6}}$	$-\frac{2}{9\sqrt{2}}$	$-\frac{2}{9\sqrt{2}}$	$-\frac{2}{3\sqrt{2}}$
4	$-\frac{1}{\sqrt{6}}$	$\frac{1}{3\sqrt{2}}$	$\frac{1}{3\sqrt{2}}$	0	0	$\frac{2}{3\sqrt{2}}$	$\frac{2}{3\sqrt{2}}$	0	0	0	$\frac{4}{9\sqrt{2}}$	0
5	$\frac{1}{\sqrt{6}}$	$\frac{1}{3\sqrt{2}}$	$\frac{1}{3\sqrt{2}}$	0	$\frac{1}{\sqrt{6}}$	0	$-\frac{1}{3\sqrt{2}}$	$\frac{1}{2\sqrt{2}}$	0	0	$\frac{4}{9\sqrt{2}}$	0
6	0	$-\frac{2}{3\sqrt{2}}$	$-\frac{2}{3\sqrt{2}}$	0	$-\frac{1}{\sqrt{6}}$	0	$-\frac{1}{3\sqrt{2}}$	$-\frac{1}{2\sqrt{2}}$	0	0	$\frac{4}{9\sqrt{2}}$	0
7	$-\frac{1}{\sqrt{6}}$	$\frac{1}{3\sqrt{2}}$	$\frac{1}{3\sqrt{2}}$	0	0	0	0	0	$\frac{2}{3\sqrt{6}}$	$-\frac{2}{9\sqrt{2}}$	$-\frac{2}{9\sqrt{2}}$	$\frac{2}{3\sqrt{2}}$
8	$\frac{1}{\sqrt{6}}$	$\frac{1}{3\sqrt{2}}$	$\frac{1}{3\sqrt{2}}$	0	0	$-\frac{1}{3\sqrt{2}}$	0	$-\frac{1}{2\sqrt{2}}$	$-\frac{2}{3\sqrt{6}}$	$-\frac{2}{9\sqrt{2}}$	$-\frac{2}{9\sqrt{2}}$	$-\frac{2}{3\sqrt{2}}$
9	0	$-\frac{2}{3\sqrt{2}}$	$-\frac{2}{3\sqrt{2}}$	0	0	$-\frac{1}{3\sqrt{2}}$	0	$\frac{1}{2\sqrt{2}}$	0	$\frac{4}{9\sqrt{2}}$	0	0
10	$-\frac{1}{\sqrt{6}}$	$\frac{1}{3\sqrt{2}}$	$\frac{1}{3\sqrt{2}}$	0	0	0	0	0	$-\frac{2}{3\sqrt{6}}$	$-\frac{2}{9\sqrt{2}}$	$-\frac{2}{9\sqrt{2}}$	$-\frac{2}{3\sqrt{2}}$
11	$\frac{1}{\sqrt{6}}$	$\frac{1}{3\sqrt{2}}$	$\frac{1}{3\sqrt{2}}$	0	0	$-\frac{1}{3\sqrt{2}}$	0	$-\frac{1}{2\sqrt{2}}$	0	$\frac{4}{9\sqrt{2}}$	0	0
12	0	$-\frac{2}{3\sqrt{2}}$	$-\frac{2}{3\sqrt{2}}$	0	0	$-\frac{1}{3\sqrt{2}}$	0	$\frac{1}{2\sqrt{2}}$	$\frac{2}{3\sqrt{6}}$	$-\frac{2}{9\sqrt{2}}$	$-\frac{2}{9\sqrt{2}}$	$\frac{2}{3\sqrt{2}}$
13	0	- - -	- - -	- - -	0	- - -	- - -	- - -	$\frac{2}{3\sqrt{2}}$	- - -	- - -	- - -
14	0	- - -	- - -	- - -	0	- - -	- - -	- - -	0	- - -	- - -	- - -
15	0	- - -	- - -	- - -	$-\frac{1}{2\sqrt{2}}$	- - -	- - -	- - -	0	- - -	- - -	- - -
16	0	- - -	- - -	- - -	$\frac{1}{2\sqrt{2}}$	- - -	- - -	- - -	$-\frac{2}{3\sqrt{2}}$	- - -	- - -	- - -
17	0	- - -	- - -	- - -	$\frac{1}{2\sqrt{2}}$	- - -	- - -	- - -	0	- - -	- - -	- - -
18	0	- - -	- - -	- - -	$-\frac{1}{2\sqrt{2}}$	- - -	- - -	- - -	$-\frac{2}{3\sqrt{2}}$	- - -	- - -	- - -

3.4.1 Simulations over the Stereographic Triangle

Next, we are interested in investigating the dependence of yield strength in tension and compression on crystal orientation at fixed temperatures. Using the parameters obtained for the CMSX4 from this study, a grid of orientations covering the stereotraphic triangle was simulated to predict the yield stress in these orientations. Simulations were performed just to yield and the 0.2% offset yield strength obtained. Temperatures of 25, 650, and 850°C were selected since the represent the behavior below, close to, and above the peak respectively. These results are plotted in Figures 3-21, through 3-23.

The trends are similar to those observed for the single phase material, Figure 2-20, except that the yield strengths are higher. At the lowest temperature the ⟨111⟩ orientation has the highest yield strength, while at the two higher temperatures, it is lowered relative to the ⟨001⟩ orientation. Tension is always higher for the ⟨001⟩ orientation, while compression is higher for the other two corner orientations.

3.5 Discussion

In the single-phase material, the mechanisms of deformation are fairly well-understood, and a macroscopic constitutive model accounting for the microscopic mechanisms has been formulated. However, in the two-phase material, the system is significantly more complicated. Two materials with widely disparate strengths coexist in this micro-composite. The matrix phase is fcc while the precipitate phase is $L1_2$. This implies different dislocation behavior in the two phases even on the same slip system. Injection of a dislocation from the matrix to the precipitate requires the creation of an antiphase boundary. TEM observations show that in the early stages of deformation dislocations are concentrated in the narrow matrix channels, especially at the interfaces to relieve any lattice mismatch. The present model does not explicitly address the issue of how dislocations are initiated in the γ', or how differences in γ' volume fraction and morphology affect the yield behavior. The threshold strength proposed in this chapter attempts to account for several phenomena through a single parameter. The relative contributions to the value of s_{th} from the variety of these microscopic mechanisms is not easily assessed.

It bears emphasis that the range of temperatures and loading conditions over which our model is valid is limited – it is valid for monotonic loading between room temperature and

$\sim$ 850°C, above which microstructural evolution, such as coarsening of the γ' and rafting, begins to occur, changing the material properties. Also, proper accounting of cyclic loading and coupled thermo-mechanical effects require some further modifications to our model [Lin, 1994].

In the present study, we have made a first attempt at formulating a constitutive model for the yielding response of two-phase γ/γ' superalloys under monotonic loading. We began first by determining the properties of the majority phase, γ', and then added a parameter to account for the differences between the single- and the two-phase material. This approach assumes that the γ' phase of the material being tested is well-characterized. However, this is not the usual case, so it is necessary to use available data for the bulk γ' from the literature. Overall, for the conditions tested here, our model provides an adequate first order representation of the behavior of the material.

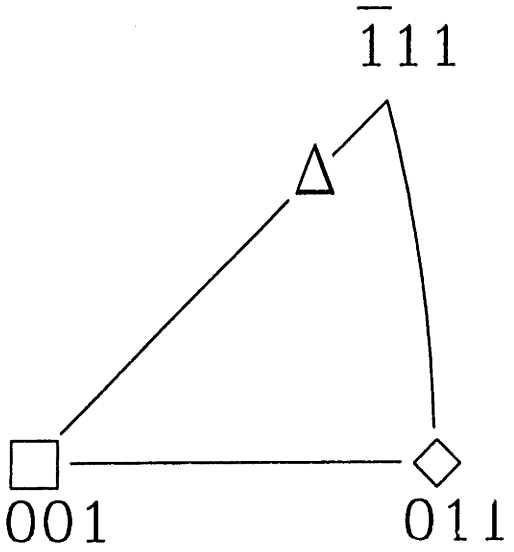

Figure 3-1: Orientations tested in tension and compression

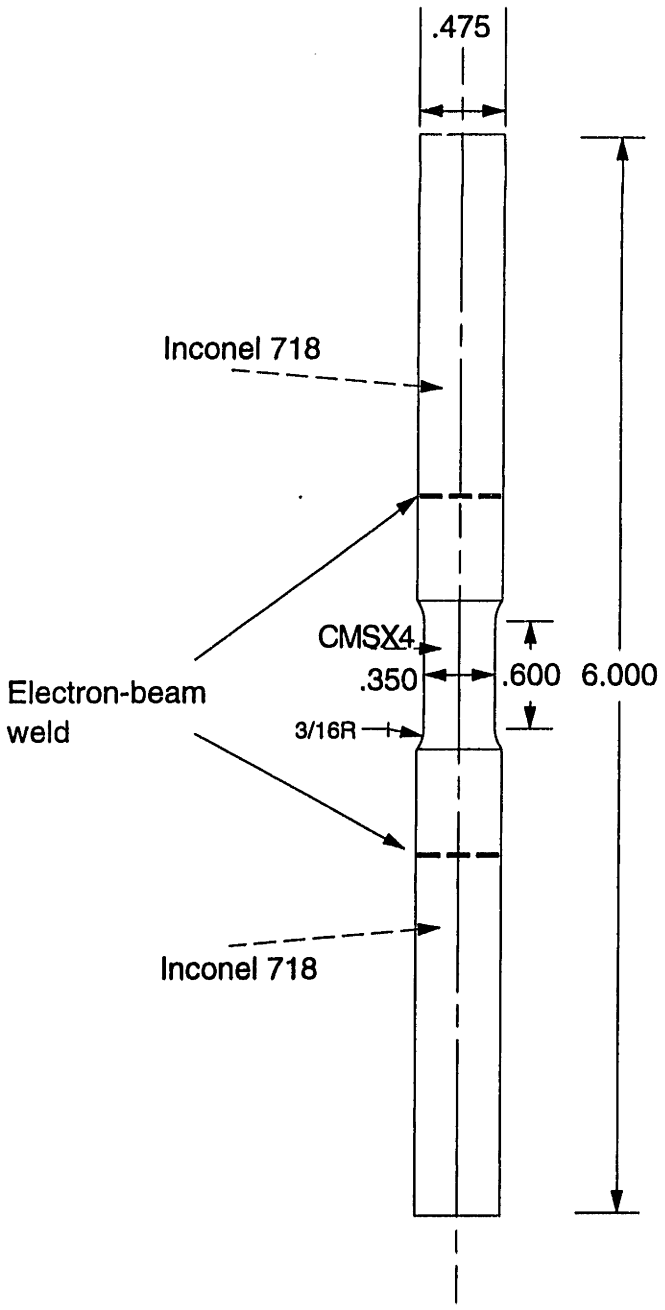

Dimensions in inches

Figure 3-2: Specimen geometry for tension and compression experiments

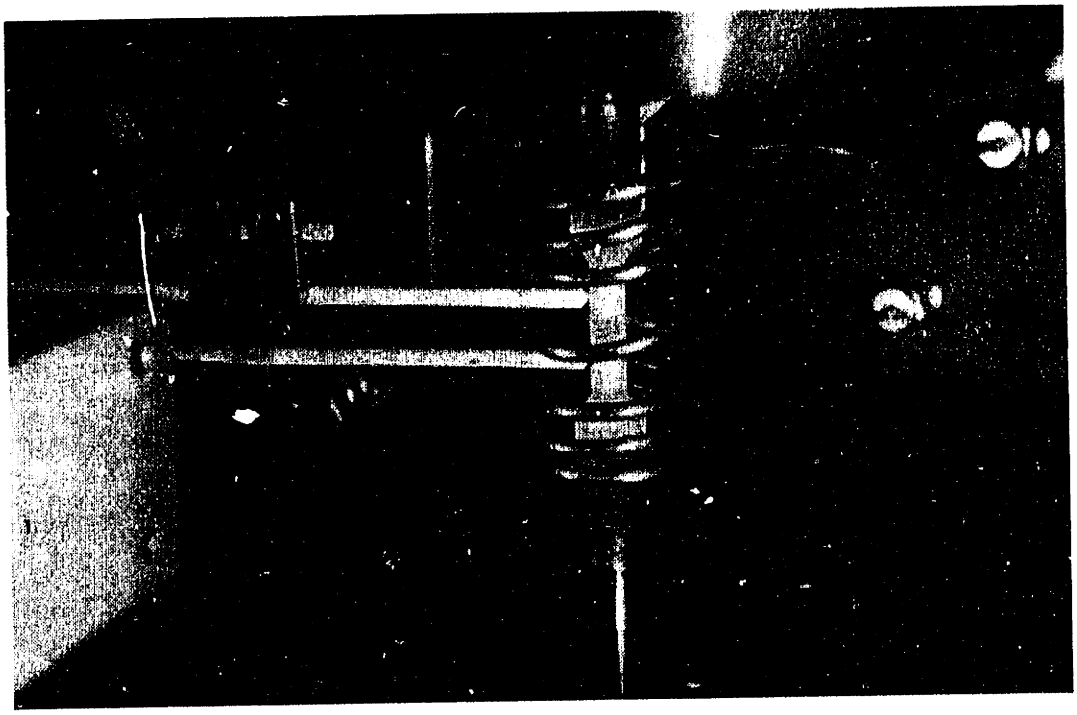

Figure 3-3: Experimental setup for tension and compression experiments

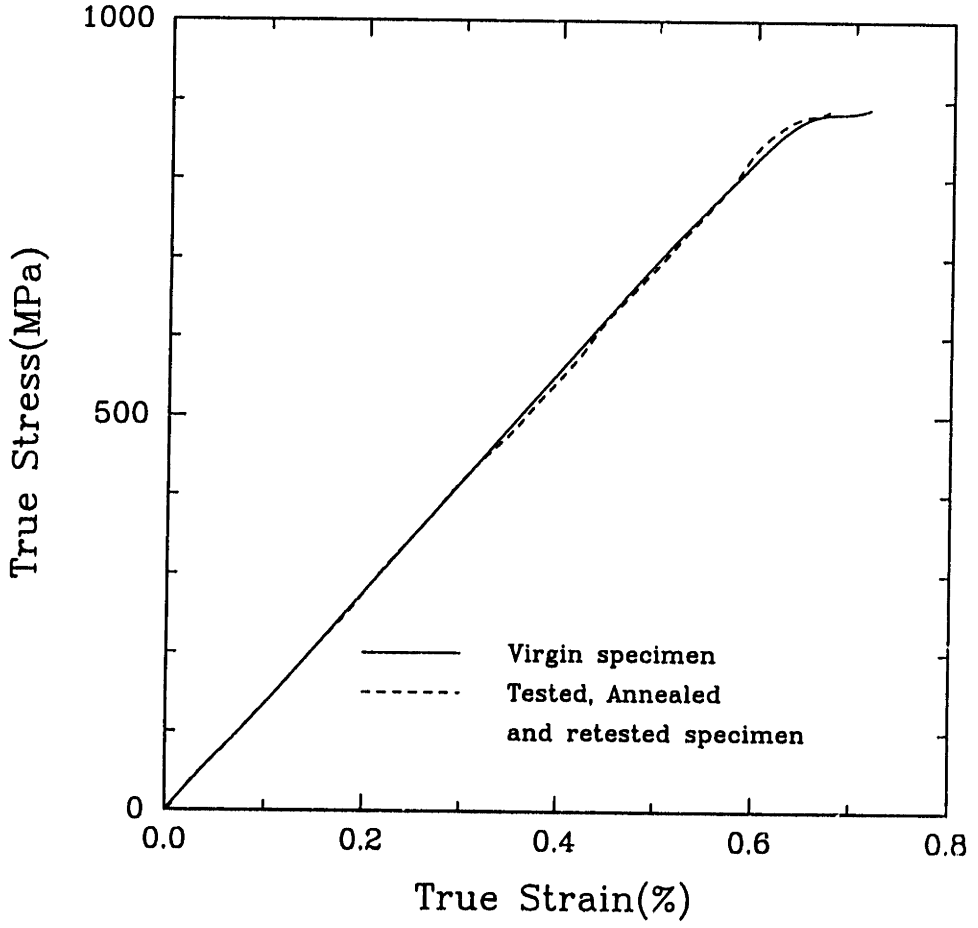

Figure 3-4: Results of room temperature tension experiments on CMSX3 before and after annealing

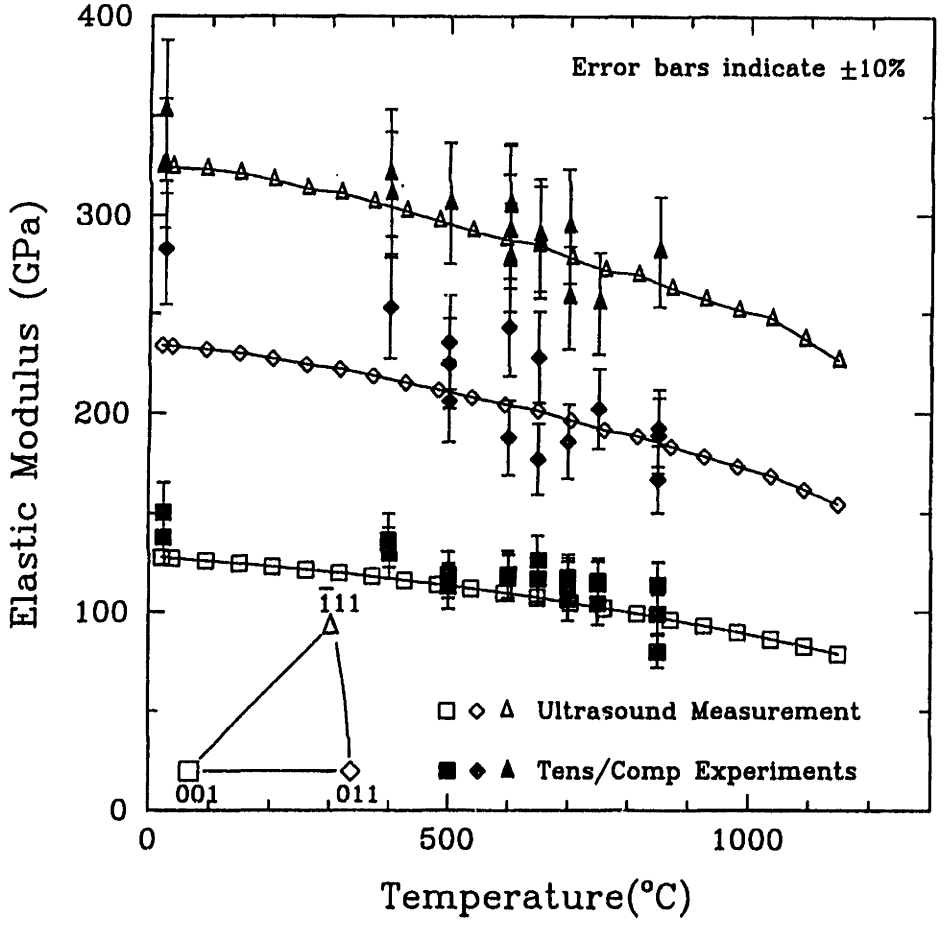

Figure 3-5: Variation of elastic modulus calculated from ultrasound measurements with temperature compared to values obtained in tension/compression experiments

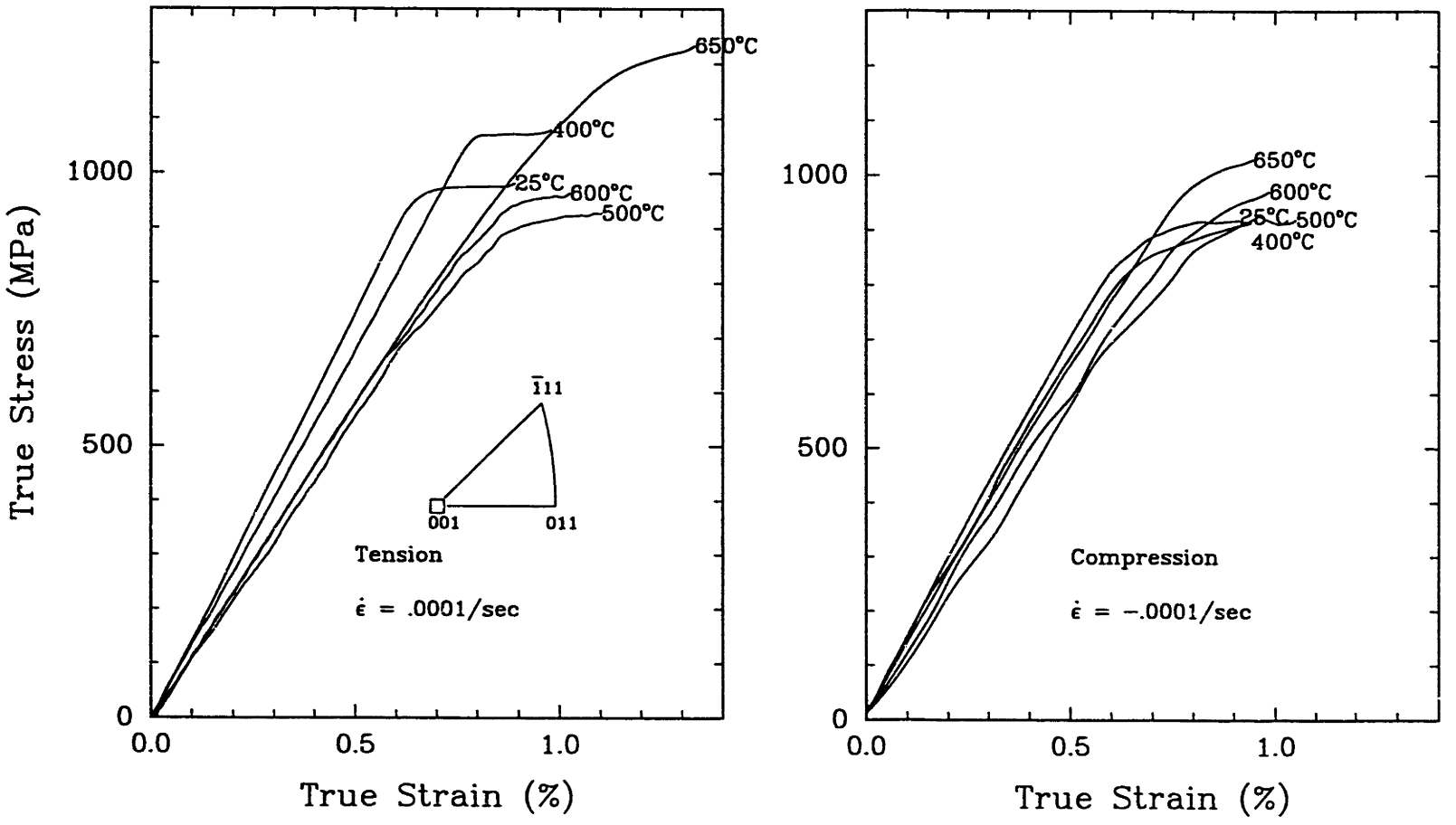

Figure 3-6: Stress vs. strain curves for the ⟨001⟩ orientation, $\dot{\epsilon} = \pm.0001$/sec. (a) Tension (b) Compression: below the peak temperature

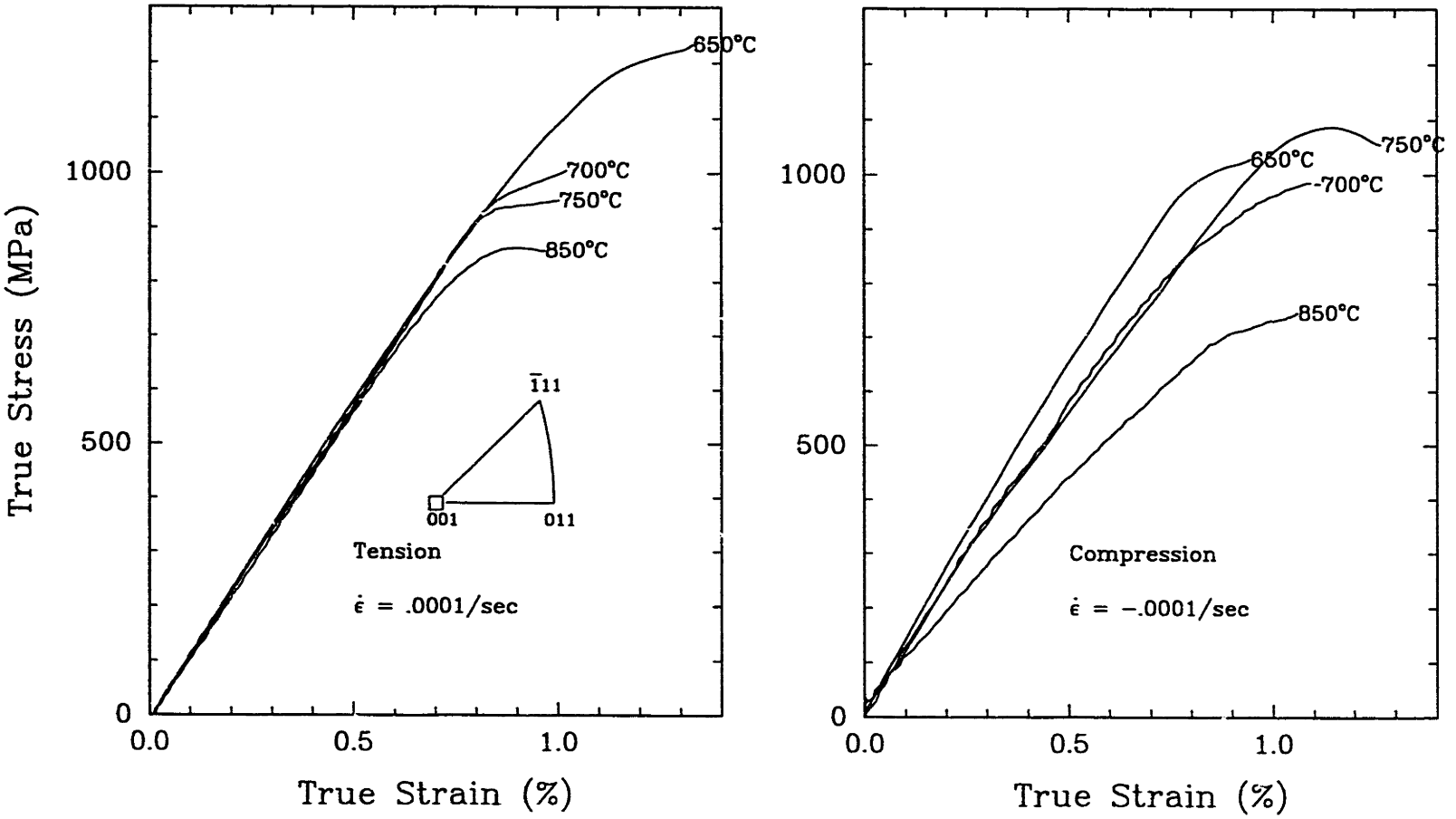

(c) (d)

Figure 3-6: Stress vs. . in curves for the ⟨001⟩ orientation, $\dot{\epsilon} = \pm .0001/\text{sec}$. (c) Tension (d) Compression: above the peak temperature

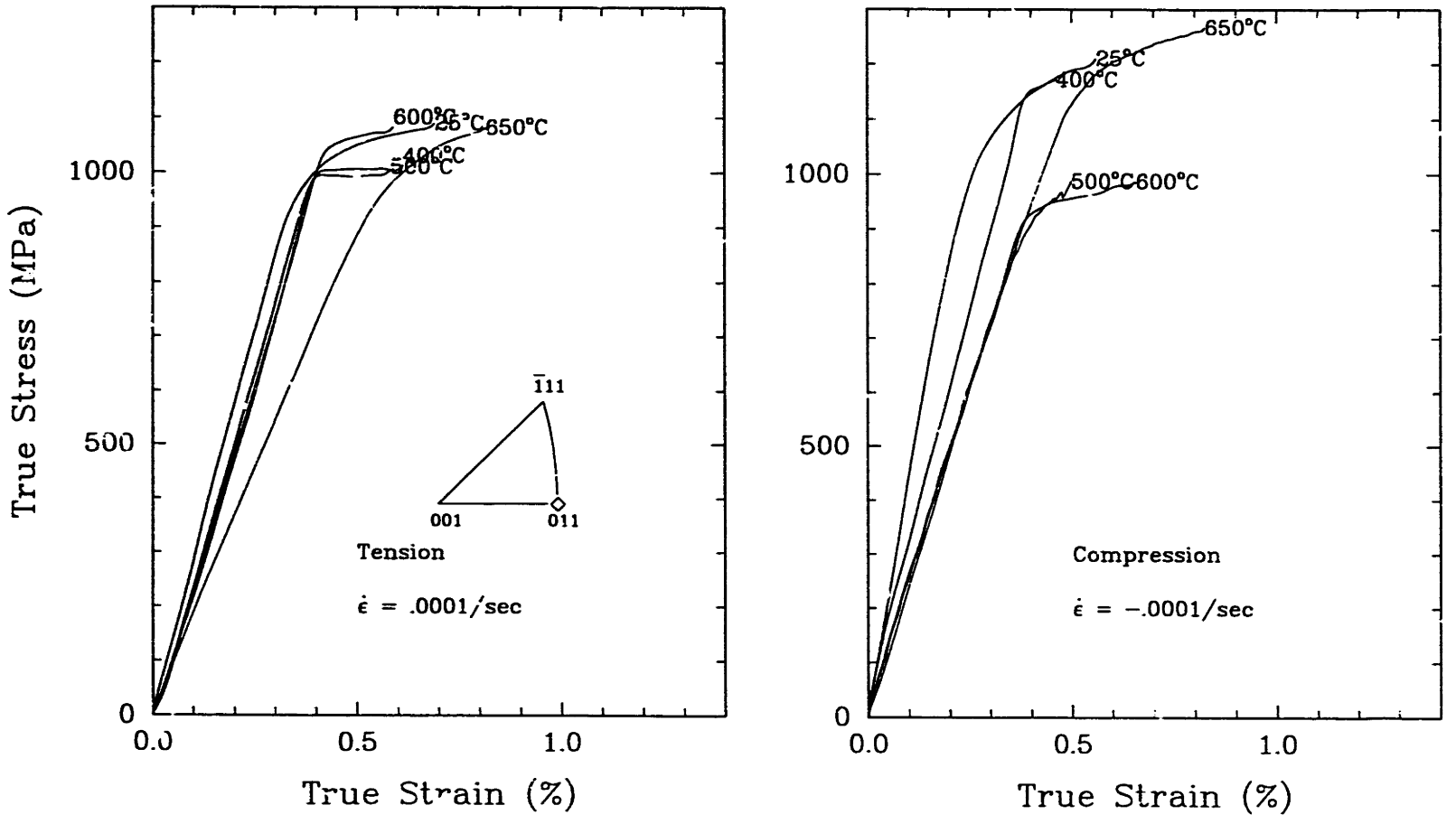

(a) (b)

Figure 3-7: Stress vs. strain curves for the $\langle 01\bar{1} \rangle$ orientation, $\dot{\epsilon} = \pm .0001$/sec. (a) Tension (b) Compression: below the peak temperature

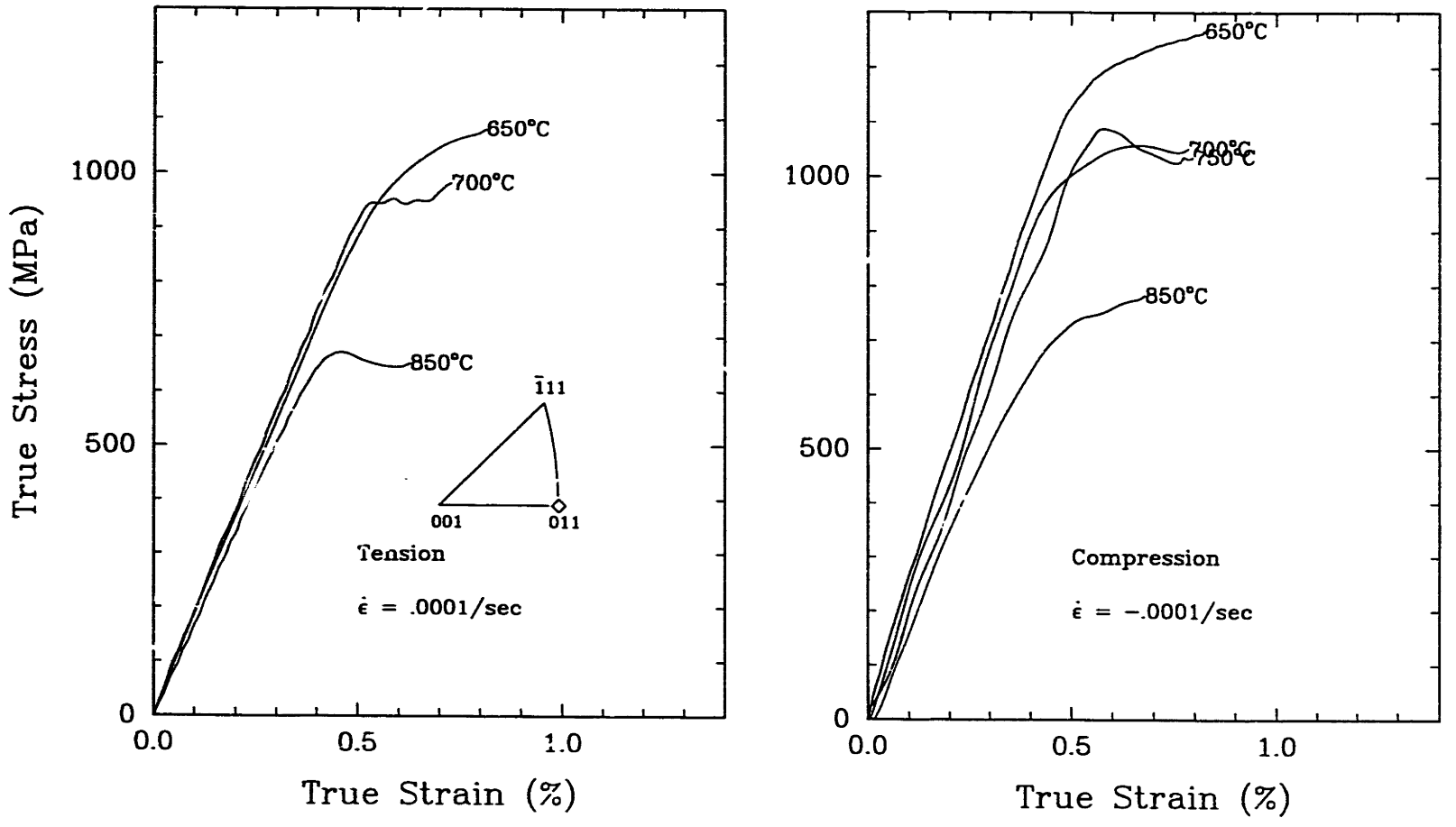

(c) (d)

Figure 3-7: Stress vs. strain curves for the ⟨011⟩ orientation, $\dot{\epsilon} = \pm .0001$/sec. (c) Tension (d) Compression: above the peak temperature

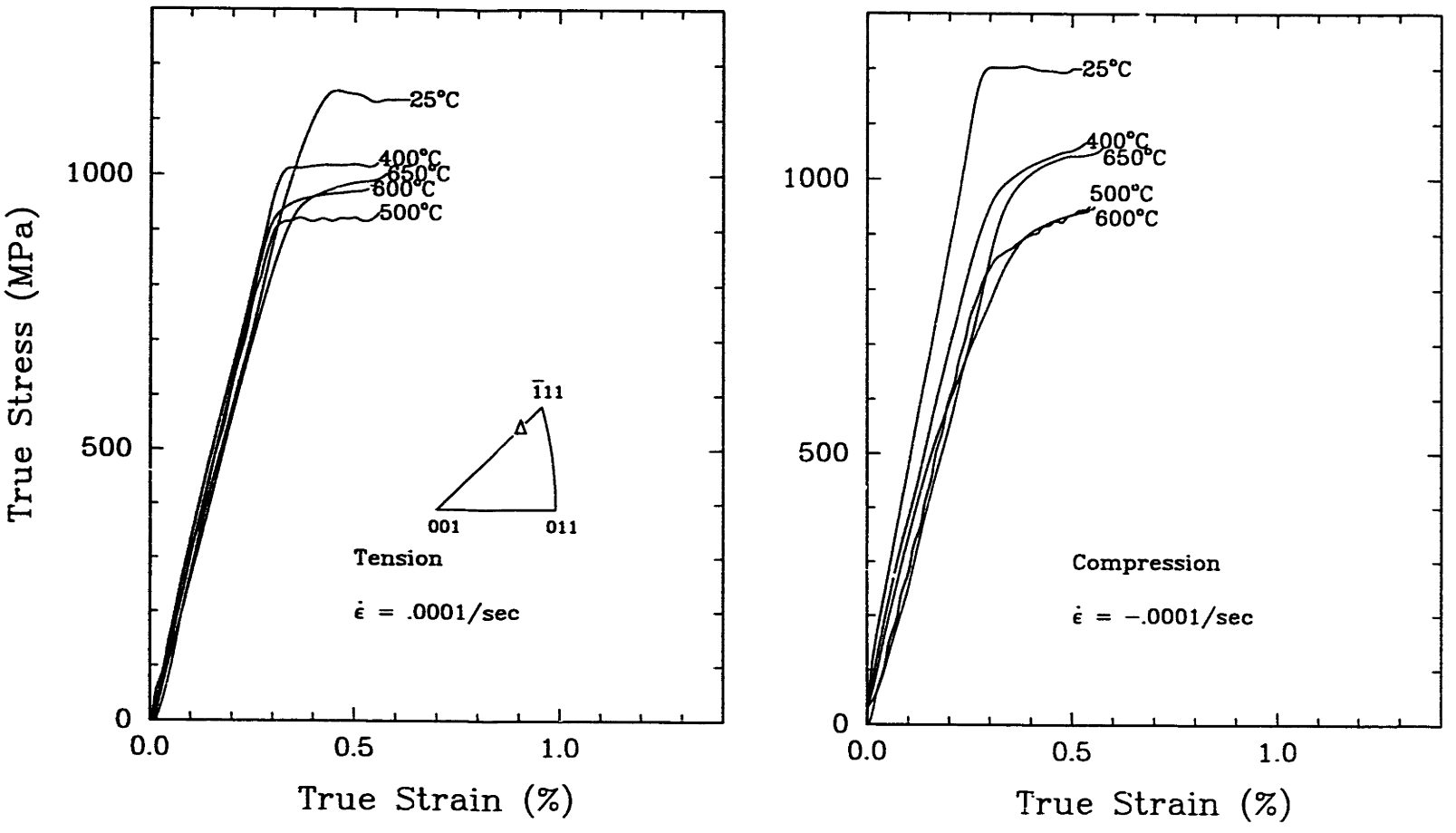

Figure 3-8: Stress vs. strain curves for the ⟨111⟩ orientation, $\dot{\epsilon} = \pm.0001$/sec. (a) Tension (b) Compression: below the peak temperature

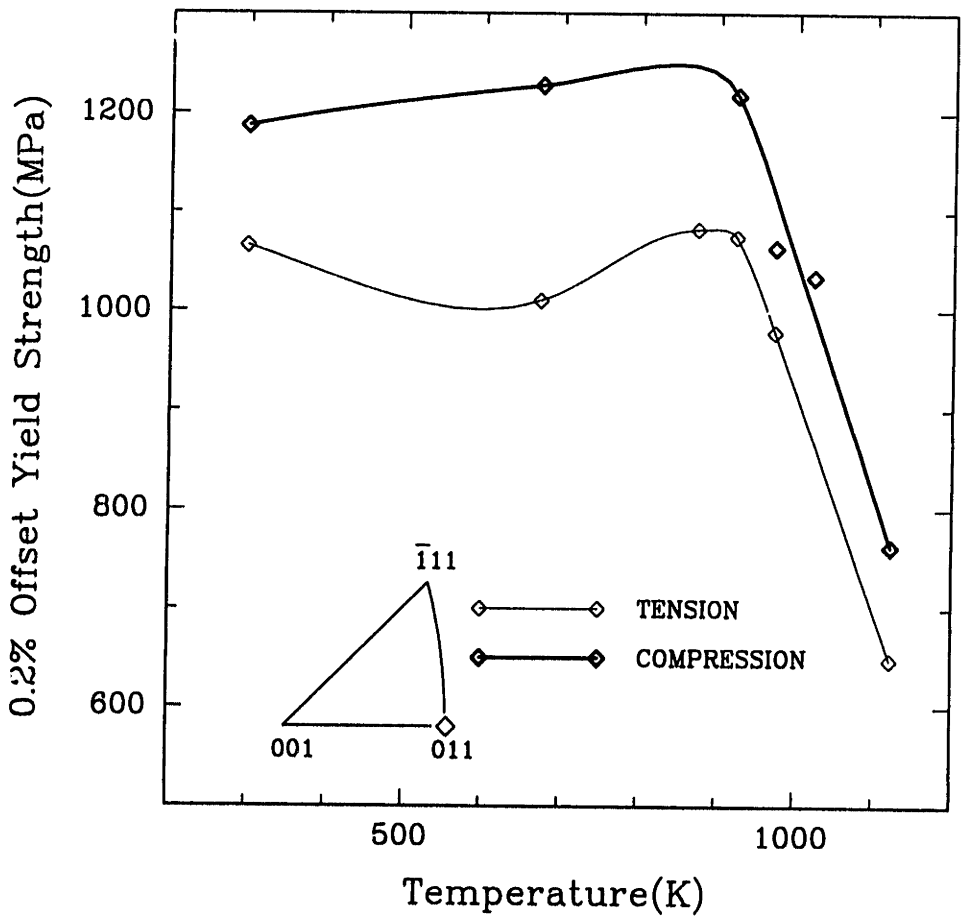

Figure 3-10: 0.2% offset yield strength vs. temperature curves for the $\langle 011 \rangle$ orientation, $\dot{\epsilon} = \pm .0001/\text{sec}$: Tension and Compression

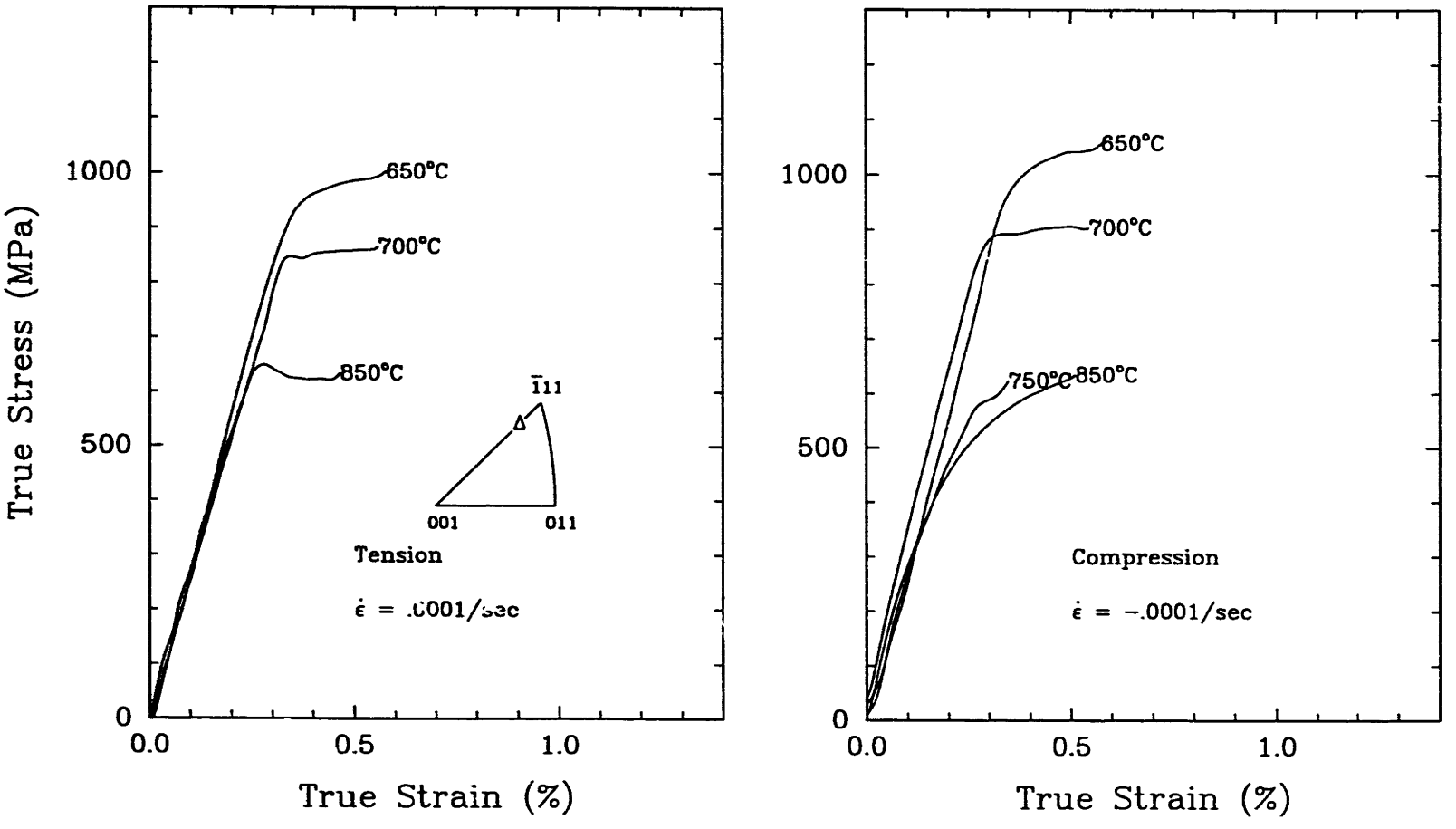

Figure 3-8: Stress vs. strain curves for the $\langle 111 \rangle$ orientation, $\dot{\epsilon} = \pm .0001$/sec. (c) Tension (d) Compression: above the peak temperature

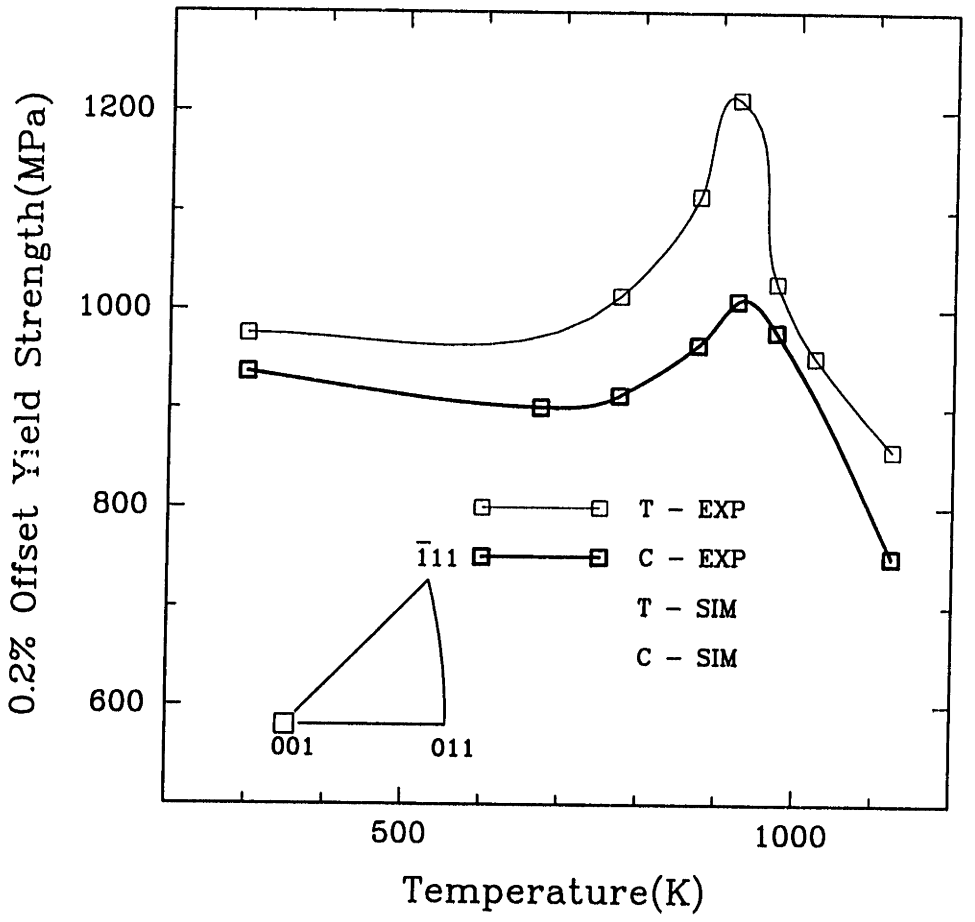

Figure 3-9: 0.2% offset yield strength vs. temperature curves for the $\langle 001 \rangle$ orientation, $\dot{\epsilon} = \pm .0001/\text{sec}$: Tension and Compression

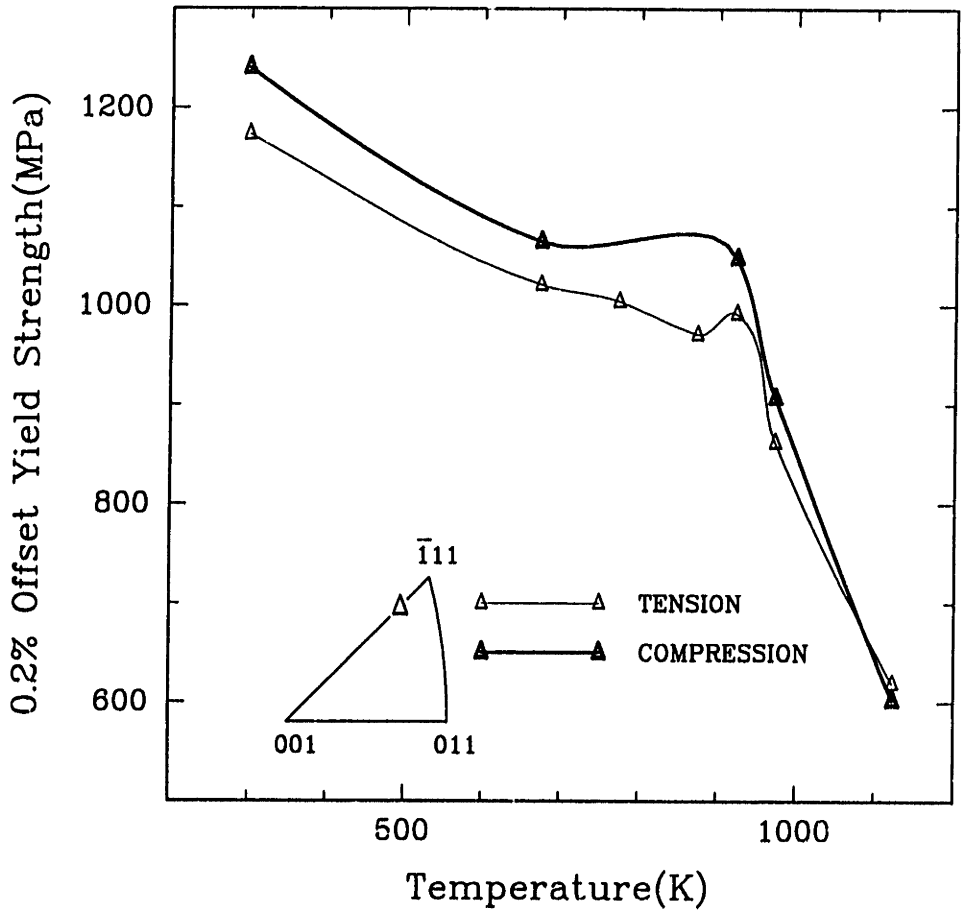

Figure 3-11: 0.2% offset yield strength vs. temperature curves for the $\langle 111 \rangle$ orientation, $\dot{\epsilon} = \pm .0001/\text{sec}$: Tension and Compression

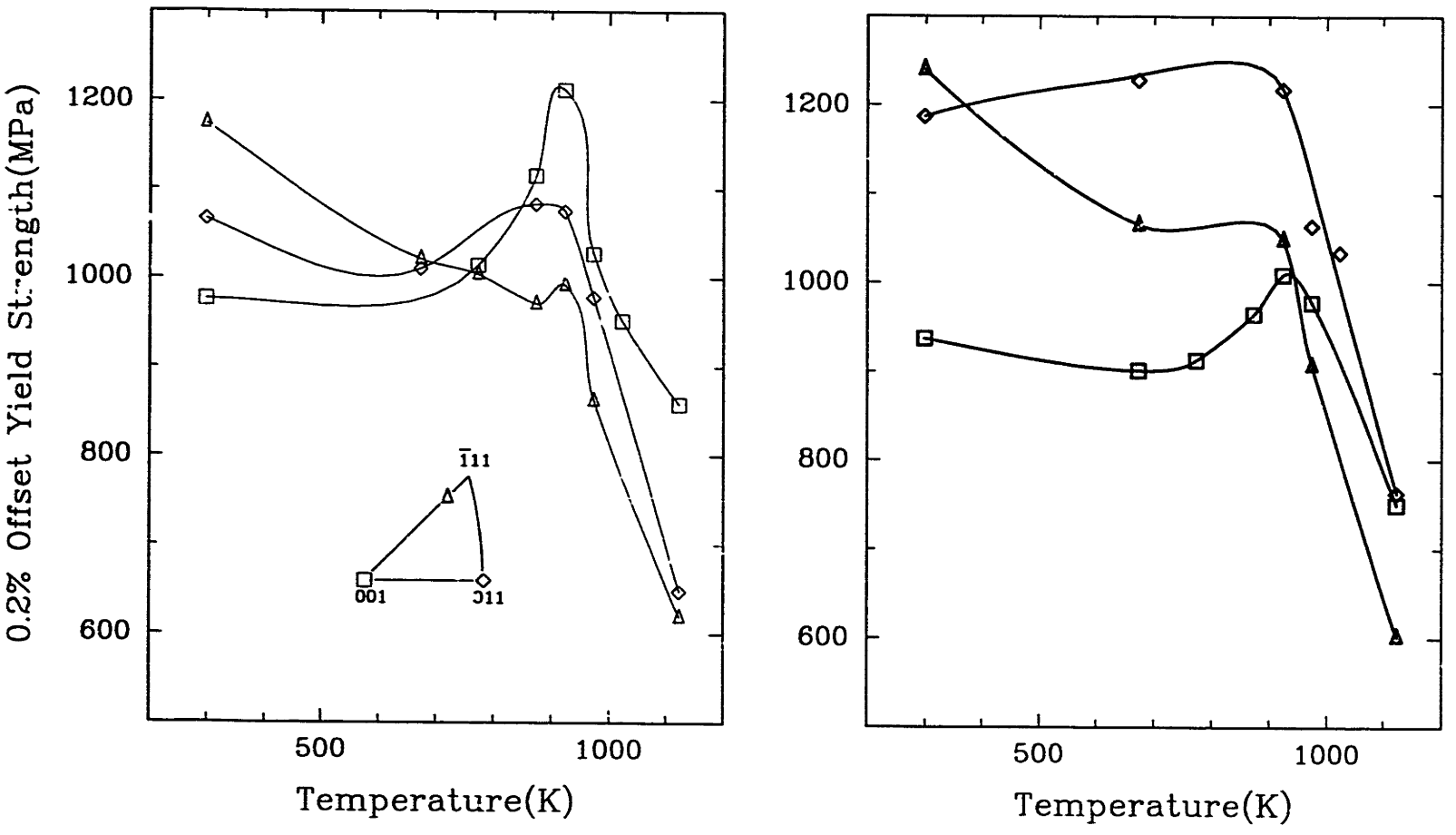

(a) (b)

Figure 3-12: 0.2% offset yield strength vs. temperature curves for the three orientations, $\dot{\epsilon} = \pm .0001/\text{sec}$: (a) Tension (b) Compression

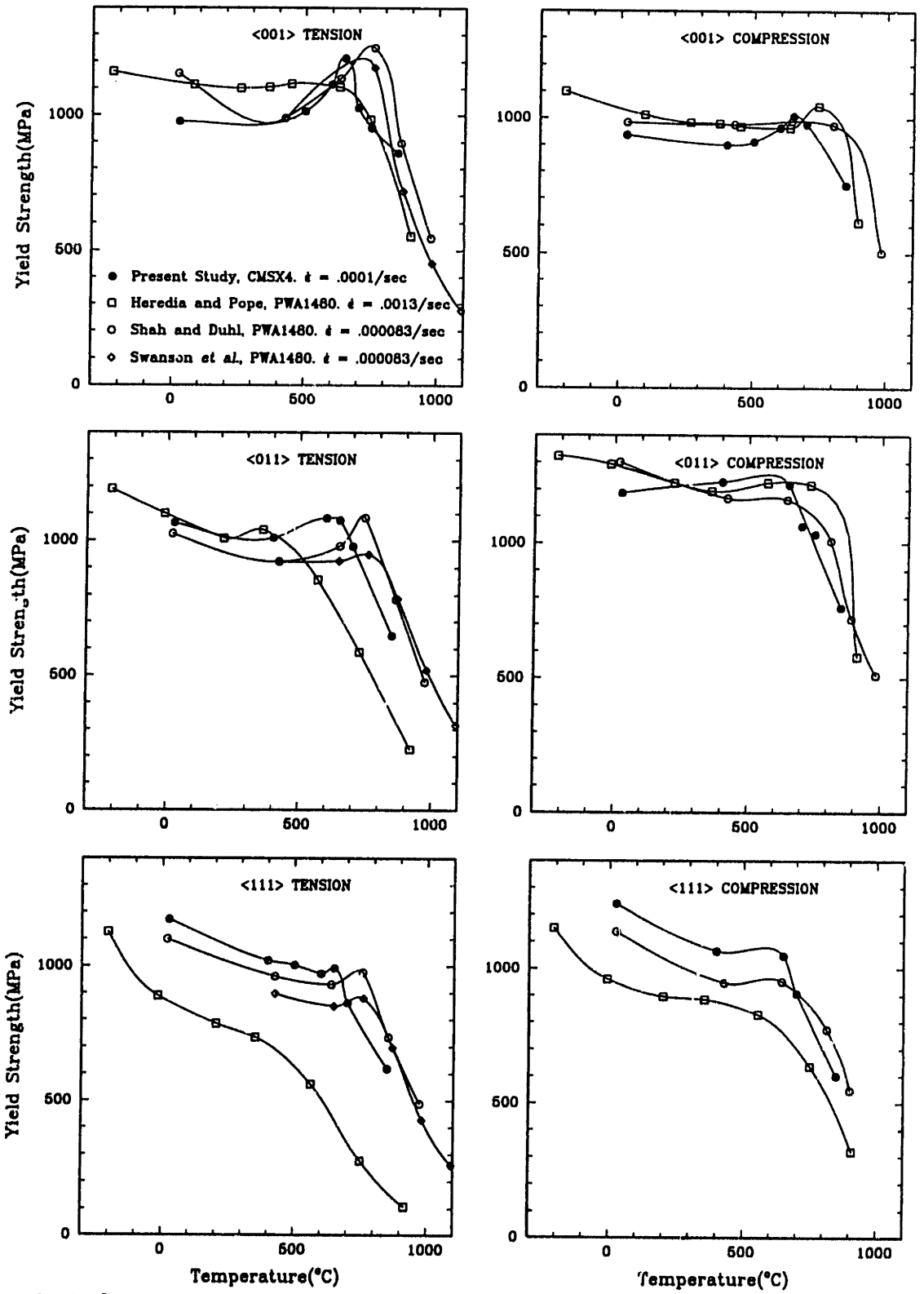

Figure 3-13: Comparison of variation of 0.2% offset yield stress with temperature for CMSX4 from this study, to that for PWA1480 from the literature at comparable strain rates

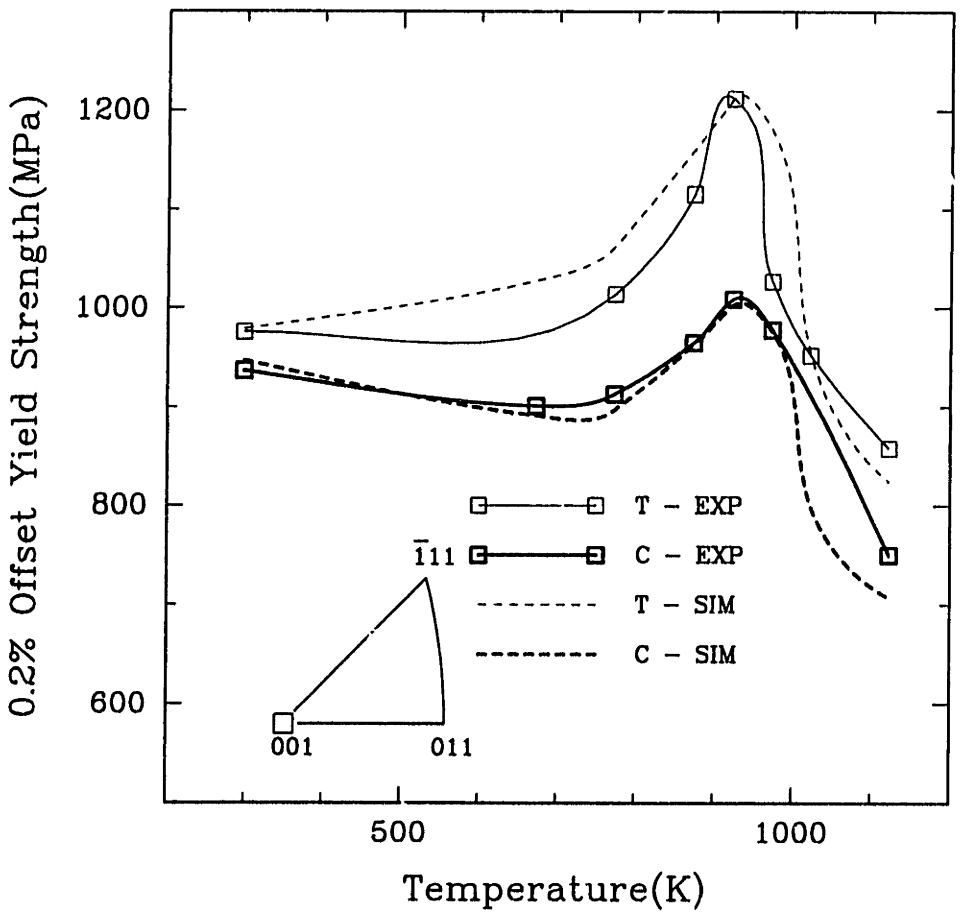

Figure 3-14: Experimental and simulated yield strength vs. temperature curves for the $\langle 001 \rangle$ orientation, $\dot{\epsilon} = \pm .0001/\text{sec}$: Tension and Compression

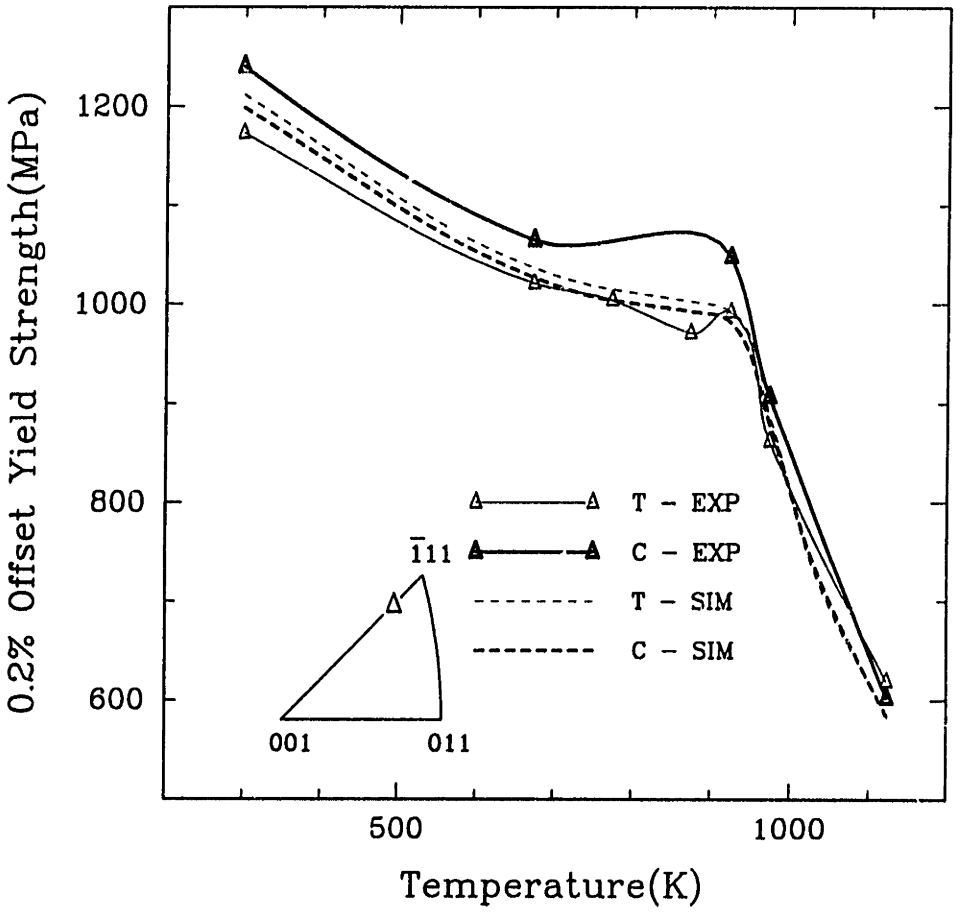

Figure 3-15: Experimental and simulated yield strength vs. temperature curves for the $\langle 111 \rangle$ orientation, $\dot{\epsilon} = \pm .0001/\text{sec}$: Tension and Compression

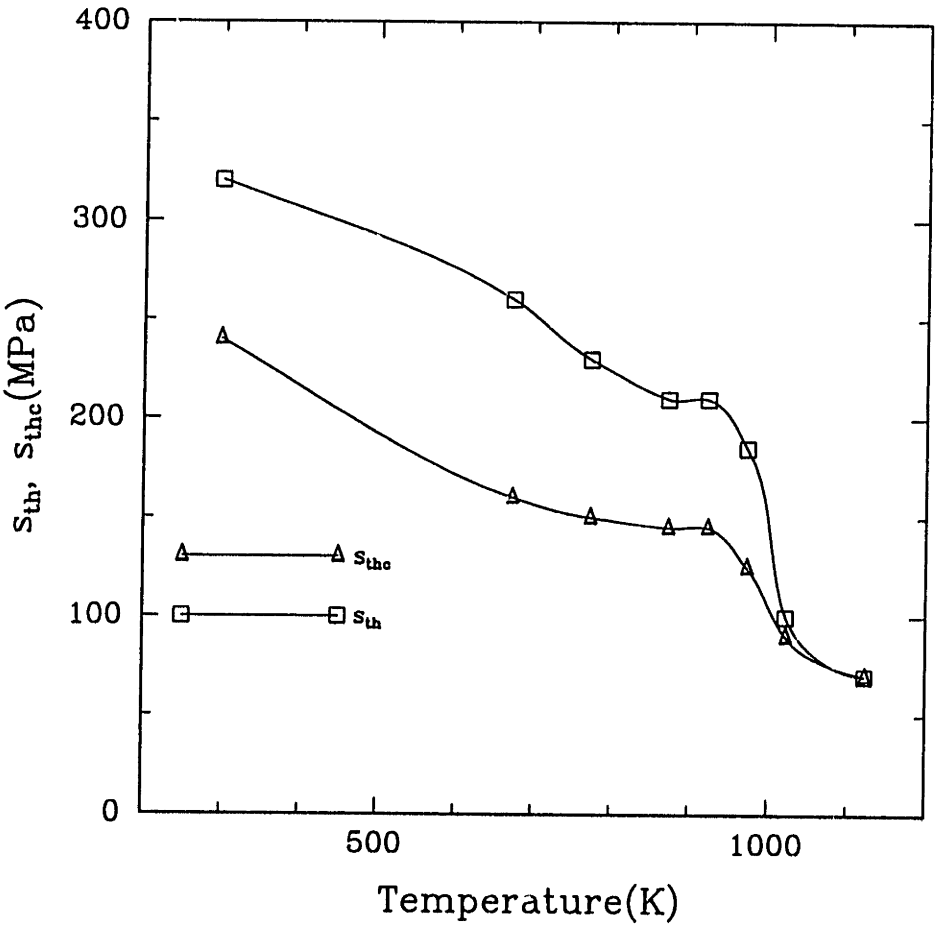

Figure 3-16: Variation of s_{th} with temperature for the octahedral and cube slip systems

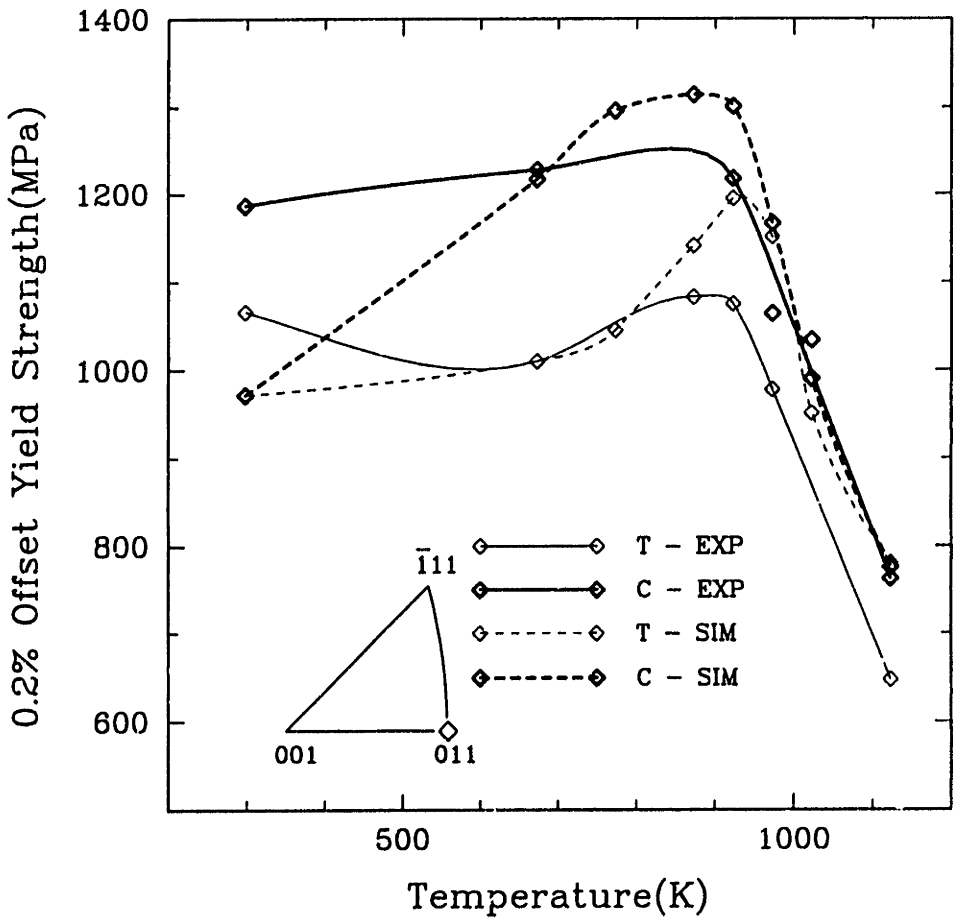

Figure 3-17: Experimental and simulated yield strength vs. temperature curves for the $\langle 011 \rangle$ orientation, $\dot{\epsilon} = \pm .0001/\text{sec}$: Tension and Compression

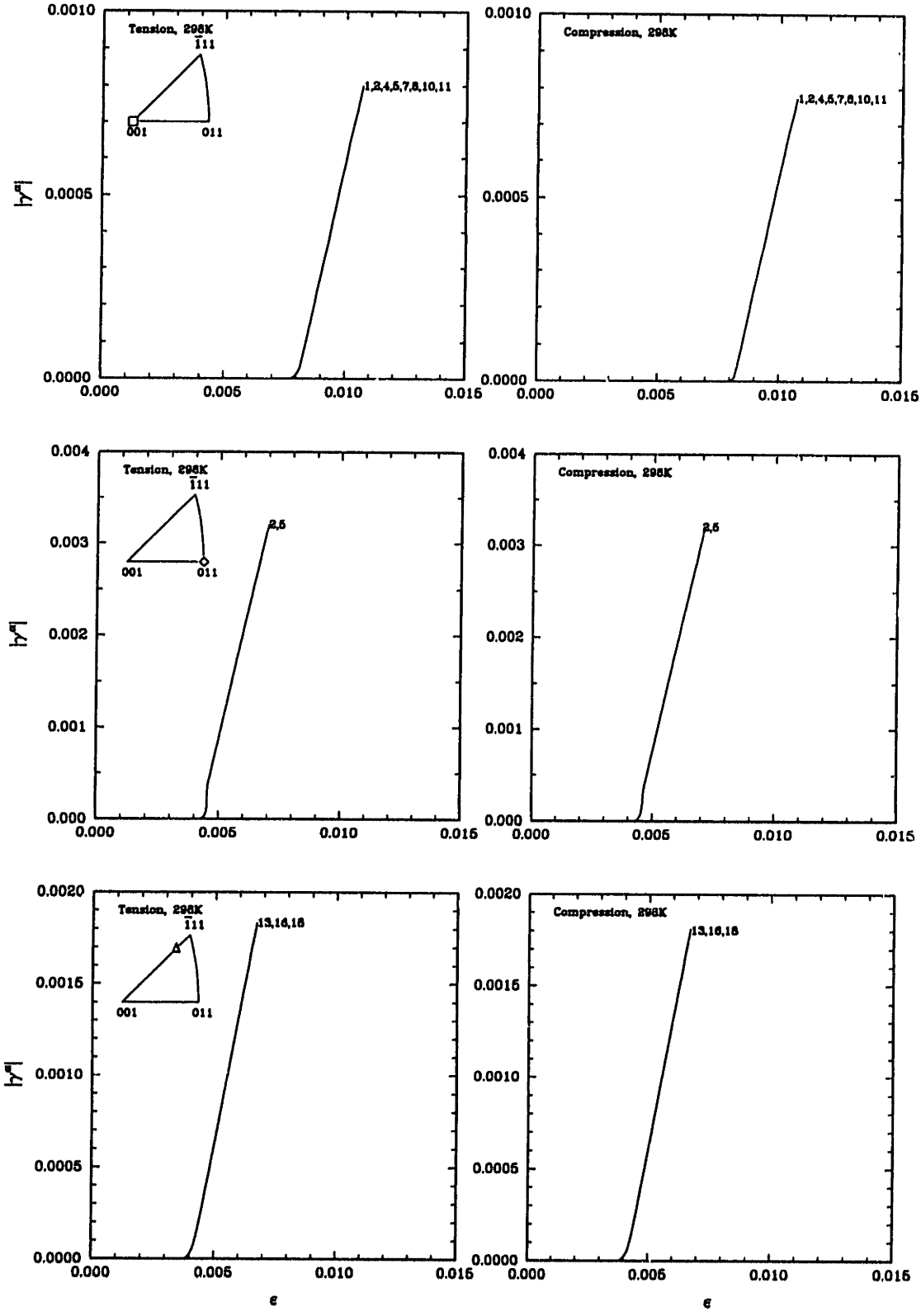

Figure 3-18: Accumulated strain on slip systems at 25°C

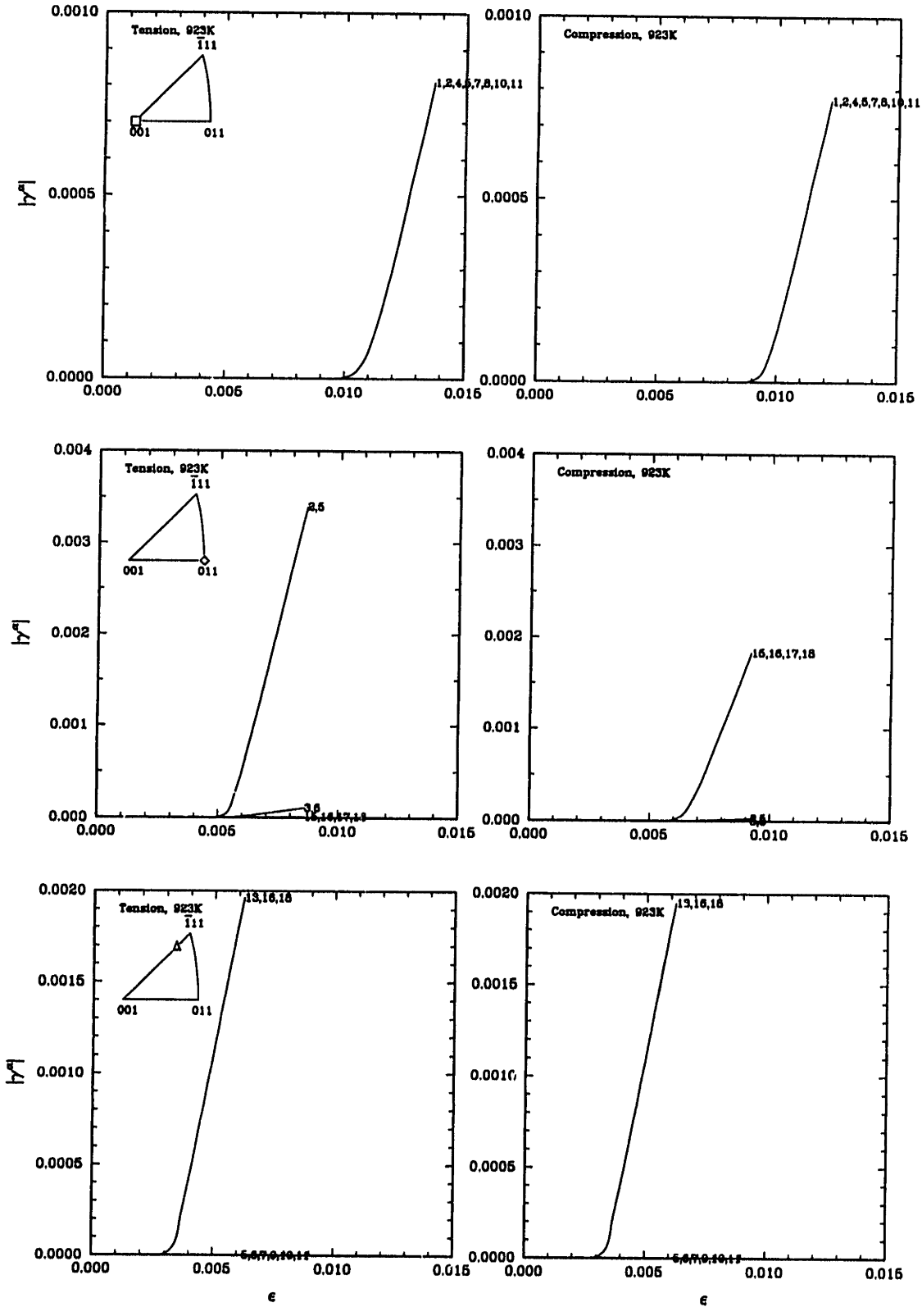

Figure 3-19: Accumulated strain on slip systems at 650°C

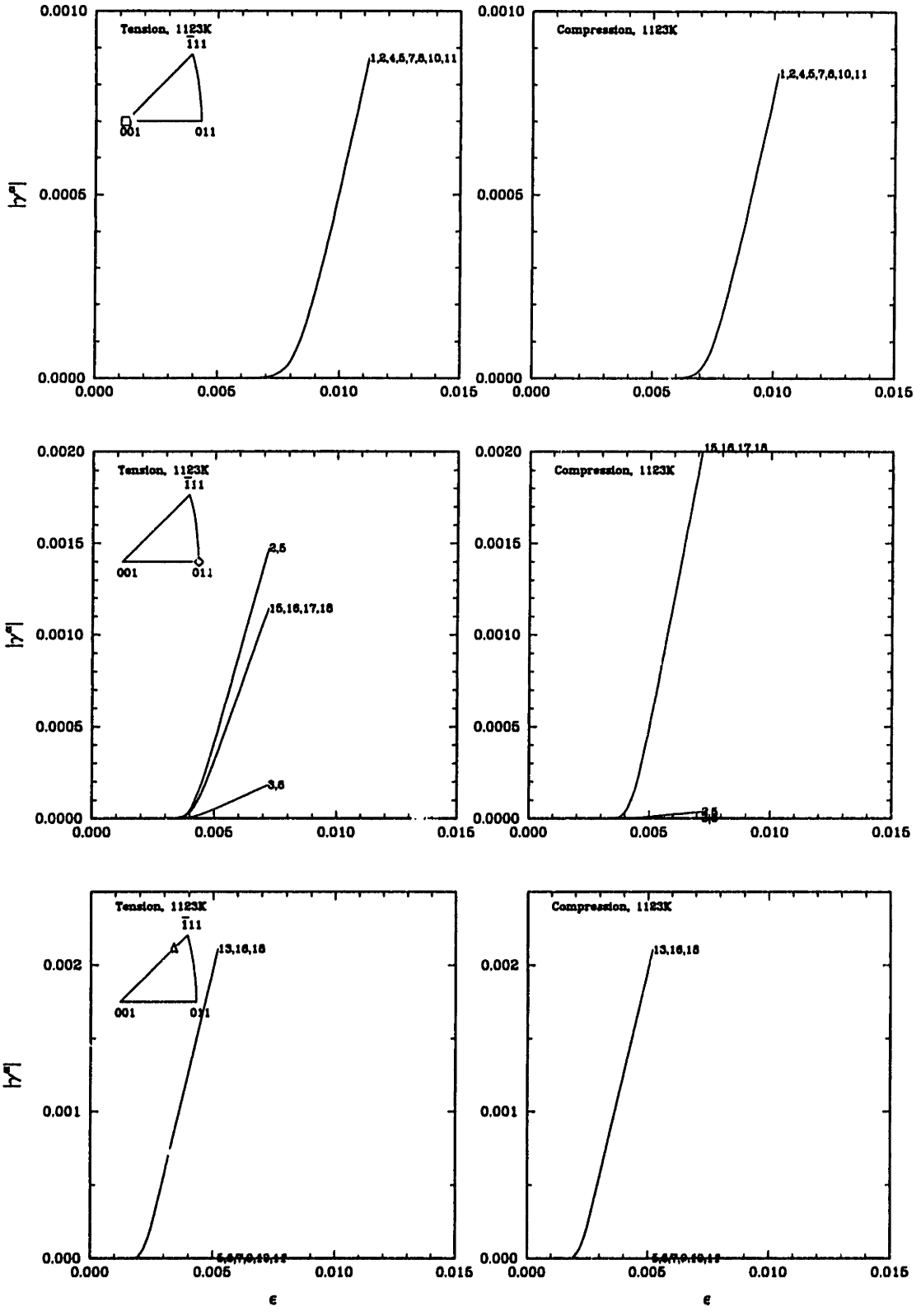

Figure 3-20: Accumulated strain on slip systems at 850°C

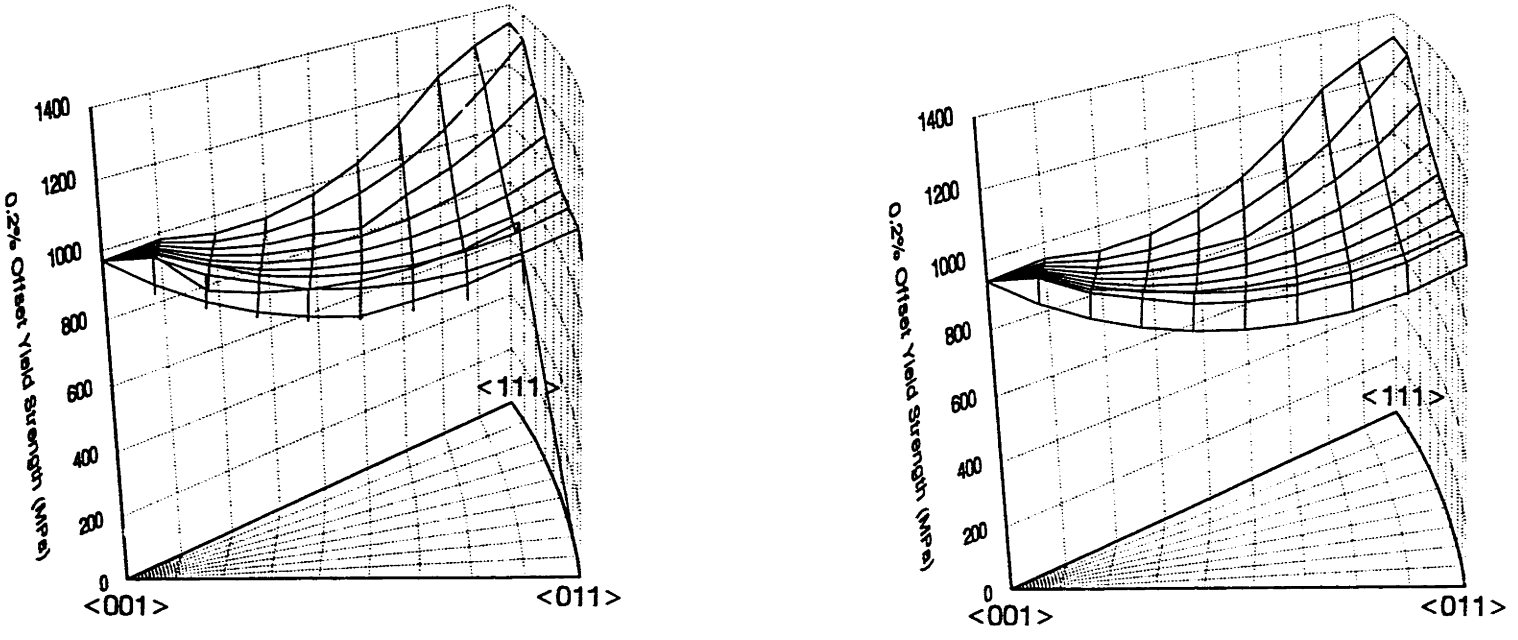

(a) (b)

Figure 3-21: Variation of yield strength with orientation at 25°C (a) Tension (b) Compression

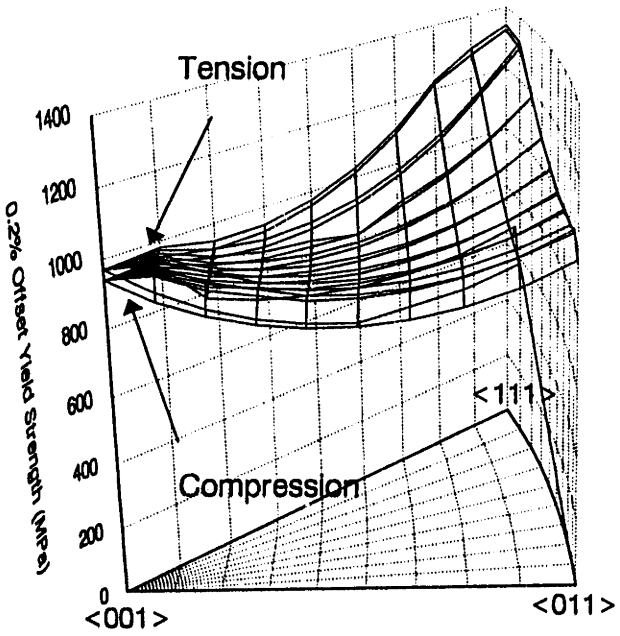

Figure 3-21: Variation of yield strength with orientation at 25°C (c) Tension vs. Compression

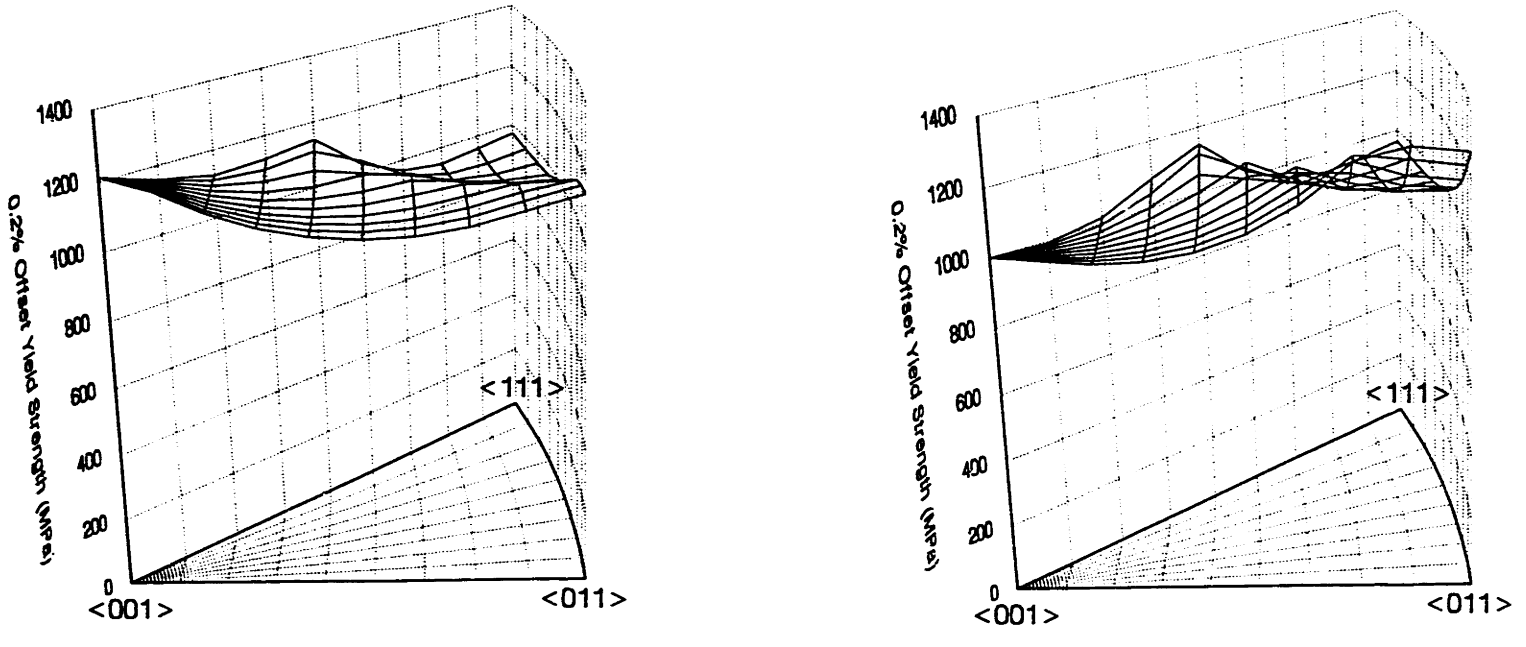

(a) (b)

Figure 3-22: Variation of yield strength with orientation at 650°C (a) Tension (b) Compression

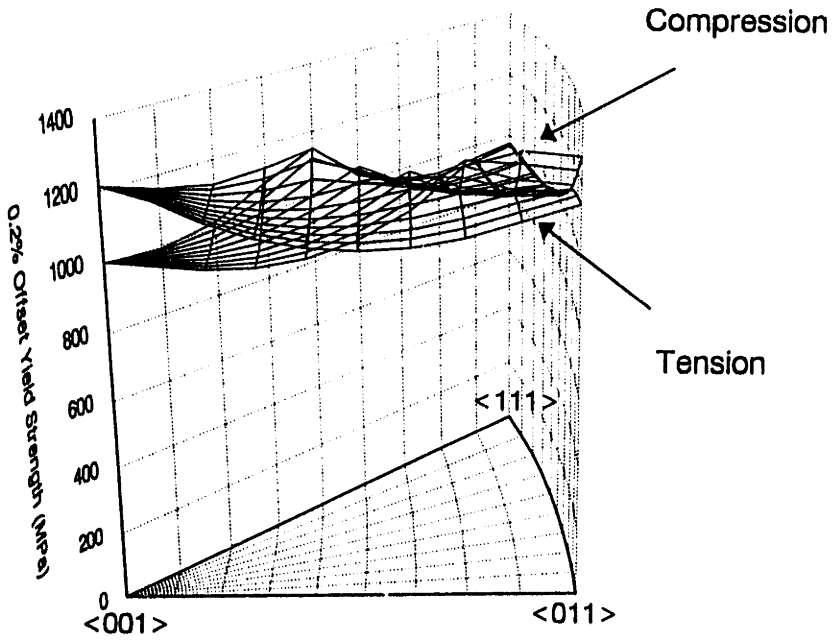

Figure 3-22: Variation of yield strength with orientation at 650°C (c) Tension vs. Compression

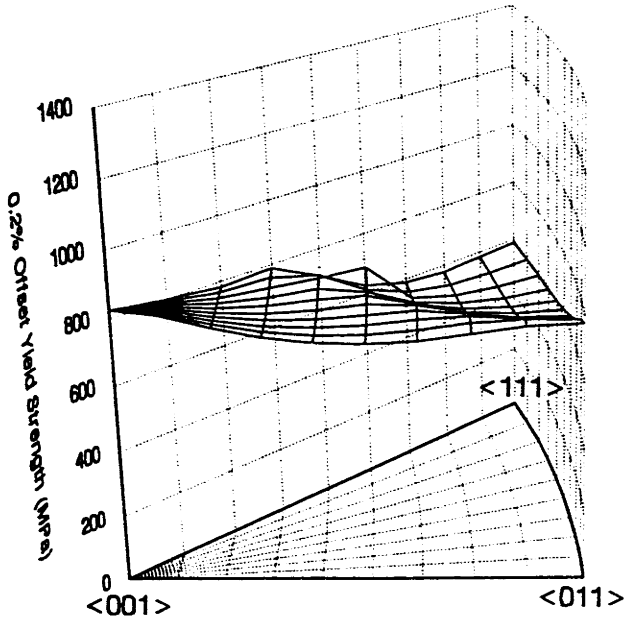

(a)

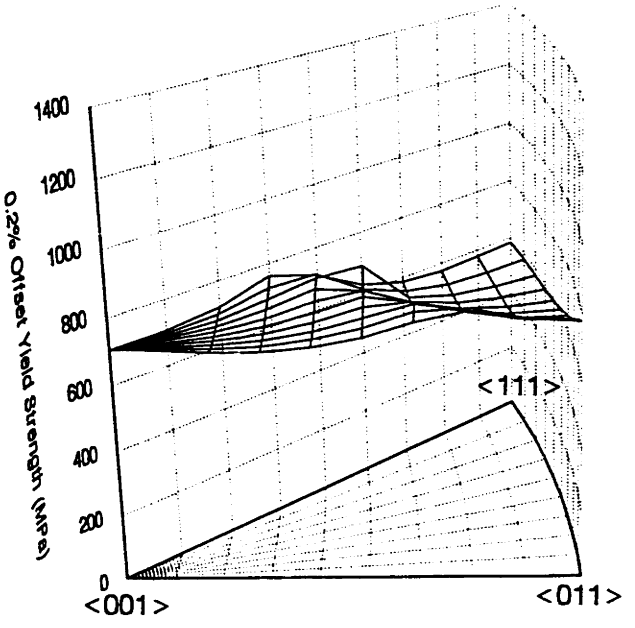

(b)

Figure 3-23: Variation of yield strength with orientation at 850°C (a) Tension (b) Compression

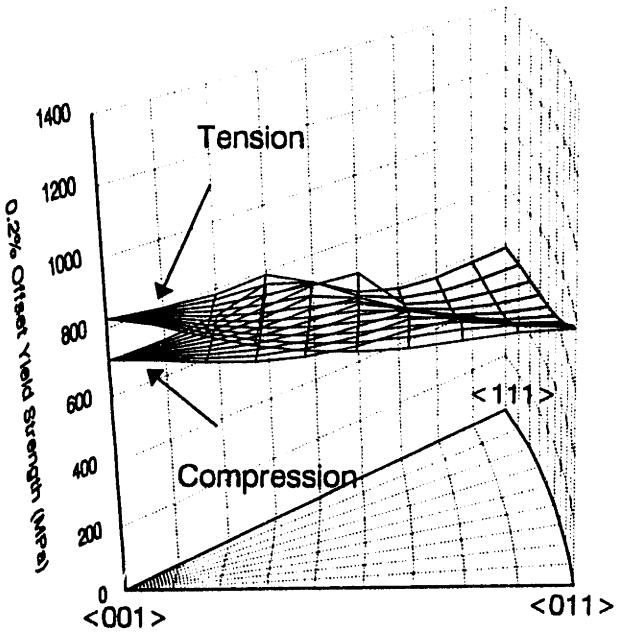

Figure 3-23: Variation of yield strength with orientation at 850°C (c) Tension vs. Compression

Chapter 4

Experiments for Verification of Constitutive Model

In this chapter we assess the predictive capability of the constitutive model for non-homogeneous deformations of CMSX4 in (*i*) torsion of a thin-walled tube, and (*ii*) tension of a notched rectangular bar.

4.1 Thin-Walled Tubular Torsion Experiment and Simulations

4.1.1 Experiments

Thin-walled tubular torsion tests were performed on single crystals of CMSX4 with the ⟨001⟩ crystal axis aligned with the axis of the tube. The specimen geometry was essentially identical to that for the tension and compression tests, with the gage section drilled out to give a wall thickness, t=.635 mm. This gives a ratio of $\frac{t}{d}$ of $\frac{1}{14}$, approximately satisfying the thin-walled criterion. The overall specimen length was 101.6 mm instead of 152.4 mm as in the tension-compression specimens. Figure 4-1 illustrates the specimen geometry used in these tests. The tests were performed at room temperature and at 650°C (near the peak), both at a rotation rate of 0.05 degrees/sec.

The rotation of the actuator was controlled and measured since no high temperature rotary extensometer was available. At each end approximately 25.4 mm of the specimen was gripped, leaving a length of 50.8 mm which undergoes deformation. The gage section

of the specimen was polished to a 1μm finish using diamond paste to allow slip trace observations. Laue measurements were made at various points in the gage section of the specimen following the test to determine the position of the slip traces.

Finite element simulations were also performed for this test using 400 8-noded 3D elements (ABAQUS type C3D8), modeling the entire specimen geometry. The mesh is shown in Figure 4-2. The mesh was made 50.8 mm long. Assuming no compliance of the machine load train (a reasonable assumption for our high stiffness testing machine), this is an accurate representation of the experimental conditions. The material parameters obtained for CMSX4 in Chapter 3 were used in the numerical simulations.

Recall that the resolved shear stress on slip system α is given by

$$\tau^{\alpha} \approx \mathbf{T}^{*} \cdot \mathbf{S}^{\alpha} \tag{4.1}$$

In pure torsion the only stress present is the shear stress τ in the Θz direction (in cylindrical coordinates). In this experiment, the ends are kept fixed, so that there is also an axial stress, $\sigma_{zz} \ll \tau$. Neglecting σ_{zz}, the stress tensor (in rectangular coordinates) is approximately given as a function of a parameter Θ by

$$\mathbf{T}^{*} = \begin{bmatrix} 0 & 0 & -\tau \sin\Theta \\ 0 & 0 & \tau \cos\Theta \\ -\tau \sin\Theta & \tau \cos\Theta & 0 \end{bmatrix} \tag{4.2}$$

where $\Theta = 0$ corresponds to the [100] direction. We may also calculate $\mathbf{S}_{\mathbf{0}}^{\alpha}$ for each of the 18 slip systems. Given that for the $\langle 001 \rangle$ orientation, $\phi = \theta = \omega = 0 \implies \mathbf{Q} \equiv \mathbf{1}$, we obtain the values for $\mathbf{S}_{o}^{\alpha}$ shown in Table 4.1.

Using equation 4.1 and Table 4.1, we may obtain the resolved shear stresses for different values of the angle Θ. From this, we may define a "Schmid factor" $m^{\alpha} = \frac{\tau^{\alpha}}{\tau}$. The values for m^{α} as a function of Θ are plotted for all 18 slip systems in Figure 4-3. The values at the $\langle 001 \rangle$ and $\langle 011 \rangle$ locations are listed in Table 4.2 and illustrated schematically in Figure 4-4 [Nouailhas *et al.*, 1993]. We see that in torsion both octahedral and cube slips systems may be active, and the largest resolved shear stresses occur on the cube planes. In the [110] and $[\bar{1}\bar{1}0]$ directions, $\Theta = 45^{o}$ and 225^{o} respectively, slip system 18 should be dominant, while in the $[\bar{1}10]$ and $[1\bar{1}0]$ directions, $\Theta = 135^{o}$ and 315^{o} respectively, slip system 17

Table 4.1: Values of $\mathbf{S}_o^\alpha$ for the $\langle 001 \rangle$ orientation

(a) Octahedral Slip Systems

α	$\mathbf{n}_o^\alpha = \mathbf{Q}\mathbf{n}_c^\alpha$	$\mathbf{m}_o^\alpha = \mathbf{Q}\mathbf{m}_c^\alpha$	$\mathbf{S}_o^\alpha = \mathbf{m}_o^\alpha \otimes \mathbf{n}_o^\alpha$
1	$\left\{ \frac{1}{\sqrt{3}} \quad \frac{1}{\sqrt{3}} \quad \frac{1}{\sqrt{3}} \right\}$	$\left\{ 0 \quad \frac{1}{\sqrt{2}} \quad -\frac{1}{\sqrt{2}} \right\}$	$\begin{bmatrix} 0 & 0 & 0 \\ \frac{1}{\sqrt{6}} & \frac{1}{\sqrt{6}} & \frac{1}{\sqrt{6}} \\ -\frac{1}{\sqrt{6}} & -\frac{1}{\sqrt{6}} & -\frac{1}{\sqrt{6}} \end{bmatrix}$
2	$\left\{ \frac{1}{\sqrt{3}} \quad \frac{1}{\sqrt{3}} \quad \frac{1}{\sqrt{3}} \right\}$	$\left\{ -\frac{1}{\sqrt{2}} \quad 0 \quad \frac{1}{\sqrt{2}} \right\}$	$\begin{bmatrix} -\frac{1}{\sqrt{6}} & -\frac{1}{\sqrt{6}} & -\frac{1}{\sqrt{6}} \\ 0 & 0 & 0 \\ \frac{1}{\sqrt{6}} & \frac{1}{\sqrt{6}} & \frac{1}{\sqrt{6}} \end{bmatrix}$
3	$\left\{ \frac{1}{\sqrt{3}} \quad \frac{1}{\sqrt{3}} \quad \frac{1}{\sqrt{3}} \right\}$	$\left\{ \frac{1}{\sqrt{2}} \quad -\frac{1}{\sqrt{2}} \quad 0 \right\}$	$\begin{bmatrix} \frac{1}{\sqrt{6}} & \frac{1}{\sqrt{6}} & \frac{1}{\sqrt{6}} \\ -\frac{1}{\sqrt{6}} & -\frac{1}{\sqrt{6}} & -\frac{1}{\sqrt{6}} \\ 0 & 0 & 0 \end{bmatrix}$
4	$\left\{ \frac{1}{\sqrt{3}} \quad -\frac{1}{\sqrt{3}} \quad -\frac{1}{\sqrt{3}} \right\}$	$\left\{ 0 \quad -\frac{1}{\sqrt{2}} \quad \frac{1}{\sqrt{2}} \right\}$	$\begin{bmatrix} 0 & 0 & 0 \\ -\frac{1}{\sqrt{6}} & \frac{1}{\sqrt{6}} & \frac{1}{\sqrt{6}} \\ \frac{1}{\sqrt{6}} & -\frac{1}{\sqrt{6}} & -\frac{1}{\sqrt{6}} \end{bmatrix}$
5	$\left\{ \frac{1}{\sqrt{3}} \quad -\frac{1}{\sqrt{3}} \quad -\frac{1}{\sqrt{3}} \right\}$	$\left\{ -\frac{1}{\sqrt{2}} \quad 0 \quad -\frac{1}{\sqrt{2}} \right\}$	$\begin{bmatrix} -\frac{1}{\sqrt{6}} & \frac{1}{\sqrt{6}} & \frac{1}{\sqrt{6}} \\ 0 & 0 & 0 \\ -\frac{1}{\sqrt{6}} & \frac{1}{\sqrt{6}} & \frac{1}{\sqrt{6}} \end{bmatrix}$
6	$\left\{ \frac{1}{\sqrt{3}} \quad -\frac{1}{\sqrt{3}} \quad -\frac{1}{\sqrt{3}} \right\}$	$\left\{ \frac{1}{\sqrt{2}} \quad \frac{1}{\sqrt{2}} \quad 0 \right\}$	$\begin{bmatrix} \frac{1}{\sqrt{6}} & -\frac{1}{\sqrt{6}} & -\frac{1}{\sqrt{6}} \\ \frac{1}{\sqrt{6}} & -\frac{1}{\sqrt{6}} & -\frac{1}{\sqrt{6}} \\ 0 & 0 & 0 \end{bmatrix}$
7	$\left\{ -\frac{1}{\sqrt{3}} \quad \frac{1}{\sqrt{3}} \quad -\frac{1}{\sqrt{3}} \right\}$	$\left\{ 0 \quad \frac{1}{\sqrt{2}} \quad \frac{1}{\sqrt{2}} \right\}$	$\begin{bmatrix} 0 & 0 & 0 \\ -\frac{1}{\sqrt{6}} & \frac{1}{\sqrt{6}} & -\frac{1}{\sqrt{6}} \\ -\frac{1}{\sqrt{6}} & \frac{1}{\sqrt{6}} & -\frac{1}{\sqrt{6}} \end{bmatrix}$
8	$\left\{ -\frac{1}{\sqrt{3}} \quad \frac{1}{\sqrt{3}} \quad -\frac{1}{\sqrt{3}} \right\}$	$\left\{ \frac{1}{\sqrt{2}} \quad 0 \quad -\frac{1}{\sqrt{2}} \right\}$	$\begin{bmatrix} -\frac{1}{\sqrt{6}} & \frac{1}{\sqrt{6}} & -\frac{1}{\sqrt{6}} \\ 0 & 0 & 0 \\ \frac{1}{\sqrt{6}} & -\frac{1}{\sqrt{6}} & \frac{1}{\sqrt{6}} \end{bmatrix}$
9	$\left\{ -\frac{1}{\sqrt{3}} \quad \frac{1}{\sqrt{3}} \quad -\frac{1}{\sqrt{3}} \right\}$	$\left\{ -\frac{1}{\sqrt{2}} \quad -\frac{1}{\sqrt{2}} \quad 0 \right\}$	$\begin{bmatrix} \frac{1}{\sqrt{6}} & -\frac{1}{\sqrt{6}} & \frac{1}{\sqrt{6}} \\ \frac{1}{\sqrt{6}} & -\frac{1}{\sqrt{6}} & \frac{1}{\sqrt{6}} \\ 0 & 0 & 0 \end{bmatrix}$
10	$\left\{ -\frac{1}{\sqrt{3}} \quad -\frac{1}{\sqrt{3}} \quad \frac{1}{\sqrt{3}} \right\}$	$\left\{ 0 \quad -\frac{1}{\sqrt{2}} \quad -\frac{1}{\sqrt{2}} \right\}$	$\begin{bmatrix} 0 & 0 & 0 \\ \frac{1}{\sqrt{6}} & \frac{1}{\sqrt{6}} & -\frac{1}{\sqrt{6}} \\ \frac{1}{\sqrt{6}} & \frac{1}{\sqrt{6}} & -\frac{1}{\sqrt{6}} \end{bmatrix}$
11	$\left\{ -\frac{1}{\sqrt{3}} \quad -\frac{1}{\sqrt{3}} \quad \frac{1}{\sqrt{3}} \right\}$	$\left\{ \frac{1}{\sqrt{2}} \quad 0 \quad \frac{1}{\sqrt{2}} \right\}$	$\begin{bmatrix} -\frac{1}{\sqrt{6}} & -\frac{1}{\sqrt{6}} & \frac{1}{\sqrt{6}} \\ 0 & 0 & 0 \\ -\frac{1}{\sqrt{6}} & -\frac{1}{\sqrt{6}} & \frac{1}{\sqrt{6}} \end{bmatrix}$
12	$\left\{ -\frac{1}{\sqrt{3}} \quad -\frac{1}{\sqrt{3}} \quad \frac{1}{\sqrt{3}} \right\}$	$\left\{ -\frac{1}{\sqrt{2}} \quad \frac{1}{\sqrt{2}} \quad 0 \right\}$	$\begin{bmatrix} \frac{1}{\sqrt{6}} & \frac{1}{\sqrt{6}} & -\frac{1}{\sqrt{6}} \\ -\frac{1}{\sqrt{6}} & -\frac{1}{\sqrt{6}} & \frac{1}{\sqrt{6}} \\ 0 & 0 & 0 \end{bmatrix}$

(b)Cube Slip Systems

α	$\mathbf{n}_o^\alpha = \mathbf{Q}\mathbf{n}_c^\alpha$	$\mathbf{m}_o^\alpha = \mathbf{Q}\mathbf{m}_c^\alpha$	$\mathbf{S}_o^\alpha = \mathbf{m}_o^\alpha \otimes \mathbf{n}_o^\alpha$
13	$\left\{ 1 \quad 0 \quad 0 \right\}$	$\left\{ 0 \quad \frac{1}{\sqrt{2}} \quad \frac{1}{\sqrt{2}} \right\}$	$\begin{bmatrix} 0 & \frac{1}{\sqrt{2}} & \frac{1}{\sqrt{2}} \\ 0 & 0 & 0 \\ 0 & 0 & 0 \end{bmatrix}$
14	$\left\{ 1 \quad 0 \quad 0 \right\}$	$\left\{ 0 \quad \frac{1}{\sqrt{2}} \quad -\frac{1}{\sqrt{2}} \right\}$	$\begin{bmatrix} 0 & \frac{1}{\sqrt{2}} & -\frac{1}{\sqrt{2}} \\ 0 & 0 & 0 \\ 0 & 0 & 0 \end{bmatrix}$
15	$\left\{ 0 \quad 1 \quad 0 \right\}$	$\left\{ \frac{1}{\sqrt{2}} \quad 0 \quad \frac{1}{\sqrt{2}} \right\}$	$\begin{bmatrix} 0 & 0 & 0 \\ \frac{1}{\sqrt{2}} & 0 & \frac{1}{\sqrt{2}} \\ 0 & 0 & 0 \end{bmatrix}$
16	$\left\{ 0 \quad 1 \quad 0 \right\}$	$\left\{ \frac{1}{\sqrt{2}} \quad 0 \quad -\frac{1}{\sqrt{2}} \right\}$	$\begin{bmatrix} 0 & 0 & 0 \\ \frac{1}{\sqrt{2}} & 0 & -\frac{1}{\sqrt{2}} \\ 0 & 0 & 0 \end{bmatrix}$
17	$\left\{ 0 \quad 0 \quad 1 \right\}$	$\left\{ \frac{1}{\sqrt{2}} \quad \frac{1}{\sqrt{2}} \quad 0 \right\}$	$\begin{bmatrix} 0 & 0 & 0 \\ 0 & 0 & 0 \\ \frac{1}{\sqrt{2}} & \frac{1}{\sqrt{2}} & 0 \end{bmatrix}$
18	$\left\{ 0 \quad 0 \quad 1 \right\}$	$\left\{ \frac{1}{\sqrt{2}} \quad -\frac{1}{\sqrt{2}} \quad 0 \right\}$	$\begin{bmatrix} 0 & 0 & 0 \\ 0 & 0 & 0 \\ \frac{1}{\sqrt{2}} & -\frac{1}{\sqrt{2}} & 0 \end{bmatrix}$

should be dominant. Note that 17 and 18 are both *cube* slip systems[1]. The strength of the slip systems, given by the temperature-dependent values of s_o and s_{th}, together with the resolved shear stresses determine the shearing rate on a slip system.

4.1.2 Results

Room Temperature Experiment

Figure 4-5 shows the experimental and simulated nominal shear and normal stress versus strain curves at room temperature. In the simulations we utilize 3D continuum elements (ABAQUS type C3D8) which do not have rotational degrees of freedom. Therefore, we obtain three components of the force from the simulation, lumped at one node (on the outer diameter). The magnitude of the force tangential to the circle of the mesh is given by:

$$F = \sqrt{F_1^2 + F_2^2} \tag{4.3}$$

[1]The resolved shear stresses on the octahedral slip systems are lower by a factor of about $\frac{1}{\sqrt{3}}$

Table 4.2: Schmid Factors, m^α for each slip system for the $\langle 001 \rangle$ and $\langle 011 \rangle$ directions

α	$\Theta = 0$ [100]	$\Theta = 45$ [110]	$\Theta = 90$ [010]	$\Theta = 135$ [$\bar{1}10$]	$\Theta = 180$ [$\bar{1}00$]	$\Theta = 225$ [$\bar{1}\bar{1}0$]	$\Theta = 270$ [$0\bar{1}0$]	$\Theta = 315$ [$1\bar{1}0$]
1	0	$\frac{1}{2\sqrt{3}}$	$\frac{1}{\sqrt{6}}$	$\frac{1}{2\sqrt{3}}$	0	$-\frac{1}{2\sqrt{3}}$	$-\frac{1}{\sqrt{6}}$	$-\frac{1}{2\sqrt{3}}$
2	$\frac{1}{\sqrt{6}}$	$\frac{1}{2\sqrt{3}}$	0	$-\frac{1}{2\sqrt{3}}$	$-\frac{1}{\sqrt{6}}$	$-\frac{1}{2\sqrt{3}}$	0	$\frac{1}{2\sqrt{3}}$
3	$-\frac{1}{\sqrt{6}}$	$-\frac{1}{\sqrt{3}}$	$-\frac{1}{\sqrt{6}}$	0	$\frac{1}{\sqrt{6}}$	$\frac{1}{\sqrt{3}}$	$\frac{1}{\sqrt{6}}$	0
4	0	$-\frac{1}{2\sqrt{3}}$	$-\frac{1}{\sqrt{6}}$	$-\frac{1}{2\sqrt{3}}$	0	$\frac{1}{2\sqrt{3}}$	$\frac{1}{\sqrt{6}}$	$\frac{1}{2\sqrt{3}}$
5	$\frac{1}{\sqrt{6}}$	$\frac{1}{2\sqrt{3}}$	0	$-\frac{1}{2\sqrt{3}}$	$-\frac{1}{\sqrt{6}}$	$-\frac{1}{2\sqrt{3}}$	0	$\frac{1}{2\sqrt{3}}$
6	$-\frac{1}{\sqrt{6}}$	0	$\frac{1}{\sqrt{6}}$	$\frac{1}{\sqrt{3}}$	$\frac{1}{\sqrt{6}}$	0	$-\frac{1}{\sqrt{6}}$	$-\frac{1}{\sqrt{3}}$
7	0	$\frac{1}{2\sqrt{3}}$	$\frac{1}{\sqrt{6}}$	$\frac{1}{2\sqrt{3}}$	0	$-\frac{1}{2\sqrt{3}}$	$-\frac{1}{\sqrt{6}}$	$-\frac{1}{2\sqrt{3}}$
8	$-\frac{1}{\sqrt{6}}$	$-\frac{1}{2\sqrt{3}}$	0	$\frac{1}{2\sqrt{3}}$	$\frac{1}{\sqrt{6}}$	$\frac{1}{2\sqrt{3}}$	0	$-\frac{1}{2\sqrt{3}}$
9	$\frac{1}{\sqrt{6}}$	0	$-\frac{1}{\sqrt{6}}$	$-\frac{1}{\sqrt{3}}$	$-\frac{1}{\sqrt{6}}$	0	$\frac{1}{\sqrt{6}}$	$\frac{1}{\sqrt{3}}$
10	0	$-\frac{1}{2\sqrt{3}}$	$-\frac{1}{\sqrt{6}}$	$-\frac{1}{2\sqrt{3}}$	0	$\frac{1}{2\sqrt{3}}$	$\frac{1}{\sqrt{6}}$	$\frac{1}{2\sqrt{3}}$
11	$-\frac{1}{\sqrt{6}}$	$-\frac{1}{2\sqrt{3}}$	0	$\frac{1}{2\sqrt{3}}$	$\frac{1}{\sqrt{6}}$	$\frac{1}{2\sqrt{3}}$	0	$-\frac{1}{2\sqrt{3}}$
12	$\frac{1}{\sqrt{6}}$	$\frac{1}{\sqrt{3}}$	$\frac{1}{\sqrt{6}}$	0	$-\frac{1}{\sqrt{6}}$	$-\frac{1}{\sqrt{3}}$	$-\frac{1}{\sqrt{6}}$	0
13	0	$-\frac{1}{2}$	$-\frac{1}{\sqrt{2}}$	$-\frac{1}{2}$	0	$\frac{1}{2}$	$\frac{1}{\sqrt{2}}$	$\frac{1}{2}$
14	0	$\frac{1}{2}$	$\frac{1}{\sqrt{2}}$	$\frac{1}{2}$	0	$-\frac{1}{2}$	$-\frac{1}{\sqrt{2}}$	$-\frac{1}{2}$
15	$\frac{1}{\sqrt{2}}$	$\frac{1}{2}$	0	$-\frac{1}{2}$	$-\frac{1}{\sqrt{2}}$	$-\frac{1}{2}$	0	$\frac{1}{2}$
16	$-\frac{1}{\sqrt{2}}$	$-\frac{1}{2}$	0	$\frac{1}{2}$	$\frac{1}{\sqrt{2}}$	$\frac{1}{2}$	0	$-\frac{1}{2}$
17	$\frac{1}{\sqrt{2}}$	0	$-\frac{1}{\sqrt{2}}$	-1	$-\frac{1}{\sqrt{2}}$	0	$\frac{1}{\sqrt{2}}$	1
18	$-\frac{1}{\sqrt{2}}$	-1	$-\frac{1}{\sqrt{2}}$	0	$\frac{1}{\sqrt{2}}$	1	$\frac{1}{\sqrt{2}}$	0

where the loading direction is 3. The nominal shear stress is calculated by dividing this force by the cross-sectional area of the gage section, i.e.

$$\tau = \frac{F}{\pi(r_o^2 - r_i^2)} \tag{4.4}$$

where r_o and r_i are the inner and outer radii of the gage section, respectively. The prediction of the model gives a very good match.

Figure 4-6(a) through (d) shows the slip traces formed on the surface of the gage section of the specimen after a twist of about 4°, corresponding to a nominal shear strain of roughly 5%. They are localized in 8 roughly equally spaced areas located midway between the ⟨001⟩ and the ⟨011⟩ directions, ($\Theta = 22.5° + n * 45°$). The figure also shows the experimental and simulated Laue patterns at each of the localized zones and midway between them.

This is consistent with the slip system activity calculated above. At $\Theta = 45°$ and $\Theta = 225°$ the resolved shear stress has a maximum on slip system 18, Figure 4-3. Moving away from these locations in either direction the resolved shear stresses on this slip system decreases sinusoidally. At and near these locations, therefore, slip system 18 is active, causing slip on the (001) plane, in the $[1\bar{1}0]$ direction. *This direction is tangential to the tube at the* [110] *location* ($\Theta = 45°$) *and the* $[\bar{1}\bar{1}0]$ *location* ($\Theta = 225°$), *so the slip traces do not show up in those positions, but rather symmetrically on either side.* The same is true of slip system 17 at $\Theta = 135°$ and $\Theta = 315°$. This leads to 8 areas where slip traces are most evident, Figure 4-7. Figure 4-8 plots the non-zero accumulated plastic strains, close to the ⟨001⟩ position and at the ⟨011⟩ position, over one half of the circumference. By symmetry, the other half is identical. At $\Theta = 45°$ slip system 18 is active, Figure 4-8(a), while at $\Theta = 135°$ slip system 17 is active, Figure 4-8(c), as expected. Close to the ⟨001⟩ positions, either slip sytem 17 or 18 is active, depending on which ⟨011⟩ position is closer, with the accumulated plastic strain being much lower than that at the ⟨011⟩ positions, Figure 4-8(b) and (d).

Figure 4-9(a) and (b) show the contours of accumulated plastic strain on the deformed mesh after the same amount of strain as in the experiment for slip system 17 and slip system 18, respectively. The model predicts that the accumulated strain on slip system 17 is highest at $\Theta = 135°$ (not visible in the view seen) and $\Theta = 315°$, and much less elsewhere; the accumulated strain on slip system 18 is highest at $\Theta = 45°$ and $\Theta = 225°$

(not visible in the view seen).

These room temperature experimental results agree qualitatively with those of Nouailhas *et al.* [1993]. That group performed biaxial tension-torsion tests on single crystals of CMSX2 at room temperature and higher temperatures. They too found that at room temperature there were eight zones of cube slip traces, obviously due to the torsion since the resolved shear stress on these slip systems due to tension in the ⟨001⟩ direction is zero. The slip traces from their experiment are illustrated schematically in Figure 4-10.

Experiment at 650°C

The nominal shear and normal stress versus strain curves at 650°C are shown in Figure 4-11. At this temperature the slip traces are more diffuse and far less pronounced than at 25°C, and octahedral slip traces are also observed, Figure 4-12(a) through (d). This is illustrated by the detail shown in Figure 4-13. Figure 4-14 shows the contours of accumulated plastic strain rate after the same amount of strain as in the experiment at this temperature. The maximum on slip systems 17 and 18 occur as expected. Figure 4-15 plots the accumulated plastic strain on each of the 18 slip systems. The result is qualitatively the same as that observed in the room temperature experiment. *No octahedral slip is predicted in this simulation although it is clearly observed in the experiments.* This indicates that the relative magnitudes of the octahedral and cube resistances need to be slightly adjusted to allow octahedral slip at this temperature for this experiment.

4.1.3 Discussion

Using the parameters obtained in the previous chapter from simple tension and compression experiments on this material at the temperatures tested, the simulations of the torsion experiment were performed as described above. The model gives a very good match to the stress-strain curve at 25°C, and less so for the higher temperature of 650°C. Also, the observed slip lines correspond to the expected slip activity for a ⟨001⟩-oriented bar in torsion. The plots of accumulated slip on the slip systems with deformation shows that the active slip systems are those that are expected: slip system 18 in the quadrant where $0 \leq \Theta \leq 90$, and 17 in the quadrant where $90 \leq \Theta \leq 180$.

4.2 Double-Notched Tension Experiment and Simulation

4.2.1 Geometry

The fir tree root structure of a turbine blade leads to areas of stress concentration at notches in the blade root, Figure 1-2. Accordingly, this study includes a notched bar tension experiment and simulation. The geometry of the notched specimen is sketched in Figure 4-16. The ratio $\frac{r}{d}$ with semi-circular notches gives a stress concentration factor for this geometry of $K_t \approx 1.7$ [Peterson, 1974], where r is the radius of the notch, and d is the distance between the notch roots. The cross-section perpendicular to the loading direction was square. A full 3-dimensional finite element simulation of this geometry was performed, using 2560 C3D8 8-noded 3D elements. Only one-eighth of the geometry was simulated because of the symmetry of the specimen in all three dimensions. The finite element mesh is shown in Figure 4-17. The figure shows the refined mesh to better pick up the expected localization. The entire notched area is shown in Figure 4-18.

4.2.2 Experiment

A double-notched-bar tension test was performed on a single crystal of ⟨001⟩-oriented CMSX4 at room temperature. The side faces of the specimen were oriented in the ⟨001⟩ directions. Laue measurements on the axis of the specimen — 3-direction, [001], and on the notched side face of the specimen — 2-direction, [010], showed that the specimen axis and the notch faces were within a couple of degrees of ⟨001⟩, Figure 4-19. A room temperature Instron extensometer with a half inch gage length was used to control the actuator displacement and measure the specimen deformation in the vicinity of the notch. The displacment rate was 1.27×10^{-3}mm/sec, giving a nominal strain rate of .0001/sec. The half inch length of material over which the strain was measured was simulated in the finite element calculations. The front faces of the specimen were polished to a 1μm finish using diamond paste to allow slip trace observations.

4.2.3 Results

Finite element simulations of this test were performed with the mesh described above, using the CMSX4 model parameters obtained from the tension and compression tests of Chapter 3 at this temperature. Figure 4-20 shows the experimental load displacement curve

plotted along with the predicted curve. The match between the experiment and simulation is extremely good.

Figure 4-21 shows contours of equivalent plastic strain and plastic strain rate at the end of the simulation. The 3D views show that the maximum strain and strain rate occur at the center of the specimen at the notch root. However, in the 1-direction definite shear bands are observed. Figure 4-22(a) shows a micrograph of the specimen after testing. A clearly defined diamond-shaped series of shear bands is observed. Figure 4-22(b) shows the [010] view of the entire mesh, constructed by appropriate reflections of the quadrant of the cross-section which was simulated. This closely mimics the experimental result in the direction of the shear bands observed experimentally. The experiment showed a slightly higher concentration of slip traces at one notch. This could be due to the slight misalignment of the crystal, or of the testing machine.

Comparison with simulations using other material models

The notch geometry was simulated again at room temperature, but using two other material models: (*i*) orthotropic elasticity and perfect plasticity, using the known elastic constants for the material at this temperature: C_{11} = 272GPa, C_{12} =181GPa, C_{44} = 130GPa, and the yield strength obtained from the ⟨001⟩ tension test at this temperature: σ_y = 976MPa; and (*ii*) isotropic elasticity and perfectly plastic, using the value of the modulus calculated from the anisotropic constants (E = 127GPa), and $\nu = 0.3$, and the yield strength obtained from the ⟨001⟩ tension test at this temperature: σ_y = 976MPa. This allowed us to observe qualitatively the effect of the anisotropy in elasticity and plasticity on the material behavior.

The resulting load-displacement curves are shown in Figure 4-23. The predictions are higher than the experiment in both cases. The equivalent plastic strain contours are shown in Figure 4-24. The experimentally observed localization behavior is clearly altered by the plastic anisotropy; the shear bands are more developed in the experiment and in the simulations of our model than in the simulations with isotropic plasticity, and they form a sharp diamond shape. The isotropic plasticity models predict that the highest strains remain concentrated at the center of the notch root, rather than at angles of roughly 54°, which is the trace of the ⟨111⟩ planes on ⟨001⟩-type faces. The results of these classical isotropic models are non-conservative; they overpredict the yield load of the notched specimen, and they predict small levels of strain concentration at the notch root at macroscopic yield.

From a design point of view these are serious flaws since they could lead to underdesign of a part. This clearly indicates the importance of the phenomena incorporated into the current model, since the classical models do not adequately capture the experimental result, and also do not yield conservative predictions.

4.2.4 Discussion

The match between experiment and simulation for the load-displacement curve, as well as for the slip traces, is excellent. Modeling the material with a simple anisotropic elastic but isotropic plasticity model may allow us to match the load-displacement curve, but does not predict the localization accurately. Using a crystal plasticity model without the tension-compression asymmetry and temperature dependence included should give a similar result to that obtained from our model, since at room temperature, the contributions of these effects is minimal. At higher temperatures, the difference between these two cases should be more striking. Nevertheless, the simulation performed above does verify the predictive capability of the present model, and shows that it is possible to use this model for design purposes.

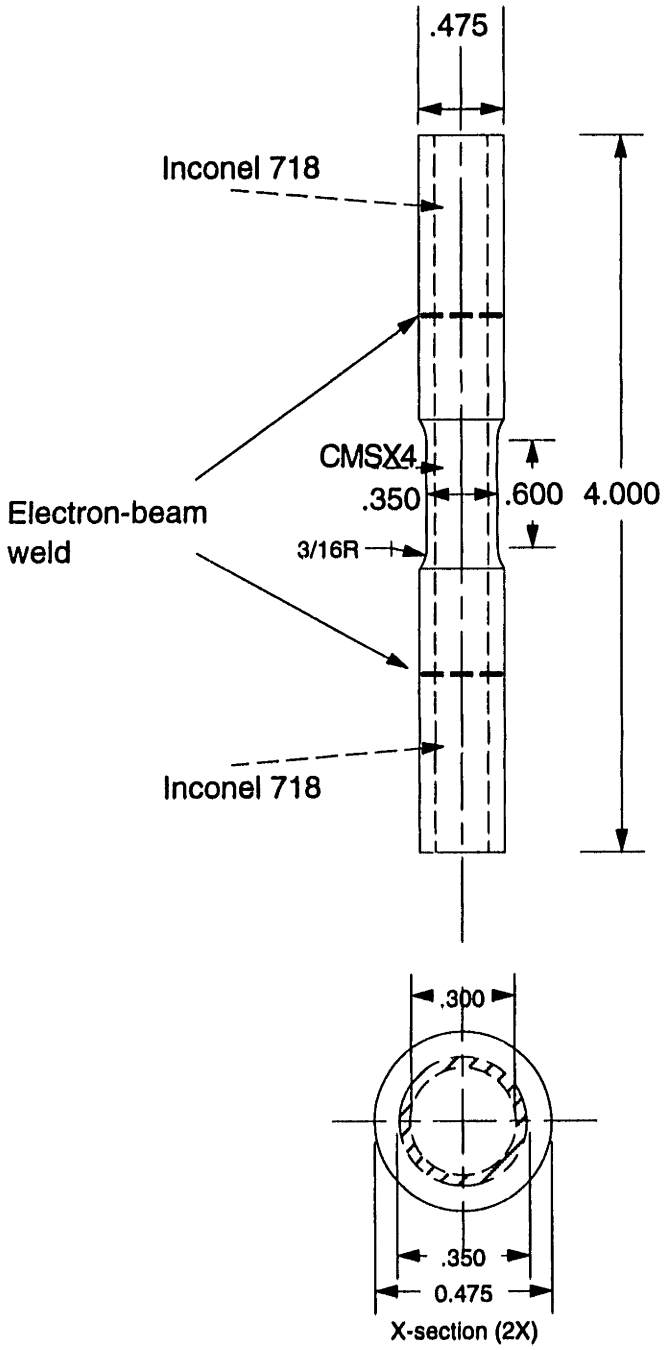

Dimensions in inches

Figure 4-1: Torsion specimen geometry

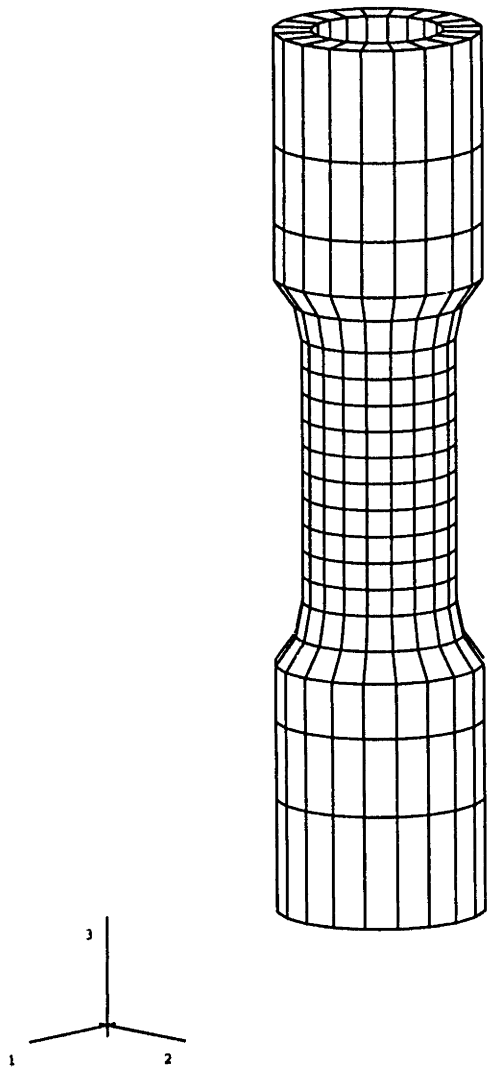

Figure 4-2: 3D finite element mesh for torsion simulations

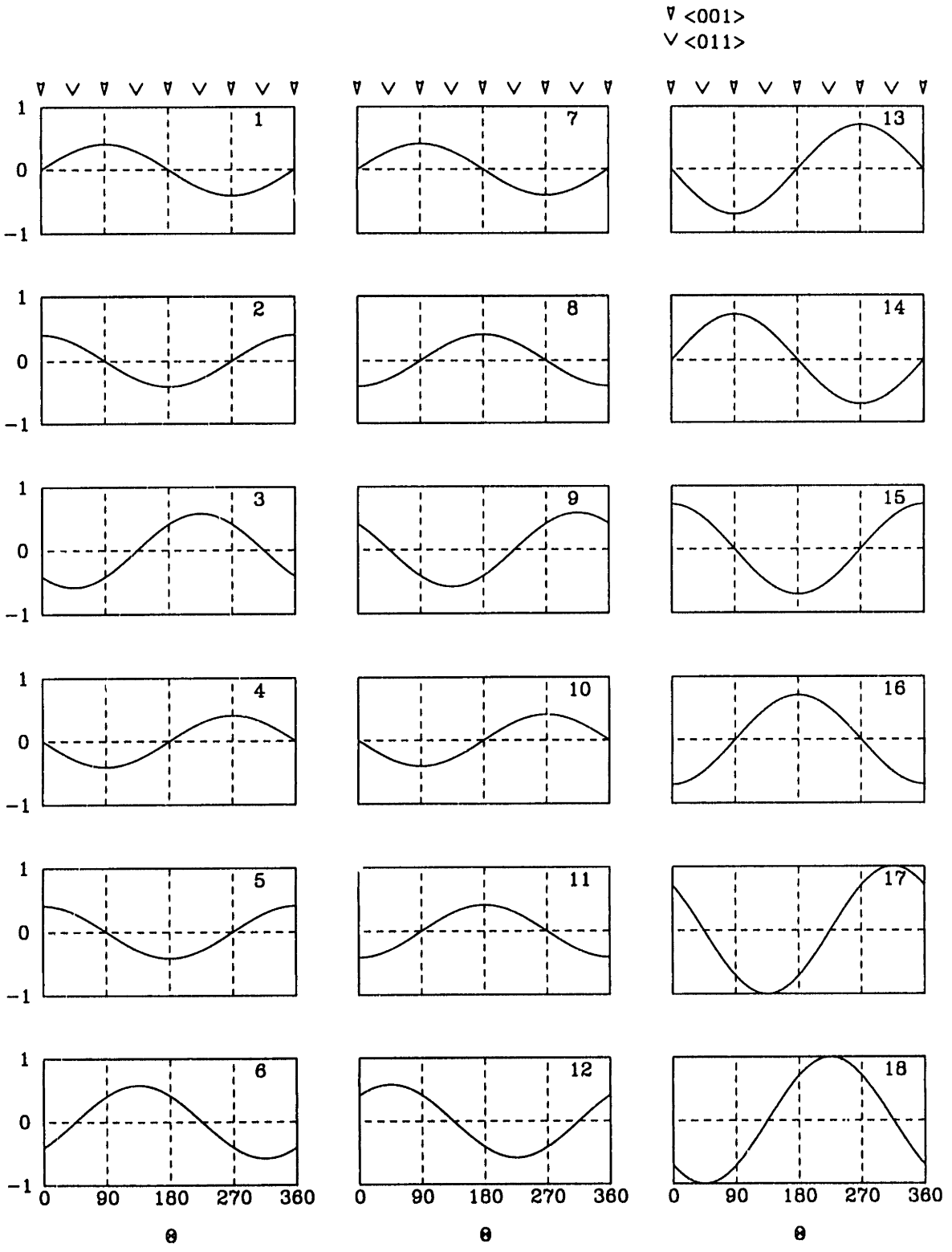

Figure 4-3: Variation of Schmid factors with angular position Θ for all octahedral and cube slip systems. Θ = 0 corresponds to the [100] direction

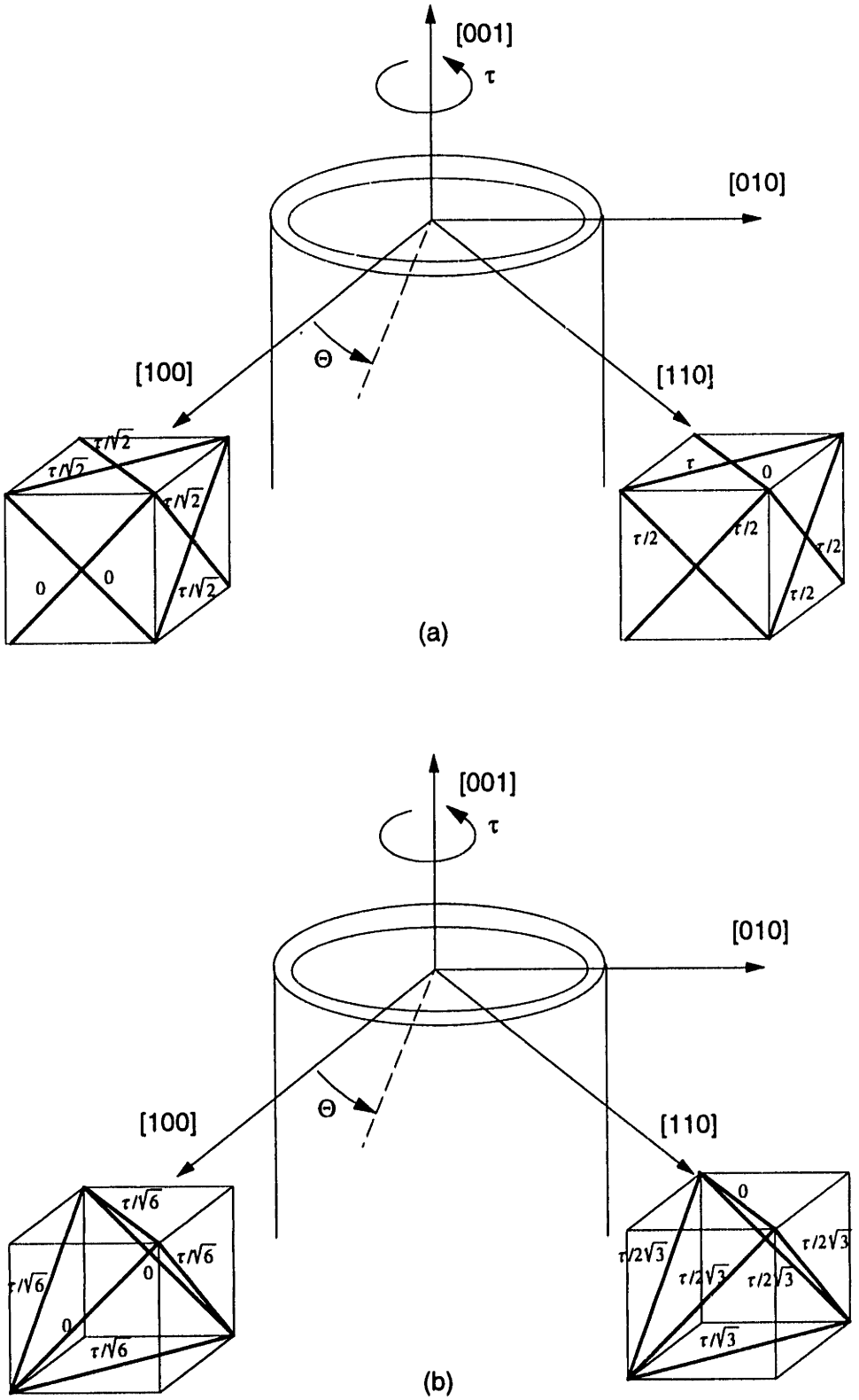

Figure 4-4: Schematic representation of the resolved shear stresses on (a) the cube and (b) the octahedral slip systems in the ⟨001⟩ and ⟨011⟩ directions. $\tau \equiv \tau_{\Theta z}$ [Nouailhas *et al.*, 1993]

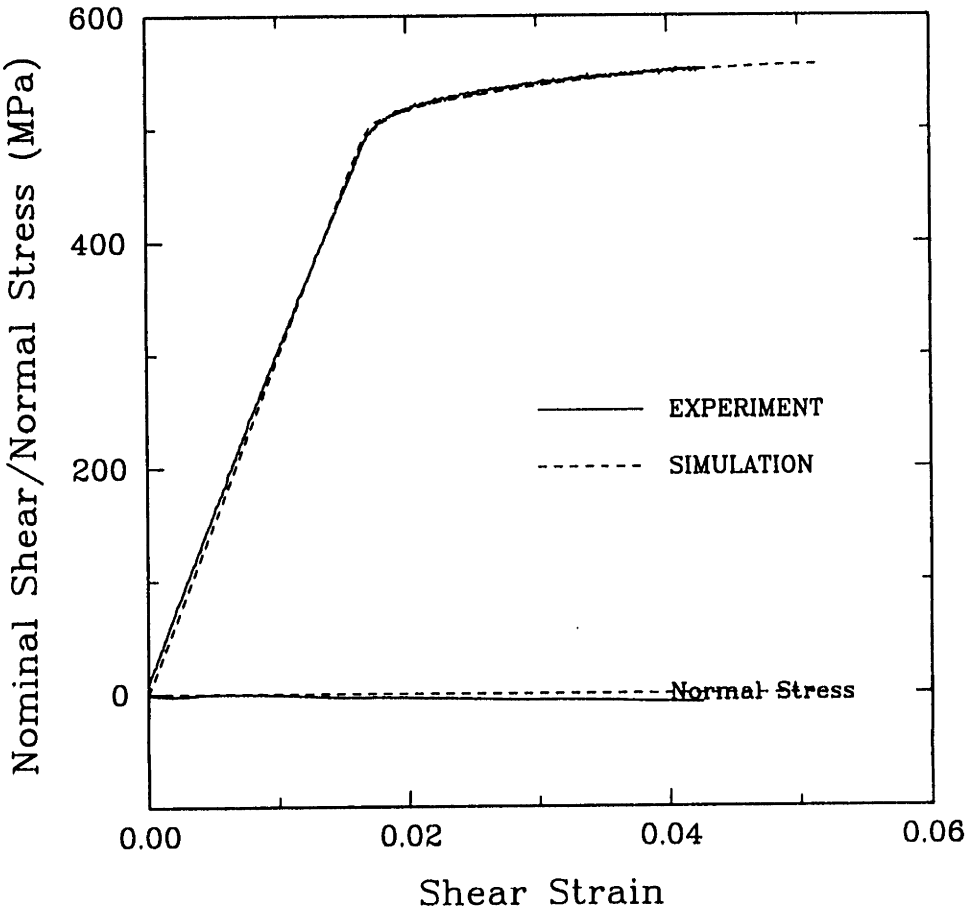

Figure 4-5: Experimental and simulated stress-strain curves for the torsion experiment at 25°C

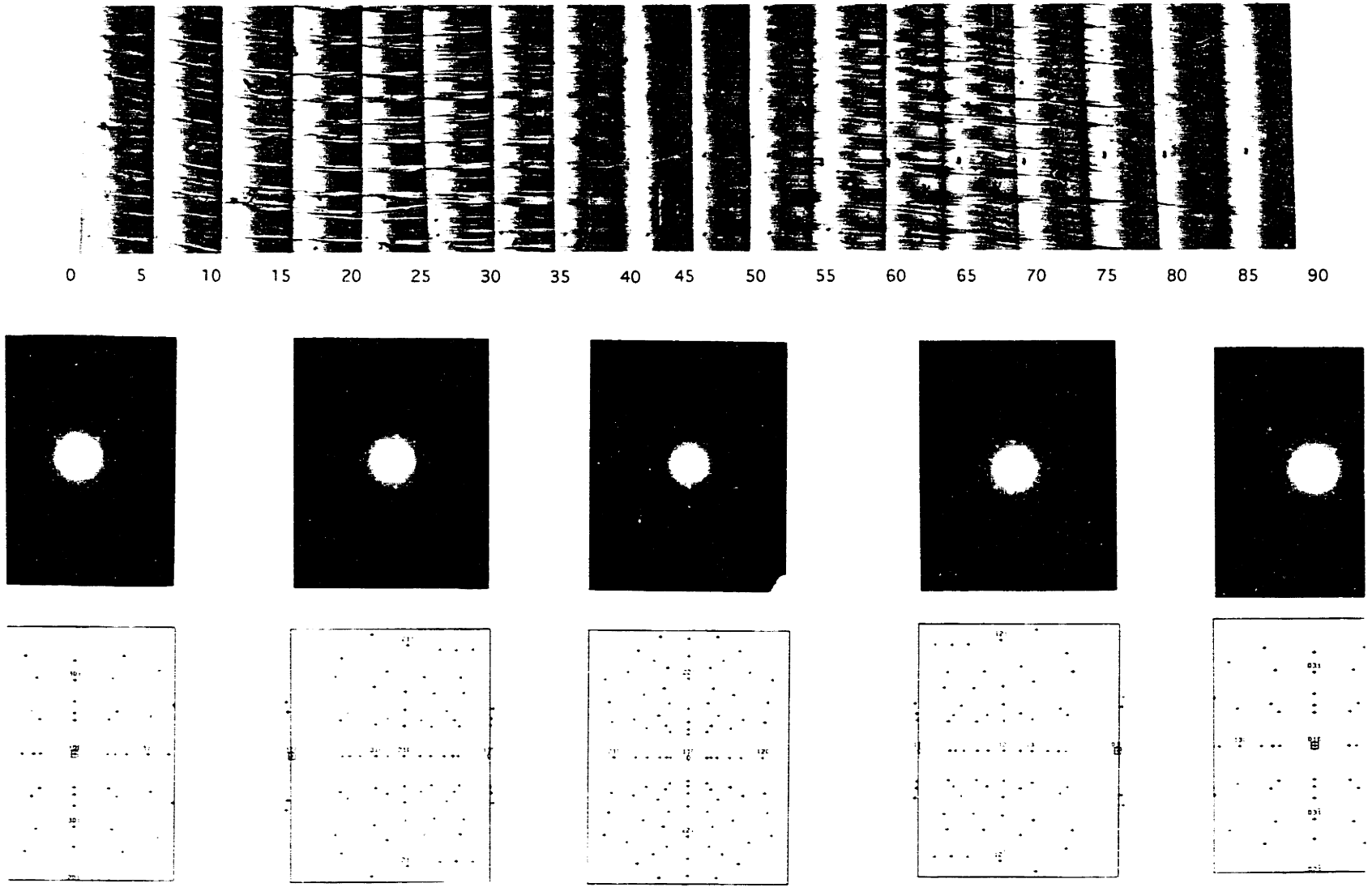

Figure 4-6: (a) Micrograph of slip traces on gage section of torsion specimen deformed at 25°C with accompanying Laue patterns – Θ = 0–90°

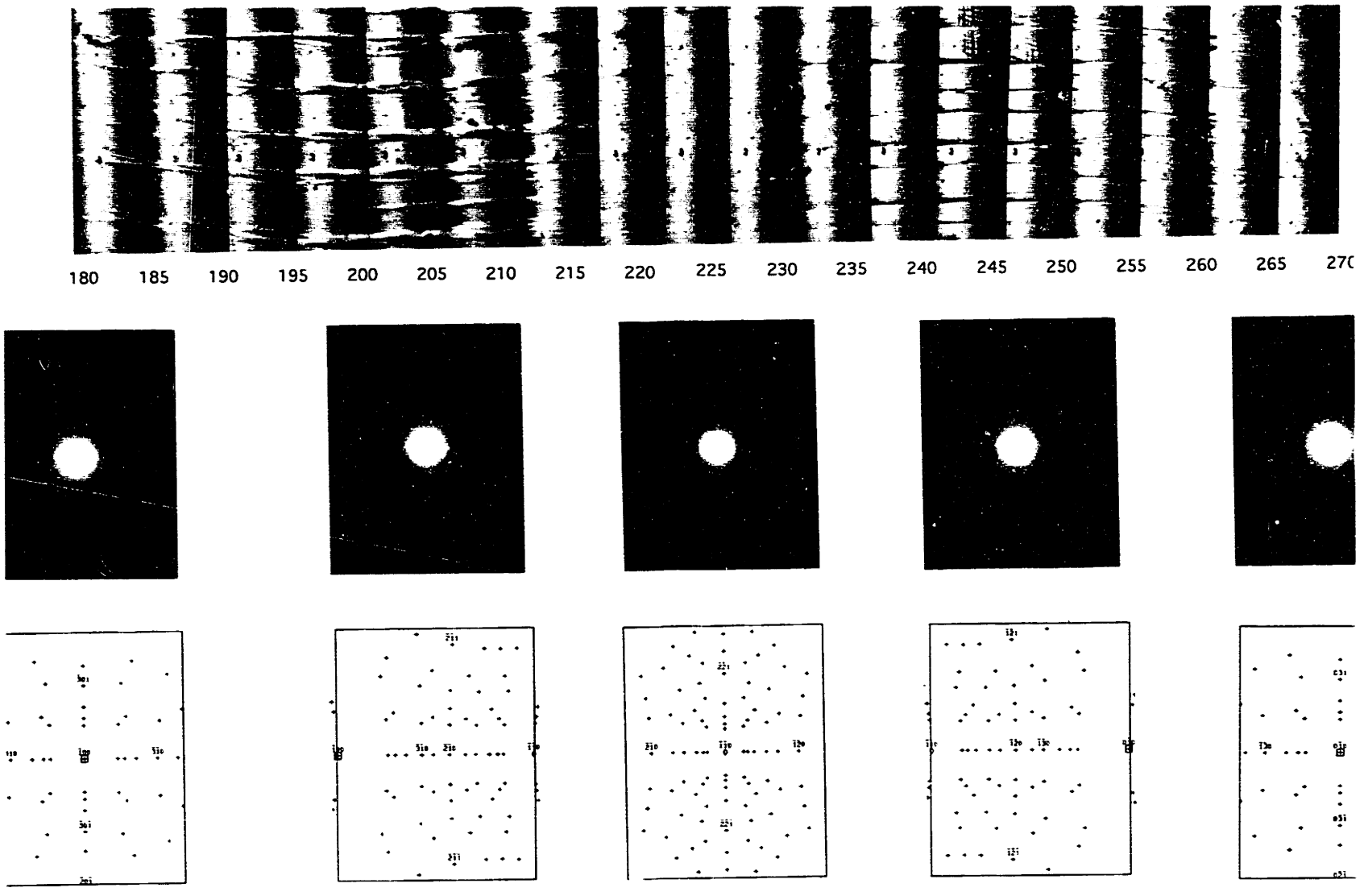

Figure 4-6: (b) Micrograph of slip traces on gage section of torsion specimen deformed at 25°C with accompanying Laue patterns – Θ = 90–180°

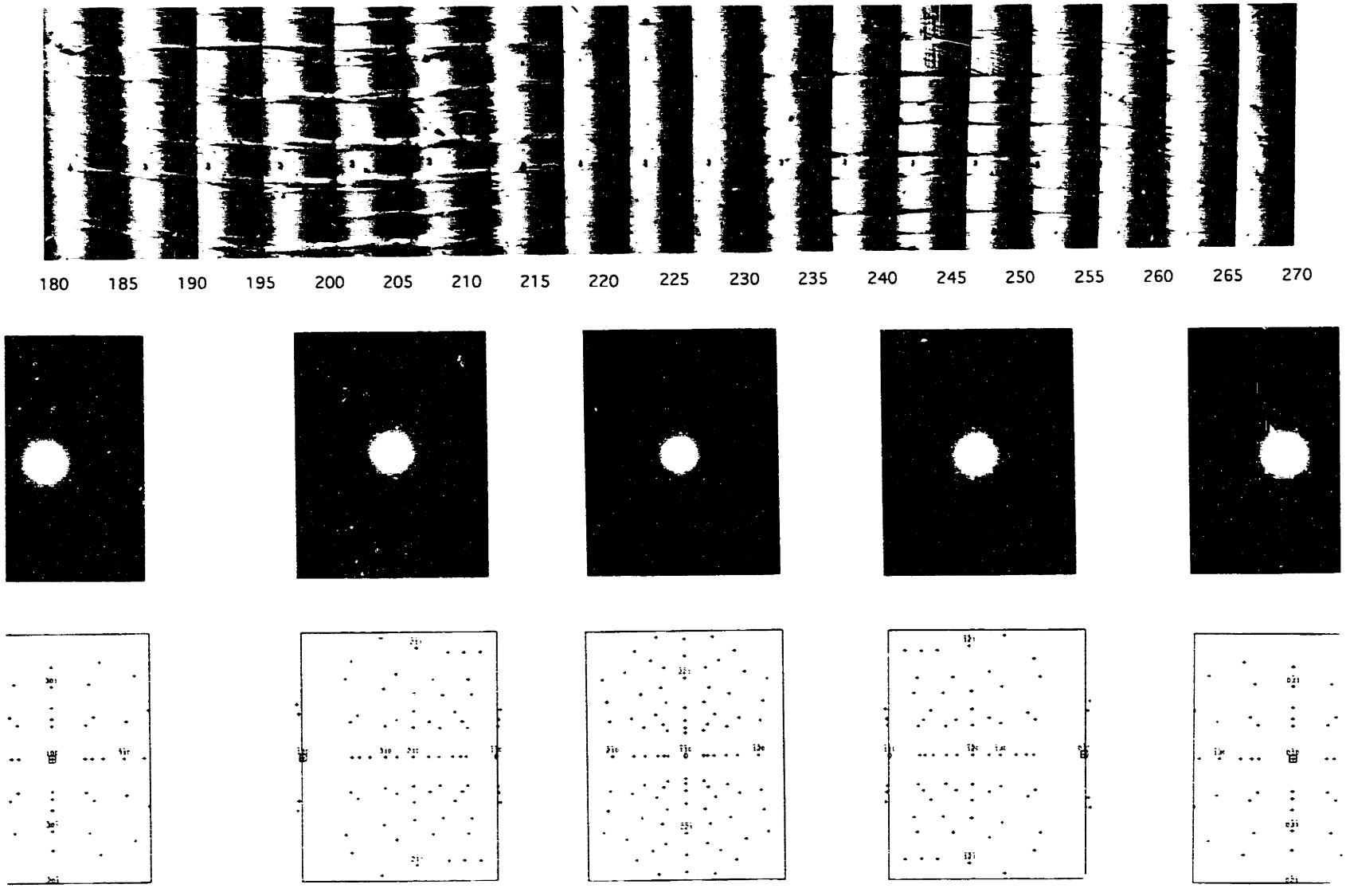

Figure 4-6: (c) Micrograph of slip traces on gage section of torsion specimen deformed at 25°C with accompanying Laue patterns - Θ = 180–270°

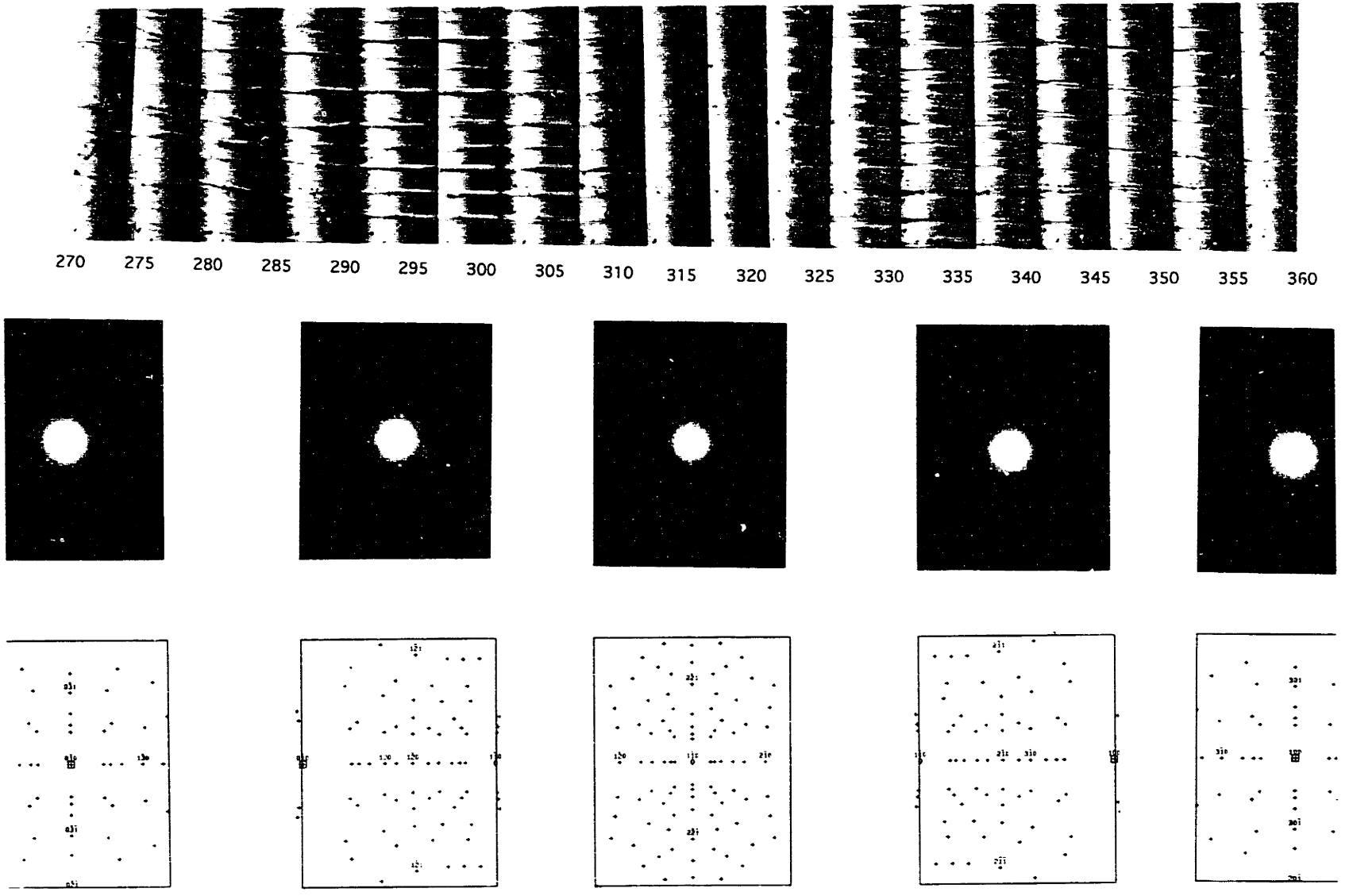

Figure 4-6: (d) Micrograph of slip traces on gage section of torsion specimen deformed at 25°C with accompanying Laue patterns – Θ = 270–360°

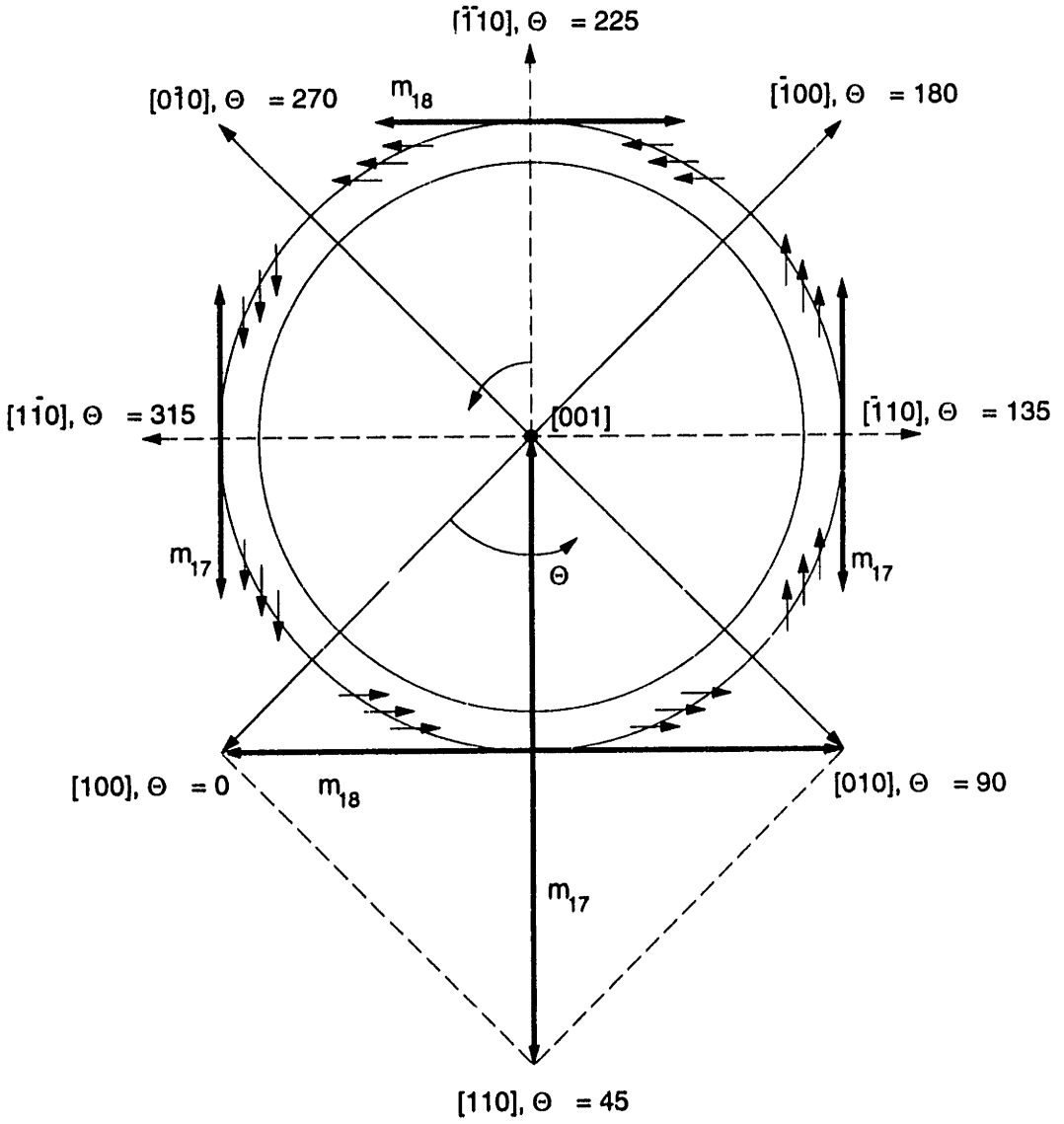

Figure 4-7: Schematic of development of slip bands during torsional deformation of a ⟨001⟩-oriented tube

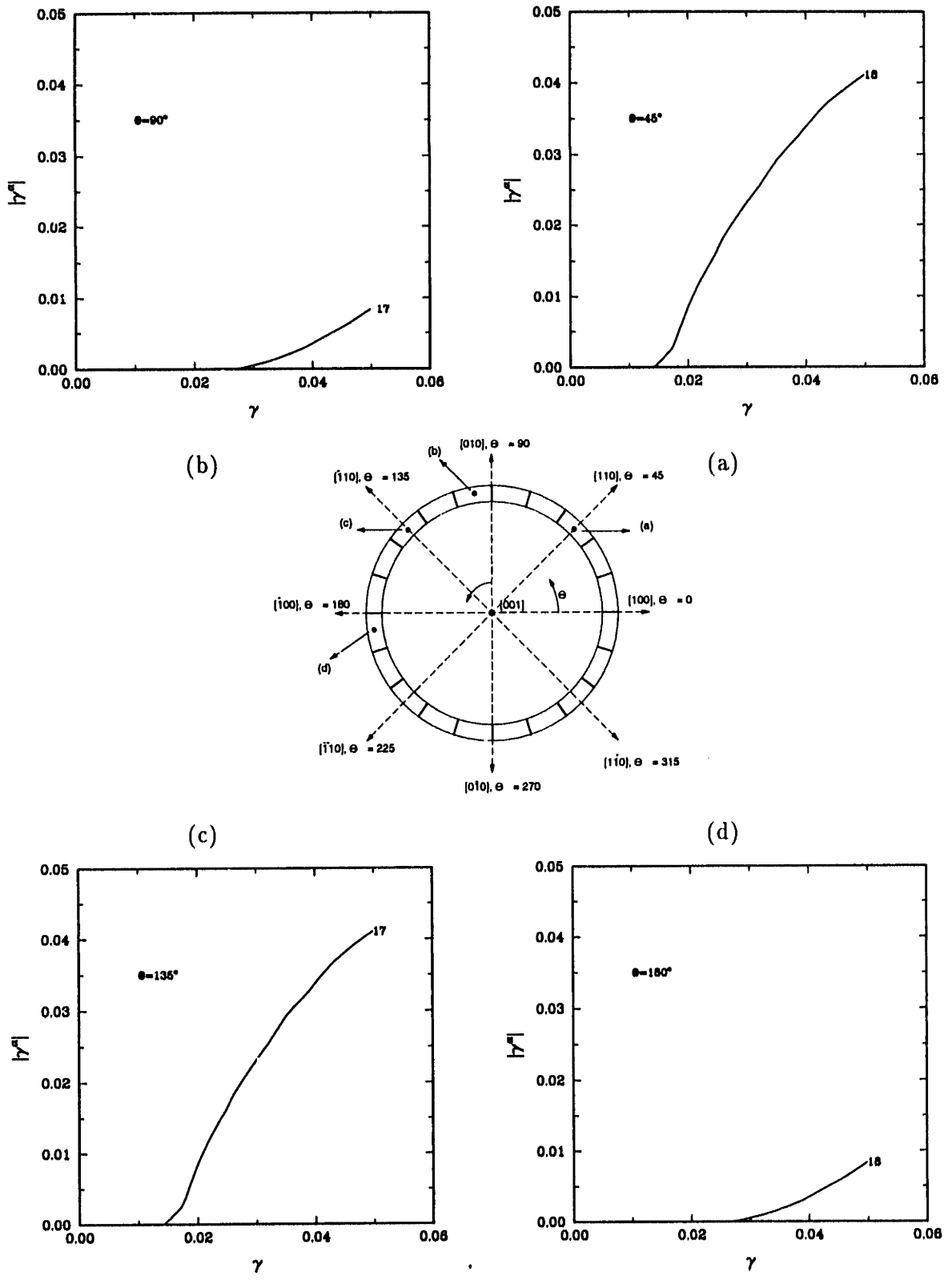

Figure 4-8: Accumulated strain on slip systems after torsion at 25°C at different positions around the tube

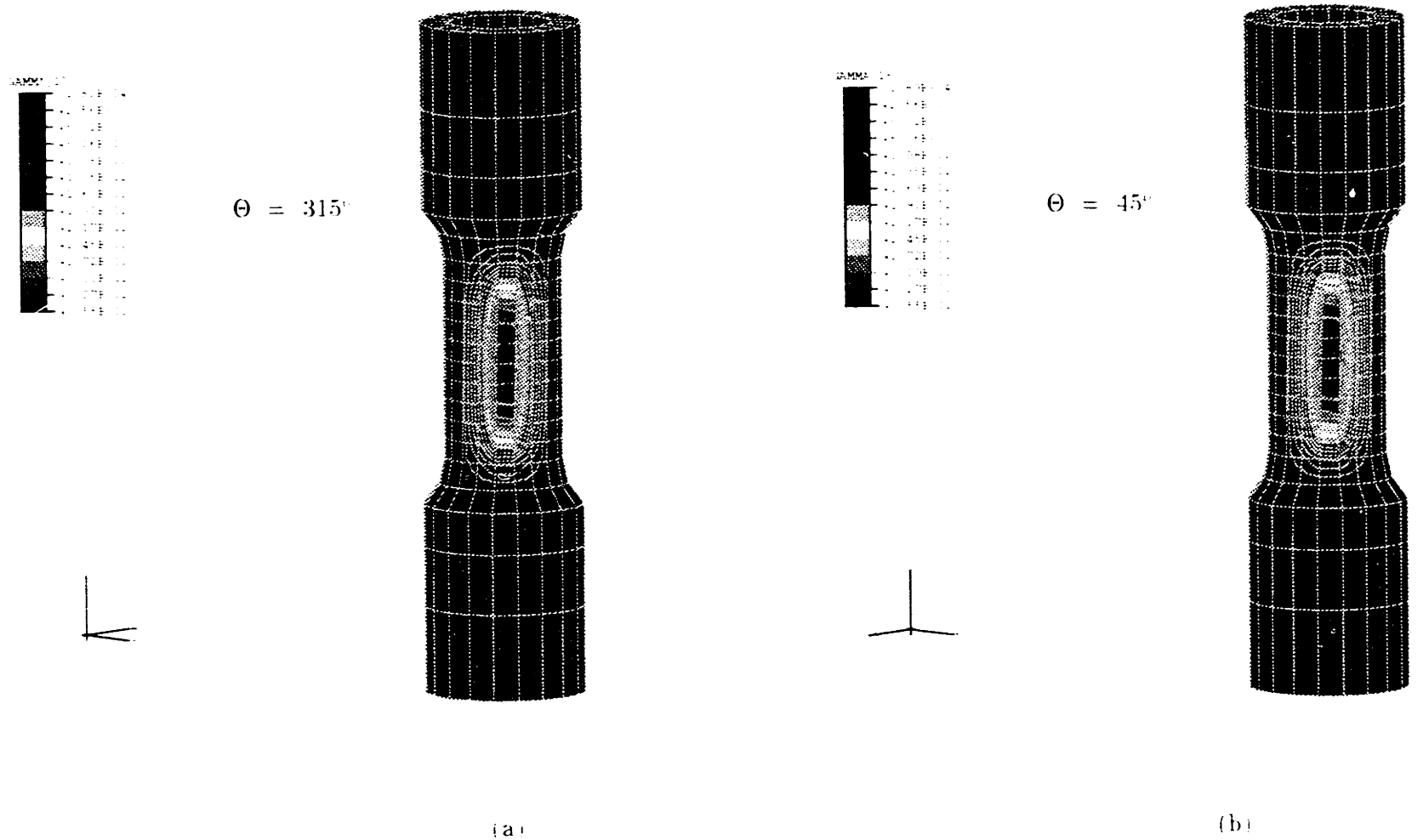

Figure 4-9: Contours of accumulated plastic strain from FE simulations of the torsion experiment at 25°C (a) Slip system 17, $[1\bar{1}0]$ view (b) Slip system 18, $[110]$ view

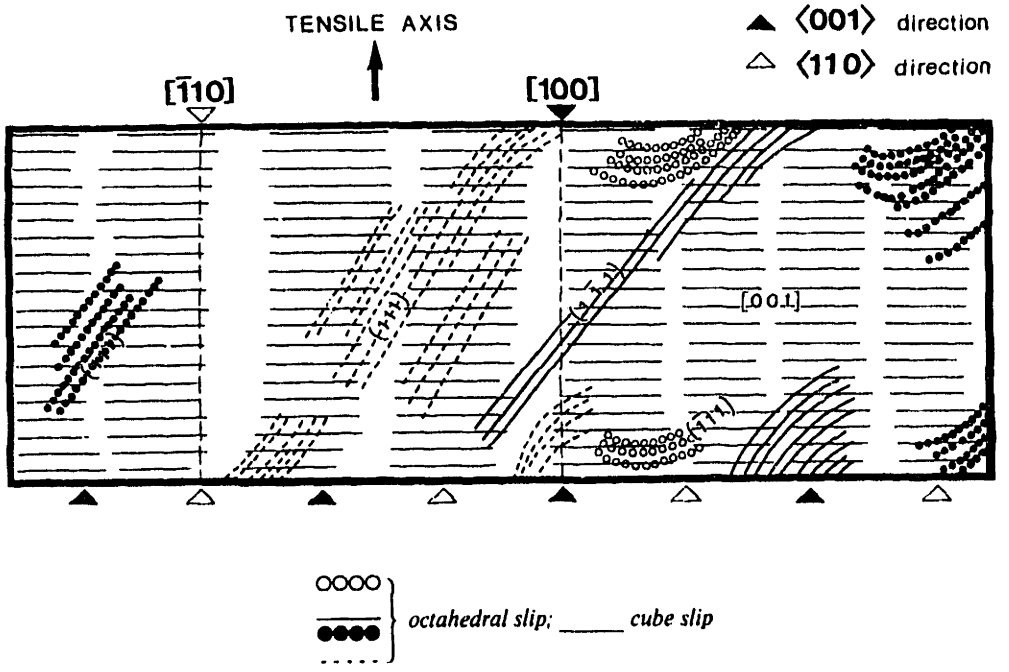

Figure 4-10: Scheme of slip bands on surface replica following combined tension-torsion experiment at 25°C [Nouailhas *et al.*, 1993]

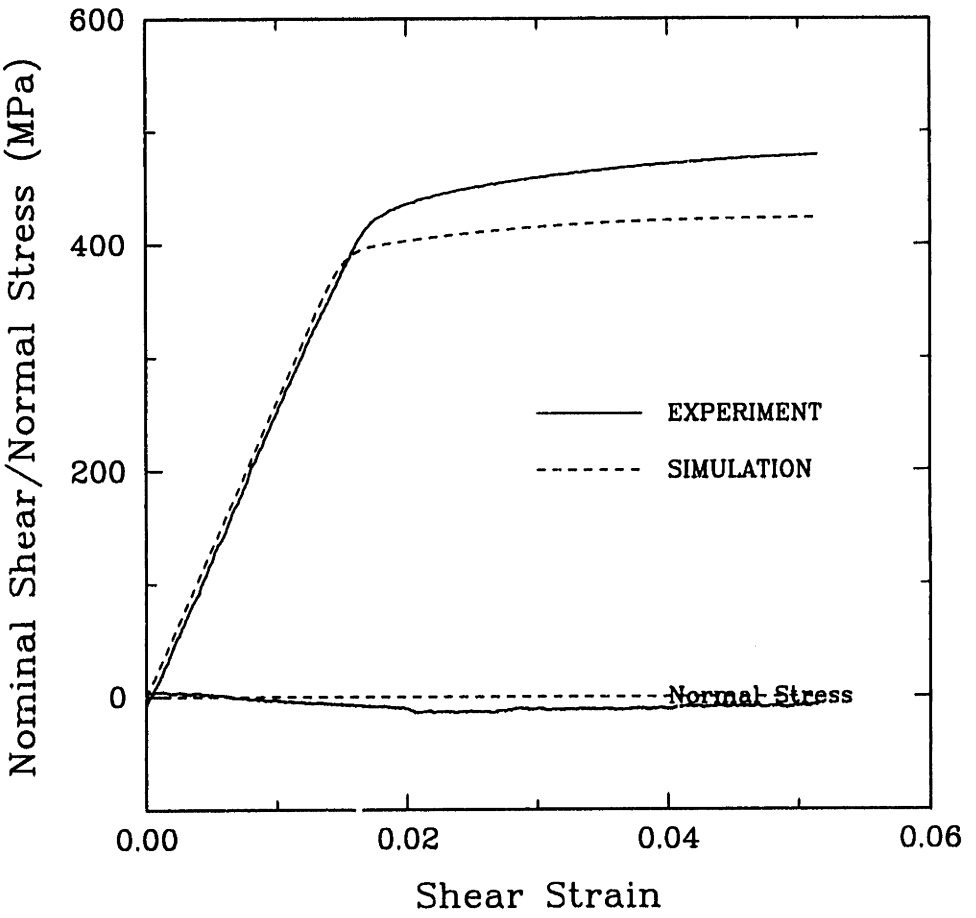

Figure 4-11: Experimental and simulated stress-strain curves for the torsion experment at 650°C

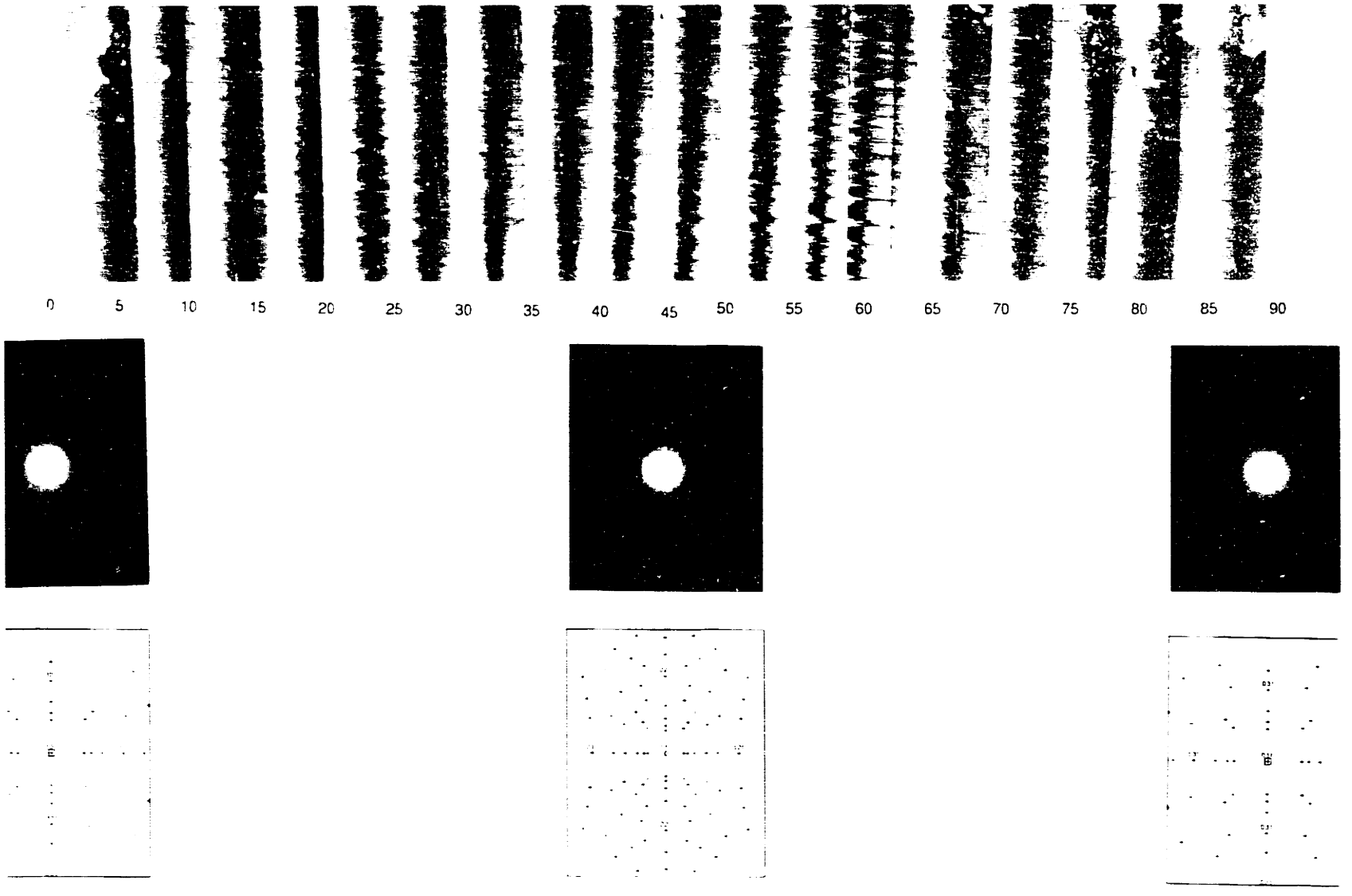

Figure 4-12: (a) Micrograph of slip traces on gage section of torsion specimen deformed at 650°C with accompanying Laue patterns - $\Theta = 0$-90

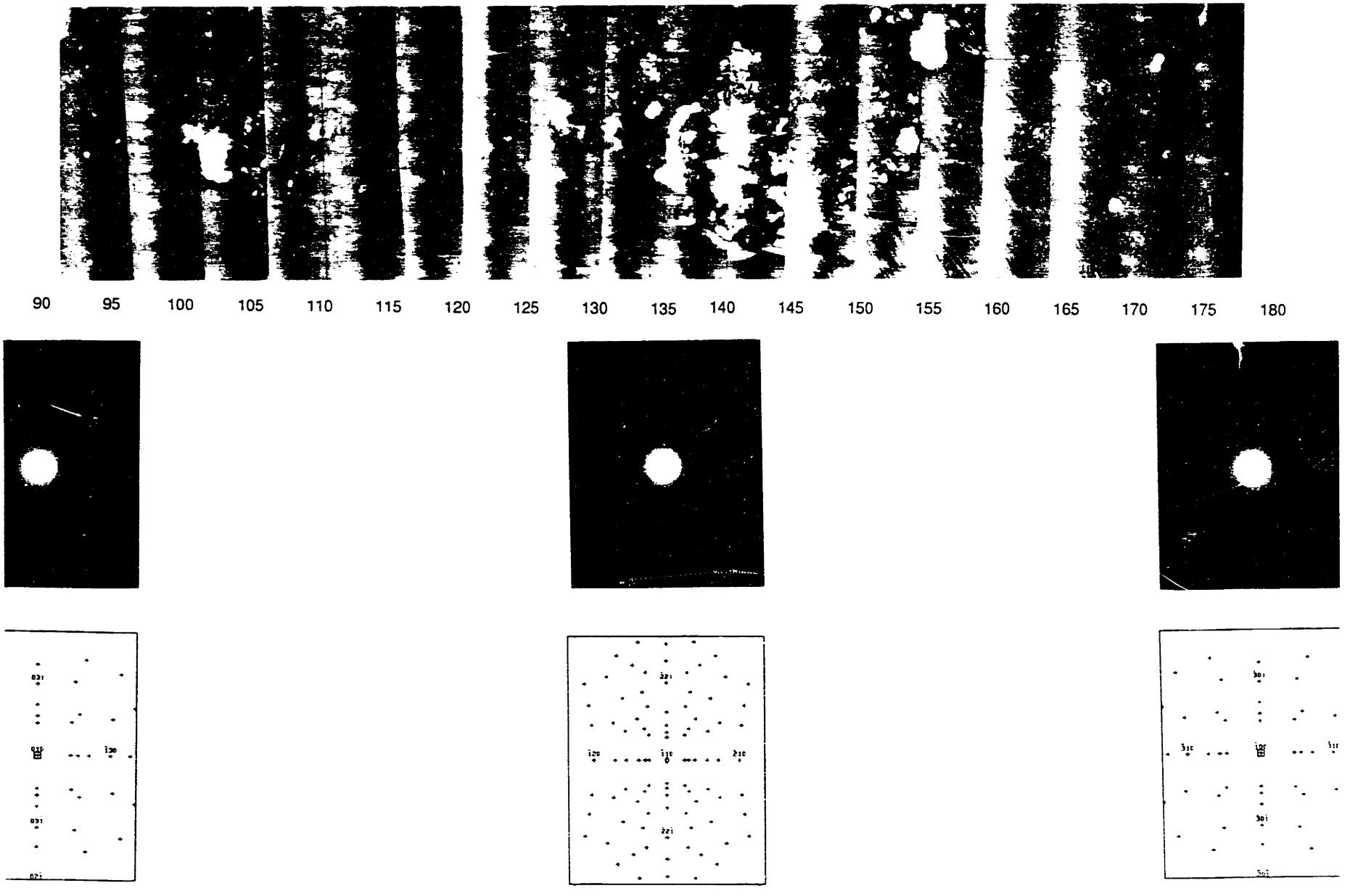

Figure 4-12: (b) Micrograph of slip traces on gage section of torsion specimen deformed at 650°C with accompanying Laue patterns - Θ = 90-180°

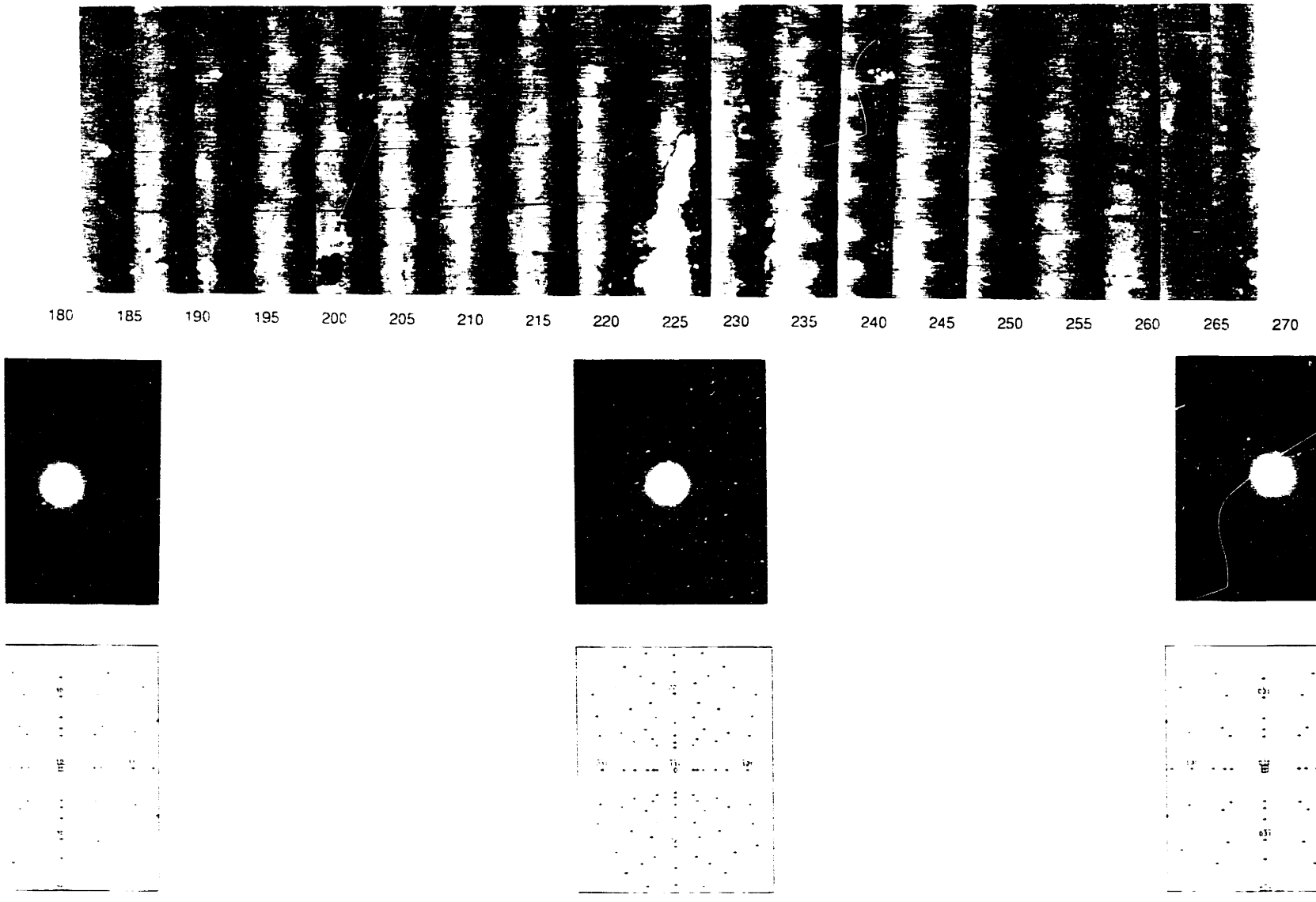

Figure 4-12: (c) Micrograph of slip traces on gage section of torsion specimen deformed at 650°C with accompanying Laue patterns - Θ = 180-270°

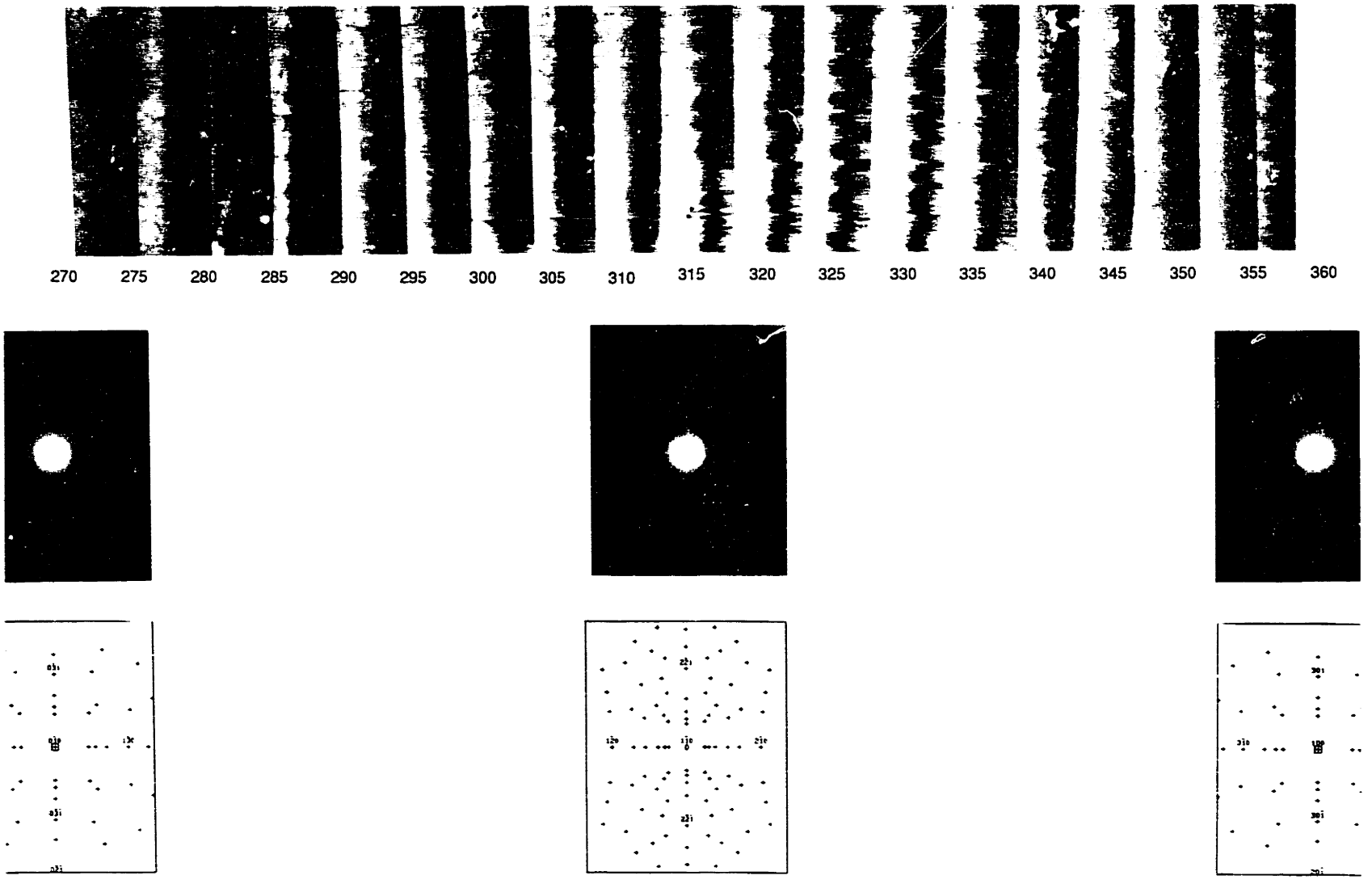

Figure 4-12: (d) Micrograph of slip traces on gage section of torsion specimen deformed at 650°C with accompanying Laue patterns - Θ = 270-360°

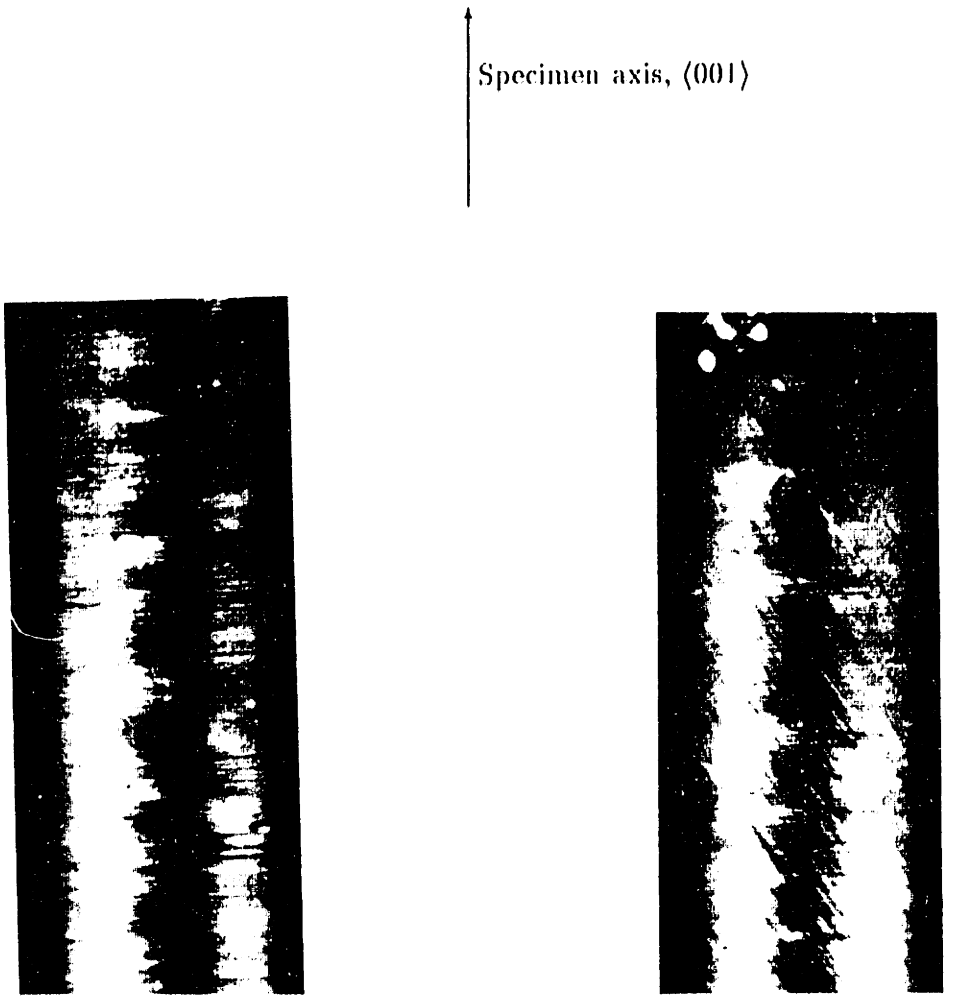

(a) (b)

Figure 4-13: Details of slip traces on gage section of torsion specimen deformed at 650°C: (a) $\Theta = 50^{o}$ (b) $\Theta = 65^{o}$

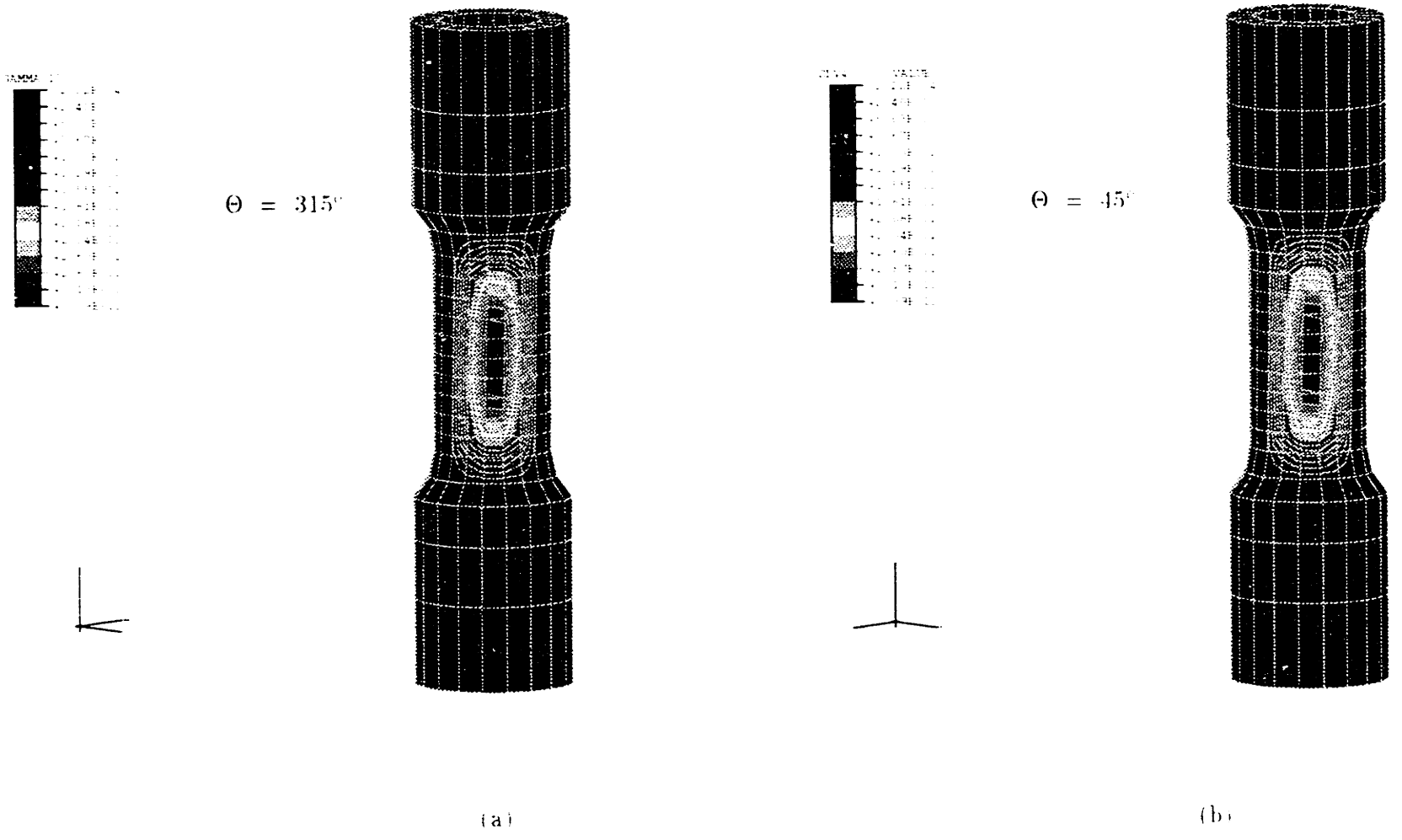

Figure 4-14: Contours of accumulated plastic strain from FE simulations of the torsion experiment at 650°C (a) Slip system 17, $[1\bar{1}0]$ view (b) Slip system 18, $[110]$ view

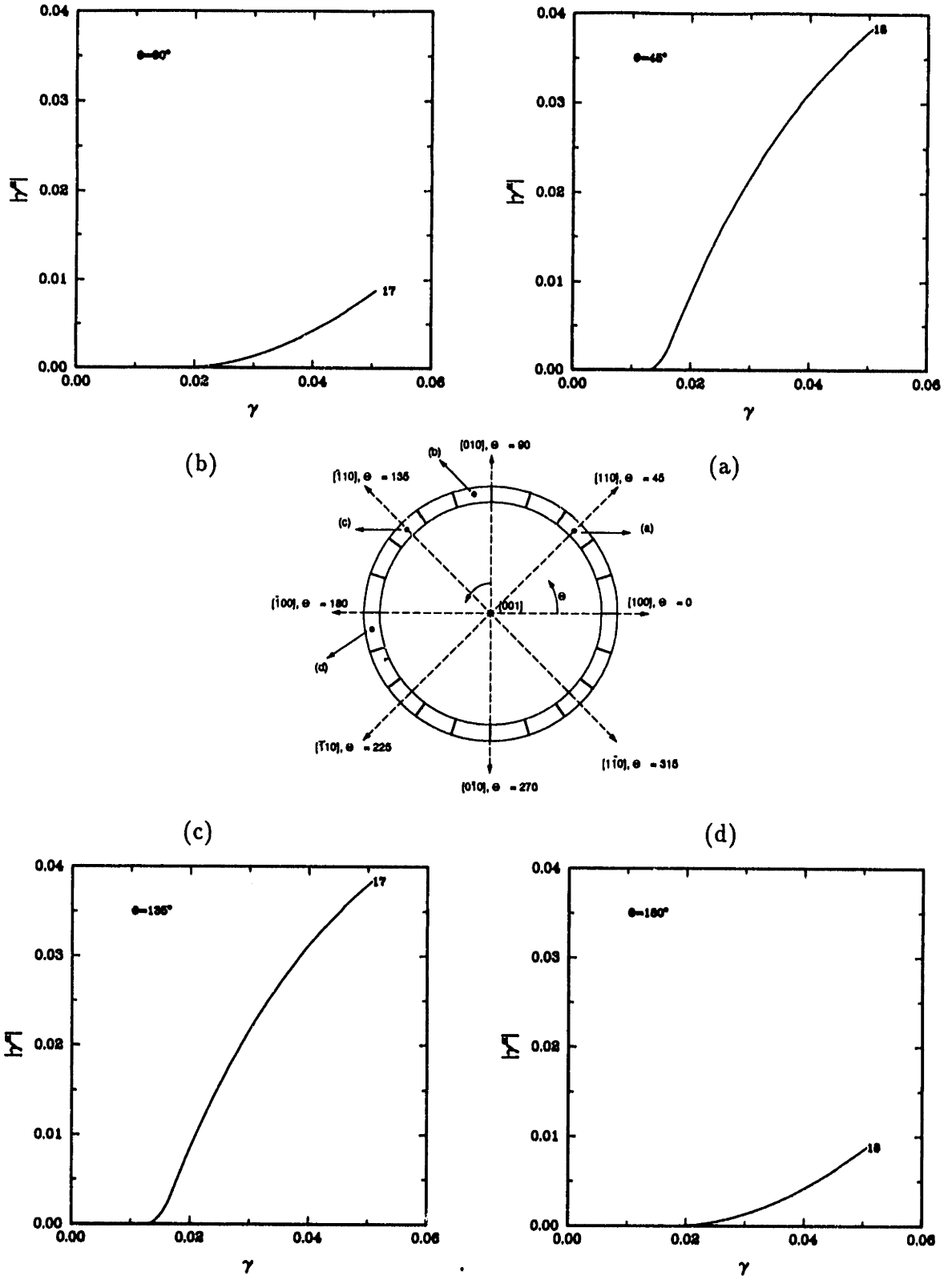

Figure 4-15: Accumulated strain on slip systems after torsion at 650°C at different positions around the tube

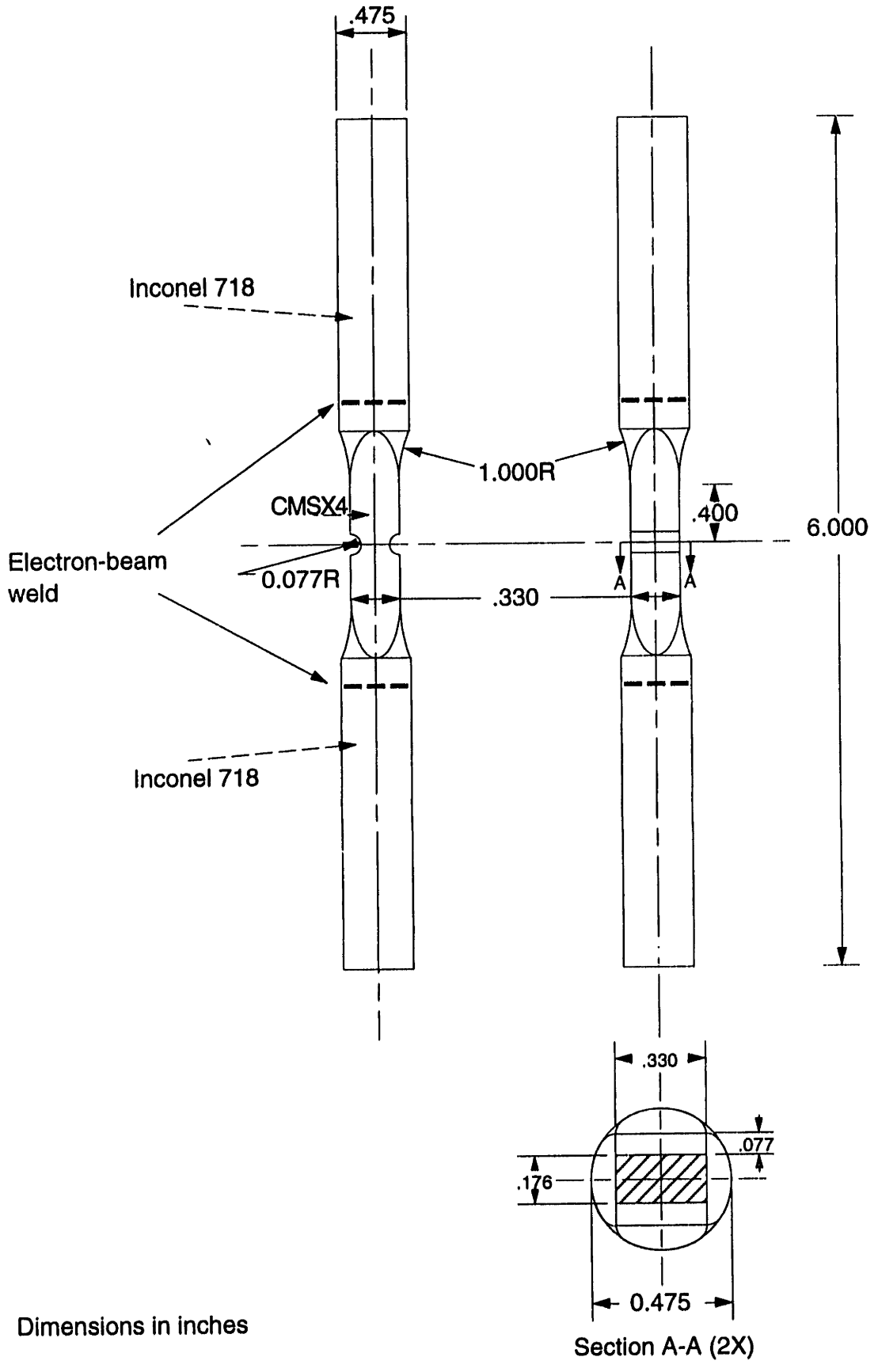

Figure 4-16: Notched-bar tension specimen geometry

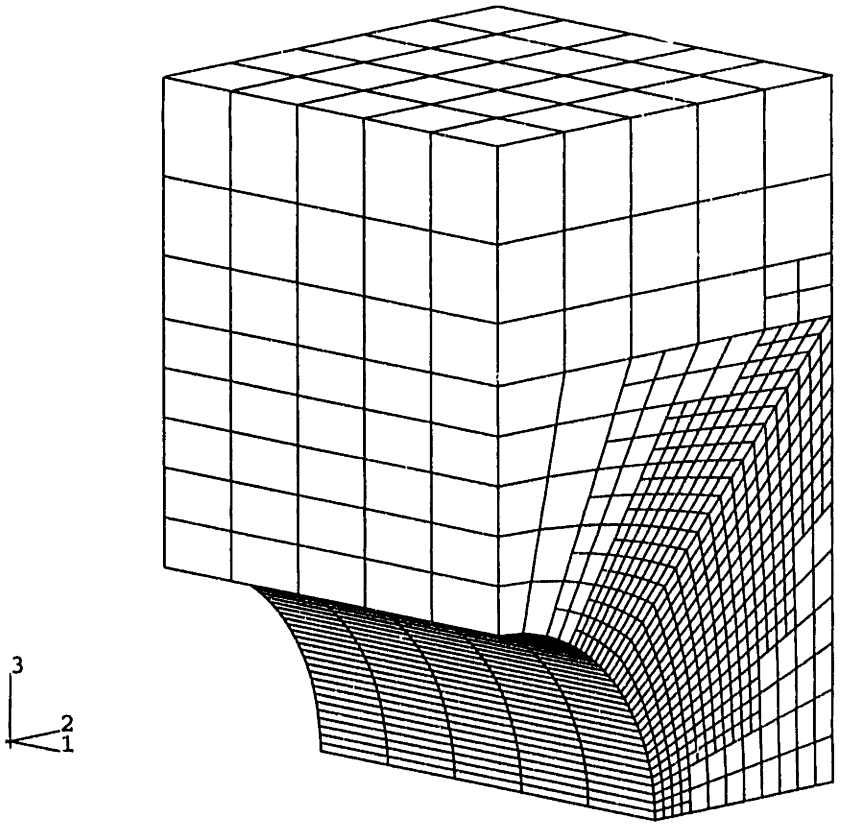

Figure 4-17: 3D finite element mesh for notched-bar specimen

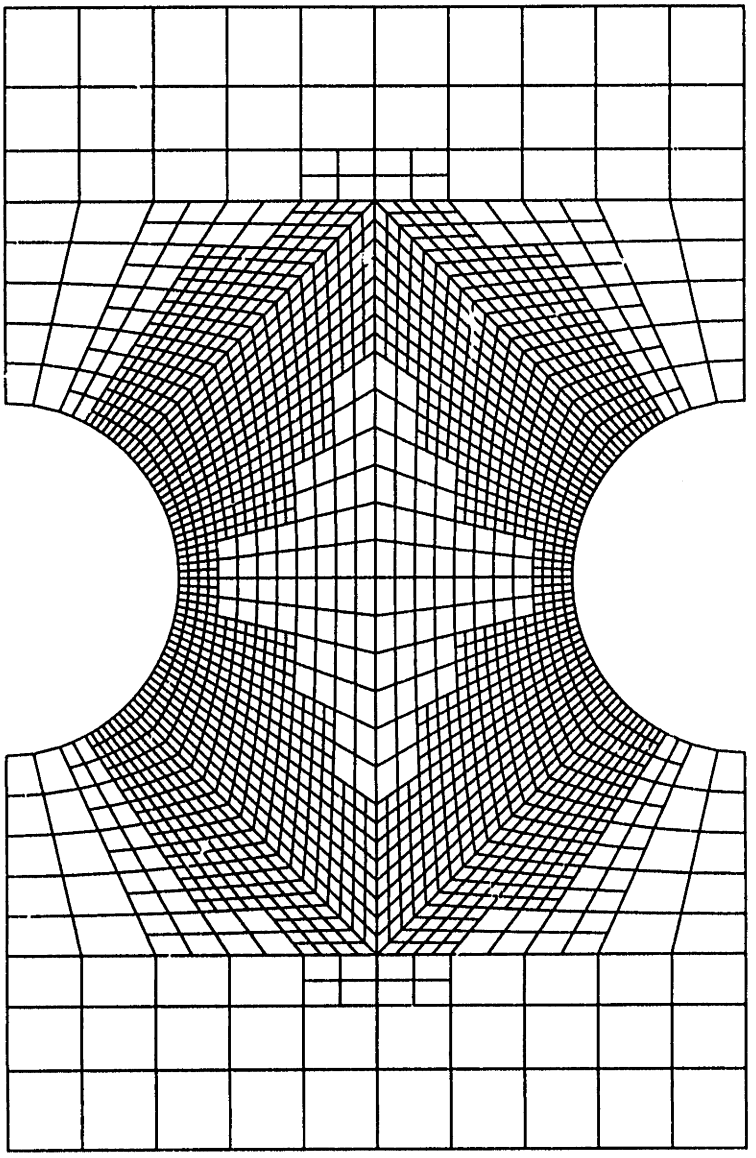

Figure 4-18: Cross-section of entire double-notched specimen

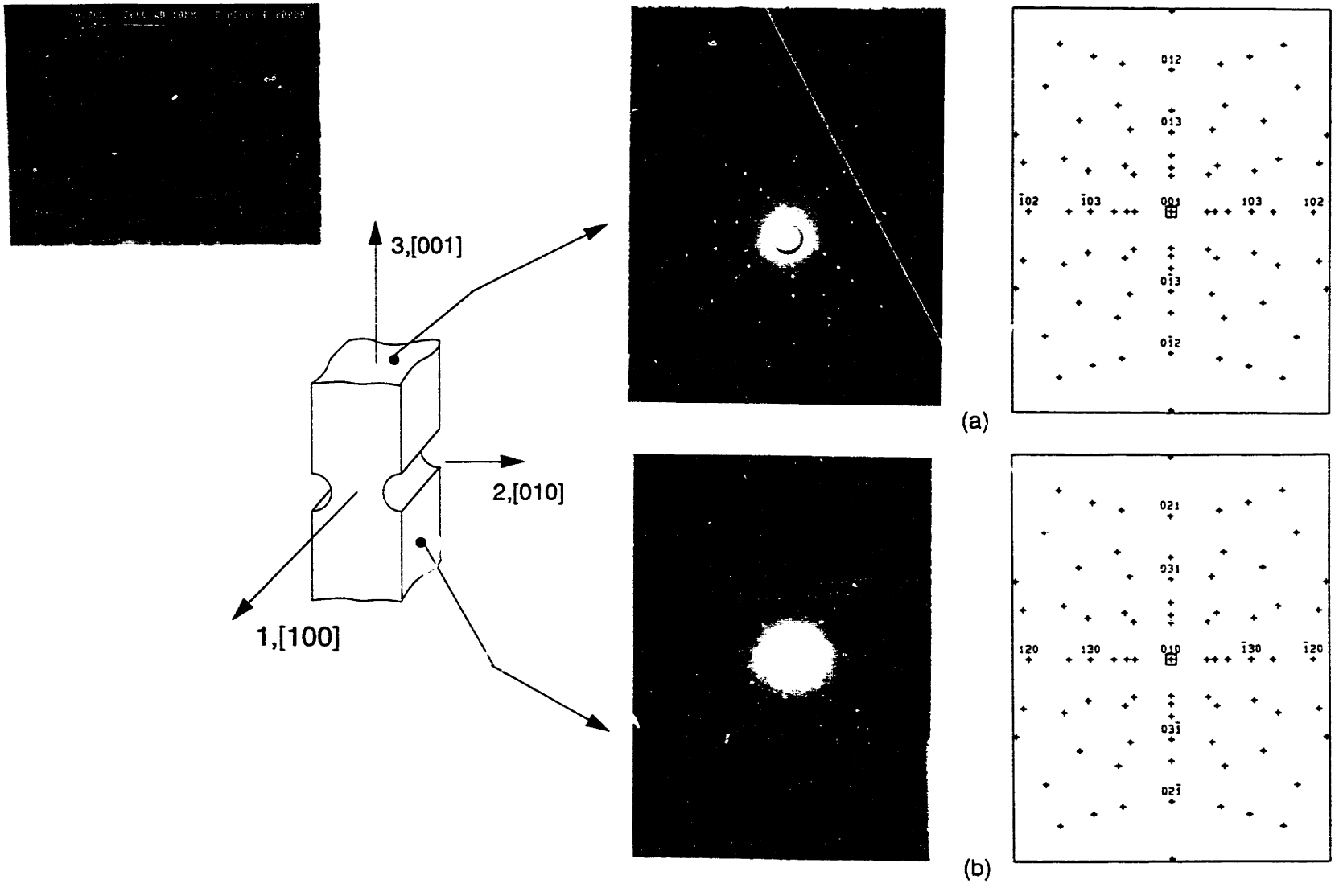

Figure 4-19: Experimental and simulated Laue patterns from the notch specimen: (a) Axial direction, [001] (b) Notched side face, [010]

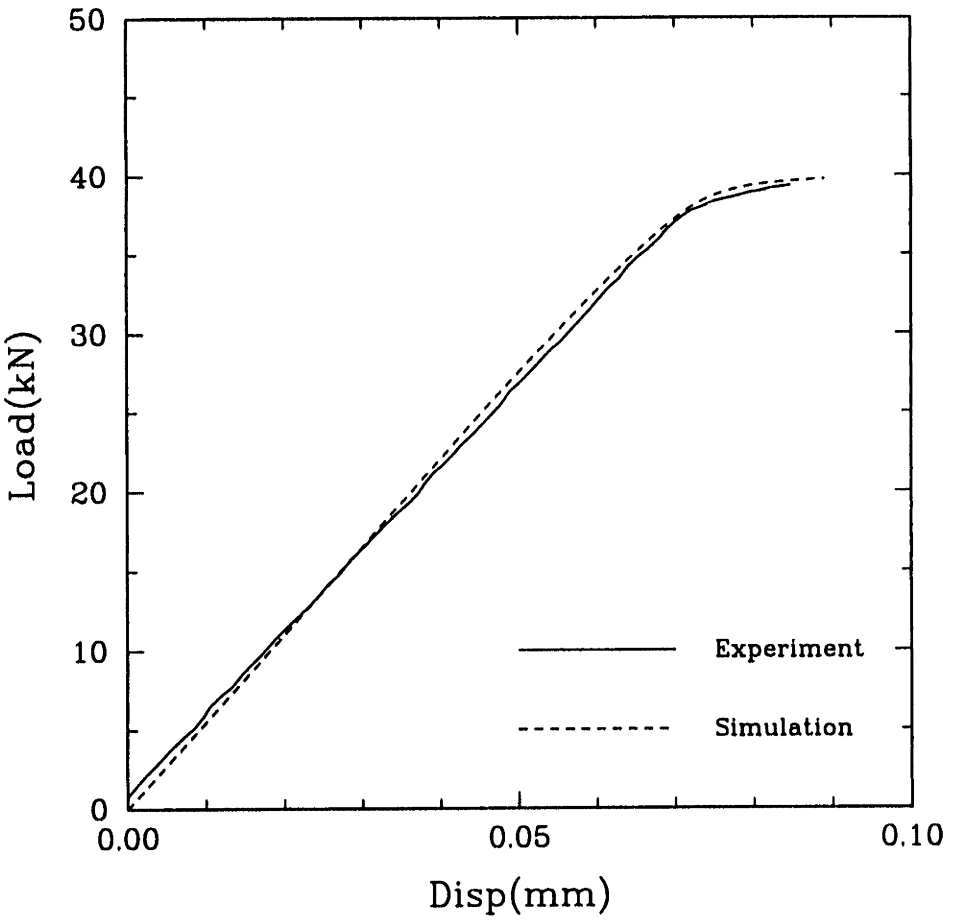

Figure 4-20: Experimental and simulated load-displacement curve for double-notched tension experiment

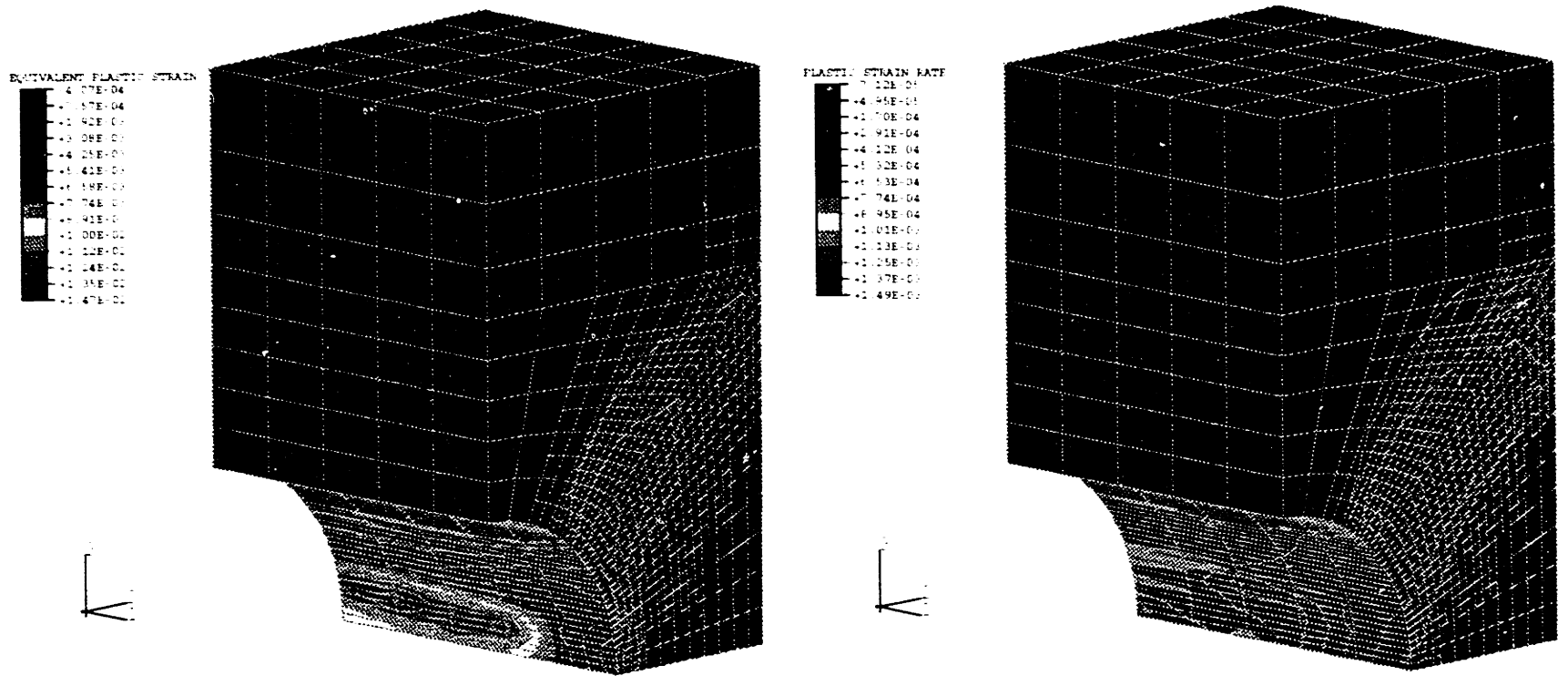

(a) (b)

Figure 4-21: (a) Equivalent plastic strain contours (b) Plastic strain rate contours from FE simulations

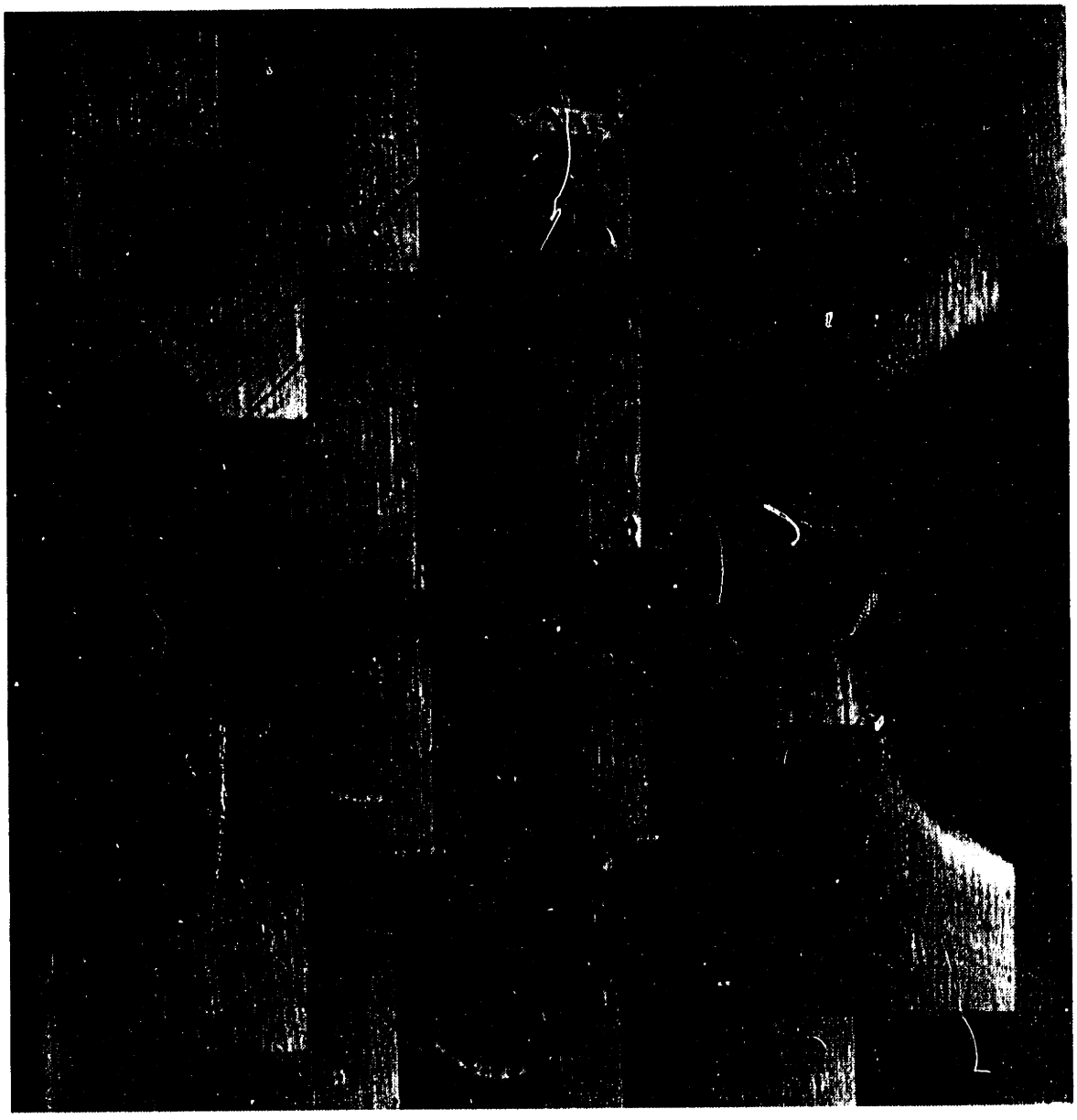

Figure 4-22: (a) Micrograph of deformed specimen

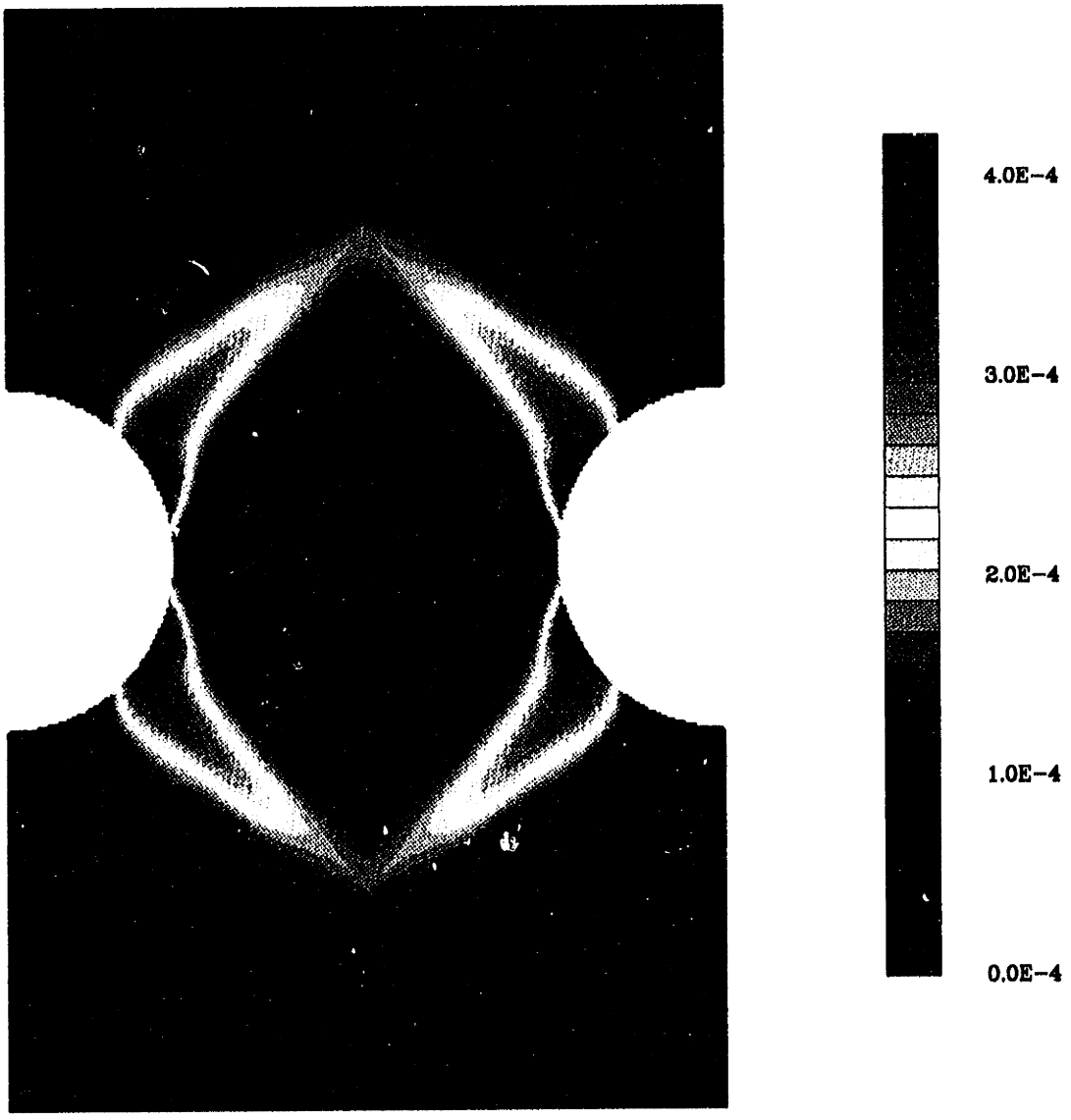

Figure 4-22: (b) Plastic strain contours from FE simulation of notch experiment

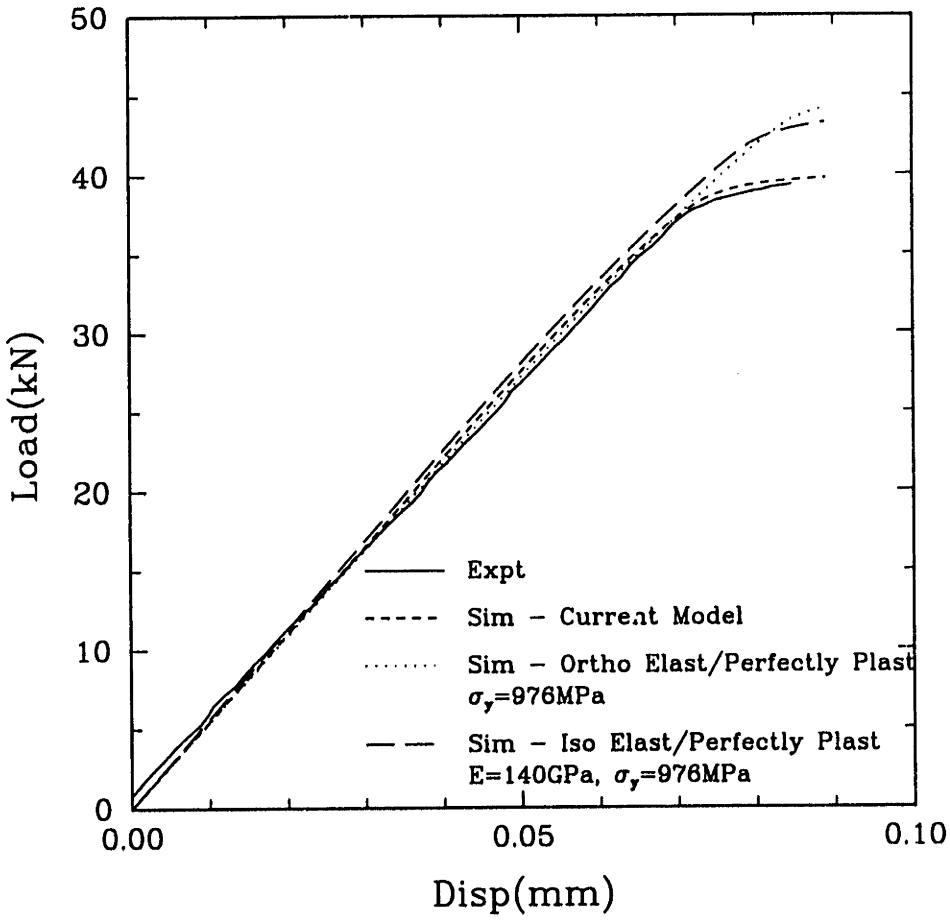

Figure 4-23: Experimental load-displacement curve for double-notched tension experiment and simulation using three models

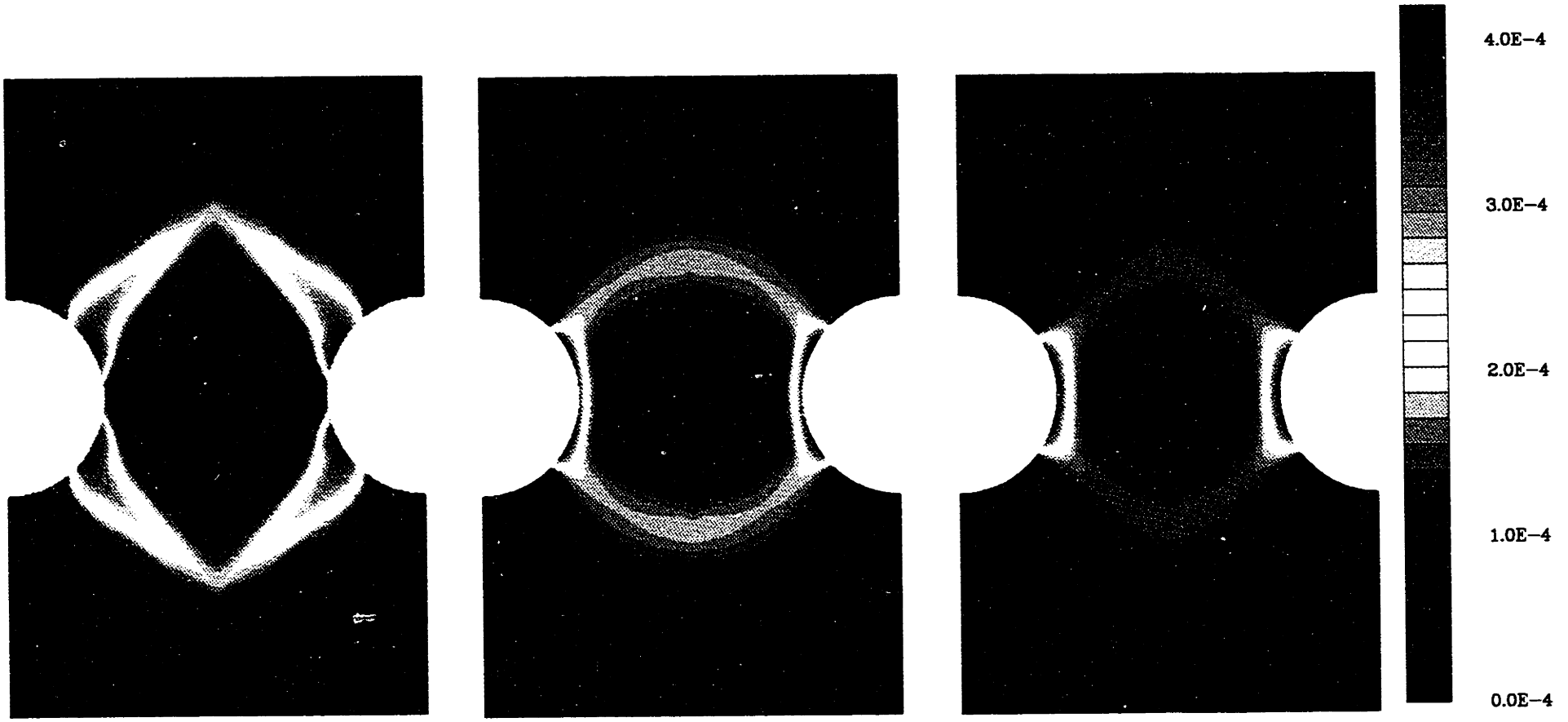

Figure 4-24: Equivalent plastic strain contours from FE simulations using different models: (a) Present model: Orthotropic elastic, crystal plasticity with anomalies (b) Orthotropic elastic, perfectly plastic (c) Isotropic elastic, perfectly plastic

Chapter 5

Determination of Material Parameters

5.1 Summary

The following text describes a systematic approach to determining the parameters in our model. The constitutive model developed in this study may be summarized in the following equations:

$$\mathbf{T}^* = \mathcal{L}[\mathbf{E}^*], \tag{5.1}$$

$$\mathbf{E}^* \equiv (\frac{1}{2})\{\mathbf{F}^{*T}\mathbf{F}^* - 1\}, \qquad \mathbf{T}^* \equiv \mathbf{F}^{*-1}\{(\det \mathbf{F}^*)\mathbf{T}\}\mathbf{F}^{*-T} \tag{5.2}$$

$$\mathbf{F}^* \equiv \mathbf{F}\mathbf{F}^{p^{-1}}, \qquad \det \mathbf{F}^* > 0 \tag{5.3}$$

$$\dot{\mathbf{F}}^p = \mathbf{L}^p\mathbf{F}^p \tag{5.4}$$

$$\mathbf{L}^p = \sum_\alpha \dot{\gamma}^\alpha \mathbf{S}_o^\alpha, \qquad \mathbf{S}_o^\alpha \equiv \mathbf{m}_o^\alpha \otimes \mathbf{n}_o^\alpha \tag{5.5}$$

$$\dot{\gamma}^\alpha = \begin{cases} 0, & |\tau^\alpha| - s_{th} \le 0 \\ \dot{\gamma}_o \left\{ \frac{|\tau^\alpha| - s_{th}}{s^\alpha} \right\}^{\frac{1}{m}}, & |\tau^\alpha| - s_{th} > 0 \end{cases} \tag{5.6}$$

$$s^\alpha = \begin{cases} s_o + \xi\mu b\sqrt{\psi^\alpha}, & \alpha = 1, \ldots, 12 \\ s_{oc}, & \alpha = 13, \ldots, 18 \end{cases} \tag{5.7}$$

$$\xi = \xi_o \exp\left(\frac{A}{\theta - \theta_c}\right), \qquad \theta < \theta_c \tag{5.8}$$

$$\psi^\alpha = \psi_*^\alpha \exp\left(-\frac{H}{k\theta}\right) \tag{5.9}$$

$$H = \frac{\mu b^3}{4\pi}\left\{h + c + \kappa_1(t_{pe} - \kappa_2 t_{se}) - \sqrt{\left(\frac{1}{\sqrt{3}} - \frac{\Gamma^{\{001\}}}{\Gamma^{\{111\}}} + |t_{cb}|\right)\frac{b}{B}}\right\} \quad (5.10)$$

The terms used here are all defined in Chapters 2 and 3.

5.2 Methodology

To complete the definition of the model, it is necessary to determine the following parameters:

C_{11}, C_{12}, C_{44}	—	Temperature-dependent anisotropic elastic constants
$\dot{\gamma}_o, m$	—	Reference strain rate, and temperature-dependent strain rate sensitivity parameter.
s_o, s_{oc}	—	The initial slip system resistance on the octahedral and cube slip systems, respectively.
$\xi_o, A, \theta_c, \psi_*^\alpha$	—	Constants which determine the rate with which the deformation resistance rises and drops, and the position of the peak temperature, with ψ_*^α the obstacle density at gross yield.
b, h, c	—	Constants appearing in the expression for the activation enthalpy of cross-slip.
$\Gamma^{\{001\}}, \Gamma^{\{111\}}$	—	The antiphase boundary energy per unit area on the octahedral and cube planes, respectively.
κ_1, κ_2	—	The weighting coefficients of τ_{pe} and τ_{se}, respectively, which determine the amount of tension-compresion asymmetry and the orientations of zero asymmetry.
s_{th}, s_{thc}	—	The threshold strength on the octahedral and cube slip systems, respectively.

The elastic constants may be measured directly for the material being tested and good data for γ/γ' materials is available from suppliers, [Thomas, 1993]. $\dot{\gamma}_o$ is set approximately equal to the macroscopic strain rate; m may be obtained from strain rate jump experiments (or experiments at different strain rates) at different temperatures.

The temperature-dependent slip system resistances s_o and s_{oc} are determined by fitting the single-phase (for this material, $s_{th} = s_{thc} = 0$) data at each temperature. Since the asymmetry is maximum around the peak temperature, and the $\langle 001 \rangle$ orientation can exhibit

only octahedral slip, we start at the peak temperature in the ⟨001⟩ orientation, and fit the tension and compression data to determine s_o and κ_1 simultaneously. From theoretical calculations, Paidar *et al.* [1984] found that κ_2 should be around 0.7, we fixed that parameter at that value for our simulations.

The ⟨111⟩ data has the highest resolved shear stress on the cube slip systems, so is the orientation most sensitive to changes in the cube parameters. This orientation is fit to determine s_{oc}, using the previously determined values of s_o, κ_1, and κ_2. Using these constant values of κ_1 and κ_2, the data for these two orientations are fit at the other temperatures to determine the temperature-dependent s_o and s_{oc} values. These parameters are then expressed as functions of absolute temperature, θ, allowing us to simulate any temperature in the range of fit.

The parameters ξ_o and A may also be adjusted to change the rise and drop of the yield strength versus temperature curve Note that, technically, the term ψ^α controls the rising portion of the curve, while ξ controls the dropping portion. However, since these two terms are simply multiplied, their premultipliers, ψ^α_*, and ξ_o respectively, are really a single parameter. Once a reasonably physical value for ψ^α_* is chosen, only ξ_o needs to be adjusted. The other orientations are then simulated using these parameters.

After the "single-phase parameters" have been determined, the two-phase data is used to determine the temperature-dependent values of the additional parameters, s_{th} and s_{thc}. Once again, the ⟨001⟩ tension and compression data are fit to determine s_{th} and κ_1, while the ⟨111⟩ data are fit to determine s_{thc}. Since, in the present study, the γ' material simulated is not truly the precipitate phase of our two-phase material it was necessary to adjust the parameters κ_1 and κ_2 to get the correct tension-compression asymmetry for our superalloy. Those were the only parameters obtained from the single-phase data that had to be changed. The parameter s_{th} was able to account for all other differences between the two materials. The procedure for finding these new values is the same as described above. [1]

---

[1]The corner orientations of the stereographic triangle have a uniquely simple relationship between τ_{pc} and τ_{sc} for the active slip systems. For these slip systems: $\langle 001\rangle, \langle 111\rangle \longrightarrow \tau_{pc} \equiv \tau_{sc}$; $\langle 011\rangle \longrightarrow \tau_{sc} \equiv 0$

If necessary, this allows us to use the ⟨011⟩ data at a single temperature to better fit κ_1, since $\kappa_2 \tau_{sc} \equiv 0$. Using this value of κ_1, the ⟨001⟩ and ⟨111⟩ orientations may be fit as they we above by ensuring that κ_1 satisfies the following equation: $\kappa_{1,new} = \kappa_{1,old}(1 + \kappa_{2,old})$, where $\kappa_{1,new}$ is the new value found from the ⟨011⟩ data, $\kappa_{2,new}$ is the desired value, and $\kappa_{1,old}$ and $\kappa_{2,old}$ are the values obtained using the original method. Satisfying this equation will give the original result for the ⟨001⟩ and ⟨111⟩ orientations since $\tau_{pc} \equiv \tau_{sc}$, so they may be factored out of the term $\kappa_1(\tau_{pc} + \kappa_2 \tau_{sc})$, see equation 2.1. This iterative process allows us to get the best fit to the data, using just one more data point.

The values used for the single- and two-phase materials in this study are tabulated below, with the temperature-varying quantities given in the following equations (See also Figures 2-19, 3-5 and 3-16).

$$C_{11} = 307 - 0.089\theta, \quad C_{12} = 204 - 0.052\theta, \quad C_{44} = 143 - 0.032\theta \tag{5.11}$$

Table 5.1: Model parameters — Single Phase Material

$\dot{\gamma}_o(\text{sec}^{-1})$	.001
$b(\text{m})$	2.5×10^{-10}
$\Gamma^{\{111\}}(\text{Jm}^{-2})$	0.300
$\Gamma^{\{001\}}(\text{Jm}^{-2})$	0.083
h	0.2
c	0.5
κ_1	0.282
κ_2	0.7
$\psi_*^\alpha(m^{-2})$	5.0×10^{15}
ξ_o	1.15
$A(K)$	325
$\theta_c(\text{K})$	1500

$$s_o = \begin{cases} 115. - 0.144\theta, & \theta \leq 659\text{K} \\ 20., & 659\text{K} < \theta < 1000\text{K} \\ 132. - 0.1124\theta, & 1000\text{K} < \theta < 1174\text{K} \\ 0.01, & \theta \geq 1174\text{K} \end{cases} \qquad s_{oc} = \begin{cases} 330., & \theta \leq 915\text{K} \\ 858. - 0.577\theta, & \text{otherwise} \end{cases} \tag{5.12}$$

Table 5.2: Additional model parameters — Two-Phase Material

$\dot{\gamma}_o(\text{sec}^{-1})$	.0001
κ_1	0.3
κ_2	−0.333

Temp.(°C)	s_{th}(MPa)	s_{thc}(MPa)
25	320	240
400	260	160
500	230	150
600	210	145
650	210	145
700	185	125
750	100	90
850	70	70

This full set of parameters for CMSX4 was then used to simulate the other geometries tested in this study, with very good results.

Chapter 6

Conclusions

6.1 Summary

A new viscoplastic constitutive model for the deformation of γ/γ' superalloys has been developed, guided by the current understanding of the micromechanisms of their deformation behavior.

The precipitate phase of these superalloys has the $L1_2$ crystal structure, a derivative of the fcc structure. Our approach has been to modify an existing crystal plasticity model for fcc materials, incorporating the different dislocation mechanisms which take place in this structure, and adding other (cube) slip systems which come into play in these materials. The differences in these two classes of materials lead to the observed anomalies in the yield strength of these materials. From simulations of data in the literature in multiple orientations, and over a range of temperatures, we have obtained the necessary parameters and tested the predictive capability of the model for this single-phase material.

For the γ/γ' superalloys used in practice, the $L1_2$ material is the precipitate phase, γ', of the two-phase micro-composite, constituting about 68% volume fraction. The deformation mechanisms of the $L1_2$ therefore dominate in this two-phase material, leading to the same anomalous behavior of the yield strength. Our basic understanding of the underlying mechanisms, obtained from the single-phase material, is therefore crucial to modeling the two-phase material. The single-phase material model has been modified by adding a temperature-dependent parameter, a threshold strength, on each slip system. For resolved shear stress levels below this threshold no plastic deformation can occur in the

two-phase material[1]. The remaining parameters, other than κ_1 and κ_2, are those obtained from the single-phase simulations. This threshold strength lumps several phenomena (low initial dislocation structure of γ' particles in the two-phase material, bowing of dislocations between γ' particles, injection of dislocations into γ' particles, etc.) together, giving their combined effects, so it cannot be considered to be a direct measure of any single effect. However, as a first order approach the present model captures the essential features of the behavior of these materials rather well, while remaining relatively simple.

6.2 Discussion

The model proposed in this study has several advantages and some limitations:

- The approach uses a progression from fcc structure to $L1_2$ structure (single-phase) to two-phase material, building on the understanding which already exists of the behavior of these other materials. From our comparisons of the predictive capabilities of the model against experiments, we see that the complexity incorporated is necessary, since classical models do not adequately represent the material response. However, our approach presumes knowledge of the response of the γ' phase of the material (which is not always possible to obtain), and assumes that going from a bulk material to cubic particles in a microcomposite which are separated from each other does not significantly change the fundamental material properties of the dispersed phase.

- The formulation is relatively simple. The parameters are fewer, and the experiments necessary to deterimine them well-defined, yet the performance of the model has been shown to be rather good - we are able to predict behavior under complex loading conditions based on parameters obtained from simple tension and compression experiments. This makes it an attractive option for design applications where more complex geometries and loading conditions prevail.

- The model appears to perform well over a fairly wide range of temperatures - $\sim$ 25 - 850°C. The mechanisms responsible for the increase of yield strength with temperature seem to dominate in that temperature window. At temperatures below

[1] We are concerned here with a model for gross yielding; the material, however, does show creep at lower stresses

$\sim$ 25°C experimental data shows a slight decrease of yield strength with temperature, while at temperatures above $\sim$ 850°C, microstructural evolution begins to occur. In these temperature ranges, the model is no longer valid and is not expected to perform well.

6.3 Future Work

The material system being treated in this study, and the interactions of its parts over a wide range of temperatures is very complicated. In this study, every attempt was made to strike a judicious compromise between incorporating the major physical mechanisms and yet obtaining a simple, easily implementable constitutive model. This means that some of the microscale physical aspects of the material or its behavior are either ignored or approximated in some way. To better approach the real material some further modifications which may be considered include:

- Include thermal expansion effects and thermo-mechanical coupling into the model. This is especially necessary since under service conditions, the turbine blade is subject to very non-uniform temperatures from the root to the tip of the airfoil (e.g. Figure 6-1).
- Extend the model to cyclic loading conditions.
- Full 3-dimensional simulations of the turbine blade geometry and loading conditions.
- Bring together the above-mentioned features and the two-phase simulations as described in Appendix D.
- Add strain hardening to the model.

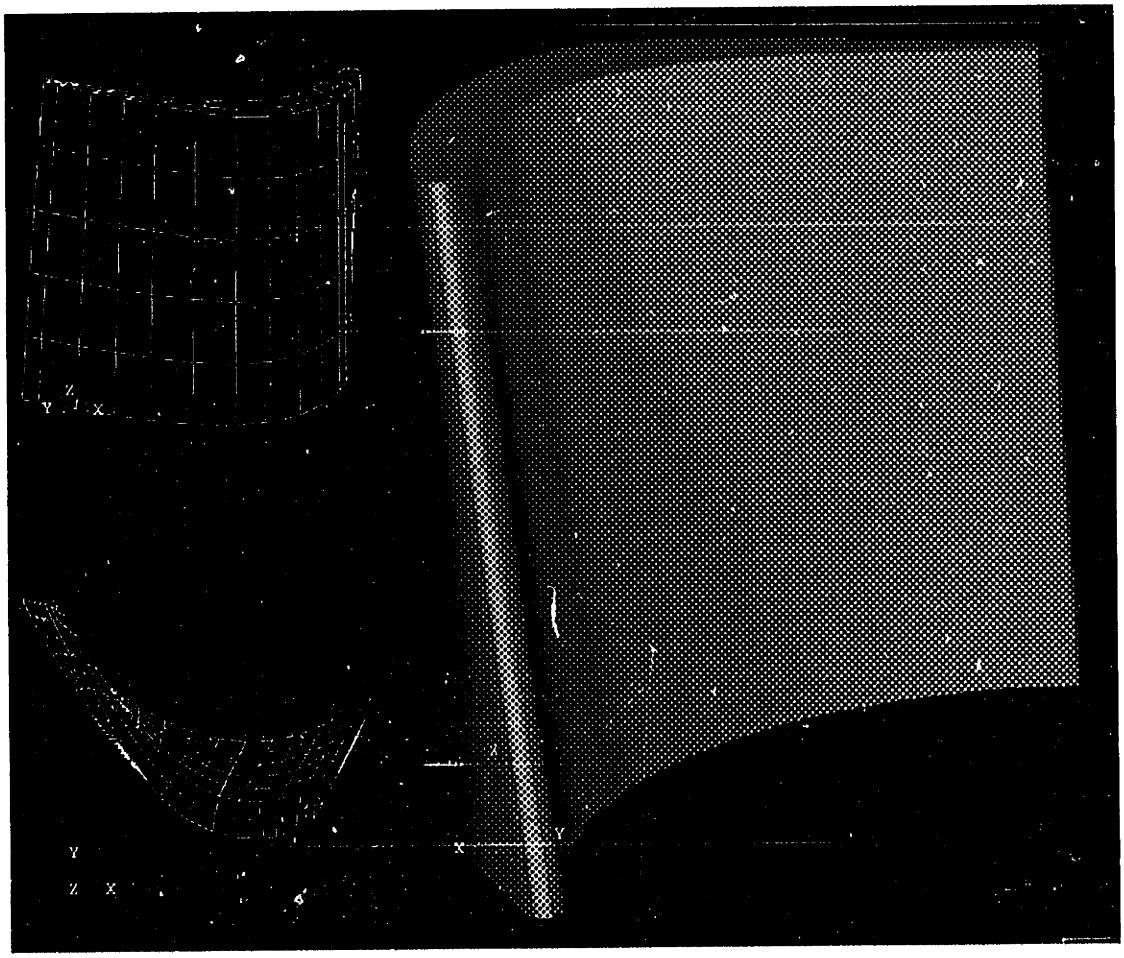

Figure 6-1: Airfoil portion of turbine blade

Bibliography

[Anand, 1985] L. Anand. Constitutive Equations for Hot-Working of Metals. *Int. J. of Plasticity*, 1, pp. 213–231, 1985.

[Asaro, 1983] R. J. Asaro. *Micromechanics of Crystals and Polycrystals*, volume 23 of *Advances in Applied Mechanics*, pages 1–116. Academic Press, 1983.

[Copley and Kear, 1967] S. M. Copley and B. H. Kear. Temperature and Orientation Dependence of the Flow Stress in Off-Stoichiometric Ni_3Al (γ' Phase). *Trans. Metallurgical Society of AIME*, 239, pp. 977–984, July 1967.

[Cuitiño and Ortiz, 1993] A. M. Cuitiño and M. Ortiz. Constitutive modeling of $L1_2$ intermetallic crystals. *Materials Science and Engineering*, A170, pp. 111–123, 1993.

[Cullity, 1978] B. D. Cullity. *Elements of X-Ray Diffraction.* Addison-Wesley Publishing Co., 1978.

[Dalal *et al.*, 1984] R. P. Dalal, C. R. Thomas, and L. E. Dardi. The Effect of Crystallographic Orientation on the Physical and MechanicalProperties of an Investment Cast Single Crystal Nickel-Base superalloy. *Proceedings 5th International Symposium On Superalloys*, ASM, Metals Park, OH, pp. 185–197, 1984.

[Flinn, 1960] P. A. Flinn. Theory of Deformation in Superlattices. *Trans. AIME*, 218, pp. 145–154, 1960.

[Harris *et al.*, 1984] K. Harris, G. L. Erickson, and R. E. Schwer. MAR M 247 Derivations - CM 247 LC DS Alloy, CMSX Single Crystal Alloys, Properties and Performance. *Proceedings 5th International Symposium On Superalloys*, ASM, Metals Park, OH, pp. 221–230, 1984.

[Heredia and Pope, 1986] F. E. Heredia and D. P. Pope. The Tension/Compression Flow Asymmetry in a High γ' Volume Fraction Nickle Base Alloy. *Acta. Metall. Mater.*, 34(2), pp. 279–285, 1986.

[Heredia and Pope, 1991] F. E. Heredia and D. P. Pope. The Plastic Flow of Binary Ni_3Al Single Crystals. *Acta. Metall. Mater.*, 39(8), pp. 2027–2036, 1991.

[Heredia, 1990] F. E. Heredia. *Solid Solution Strengthening and Fracture of Ni_3Al Single Crystals.* PhD thesis, University of Pennsylvania, 1990.

[Hib, 1991] Hibbit, Karlsson & Sorenson, Inc., 100 Medway Street, Providence, RI 02906-4402. *ABAQUS Reference Manuals*, 1991.

[Hirsch and Sun, 1993] P. B. Hirsch and Y. Q. Sun. Observations of dislocations relevant to the anomalous yield stress in $L1_2$ alloys. *Materials Science and Engineering*, A164, pp. 395–400, 1993.

[Hirsch, 1992a] P. B. Hirsch. A model for the anomalous yield stress for (111) slip in $L1_2$ alloys. *Progress in Materials Science*, 36, pp. 63–88, 1992.

[Hirsch, 1992b] P. B. Hirsch. A new theory of the anomalous yield stress in $L1_2$ alloys. *Philosophical Magazine A*, 65(3), pp. 569–612, 1992.

[Hirth and Lothe, 1982] J. P. Hirth and J. Lothe. *Theory of Dislocations.* John Wiley and Sons, 2nd edition, 1982.

[Hosford, 1990] W. F. Hosford. *Crystal Mechanics.* unpublished, 1990.

[Hull and Bacon, 1984] D. Hull and D. J. Bacon. *Introduction to Dislocations.* Pergamon Press, 3rd edition, 1984.

[Jordan and Walker, 1992] E. H. Jordan and K. P. Walker. A Viscoplastic Model For Single Crystals. *ASME, J. Engineering Materials and Technology*, 114, pp. 19–26, October 1992.

[Kalidindi *et al.*, 1992] S. R. Kalidindi, C. A. Bronkhorst, and L Anand. Crystallographic Texture Evolution in Bulk Deformation Processing of FCC Metals. *ASME, J. Mech. Phys. Solids*, 40, pp. 537–569, 1992.

[Kalidindi, 1992] S. R. Kalidindi. *Polycrystal Plasticity: Constitutive Modeling and Deformation Processing.* PhD thesis, Massachusetts Institute of Technology, June 1992.

[Kear and Hornbecker, 1966] B. H. Kear and M. F. Hornbecker. Deformation Structures in Polycrystalline Ni_3Al. *Trans. ASM*, 59, pp. 155–161, 1966.

[Kear and Wilsdorf, 1962] B. H. Kear and H. G. F. Wilsdorf. Dislocation Configurations in Plastically Deformed Polycrystalline Cu_3Au Alloys. *Trans. AIME*, 224, pp. 382–386, 1962.

[Kear, 1964] B. H. Kear. Dislocation Configurations and Work Hardening in Cu_3Au Crystals. *Acta Metall.*, 12, pp. 555–569, 1964.

[Lall *et al.*, 1979] C. Lall, S. Chin, and D. P. Pope. The Orientation and Temperature Dependence of the Yield Stress of Ni_3(Al, Nb) Single Crystals. *Metall. Trans.*, 10A, pp. 1323–1332, 1979.

[Lin, 1994] C. C. Lin. . Master's thesis, Massachusetts Institute of Technology, December 1994.

[Marcinkowski *et al.*, 1961] M. J. Marcinkowski, N. Brown, and R. M. Fisher. Dislocation Configurations in $AuCu_3$ and $AuCu$ Type Superlattices. *Acta. Metall.*, 9, pp. 129–137, 1961.

[Méric *et al.*, 1991] L. Méric, P. Poubanne, and G. Cailletaud. Single Crystal Modeling for Structural Calculations: Part 1 — Model Presentation. *ASME, J. Engineering Materials and Technology*, 113, pp. 162–170, 1991.

[Molloy, 1990] W. J. Molloy. Investment-Cast SUPERALLOYS a Good Investment. *ASM, Advanced Materials and Processes*, 10/90, pp. 23–30, 1990.

[Mulford and Pope, 1973] R. A. Mulford and D. P. Pope. The Yield Stress of Ni_3(Al,W). *Acta. Metall.*, 21(10), pp. 1375–1380, October 1973.

[Nouailhas *et al.*, 1993] D. Nouailhas, D. Pacou, G. Cailletaud, F. Hanriot, and L. Rémy. *Experimental Study of the Anisotropic Behavior of the CMSX2 Single-Crystal Superalloy Under Tension-Torsion Loadings*, volume PCN 04-011910-30 of *Advances in Multiaxial Fatigue*, pages 244–258. ASTM, 1993.

[Paidar *et al.*, 1984] V. Paidar, D. P. Pope, and V Vitek. A Theory of the Anomalous Yield Behavior in $L1_2$ Ordered Alloys. *Acta. Metall.*, 32(3), pp. 435–448, 1984.

[Peterson, 1974] R. E. Peterson. *Stress Concentration Factors.* John Wiley and Sons, 1974.

[Pollock and Argon, 1988] T. M. Pollock and A. S. Argon. Intermediate Temperature Creep Deformation in CMSX-3 Single Crystals. *Proceedings 6th International Symposium On Superalloys*, ASM, Metals Park, OH, pp. 285–294, 1988.

[Pollock, 1989] T. M. Pollock. *Creep Deformation in Nickel Base Superalloy Single Crystals.* PhD thesis, Massachusetts Institute of Technology, June 1989.

[Pope and Ezz, 1984] D. P. Pope and S. S. Ezz. Mechanical properties of Ni_3Al and nickel-base alloys with high volume fraction of γ/γ'. *Int. Metals Reviews*, 29(3), pp. 136–167, 1984.

[Qin and Bassani, 1992] Q. Qin and J. L. Bassani. Non-Schmid Yield Behavior in Single Crystals. *ASME, J. Mech. Phys. Solids*, 40(4), pp. 813–833, 1992.

[Shah and Duhl, 1984] D. M. Shah and D. N. Duhl. The effect of Orientation, Temperature and Gamma Prime Size On The Yield Strength Of A Single Crystal Nickel-Based Superalloy. *Proceedings 5th International Symposium On Superalloys*, ASM, Metals Park, OH, pp. 105–114, 1984.

[Sheh and Stouffer, 1990] M. Y. Sheh and D. C. Stouffer. A Crystallographic Model for the Tensile and Fatigue Response for René N4 at 982*C*. *ASME, J. Applied Mechanics*, 57, pp. 25–31, March 1990.

[Simmons and Wang, 1971] G. Simmons and H. Wang. *Single Crystal Elastic Constants and Calculated Aggregate Properties.* MIT Press, 1971.

[Stouffer *et al.*, 1990] D. C. Stouffer, V. G. Ramaswamy, J. H. Laflen, Van Stone R. H., and R. Williams. A Constitutive Model for the Inelastic Multiaxial Response of René 80 at 871C and 982C. *ASME, J. Engineering Materials and Technology*, 112, pp. 241–246, April 1990.

[Swanson *et al.*, 1986] G. A. Swanson, I. Linask, D. M. Nissley, P. P. Norris, T. G. Meyer, and K. P. Walker. Life Prediciton and Constitutive Models for Engine Hot Section

Anisotropic Materials Program: Annual Status Report. *NASA CR174952*, pages 2–16, February 1986.

[Takeuchi and Kuramoto, 1973] S. Takeuchi and E. Kuramoto. Temperature and Orientation Dependence of the Yield Stress in Ni_3Ga Single Crystals. *Acta Metall.*, 21, pp. 415–425, April 1973.

[Thomas, 1993] Dr. Malcolm Thomas. Personal communication, April 1993.

[Thornton *et al.*, 1970] P. H. Thornton, R. G. Davies, and T. L. Johnston. The Temperature Dependence of the Flow Stress of the γ' Phase Based upon Ni_3Al. *Metall. Trans.*, 1, pp. 207–218, 1970.

[Westbrook, 1957] J. H. Westbrook. Temperature Dependence of the Hardness Of Secondary Phases Common in Turbine Bucket Alloys. *Trans. AIME*, 209, pp. 898–904, 1957.

Appendix A

Definition and Determination of Crystal Orientations

A crystal direction is given by its "Miller Indicies". These indicies, (hkl) (in parentheses), define the orientation of a plane or, equivalently, the normal to that plane, $[hkl]$ (in square brackets). Many material properties are given in tensor form. These tensors must be referred to a basis. This basis is usually taken to be the axes defining the crystal orientation. Typically, elastic constants, for example, are given with respect to the [001] orientation. In order to do a simulation for another orientation, such as the [011], the elastic constants must be determined for this orientation. The two orientations are related by a set of rotations given by the "Euler Angles", (ϕ, θ, ω). Figure A-1 shows a reference cube with the crystal coordinates and global coordinates shown. The crystal coordinates are those with respect to which the material properties are defined, while the global coordinates are those with respect to which the material will be deformed. The shaded areas in the figures represent the perpendiculars to the axes of rotation. The procedure in going from the basis $\mathbf{e}^c$ to the basis $\mathbf{e}^g$ is as follows:

1. Rotate an angle ϕ around the c-axis. $a \longrightarrow a'$ and $b \longrightarrow b'$.

2. Rotate an angle θ around the a'-axis. $b' \longrightarrow b''$ and $c \longrightarrow c'$ (or $\mathbf{e}_3^g$).

3. Rotate an angle ω around the c'-axis. $b'' \longrightarrow b'''$ (or $\mathbf{e}_2^g$) and $a' \longrightarrow a''$ (or $\mathbf{e}_1^g$).

The rotations are denoted by the following matricies:

$$\mathbf{Q}_\phi = \begin{bmatrix} \cos\phi & \sin\phi & 0 \\ -\sin\phi & \cos\phi & 0 \\ 0 & 0 & 1 \end{bmatrix}, \mathbf{Q}_\theta = \begin{bmatrix} 1 & 0 & 0 \\ 0 & \cos\theta & \sin\theta \\ 0 & -\sin\theta & \cos\theta \end{bmatrix}, \mathbf{Q}_\omega = \begin{bmatrix} \cos\omega & \sin\omega & 0 \\ -\sin\omega & \cos\omega & 0 \\ 0 & 0 & 1 \end{bmatrix} \quad \text{(A.1)}$$

Hence, the total rotation from the crystal to the global orientation, $\mathbf{Q}$, is given by:

$$\mathbf{Q} = \mathbf{Q}_\omega \mathbf{Q}_\theta \mathbf{Q}_\phi \quad \text{(A.2)}$$

$$= \begin{bmatrix} \cos\phi\cos\omega & \sin\phi\cos\omega & \sin\omega\sin\theta \\ -\sin\phi\sin\omega\cos\theta & +\cos\phi\sin\omega\cos\theta & \\ -\cos\phi\sin\omega & -\sin\phi\sin\omega & \cos\omega\sin\theta \\ -\sin\phi\cos\omega\cos\theta & +\cos\phi\cos\omega\cos\theta & \\ \sin\phi\sin\theta & -\cos\phi\sin\theta & \cos\theta \end{bmatrix}$$

All of the orientations in space are obviously not unique. For example, the [100] orientation is identical to the [010] and [001] orientations. Hence, all orientations may be represented by a subsection of space. The usual representation is the stereographic projection. The advantage to this projection is that it preserves the angular relationships between the crystal planes. Details of its construction may be found in Cullity [1978]. Each orientation is denoted by a vector radiating from a point C in space, thus forming a sphere. The plane C is represented by its normal CP, which is in turn represented by its pole P, the intersection with the sphere, and P is represented by its projection P′. The projection of every point on this sphere from one point B on a major diameter of the sphere to a plane tangent to the point A opposite that point on the diameter is taken. These projections form a circle on the plane; this is the stereographic projection. Figure A-2 shows the [001] projection. The subset of these orientations which are unique are contained in a unit stereographic triangle with corners at the [001], [011] and [$\bar{1}$11] orientations, Figure A-3.

Within this unit triangle, the Euler angle θ varies with the radial distance from the [001] pole and is constant for constant radius, being 0° for [001], -45° for [011], and -54.7356° for [$\bar{1}$11]. The Miller indicies k and l are constant along great circles. The relationship between the Miller indicies [hkl] of the points in this unit stereographic triangle and the Euler angles

(ϕ, θ, ω) is given by:

$$\phi = \tan^{-1}\left(-\frac{h}{k}\right) \tag{A.3}$$

$$\theta = -\cos^{-1}\left(\frac{l}{\sqrt{h^2+k^2+l^2}}\right) \tag{A.4}$$

$$\omega = indeterminate^{1} \tag{A.5}$$

where the indicies $[hkl]$ are normalized to $h = -1$ as is usual for this unit triangle except along the $[001]--[011]$ boundary where $h = 0$. In this case, the indicies are normalized to $l = 1$.

Because of the triangle of the stereographic projection that is chosen, the (x, y, z) coordinates of the point **P** on the sphere are $(k, -h, l)$, where $h^2+k^2+l^2 \equiv R$, the radius of the reference sphere. Looking at a projection of the stereographic construction, and using similar triangles (Figure A-4), with the (x, y, z) coordinate system as shown, we obtain:

$$\frac{x-0}{k-0} = \frac{-y-0}{h-0} = \frac{z+R}{l+R} \tag{A.6}$$

$$\begin{aligned} \Longrightarrow \frac{x}{2R} &= \frac{k}{l+R} \\ \frac{y}{2R} &= \frac{-h}{l+R} \\ z &= R \end{aligned} \tag{A.7}$$

We observe that θ is the angle between the lines AB and BP and ϕ is the angle between the $[001]-[011]$ line and the line joining the point P to the [001] corner. In this projection, $\phi = 0$ and if we define ψ as the value of θ at $\phi = 0$, then geometry gives us

$$\tan\left(\frac{\psi}{2}\right) = \frac{y}{2R} \qquad (x = 0) \tag{A.8}$$

Similarly, if a projection is taken at 90° to the first, and we define ξ as the value of θ at $\phi = 90$, we see that

$$\tan\left(\frac{\xi}{2}\right) = \frac{x}{2R} \qquad (y = 0) \tag{A.9}$$

[01] From Figure A-2, we see that the rotation by ω is about the e_3^g axis. Hence, this direction, the final loading orientation in global coordinates, is independent of ω. As a result, ω may not be determined simply by the condition of rotating e_3^c to e_3^g.

Defining the normalized lengths $X \equiv \frac{x}{2R}$, $Y \equiv \frac{y}{2R}$, $Z \equiv \frac{z}{2R}$, in general, we get

$$\tan\left(\frac{\theta}{2}\right) = \sqrt{X^2 + Y^2} \qquad \forall x, y \tag{A.10}$$

$$\tan\phi = \frac{Y}{X} \tag{A.11}$$

$$\omega = 0. \tag{A.12}$$

$$\Longrightarrow X = -\tan\left(\frac{\theta}{2}\right)\cos\phi \tag{A.13}$$

$$Y = -\tan\left(\frac{\theta}{2}\right)\sin\phi \tag{A.14}$$

So, given a diagram of orientations within the unit stereographic triangle, the Euler angles may be obtained directly and input to the user material subroutine for ABAQUS simulations.

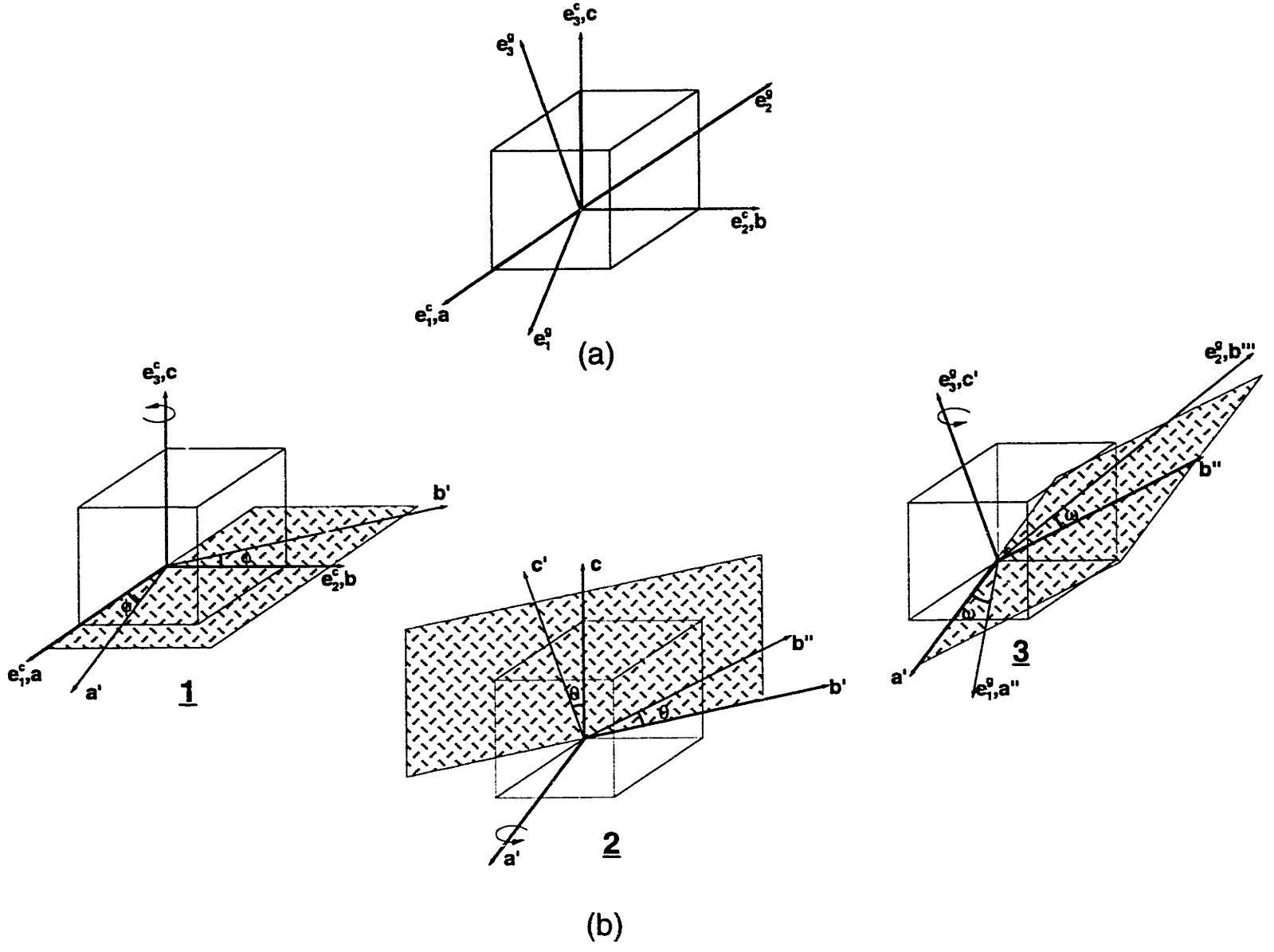

Figure A-1: (a) Definition of global coordinate system with respect to crystal coordinate system (b) Definition of Euler angles

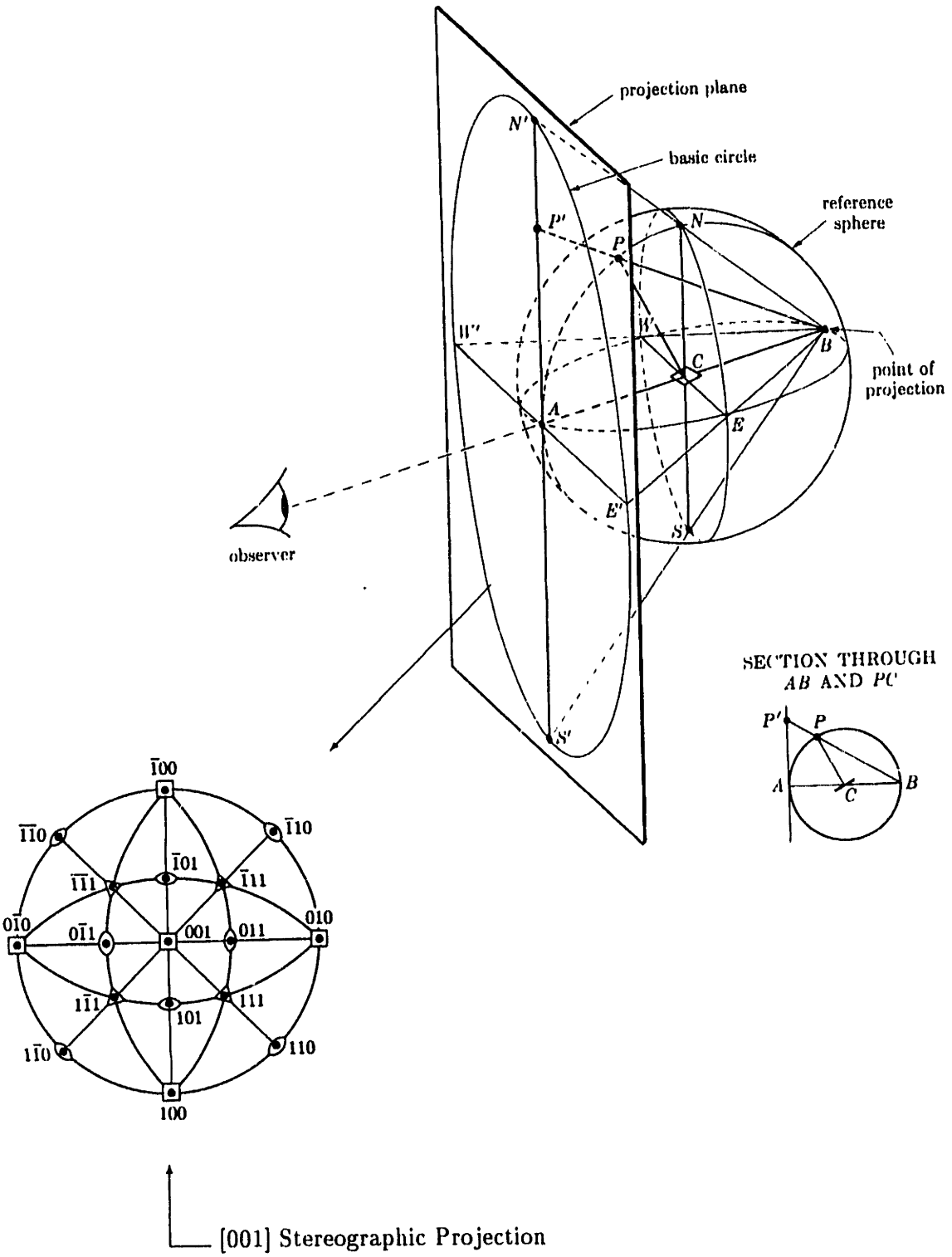

Figure A-2: Formation of stereographic projection [Cullity, 1978]

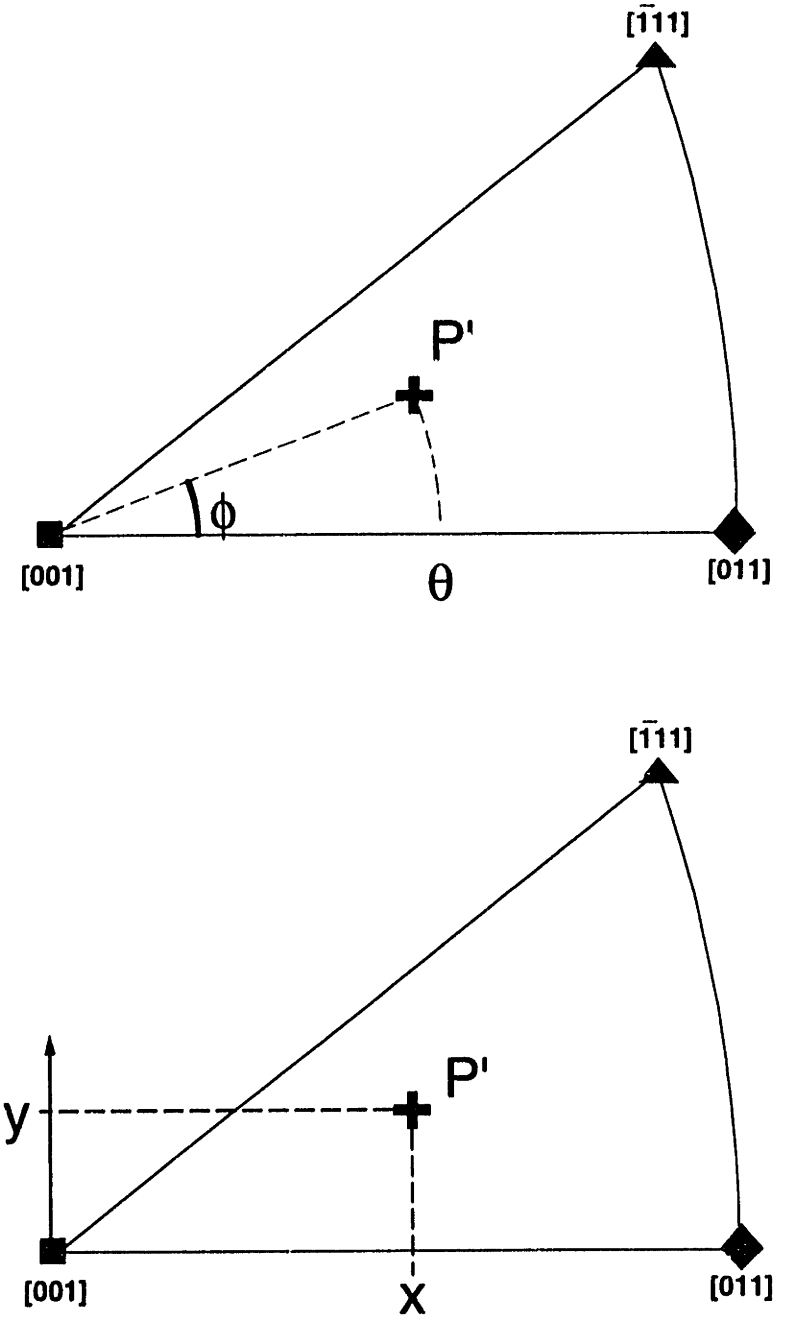

Figure A-3: Unit stereographic triangle

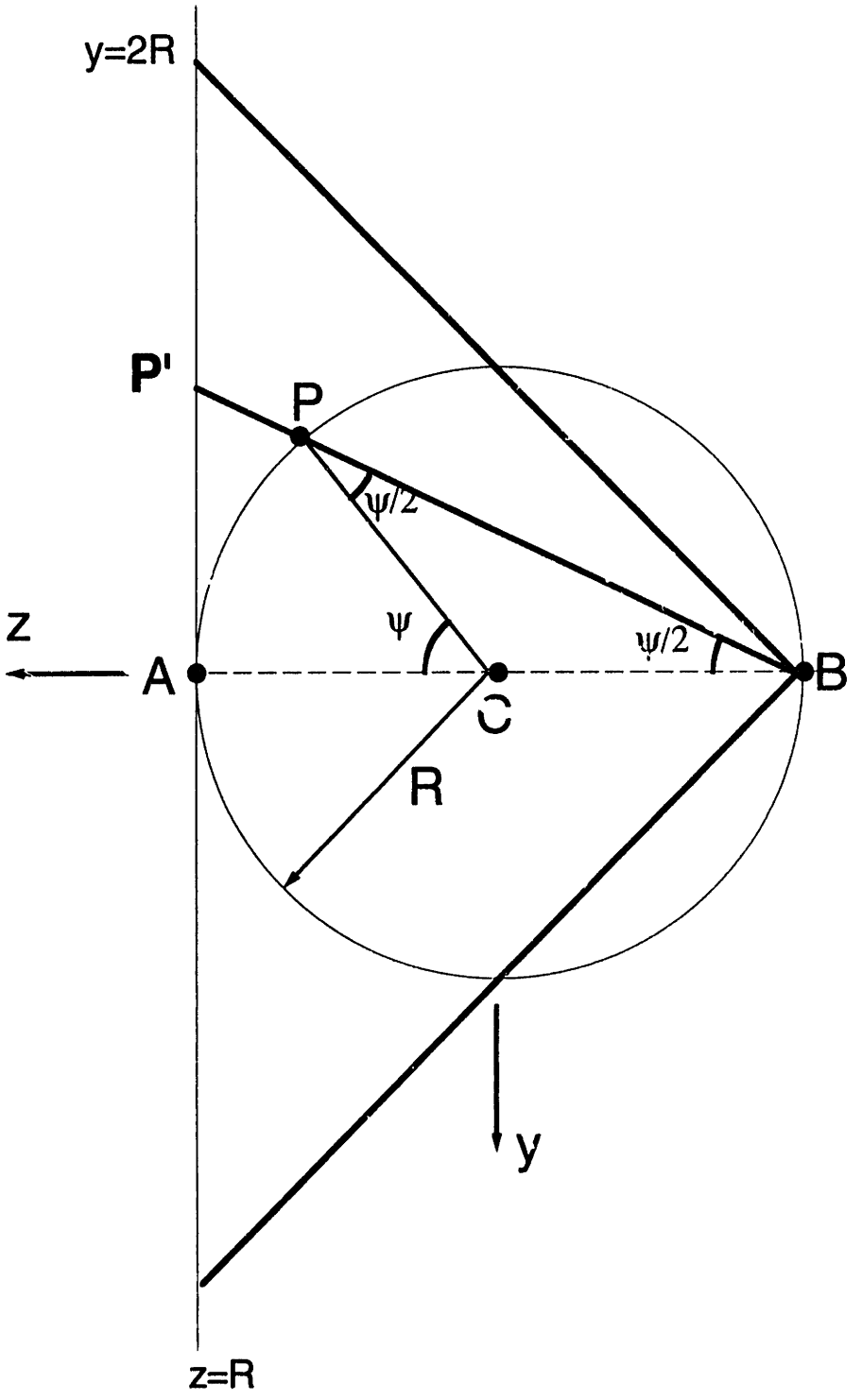

Figure A-4: yz projection of stereographic construction

Appendix B

Effect of the Non-Schmid Shear Stresses on the $\frac{1}{6}\langle 112\rangle$ Shockley Partial Dislocations

The force per unit length on a dislocation, **f**, due to an applied stress **T** is given by

$$\mathbf{f} = \mathbf{T}\mathbf{b} \times \boldsymbol{\xi} \tag{B.1}$$

where **b** is the Burgers vector and $\boldsymbol{\xi}$ is the line vector of the dislocation. The directions (not the magnitudes) of the forces on the Shockley partial dislocations due to each of the shear stresses τ_{pe}^{α} and τ_{cb}^{α} will be ascertained in order to determine their effects in tension-compression.

An **xyz** coordinate system is defined relative to the dislocation in question, where the **z** direction is coincident with the line direction and Burgers vector direction of the superpartial screw dislocation ($\frac{1}{2}[\bar{1}01]$). The Burgers vectors and line vectors of the Shockley partials in

this coordinate system are (Figure B-1(a)):

Slip System $\alpha = i$:

$$\mathbf{b}_1 = \begin{Bmatrix} 0 \\ b_y \\ b_z \end{Bmatrix} \quad \mathbf{b}_2 = \begin{Bmatrix} 0 \\ -b_y \\ b_z \end{Bmatrix}$$

$$\boldsymbol{\xi}_1 = \begin{Bmatrix} 0 \\ \xi_y \\ \xi_z \end{Bmatrix} \quad \boldsymbol{\xi}_2 = \begin{Bmatrix} 0 \\ -\xi_y \\ \xi_z \end{Bmatrix}$$

Slip System $\alpha = i + 12$:

$$\mathbf{b}_1 = \begin{Bmatrix} 0 \\ -b_y \\ -b_z \end{Bmatrix} \quad \mathbf{b}_2 = \begin{Bmatrix} 0 \\ b_y \\ -b_z \end{Bmatrix}$$

$$\boldsymbol{\xi}_1 = \begin{Bmatrix} 0 \\ \xi_y \\ \xi_z \end{Bmatrix} \quad \boldsymbol{\xi}_2 = \begin{Bmatrix} 0 \\ -\xi_y \\ \xi_z \end{Bmatrix}$$

where b_y, b_z, ξ_y and ξ_z are the (undetermined) positive **y** and **z** coordinates of the Burgers vectors and line vectors respectively.

The shear stress τ_{pe}^{α} is perpendicular to the Burgers vector direction of the superpartial $\frac{1}{2}[\bar{1}01]$. The stress matrix is given by

$$\mathbf{T} = \begin{bmatrix} 0 & \tau_{xy} & 0 \\ \tau_{xy} & 0 & 0 \\ 0 & 0 & 0 \end{bmatrix}$$

Thus,

Slip System $\alpha = i$:

$$\mathbf{Tb_1} = \begin{Bmatrix} \tau_{xy} b_y \\ 0 \\ 0 \end{Bmatrix} \Longrightarrow \mathbf{f_1} = \begin{Bmatrix} 0 \\ -\tau_{xy} b_y \xi_z \\ \tau_{xy} b_y \xi_y \end{Bmatrix}$$

$$\mathbf{Tb_2} = \begin{Bmatrix} -\tau_{xy} b_y \\ 0 \\ 0 \end{Bmatrix} \Longrightarrow \mathbf{f_2} = \begin{Bmatrix} 0 \\ \tau_{xy} b_y \xi_z \\ \tau_{xy} b_y \xi_y \end{Bmatrix}$$

Slip System $\alpha = i + 12$:

$$\mathbf{Tb_1} = \begin{Bmatrix} -\tau_{xy} b_y \\ 0 \\ 0 \end{Bmatrix} \Longrightarrow \mathbf{f_1} = \begin{Bmatrix} 0 \\ \tau_{xy} b_y \xi_z \\ -\tau_{xy} b_y \xi_y \end{Bmatrix}$$

$$\mathbf{Tb_2} = \begin{Bmatrix} \tau_{xy} b_y \\ 0 \\ 0 \end{Bmatrix} \Longrightarrow \mathbf{f_2} = \begin{Bmatrix} 0 \\ -\tau_{xy} b_y \xi_z \\ -\tau_{xy} b_y \xi_y \end{Bmatrix}$$

These force directions are illustrated in Figure B-1(b). The effect of the force on the dislocations, in this case to promote dissociation, is the same for slip system $\alpha = i$ and slip system $\alpha = i + 12$, so the slip direction $\mathbf{m}^{\alpha}_{pe}$ remains the same.

The shear stresses τ^{α} and τ^{α}_{cb} are both parallel to the Burgers vector direction of the superpartial $\frac{1}{2}[\bar{1}01]$ and result in a force perpendicular to the dislocation, moving it on the appropriate slip plane. The force on the superpartial dislocation is reversed from slip system $\alpha = i$ to slip system $\alpha = i + 12$, so the slip directions $\mathbf{m}^{\alpha}$ and $\mathbf{m}^{\alpha}_{cb}$ must also be reversed.

These modifications for slip systems 13 - 24 (these considerations are not relevant to the cube slip systems) may be summarized as:

$$\mathbf{n}^{i+12} = \mathbf{n}^{i} \qquad \mathbf{n}^{i+12}_{pe} = \mathbf{n}^{i}_{pe} \qquad \mathbf{n}^{i+12}_{cb} = \mathbf{n}^{i}_{cb}$$

$$\mathbf{m}^{i+12} = -\mathbf{m}^{i} \qquad \mathbf{m}^{i+12}_{pe} = \mathbf{m}^{i}_{pe} \qquad \mathbf{m}^{i+12}_{cb} = -\mathbf{m}^{i}_{cb}$$

The effect of the shear stress τ^{α}_{pe} in tension and compression leads to the observed tension-compression asymmetry. In one sense, the force on the partials tends to further the dissociation into Shockley partials and in the other sense it tends to recombine them, promoting cross-slip to the (010) plane. According to Lall *et al.*, when the leading Shockley partial pair has recombined, it experiences a stress pushing it further onto (010). Once the leading partial has cross-slipped, it acts as a pinning point for further dislocation motion.

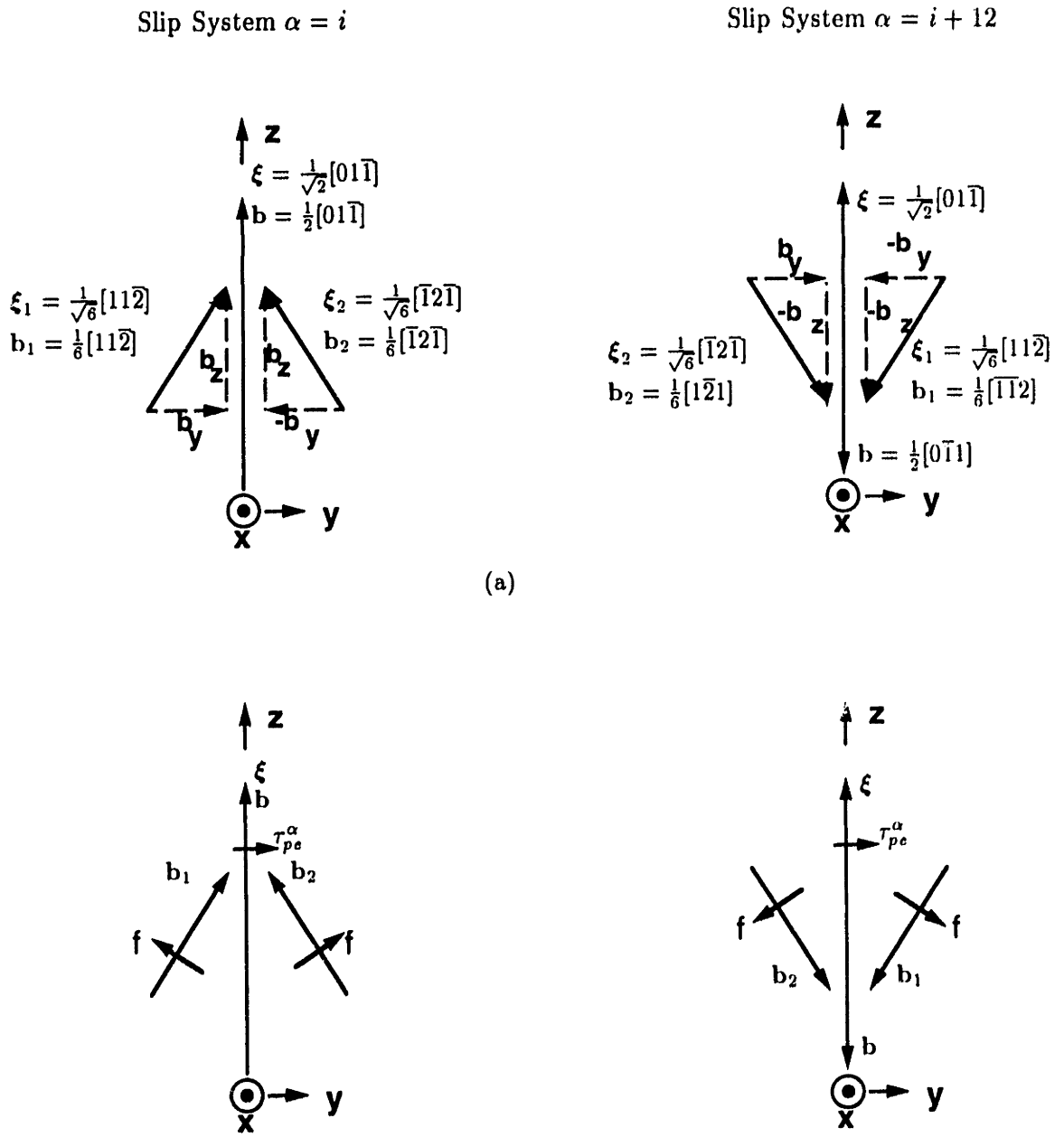

Figure B-1: (a) Dissociation of a $\frac{1}{2}[01\bar{1}]$ superpartial (b) Effect of τ_{pe}^{α} on Shockley partials

Appendix C

A Simplified Model for $L1_2$ Superalloys under Isothermal Conditions

C.1 Introduction

For simple f.c.c. materials, the specific constitutive form of the plastic shearing rate on the slip system α (Equation 2.7) is given by:

$$\dot{\gamma}^\alpha = \dot{\gamma}_o \left| \frac{\tau^\alpha}{s^\alpha} \right|^{1/m} \mathrm{sgn}(\tau^\alpha) \tag{C.1}$$

where $\dot{\gamma}_o$ is a reference shearing rate, m is a strain rate sensitivity parameter, and s^α is the slip system resistance on the slip system α. For the present case we will assume non-hardening material, so $s^\alpha = s_o = const.$ Additionally, for the $L1_2$ material we will assume that this initial slip system resistance has the same value, $s_{o,oct}$, for all 12 octahedral slip systems and the same (distinct) value, $s_{o,cub}$, for all 6 cube slip systems. The required modifications to this formulation for the $L1_2$ structure are described in what follows.

The $L1_2$ crystal structure is an f.c.c.-based superlattice structure consisting of two atom species with the formula AB_3, where the A atoms are at the corners of the unit cell and the B atoms are at the face centers, Figure C-1. Materials having the $L1_2$ crystal structure such as Ni_3Al have long been known to exhibit an anomalous yield behavior. An asymmetry exists in yielding in tension and compression. Additionally, the yield stress increases with

temperature up to a peak beyond which it drops normally. These materials have excellent high temperature properties, both by themselves and as the precipitate component in two-phase materials. As a result they have been used in such applications as turbine blades where they are subjected to extremely high and non-uniform temperatures and loads. Much attention has been given to studying these materials in an attempt to explain this behavior. In the present chapter the crystal plasticity model of Kalidindi [1992] is adapted to simulate simple tension and compression on single crystals of Ni_3Al and a 2-phase single crystal nickel-based alloy in several orientations, matching experimental yield data from the literature and accounting for the tension/compression asymmetry.

C.2 Modifications to Constitutive Model

The motivation for the changes to the constitutive model are the same as outlined in Chapter 2, but a simpler, somewhat more phenomenological approach will be taken, where the effects such as thermal activation are not considered, and an algorithm is developed for quickly obtaining the (fewer) necessary model parameters.

For the present case we will be considering isothermal conditions only. The slip rate on the slip system α is given by

$$\dot{\gamma}^{\alpha} = \dot{\gamma}_o \left\{ \frac{\tau^{\alpha}}{s^{\alpha} + \beta_1 \tau^{\alpha}_{pe} + \beta_2 \tau^{\alpha}_{cb}} \right\}^{1/m}, \qquad \tau^{\alpha} > 0 \tag{C.2}$$

(from $\dot{\gamma}^{\alpha} = \dot{\gamma}_o \left(\frac{\tau^{\alpha}}{s^{\alpha}}\right)^{1/m}$) where β_1 and β_2 are constants giving the relative weights of each of the "non-Schmid" contributions; $\dot{\gamma}_o$ is a reference strain rate; and m is the strain rate sensitivity. The magnitude and sign of β_1 determines the amount and sense of tension-compression asymmetry, a number that is dependent on slip on the primary $\{111\}$ slip plane. Physically, this make sense since this is the stress which helps or hinders dissociation of the dislocations into the Shockley partials. As we see from the above equation, $\dot{\gamma}^{\alpha} = 0$ when $\tau^{\alpha} = 0$.

C.2.1 Final form of Constitutive Model

The modified constitutive model may be summarized by the following equations, Kalidindi [1992]:

$$
\begin{aligned}
\mathbf{T}^* &= \mathcal{L}[\mathbf{E}^*], \qquad \text{where} \qquad \mathbf{E}^* \equiv 1/2\{\mathbf{F}^{*T}\mathbf{F}^* - \mathbf{1}\} \\
\mathbf{T}^* &\equiv \mathbf{F}^{*-1}\{(\det \mathbf{F}^*)\mathbf{T}\}\mathbf{F}^{*-T} \\
\mathbf{F}^* &\equiv \mathbf{F}\mathbf{F}^{p^{-1}}, \qquad \det \mathbf{F}^* > 0 \\
\dot{\mathbf{F}}^p &= \mathbf{L}^p\mathbf{F}^p \\
\mathbf{L}^p &= \sum_\alpha \dot{\gamma}^\alpha \mathbf{S}_o^\alpha, \qquad \mathbf{S}_o^\alpha \equiv \mathbf{m}_o^\alpha \otimes \mathbf{n}_o^\alpha \\
\dot{\gamma}^\alpha &= \dot{\gamma}_o \left\{ \frac{\tau^\alpha}{s^\alpha \left[1 + \beta_1 \frac{\tau_{pe}^\alpha}{\bar{\tau}} + \beta_2 \frac{\tau_{ch}}{\bar{\sigma}}\right]} \right\}^{1/m}
\end{aligned}
\tag{C.3}
$$

$\mathcal{L}$ is the fourth order elasticity tensor; $\mathbf{1}$ is the second order identity tensor; $\mathbf{T}$ is the symmetric Cauchy stress tensor, $\mathbf{F}^*$ is an elastic deformation gradient; $\dot{\gamma}^\alpha$ is the plastic shearing rate on the slip system α, given by equation C.2.

In uniaxial tension/compression in the 3-direction, $L_{33} = \dot{\epsilon}$ where $\dot{\epsilon}$ is the macroscopic imposed strain rate. If elasticity is ignored, then $\mathbf{L} = \mathbf{L}^e + \mathbf{L}^p \approx \mathbf{L}^p$ and

$$L_{33}^p \approx \dot{\epsilon} \tag{C.4}$$

For each of the low index orientations $\langle 001\rangle, \langle 011\rangle, \langle 111\rangle$ at the three corners of the standard stereographic triangle (Figure C-2), the slip rates on all active slip systems have the same magnitude, all the non-zero Schmid factors being the same (Table C.1). $\Longrightarrow \dot{\gamma}^\alpha = \pm\dot{\gamma}_i$ for all active slip systems, where $\dot{\gamma}_i$ is evaluated using equation C.2. Equation C.3 thus yields $\mathbf{L}^p$ as a matrix of constants times $\dot{\gamma}_i$. This leads to,

$$L_{33}^p = k_{[hkl]}\dot{\gamma}_i \tag{C.5}$$

where $k_{[hkl]}$ is a constant depending on the crystal orientation. We may evaluate $\mathbf{L}^p$ from equation C.3 and using the information in Tables 2.1 and C.1 as follows.

$$\mathbf{L}^p = \sum_\alpha \dot{\gamma}^\alpha \mathbf{S}^\alpha, \qquad \mathbf{S}^\alpha \equiv \mathbf{m}_o^\alpha \otimes \mathbf{n}_o^\alpha \tag{C.6}$$

Table C.1: Schmid factors for octahedral slip systems

	[001]			[011]			$[\bar{1}11]$		
α	m^α	m^α_{pe}	m^α_{cb}	m^α	m^α_{pe}	m^α_{cb}	m^α	m^α_{pe}	m^α_{cb}
1	$-\frac{1}{\sqrt{6}}$	$\frac{1}{3\sqrt{2}}$	0	0	$\frac{2}{3\sqrt{2}}$	0	0	$\frac{4}{9\sqrt{2}}$	0
2	$\frac{1}{\sqrt{6}}$	$\frac{1}{3\sqrt{2}}$	0	$\frac{1}{\sqrt{6}}$	$-\frac{1}{3\sqrt{2}}$	$\frac{1}{2\sqrt{2}}$	$\frac{2}{3\sqrt{6}}$	$-\frac{2}{9\sqrt{2}}$	$\frac{2}{3\sqrt{2}}$
3	0	$-\frac{2}{3\sqrt{2}}$	0	$-\frac{1}{\sqrt{6}}$	$-\frac{1}{3\sqrt{2}}$	$-\frac{1}{2\sqrt{2}}$	$-\frac{2}{3\sqrt{6}}$	$-\frac{2}{9\sqrt{2}}$	$-\frac{2}{3\sqrt{2}}$
4	$-\frac{1}{\sqrt{6}}$	$\frac{1}{3\sqrt{2}}$	0	0	$\frac{2}{3\sqrt{2}}$	0	0	0	0
5	$\frac{1}{\sqrt{6}}$	$\frac{1}{3\sqrt{2}}$	0	$\frac{1}{\sqrt{6}}$	$-\frac{1}{3\sqrt{2}}$	$\frac{1}{2\sqrt{2}}$	0	0	0
6	0	$-\frac{2}{3\sqrt{2}}$	0	$-\frac{1}{\sqrt{6}}$	$-\frac{1}{3\sqrt{2}}$	$-\frac{1}{2\sqrt{2}}$	0	0	0
7	$-\frac{1}{\sqrt{6}}$	$\frac{1}{3\sqrt{2}}$	0	0	0	0	$\frac{2}{3\sqrt{6}}$	$-\frac{2}{9\sqrt{2}}$	$\frac{2}{3\sqrt{2}}$
8	$\frac{1}{\sqrt{6}}$	$\frac{1}{3\sqrt{2}}$	0	0	0	$-\frac{1}{2\sqrt{2}}$	$-\frac{2}{3\sqrt{6}}$	$-\frac{2}{9\sqrt{2}}$	$-\frac{2}{3\sqrt{2}}$
9	0	$-\frac{2}{3\sqrt{2}}$	0	0	0	$\frac{1}{2\sqrt{2}}$	0	$\frac{4}{9\sqrt{2}}$	0
10	$-\frac{1}{\sqrt{6}}$	$\frac{1}{3\sqrt{2}}$	0	0	0	0	$-\frac{2}{3\sqrt{6}}$	$-\frac{2}{9\sqrt{2}}$	$-\frac{2}{3\sqrt{2}}$
11	$\frac{1}{\sqrt{6}}$	$\frac{1}{3\sqrt{2}}$	0	0	0	$-\frac{1}{2\sqrt{2}}$	0	$\frac{4}{9\sqrt{2}}$	0
12	0	$-\frac{2}{3\sqrt{2}}$	0	0	0	$\frac{1}{2\sqrt{2}}$	$\frac{2}{3\sqrt{6}}$	$-\frac{2}{9\sqrt{2}}$	$\frac{2}{3\sqrt{2}}$

Table C.2: Values of $\mathbf{S}_o^\alpha$ and $\dot{\gamma}^\alpha$ for the $\langle 001 \rangle$ orientation

$$[001]: \quad \phi = 0, \quad \theta = 0, \quad \omega = 0 \qquad \mathbf{Q} = \begin{bmatrix} 1 & 0 & 0 \\ 0 & 1 & 0 \\ 0 & 0 & 1 \end{bmatrix}$$

α	$\mathbf{n}_o^\alpha = \mathbf{Q}\mathbf{n}_c^\alpha$	$\mathbf{m}_o^\alpha = \mathbf{Q}\mathbf{m}_c^\alpha$	$\mathbf{S}_o^\alpha = \mathbf{m}_o^\alpha \otimes \mathbf{n}_o^\alpha$	m^α	$\dot{\gamma}^\alpha$
1	$\left\{ \frac{1}{\sqrt{3}} \quad \frac{1}{\sqrt{3}} \quad \frac{1}{\sqrt{3}} \right\}$	$\left\{ 0 \quad \frac{1}{\sqrt{2}} \quad -\frac{1}{\sqrt{2}} \right\}$	$\begin{bmatrix} 0 & 0 & 0 \\ \frac{1}{\sqrt{6}} & \frac{1}{\sqrt{6}} & \frac{1}{\sqrt{6}} \\ -\frac{1}{\sqrt{6}} & -\frac{1}{\sqrt{6}} & -\frac{1}{\sqrt{6}} \end{bmatrix}$	$-\frac{1}{\sqrt{6}}$	$-\dot{\gamma}_1$
2	$\left\{ \frac{1}{\sqrt{3}} \quad \frac{1}{\sqrt{3}} \quad \frac{1}{\sqrt{3}} \right\}$	$\left\{ -\frac{1}{\sqrt{2}} \quad 0 \quad \frac{1}{\sqrt{2}} \right\}$	$\begin{bmatrix} -\frac{1}{\sqrt{6}} & -\frac{1}{\sqrt{6}} & -\frac{1}{\sqrt{6}} \\ 0 & 0 & 0 \\ \frac{1}{\sqrt{6}} & \frac{1}{\sqrt{6}} & \frac{1}{\sqrt{6}} \end{bmatrix}$	$\frac{1}{\sqrt{6}}$	$\dot{\gamma}_1$
3	$\left\{ \frac{1}{\sqrt{3}} \quad \frac{1}{\sqrt{3}} \quad \frac{1}{\sqrt{3}} \right\}$	$\left\{ \frac{1}{\sqrt{2}} \quad -\frac{1}{\sqrt{2}} \quad 0 \right\}$	$\begin{bmatrix} \frac{1}{\sqrt{6}} & \frac{1}{\sqrt{6}} & \frac{1}{\sqrt{6}} \\ -\frac{1}{\sqrt{6}} & -\frac{1}{\sqrt{6}} & -\frac{1}{\sqrt{6}} \\ 0 & 0 & 0 \end{bmatrix}$	0	0
4	$\left\{ \frac{1}{\sqrt{3}} \quad -\frac{1}{\sqrt{3}} \quad -\frac{1}{\sqrt{3}} \right\}$	$\left\{ 0 \quad -\frac{1}{\sqrt{2}} \quad \frac{1}{\sqrt{2}} \right\}$	$\begin{bmatrix} 0 & 0 & 0 \\ -\frac{1}{\sqrt{6}} & \frac{1}{\sqrt{6}} & \frac{1}{\sqrt{6}} \\ \frac{1}{\sqrt{6}} & -\frac{1}{\sqrt{6}} & -\frac{1}{\sqrt{6}} \end{bmatrix}$	$-\frac{1}{\sqrt{6}}$	$-\dot{\gamma}_1$
5	$\left\{ \frac{1}{\sqrt{3}} \quad -\frac{1}{\sqrt{3}} \quad -\frac{1}{\sqrt{3}} \right\}$	$\left\{ -\frac{1}{\sqrt{2}} \quad 0 \quad -\frac{1}{\sqrt{2}} \right\}$	$\begin{bmatrix} -\frac{1}{\sqrt{6}} & \frac{1}{\sqrt{6}} & \frac{1}{\sqrt{6}} \\ 0 & 0 & 0 \\ -\frac{1}{\sqrt{6}} & \frac{1}{\sqrt{6}} & \frac{1}{\sqrt{6}} \end{bmatrix}$	$\frac{1}{\sqrt{6}}$	$\dot{\gamma}_1$
6	$\left\{ \frac{1}{\sqrt{3}} \quad -\frac{1}{\sqrt{3}} \quad -\frac{1}{\sqrt{3}} \right\}$	$\left\{ \frac{1}{\sqrt{2}} \quad \frac{1}{\sqrt{2}} \quad 0 \right\}$	$\begin{bmatrix} \frac{1}{\sqrt{6}} & -\frac{1}{\sqrt{6}} & -\frac{1}{\sqrt{6}} \\ \frac{1}{\sqrt{6}} & -\frac{1}{\sqrt{6}} & -\frac{1}{\sqrt{6}} \\ 0 & 0 & 0 \end{bmatrix}$	0	0
7	$\left\{ -\frac{1}{\sqrt{3}} \quad \frac{1}{\sqrt{3}} \quad -\frac{1}{\sqrt{3}} \right\}$	$\left\{ 0 \quad \frac{1}{\sqrt{2}} \quad \frac{1}{\sqrt{2}} \right\}$	$\begin{bmatrix} 0 & 0 & 0 \\ -\frac{1}{\sqrt{6}} & \frac{1}{\sqrt{6}} & -\frac{1}{\sqrt{6}} \\ -\frac{1}{\sqrt{6}} & \frac{1}{\sqrt{6}} & -\frac{1}{\sqrt{6}} \end{bmatrix}$	$-\frac{1}{\sqrt{6}}$	$-\dot{\gamma}_1$
8	$\left\{ -\frac{1}{\sqrt{3}} \quad \frac{1}{\sqrt{3}} \quad -\frac{1}{\sqrt{3}} \right\}$	$\left\{ \frac{1}{\sqrt{2}} \quad 0 \quad -\frac{1}{\sqrt{2}} \right\}$	$\begin{bmatrix} -\frac{1}{\sqrt{6}} & \frac{1}{\sqrt{6}} & -\frac{1}{\sqrt{6}} \\ 0 & 0 & 0 \\ \frac{1}{\sqrt{6}} & -\frac{1}{\sqrt{6}} & \frac{1}{\sqrt{6}} \end{bmatrix}$	$\frac{1}{\sqrt{6}}$	$\dot{\gamma}_1$
9	$\left\{ -\frac{1}{\sqrt{3}} \quad \frac{1}{\sqrt{3}} \quad -\frac{1}{\sqrt{3}} \right\}$	$\left\{ -\frac{1}{\sqrt{2}} \quad -\frac{1}{\sqrt{2}} \quad 0 \right\}$	$\begin{bmatrix} \frac{1}{\sqrt{6}} & -\frac{1}{\sqrt{6}} & \frac{1}{\sqrt{6}} \\ \frac{1}{\sqrt{6}} & -\frac{1}{\sqrt{6}} & \frac{1}{\sqrt{6}} \\ 0 & 0 & 0 \end{bmatrix}$	0	0
10	$\left\{ -\frac{1}{\sqrt{3}} \quad -\frac{1}{\sqrt{3}} \quad \frac{1}{\sqrt{3}} \right\}$	$\left\{ 0 \quad -\frac{1}{\sqrt{2}} \quad -\frac{1}{\sqrt{2}} \right\}$	$\begin{bmatrix} 0 & 0 & 0 \\ \frac{1}{\sqrt{6}} & \frac{1}{\sqrt{6}} & -\frac{1}{\sqrt{6}} \\ \frac{1}{\sqrt{6}} & \frac{1}{\sqrt{6}} & -\frac{1}{\sqrt{6}} \end{bmatrix}$	$-\frac{1}{\sqrt{6}}$	$-\dot{\gamma}_1$
11	$\left\{ -\frac{1}{\sqrt{3}} \quad -\frac{1}{\sqrt{3}} \quad \frac{1}{\sqrt{3}} \right\}$	$\left\{ \frac{1}{\sqrt{2}} \quad 0 \quad \frac{1}{\sqrt{2}} \right\}$	$\begin{bmatrix} -\frac{1}{\sqrt{6}} & -\frac{1}{\sqrt{6}} & \frac{1}{\sqrt{6}} \\ 0 & 0 & 0 \\ -\frac{1}{\sqrt{6}} & -\frac{1}{\sqrt{6}} & \frac{1}{\sqrt{6}} \end{bmatrix}$	$\frac{1}{\sqrt{6}}$	$\dot{\gamma}_1$
12	$\left\{ -\frac{1}{\sqrt{3}} \quad -\frac{1}{\sqrt{3}} \quad \frac{1}{\sqrt{3}} \right\}$	$\left\{ -\frac{1}{\sqrt{2}} \quad \frac{1}{\sqrt{2}} \quad 0 \right\}$	$\begin{bmatrix} \frac{1}{\sqrt{6}} & \frac{1}{\sqrt{6}} & -\frac{1}{\sqrt{6}} \\ -\frac{1}{\sqrt{6}} & -\frac{1}{\sqrt{6}} & \frac{1}{\sqrt{6}} \\ 0 & 0 & 0 \end{bmatrix}$	0	0

Table C.3: Values of $\mathbf{S}_o^\alpha$ and $\dot{\gamma}^\alpha$ for the $\langle 011 \rangle$ orientation

$$[011]: \quad \phi = 0, \quad \theta = -45^o, \quad \omega = 0 \qquad \mathbf{Q} = \begin{bmatrix} 1 & 0 & 0 \\ 0 & \frac{1}{\sqrt{2}} & -\frac{1}{\sqrt{2}} \\ 0 & \frac{1}{\sqrt{2}} & \frac{1}{\sqrt{2}} \end{bmatrix}$$

α	$\mathbf{n}_o^\alpha = \mathbf{Q}\mathbf{n}_c^\alpha$	$\mathbf{m}_o^\alpha = \mathbf{Q}\mathbf{m}_c^\alpha$	$\mathbf{S}_o^\alpha = \mathbf{m}_o^\alpha \otimes \mathbf{n}_o^\alpha$	m^α	$\dot{\gamma}^\alpha$
1	$\left\{ \frac{1}{\sqrt{3}} \quad 0 \quad \frac{2}{\sqrt{6}} \right\}$	$\left\{ 0 \quad 1 \quad 0 \right\}$	$\begin{bmatrix} 0 & 0 & 0 \\ \frac{1}{\sqrt{3}} & 0 & \frac{2}{\sqrt{6}} \\ 0 & 0 & 0 \end{bmatrix}$	0	0
2	$\left\{ \frac{1}{\sqrt{3}} \quad 0 \quad \frac{2}{\sqrt{6}} \right\}$	$\left\{ -\frac{1}{\sqrt{2}} \quad \frac{1}{2} \quad \frac{1}{2} \right\}$	$\begin{bmatrix} -\frac{1}{\sqrt{6}} & 0 & -\frac{1}{\sqrt{3}} \\ -\frac{1}{2\sqrt{3}} & 0 & -\frac{1}{\sqrt{6}} \\ \frac{1}{2\sqrt{3}} & 0 & \frac{1}{\sqrt{6}} \end{bmatrix}$	$\frac{1}{\sqrt{6}}$	$\dot{\gamma}_2$
3	$\left\{ \frac{1}{\sqrt{3}} \quad 0 \quad \frac{2}{\sqrt{6}} \right\}$	$\left\{ -\frac{1}{\sqrt{2}} \quad -\frac{1}{2} \quad -\frac{1}{2} \right\}$	$\begin{bmatrix} \frac{1}{\sqrt{6}} & 0 & \frac{1}{\sqrt{3}} \\ -\frac{1}{2\sqrt{3}} & 0 & -\frac{1}{\sqrt{6}} \\ -\frac{1}{2\sqrt{3}} & 0 & -\frac{1}{\sqrt{6}} \end{bmatrix}$	$-\frac{1}{\sqrt{6}}$	$-\dot{\gamma}_2$
4	$\left\{ \frac{1}{\sqrt{3}} \quad 0 \quad -\frac{2}{\sqrt{6}} \right\}$	$\left\{ 0 \quad -1 \quad 0 \right\}$	$\begin{bmatrix} 0 & 0 & 0 \\ -\frac{1}{\sqrt{3}} & 0 & \frac{2}{\sqrt{6}} \\ 0 & 0 & 0 \end{bmatrix}$	0	0
5	$\left\{ \frac{1}{\sqrt{3}} \quad 0 \quad -\frac{2}{\sqrt{6}} \right\}$	$\left\{ -\frac{1}{\sqrt{2}} \quad \frac{1}{2} \quad -\frac{1}{2} \right\}$	$\begin{bmatrix} -\frac{1}{\sqrt{6}} & 0 & \frac{1}{\sqrt{3}} \\ \frac{1}{2\sqrt{3}} & 0 & -\frac{1}{\sqrt{6}} \\ -\frac{1}{2\sqrt{3}} & 0 & \frac{1}{\sqrt{6}} \end{bmatrix}$	$\frac{1}{\sqrt{6}}$	$\dot{\gamma}_2$
6	$\left\{ \frac{1}{\sqrt{3}} \quad 0 \quad -\frac{2}{\sqrt{6}} \right\}$	$\left\{ \frac{1}{\sqrt{2}} \quad \frac{1}{2} \quad \frac{1}{2} \right\}$	$\begin{bmatrix} \frac{1}{\sqrt{6}} & 0 & -\frac{1}{\sqrt{3}} \\ \frac{1}{2\sqrt{3}} & 0 & -\frac{1}{\sqrt{6}} \\ \frac{1}{2\sqrt{3}} & 0 & -\frac{1}{\sqrt{6}} \end{bmatrix}$	$-\frac{1}{\sqrt{6}}$	$-\dot{\gamma}_2$
7	$\left\{ -\frac{1}{\sqrt{3}} \quad \frac{2}{\sqrt{6}} \quad 0 \right\}$	$\left\{ 0 \quad 0 \quad 1 \right\}$	$\begin{bmatrix} 0 & 0 & 0 \\ 0 & 0 & 0 \\ -\frac{1}{\sqrt{3}} & \frac{2}{\sqrt{6}} & 0 \end{bmatrix}$	0	0
8	$\left\{ -\frac{1}{\sqrt{3}} \quad \frac{2}{\sqrt{6}} \quad 0 \right\}$	$\left\{ \frac{1}{\sqrt{2}} \quad \frac{1}{2} \quad -\frac{1}{2} \right\}$	$\begin{bmatrix} -\frac{1}{\sqrt{6}} & \frac{1}{\sqrt{3}} & 0 \\ -\frac{1}{2\sqrt{3}} & \frac{1}{\sqrt{6}} & 0 \\ \frac{1}{2\sqrt{3}} & -\frac{1}{\sqrt{6}} & 0 \end{bmatrix}$	0	0
9	$\left\{ -\frac{1}{\sqrt{3}} \quad \frac{2}{\sqrt{6}} \quad 0 \right\}$	$\left\{ -\frac{1}{\sqrt{2}} \quad -\frac{1}{2} \quad -\frac{1}{2} \right\}$	$\begin{bmatrix} \frac{1}{\sqrt{6}} & -\frac{1}{\sqrt{3}} & 0 \\ \frac{1}{2\sqrt{3}} & -\frac{1}{\sqrt{6}} & 0 \\ \frac{1}{2\sqrt{3}} & -\frac{1}{\sqrt{6}} & 0 \end{bmatrix}$	0	0
10	$\left\{ -\frac{1}{\sqrt{3}} \quad -\frac{2}{\sqrt{6}} \quad 0 \right\}$	$\left\{ 0 \quad 0 \quad -1 \right\}$	$\begin{bmatrix} 0 & 0 & 0 \\ 0 & 0 & 0 \\ \frac{1}{\sqrt{3}} & \frac{2}{\sqrt{6}} & 0 \end{bmatrix}$	0	0
11	$\left\{ -\frac{1}{\sqrt{3}} \quad -\frac{2}{\sqrt{6}} \quad 0 \right\}$	$\left\{ \frac{1}{\sqrt{2}} \quad -\frac{1}{2} \quad \frac{1}{2} \right\}$	$\begin{bmatrix} -\frac{1}{\sqrt{6}} & -\frac{1}{\sqrt{2}} & 0 \\ \frac{1}{2\sqrt{3}} & \frac{1}{\sqrt{6}} & 0 \\ -\frac{1}{2\sqrt{3}} & -\frac{1}{\sqrt{6}} & 0 \end{bmatrix}$	0	0
12	$\left\{ -\frac{1}{\sqrt{3}} \quad -\frac{2}{\sqrt{6}} \quad 0 \right\}$	$\left\{ -\frac{1}{\sqrt{2}} \quad \frac{1}{2} \quad \frac{1}{2} \right\}$	$\begin{bmatrix} \frac{1}{\sqrt{6}} & \frac{1}{\sqrt{3}} & 0 \\ -\frac{1}{2\sqrt{3}} & -\frac{1}{\sqrt{6}} & 0 \\ -\frac{1}{2\sqrt{3}} & -\frac{1}{\sqrt{6}} & 0 \end{bmatrix}$	0	0

Table C.4: Values of $\mathbf{S}_o^\alpha$ and $\dot{\gamma}^\alpha$ for the $\langle 111 \rangle$ orientation

$\phi = 45^o$

$[\bar{1}11]: \ \theta = -54.7^o$

$\omega = 0$

$$\mathbf{Q} = \begin{bmatrix} \frac{1}{\sqrt{2}} & \frac{1}{\sqrt{2}} & 0 \\ -\frac{1}{\sqrt{6}} & \frac{1}{\sqrt{6}} & -\frac{2}{\sqrt{6}} \\ -\frac{1}{\sqrt{3}} & \frac{1}{\sqrt{3}} & \frac{1}{\sqrt{3}} \end{bmatrix}$$

α	$\mathbf{n}_o^\alpha = \mathbf{Q}\mathbf{n}_c^\alpha$	$\mathbf{m}_o^\alpha = \mathbf{Q}\mathbf{m}_c^\alpha$	$\mathbf{S}_o^\alpha = \mathbf{m}_o^\alpha \otimes \mathbf{n}_o^\alpha$	m^α	$\dot{\gamma}^\alpha$
1	$\left\{ \frac{2}{\sqrt{6}} \ -\frac{2}{3\sqrt{2}} \ \frac{1}{3} \right\}$	$\left\{ \frac{1}{2} \ \frac{3}{2\sqrt{3}} \ 0 \right\}$	$\begin{bmatrix} \frac{1}{\sqrt{6}} & -\frac{1}{3\sqrt{2}} & \frac{1}{6} \\ \frac{1}{\sqrt{2}} & -\frac{1}{\sqrt{6}} & \frac{1}{2\sqrt{3}} \\ 0 & 0 & 0 \end{bmatrix}$	0	0
2	$\left\{ \frac{2}{\sqrt{6}} \ -\frac{2}{3\sqrt{2}} \ \frac{1}{3} \right\}$	$\left\{ -\frac{1}{2} \ -\frac{1}{2\sqrt{3}} \ \frac{2}{\sqrt{6}} \right\}$	$\begin{bmatrix} -\frac{1}{\sqrt{6}} & \frac{1}{3\sqrt{2}} & -\frac{1}{6} \\ -\frac{1}{3\sqrt{2}} & \frac{1}{3\sqrt{6}} & -\frac{1}{6\sqrt{3}} \\ \frac{2}{3} & -\frac{2}{3\sqrt{3}} & \frac{2}{3\sqrt{6}} \end{bmatrix}$	$\frac{2}{3\sqrt{6}}$	$\dot{\gamma}_3$
3	$\left\{ \frac{2}{\sqrt{6}} \ -\frac{2}{3\sqrt{2}} \ \frac{1}{3} \right\}$	$\left\{ 0 \ -\frac{1}{\sqrt{3}} \ -\frac{2}{\sqrt{6}} \right\}$	$\begin{bmatrix} 0 & 0 & 0 \\ -\frac{2}{3\sqrt{2}} & \frac{2}{3\sqrt{6}} & -\frac{1}{3\sqrt{3}} \\ -\frac{2}{3} & \frac{2}{3\sqrt{3}} & -\frac{2}{3\sqrt{6}} \end{bmatrix}$	$-\frac{2}{3\sqrt{6}}$	$-\dot{\gamma}_3$
4	$\left\{ 0 \ 0 \ -1 \right\}$	$\left\{ -\frac{1}{2} \ -\frac{3}{2\sqrt{3}} \ 0 \right\}$	$\begin{bmatrix} 0 & 0 & \frac{1}{2} \\ 0 & 0 & \frac{3}{2\sqrt{3}} \\ 0 & 0 & 0 \end{bmatrix}$	0	0
5	$\left\{ 0 \ 0 \ -1 \right\}$	$\left\{ -\frac{1}{2} \ \frac{3}{2\sqrt{3}} \ 0 \right\}$	$\begin{bmatrix} 0 & 0 & \frac{1}{2} \\ 0 & 0 & -\frac{3}{2\sqrt{3}} \\ 0 & 0 & 0 \end{bmatrix}$	0	0
6	$\left\{ 0 \ 0 \ -1 \right\}$	$\left\{ 1 \ 0 \ 0 \right\}$	$\begin{bmatrix} 0 & 0 & -1 \\ 0 & 0 & 0 \\ 0 & 0 & 0 \end{bmatrix}$	0	0
7	$\left\{ 0 \ \frac{4}{3\sqrt{2}} \ \frac{1}{3} \right\}$	$\left\{ \frac{1}{2} \ -\frac{1}{2\sqrt{3}} \ \frac{2}{\sqrt{6}} \right\}$	$\begin{bmatrix} 0 & \frac{2}{3\sqrt{2}} & \frac{1}{6} \\ 0 & -\frac{2}{3\sqrt{6}} & -\frac{1}{6\sqrt{3}} \\ 0 & \frac{4}{3\sqrt{3}} & \frac{2}{3\sqrt{6}} \end{bmatrix}$	$\frac{2}{3\sqrt{6}}$	$\dot{\gamma}_3$
8	$\left\{ 0 \ \frac{4}{3\sqrt{2}} \ \frac{1}{3} \right\}$	$\left\{ \frac{1}{2} \ \frac{1}{2\sqrt{3}} \ -\frac{2}{\sqrt{6}} \right\}$	$\begin{bmatrix} 0 & \frac{2}{3\sqrt{2}} & \frac{1}{6} \\ 0 & \frac{2}{3\sqrt{6}} & \frac{1}{6\sqrt{3}} \\ 0 & -\frac{4}{3\sqrt{3}} & -\frac{2}{3\sqrt{6}} \end{bmatrix}$	$-\frac{2}{3\sqrt{6}}$	$-\dot{\gamma}_3$
9	$\left\{ 0 \ \frac{4}{3\sqrt{2}} \ \frac{1}{3} \right\}$	$\left\{ -1 \ 0 \ 0 \right\}$	$\begin{bmatrix} 0 & -\frac{4}{3\sqrt{2}} & \frac{1}{3} \\ 0 & 0 & 0 \\ 0 & 0 & 0 \end{bmatrix}$	0	0
10	$\left\{ -\frac{2}{\sqrt{6}} \ -\frac{2}{3\sqrt{2}} \ \frac{1}{3} \right\}$	$\left\{ -\frac{1}{2} \ \frac{1}{2\sqrt{3}} \ -\frac{2}{\sqrt{6}} \right\}$	$\begin{bmatrix} \frac{1}{\sqrt{6}} & \frac{1}{3\sqrt{2}} & -\frac{1}{6} \\ -\frac{1}{3\sqrt{2}} & -\frac{1}{3\sqrt{6}} & \frac{1}{6\sqrt{3}} \\ \frac{2}{3} & \frac{2}{3\sqrt{3}} & -\frac{2}{3\sqrt{6}} \end{bmatrix}$	$-\frac{2}{3\sqrt{6}}$	$-\dot{\gamma}_3$
11	$\left\{ -\frac{2}{\sqrt{6}} \ -\frac{2}{3\sqrt{2}} \ \frac{1}{3} \right\}$	$\left\{ \frac{1}{2} \ -\frac{3}{2\sqrt{3}} \ 0 \right\}$	$\begin{bmatrix} -\frac{1}{\sqrt{6}} & -\frac{1}{3\sqrt{2}} & \frac{1}{6} \\ \frac{1}{\sqrt{2}} & \frac{1}{\sqrt{6}} & -\frac{1}{2\sqrt{3}} \\ 0 & 0 & 0 \end{bmatrix}$	0	0
12	$\left\{ -\frac{2}{\sqrt{6}} \ -\frac{2}{3\sqrt{2}} \ \frac{1}{3} \right\}$	$\left\{ 0 \ \frac{1}{\sqrt{3}} \ \frac{2}{\sqrt{6}} \right\}$	$\begin{bmatrix} 0 & 0 & 0 \\ -\frac{2}{3\sqrt{2}} & -\frac{2}{3\sqrt{6}} & \frac{1}{3\sqrt{3}} \\ -\frac{2}{3} & \frac{2}{3\sqrt{3}} & \frac{2}{3\sqrt{6}} \end{bmatrix}$	$\frac{2}{3\sqrt{6}}$	$\dot{\gamma}_3$

Using the numbers in the preceeding tables and equation C.6, we get the following relations for simple tension in the 3-direction:

$$\mathbf{L}^p_{[001]} = \dot{\gamma}_1 \begin{bmatrix} -2\sqrt{\frac{2}{3}} & 0 & 0 \\ 0 & -2\sqrt{\frac{2}{3}} & 0 \\ 0 & 0 & 4\sqrt{\frac{2}{3}} \end{bmatrix}$$

$$\mathbf{L}^p_{[011]} = \dot{\gamma}_2 \begin{bmatrix} -2\sqrt{\frac{2}{3}} & 0 & 0 \\ 0 & 0 & 0 \\ 0 & 0 & 2\sqrt{\frac{2}{3}} \end{bmatrix} \qquad \text{(C.7)}$$

$$\mathbf{L}^p_{[\bar{1}11]} = \dot{\gamma}_3 \begin{bmatrix} -\sqrt{\frac{2}{3}} & 0 & 0 \\ 0 & -\sqrt{\frac{2}{3}} & 0 \\ 0 & 0 & 2\sqrt{\frac{2}{3}} \end{bmatrix}$$

giving $k_{[001]} = 4\sqrt{\frac{2}{3}}$, $k_{[011]} = 2\sqrt{\frac{2}{3}}$, $k_{[\bar{1}11]} = 2\sqrt{\frac{2}{3}}$. Rearranging equation C.2, substituting $\frac{\tau^\alpha}{\bar{\sigma}} = m^\alpha$ (where m^α is the Schmid factor of slip system α), and using the values from Table C.1 yields (T≡tension, C≡compression):

$$\begin{aligned}
[001]\ \mathrm{T}: \quad & 1 + \left(\tfrac{1}{3\sqrt{2}}\right)\beta_1 + (0)\beta_2 &&= \left[\tau^\alpha_{[001],T}\left(\frac{4\sqrt{\frac{2}{3}}\dot{\gamma}_o}{\dot{\epsilon}}\right)^m\right]\frac{1}{s_o} \\
[001]\ \mathrm{C}: \quad & 1 + \left(-\tfrac{1}{3\sqrt{2}}\right)\beta_1 + (0)\beta_2 &&= \left[\tau^\alpha_{[001],C}\left(\frac{4\sqrt{\frac{2}{3}}\dot{\gamma}_o}{\dot{\epsilon}}\right)^m\right]\frac{1}{s_o} \\
[011]\ \mathrm{T}: \quad & 1 + \left(-\tfrac{1}{3\sqrt{2}}\right)\beta_1 + \left(\tfrac{1}{2\sqrt{2}}\right)\beta_2 &&= \left[\tau^\alpha_{[011],T}\left(\frac{2\sqrt{\frac{2}{3}}\dot{\gamma}_o}{\dot{\epsilon}}\right)^m\right]\frac{1}{s_o} \\
[011]\ \mathrm{C}: \quad & 1 + \left(\tfrac{1}{3\sqrt{2}}\right)\beta_1 + \left(\tfrac{1}{2\sqrt{2}}\right)\beta_2 &&= \left[\tau^\alpha_{[011],C}\left(\frac{2\sqrt{\frac{2}{3}}\dot{\gamma}_o}{\dot{\epsilon}}\right)^m\right]\frac{1}{s_o} \qquad \text{(C.8)} \\
[\bar{1}11]\ \mathrm{T}: \quad & 1 + \left(-\tfrac{2}{9\sqrt{2}}\right)\beta_1 + \left(\tfrac{2}{3\sqrt{2}}\right)\beta_2 &&= \left[\tau^\alpha_{[\bar{1}11],T}\left(\frac{2\sqrt{\frac{2}{3}}\dot{\gamma}_o}{\dot{\epsilon}}\right)^m\right]\frac{1}{s_o} \\
[\bar{1}11]\ \mathrm{C}: \quad & 1 + \left(\tfrac{2}{9\sqrt{2}}\right)\beta_1 + \left(\tfrac{2}{3\sqrt{2}}\right)\beta_2 &&= \left[\tau^\alpha_{[\bar{1}11],C}\left(\frac{2\sqrt{\frac{2}{3}}\dot{\gamma}_o}{\dot{\epsilon}}\right)^m\right]\frac{1}{s_o}
\end{aligned}$$

where $\tau^\alpha_{[001],T}, \ldots, \tau^\alpha_{[\bar{1}11],C}$ are the resolved shear stresses at yield for the six cases described. These are obtained from experimental data. The above are six linear equations in the

three variables β_1, β_2 and s_o. In principle, given the experimental data, any combination of three of the above equations may be solved for these variables, and simulations with these parameter values should predict the yield stress for other orientations. For example, rewriting the first three equations for the [001] and [011] orientations in matrix form yields the following equation, where all of the coefficients in the matrix are known:

$$\begin{bmatrix} -\frac{1}{3\sqrt{2}} & 0 & \tau^{\alpha}_{[001],T}\left(\frac{4\sqrt{\frac{2}{3}}\dot{\gamma}_o}{\dot{\epsilon}}\right)^m \\ \frac{1}{3\sqrt{2}} & 0 & \tau^{\alpha}_{[001],C}\left(\frac{4\sqrt{\frac{2}{3}}\dot{\gamma}_o}{\dot{\epsilon}}\right)^m \\ \frac{1}{3\sqrt{2}} & -\frac{1}{2\sqrt{2}} & \tau^{\alpha}_{[011],T}\left(\frac{2\sqrt{\frac{2}{3}}\dot{\gamma}_o}{\dot{\epsilon}}\right)^m \end{bmatrix} \begin{Bmatrix} \beta_1 \\ \beta_2 \\ \frac{1}{s_o} \end{Bmatrix} = \begin{Bmatrix} 1 \\ 1 \\ 1 \end{Bmatrix} \qquad \text{(C.9)}$$

C.3 Determination of Model Parameters and Match to Experimental Data

The following section describes the method for obtaining these parameter values and predicting the outputs for other orientations. Data was selected if there was both tension *and* compression for a few orientations including *at least* two of the corner orientations ([001], [011] or [$\bar{1}$11]).

Heredia [1990] performed tension and compression tests on binary Ni_3Al and $Ni_3(Al,X)$ with several different ternary additions at a strain rate of $\dot{\epsilon} = \pm 1.3 \times 10^{-3}$/sec in a few different orientations from temperatures of 77 to 1400K. Figure C-2 [Heredia, 1990] shows the temperature dependence of the critical resolved shear stress (CRSS) on the octahedral slip systems for binary Ni_3Al and Ni_3Al+1%B in tension and compression. In the present study simulations were performed in ABAQUS with the model developed here using a single C3D8 3-dimensional, 8-noded element. The element was deformed in the 3-direction at a constant true strain rate of $\dot{\epsilon} = \pm 1.3 \times 10^{-3}$/sec just to yield. Different orientations, given by their Miller indices (hkl), were represented by a set of Euler angles, (ϕ, θ, ω) which rotate the [hkl] axis of the crystal into alignment with the [001] global axis [Hirth and Lothe, 198 . The yield stress was taken as the stress corresponding to 0.2% plastic strain.

A temperature of 295K was chosen, as it is well below the peak in the yield stress versus temperature curve (Figure C-2), so cube slip systems should not be active. In the simulations, the cube slip systems are deactivated by setting the slip system resistance on those slip systems to be significantly higher than that on the octahedral slip systems,

approximately one order of magnitude.

The Ni_3Al+ 1%B at 295K was simulated since the asymmetry is more pronounced than in the binary Ni_3Al, and because there was data for an orientation near $[\bar{1}11]$. The experimental data for orientation $1(\approx [001])$ in tension and orientation $5(\approx [\bar{1}11])$ in tension and compression (equation C.8-1,5,6) were used with $\dot{\gamma}_o = 1.0 \times 10^{-2}$/sec and $m = 0.05$ in solving equation C.9 giving para- . values:

$$\beta_1 = \quad ' \quad = .0082, s_o = 191.678\text{MPa}$$

Although the model is rate dependent, calculation of a strain rate senstivity parameter m requires data at more than one strain rate. This was not available for this material, so the value obtained experimetnally in this study was also used for these simulations. Since orientations 1 and 5 were not exactly on the corners, some minor iteration was necessary in the parameter values to improve the fit to the experiments. The other orientations for which experimental data was available were also simulated with these parameter values. The results are summarized in Table C.5 with the experimental values and the corresponding simulations. The predictions are generally in excellent agreement with the experiments.

The values of β_1, β_2 and s_o obtained above were also used to simulate a grid of orientations covering the stereographic triangle to predict the complete orientation dependence of yield stress at this temperature. Figure C-3(a) shows the results of the tension simulations with the five experimental data points included, while Figure C-3(b) shows those for compression. As noted earlier, the agreement between the experiments and simulations is quite good. Additionally, we get predictions for the other orientations in the stereographic triangle. In both tension and compression, the $[\bar{1}11]$ orientation has the highest yield strength, with the greatest tension/compression asymmetry occurring at the [001] corner (Figure C-4).

This exercise may easily be repeated at any other *constant* temperature, giving parameter values at that temperature Above the peak temperature, cube slip systems become active, requiring the additional model parameter s_{oc}, the slip system resistance on the cube slip systems.

Isothermal data from the paper of Shah and Duhl [1984] for PWA 1480 at 593°C were also simulated using this model. Simple tension and compression tests were done at a strain

Table C.5: Heredia data on Ni_3Al+1%B at T=295K, and Finite Element simulations

$$\beta_1 = .4311, \beta_2 = .0082, s_o = 191.678\text{MPa}$$

Test‡	Miller Indicies (hkl)	Euler Angles (ϕ, θ, ω)(deg)	$\lvert\sigma_y\rvert_T(MPa)$		$\lvert\sigma_y\rvert_C(MPa)$	
			Expt.	Sim.	Expt.	Sim.
−*	0 0 1	0 0 0	− − −	443	− − −	356
1	$\bar{1}$ 3.4 35.5	16.390 −5.701 0	421†	424	387	348
2	$\bar{1}$ 2.6 9.3	21.038 −16.675 0	399	382	356	350
3	$\bar{1}$ 3.7 11.3	15.124 −18.736 0	335	375	357	353
4	$\bar{1}$ 8.8 10.2	6.483 −40.968 0	394	376	460	458
5	$\bar{1}$ 1.4 1.5	35.538 −48.916 0	485†	487	552†	551
−*	0 1 1	0 −45 0	− − −	374	− − −	455
−*	$\bar{1}$ 1 1	45 −54.736 0	− − −	583	− − −	662

‡ Test numbers correspond to orientations tested. These are shown again in the following stereographic triangle.

* Corner orientations of stereographic triangle

† Experiments used to determine model parameters

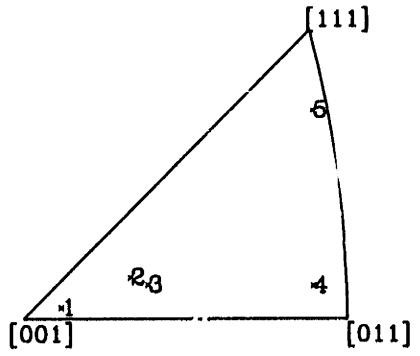

rate of $\dot{\epsilon} = \pm 5. \times 10^{-3}$/min. The same methodology was used to fit the model parameters by matching three of the data points at corners of the stereographic triangle. Here a two-phase material is treated like single phase γ' in the simulations. Figure C-5 shows the experiment and simulation using the parameters obtained by solving for the yield stress in the [011] orientation in tension and in compression as well as the [001] orientation in tension (equation C.8-1,3,4) as tabulated in Table C.6, giving values:

$$\beta_1 = 0.1444, \beta_2 = -0.4285, s_o = 648.043\text{MPa}$$

The match between experiments and simulations is fairly good along the [001] – [011] boundary, but the two diverge as the $[\bar{1}11]$ orientation is approached. This is due to the activity on the cube slip systems at this temperature. This was remedied by allowing slip on the cube slip systems. Trial and error fitting of the $[\bar{1}11]$ data was used to determine s_{oc}, the slip system resistance of the cube slip systems. A good fit necessitated changing one of the previously obtained parameters giving finally:

$$\beta_1 = 0.1700, \beta_2 = -0.4285, s_o = 648.043\text{MPa}, s_{oc} = 553.0\text{MPa}$$

The predictions are significantly improved, showing the importance of cube slip in the deformation. For comparison the results are replotted with the simulation with and without cube slip on the same graph, Figure C-7. As expected, the addition of cube slip affects the orientations in the portion of the stereographic triangle closer to $[\bar{1}11]$. The yield stresses along the [001] – [011] boundary and over some area of the triangle nearby are practically unaffected. The tension and compression data are replotted on the same graph for the case where cube slip is included in Figure C-8.

These experiments were also simulated by solving for the yield stress in the [011] orientation in tension and in compression as well as the [111] orientation in compression (equation C.8-3,4,6). Some of the predictions in this case are quite far off, especially near the [001] orientation (Table C.7) verifying that considering only the octahedral slip systems is not adequate for this temperature. Comparison of the relative magnitudes of the yield stresses at $[\bar{1}11]$ and at [001] or [011] for the data of Heredia at 295K (Table C.5), by contrast, indicates that the cube slip systems are not active at this temperature.

Table C.6: Shah and Duhl data on PWA1480 at T=593C, and Finite Element simulations

(a) Tension

$\beta_1 = 0.1700, \beta_2 = -0.4285, s_o$=648.043 MPa, s_{oc}=553.0 MPa

Test	Euler Angles (ϕ, θ, ω)(deg)			$\lvert\sigma_y\rvert_T(MPa)$		
				Expt.	Sim.$_{nocube}$	Sim.$_{cube}$
−*	0	0	0	− − −	1239	1246
1	45.000	−1.940	0	1220†	1227	1234
2	41.889	−5.192	0	1165	1183	1189
3	0.000	−4.517	0	1131	1182	1188
4	0.000	−8.349	0	1096	1106	1112
5	5.548	−13.332	0	979	1026	1030
6	6.113	−23.526	0	965	945	949
7	11.067	−33.117	0	917	955	941
8	7.438	−35.918	0	903	966	954
9	2.177	−40.116	0	910	999	989
10	2.034	−42.881	0	924	1003	993
11*	0.000	−45.000	0	993†	1001	992
12	26.128	−30.448	0	897	1037	955
13	33.419	−37.539	0	814	1108	914
14	29.675	−40.111	0	883	1058	910
15	33.325	−42.040	0	862	1105	900
16	34.796	−48.086	0	827	1138	900
17	39.303	−46.788	0	883	1228	895
18	41.889	−51.161	0	896	1332	907
−*	45.000	−54.736	0	− − −	1428	912

* Corner orientations of stereographic triangle

† Experiments used to determine model parameters, see also next table

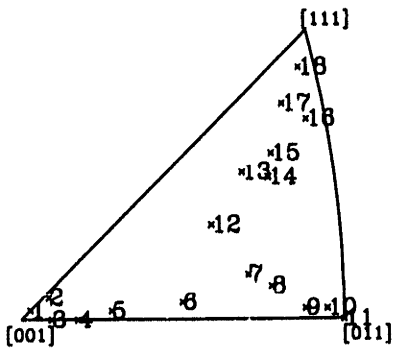

(b) Compression

$\beta_1 = 0.0700, \beta_2 = -.2755, s_o = 609.208\text{MPa}, s_{oc} = 552.0\text{MPa}$

Test	Euler Angles (ϕ, θ, ω)(deg)			$\lvert\sigma_y\rvert_C(MPa)$		
				Expt.	Sim._{nocube}	Sim._{cube}
1	45.000	−3.221	0	1054	1091	1084
2	45.000	−7.114	0	1041	1047	1042
3	3.472	−5.557	0	986	1050	1044
4	3.704	−10.171	0	924	984	979
5	0.000	−20.162	0	896	917	916
6	4.435	−27.741	0	903	939	942
7	1.303	−35.191	0	979	1004	1001
8*	0.000	0.000	0	979	1112	1105
9	7.037	−44.233	0	993	1038	1031
10	2.715	−45.011	0	1165	1059	1060
11*	0.000	−45.000	0	1076†	1066	1067
12	25.542	−32.489	0	951	1061	948
13	36.561	−37.409	0	979	1192	899
14	32.770	−40.998	0	965	1147	898
15	38.914	−43.403	0	1027	1247	878
16	34.470	−47.436	0	945	1181	892
17	39.925	−47.257	0	924	1292	886
18*	45.000	−54.736	0	903	1488	903

* Corner orientations of stereographic triangle

† Experiments used to determine model parameters, see also previous table

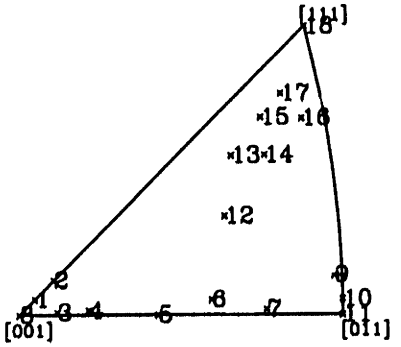

Table C.7: Finite Element simulations fit to one of [111] experiments with no cube slip

$\beta_1 = 0.0729, \beta_2 = -1.6168, s_o = 1283.66\text{MPa}$

Test	$\lvert\sigma_y\rvert_T(MPa)$		$\lvert\sigma_y\rvert_C(MPa)$	
	Expt.	Sim.	Expt.	Sim.
[001]	− − −	2444	979	2176
[011]	993	1001	1076	1066
[111]	− − −	824	903	899
1	1220	2384	1054	2066
2	1165	2182	1041	1852
3	1131	2171	986	1877
4	1096	1860	924	1583
5	979	1539	896	1168
6	965	1136	903	1028
7	917	893	979	991
8	903	880	979	2176
9	910	943	993	899
10	924	955	1165	1024
11	993†	1001	1076†	1066
12	897	890	951	900
13	814	648	979	783
14	883	639	965	716
15	862	612	1027	693
16	827	578	945	647
17	883	574	924	689
18	896	566	903†	899

† Experiments used to determine model parameters

C.4 Prediction of Shape Change in Simple Compression

Dalal *et al.* [1984] performed creep experiments to high strains on single crystals of a nickel-based superalloy SC 7-14-6 in the ⟨001⟩, ⟨011⟩, ⟨111⟩ and ⟨112⟩ orientations. Figure C-9, [Dalal *et al.*, 1984], shows the cross-sections of their deformed specimens after creep to large strain. Some ovalization of the cross-section is observed for the ⟨011⟩ and ⟨112⟩ specimens but not for the ⟨001⟩ or the ⟨111⟩.

In an attempt to verify these macroscopic results qualitatively, compression simulations were performed on similarly oriented single crystal specimens at a constant true strain rate of -0.001/sec to a final strain of 50%. The model parameters used were those obtained for PWA1480 at 593°C in the previous section, [Shah and Duhl, 1984], when both tension-compression asymmetry and cube slip were incorporated. The values were:

$$\beta_1 = 0.1700, \beta_2 = -0.4285, s_o = 648.043\text{MPa}, s_{oc} = 553.0\text{MPa}$$

The finite element mesh used was a cylinder consisting of 40 equally sized C3D6 6-noded elements, Figure C-10. From equations C.7 for $\mathbf{L}^p$ in the different orientations, we see that the ⟨001⟩ and ⟨111⟩ orientations should undergo simple compression with uniform enlargement of the cross-section, since in both cases $L^p_{11} = L^p_{22}$. Figure C-11 shows that this is indeed the case. For the ⟨011⟩ orientation, we expect the deformation of the ⟨011⟩-oriented specimen to be plane strain, i.e. no deformation in the 2-direction ($L^p_{22} = 0$) and expansion in the 3-direction, resulting in an oval cross-section. As Figure C-11 shows, the cross-section does ovalize, but there is also some rotation of the mesh.

Performing the same simple approximate calculation of the plastic velocity gradient for the ⟨112⟩ orientation, and taking account of the fact that the resolved shear stresses are not the same on all active slip systems for this orientation (Table C.8), we obtain

$$\mathbf{L}^p_{[112]} = \dot{\gamma}_2 \begin{bmatrix} -\frac{4}{9} & 0 & 0 \\ 0 & -\frac{2}{9} & -\frac{4}{9\sqrt{2}} \\ 0 & -\frac{4}{9\sqrt{2}} & \frac{2}{3} \end{bmatrix} \qquad \text{(C.10)}$$

Since $L_{11} \neq L_{22}$, we again expect to see some ovalization of the cross-section. Furthermore, since there are some non-zero off-diagonal terms to the matrix $\mathbf{L}$, namely L_{23} and L_{32}, we also expect some shearing of the mesh, which indeed takes place, but again accompanied

Table C.8: Schmid factors for octahedral slip systems for the ⟨112⟩ orientation

α	1	2	3	4	5	6	7	8	9	10	11	12
$m^{\alpha}_{[112]}$	$-\frac{2}{3\sqrt{6}}$	$\frac{2}{3\sqrt{6}}$	0	$-\frac{1}{3\sqrt{6}}$	$\frac{1}{\sqrt{6}}$	$-\frac{2}{3\sqrt{6}}$	$-\frac{1}{\sqrt{6}}$	$\frac{1}{3\sqrt{6}}$	$\frac{2}{3\sqrt{6}}$	0	0	0

by rotation.

As stated previously, the calculation of the plastic velocity gradient $\mathbf{L}^p$ is approximate. It takes into account only primary slip on the octahedral slip systems. Considerations of cube slip and of the tension-compression asymmetry terms are neglected. This is believed to be the reason for the discrepancy between the expected and the calculated final shapes of the meshes. The calculations of compression in all four orientations were repeated without the asymmetry, that is, β_1 and β_2 were set to zero. This time, the rotation of the mesh in the ⟨011⟩ and ⟨112⟩ orientations is not observed, as seen by the final cross-sections of the meshes in these orientations, Figure C-12. The contribution of the tension-compression asymmetry to the rotation of the lattice is confirmed by calculating the final texture Kalidindi *et al.* [1992]. Figures C-13 through C-16 show the initial and the final calculated ⟨111⟩, ⟨110⟩, and ⟨100⟩ pole figures at 50% strain with and without asymmetry for each of the four orientations simulated. The difference in the two cases is clearly seen. In the ⟨011⟩ and ⟨112⟩ orientations there is definite rotation of the pole figure in the case where the asymmetry is added.

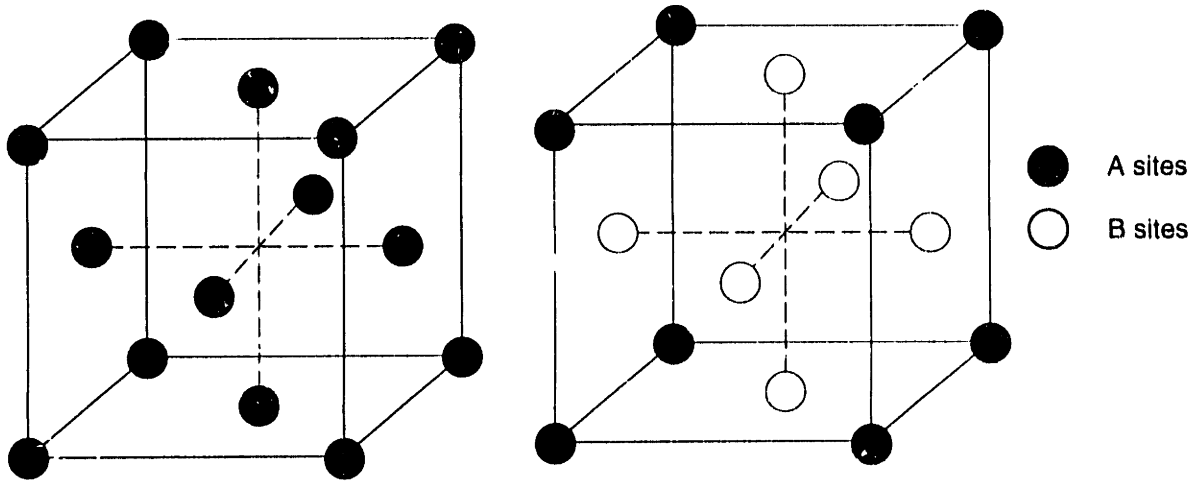

Figure C-1: The fcc unit cell and the $L1_2$ unit cell of AB_3 compounds

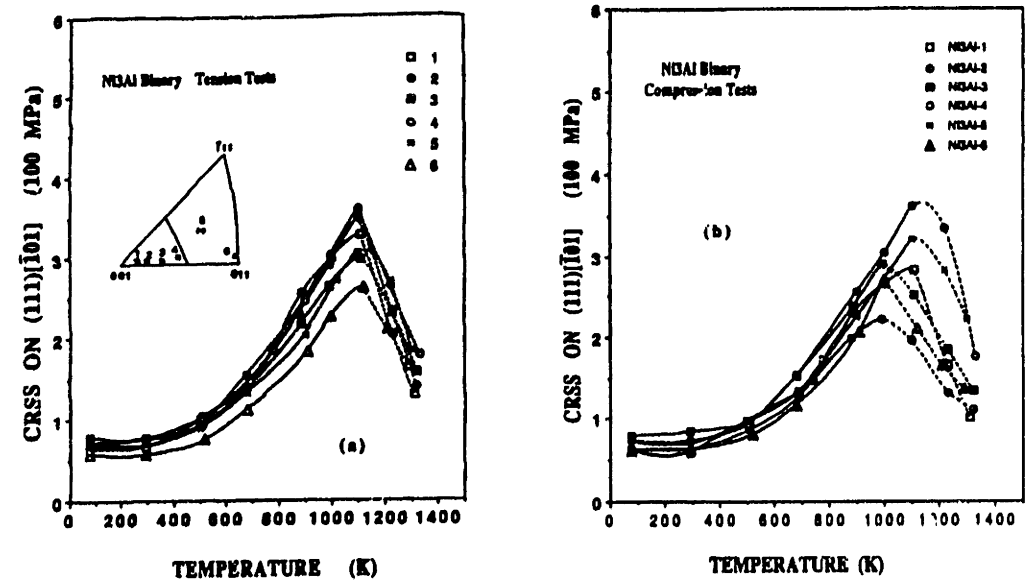

(a)

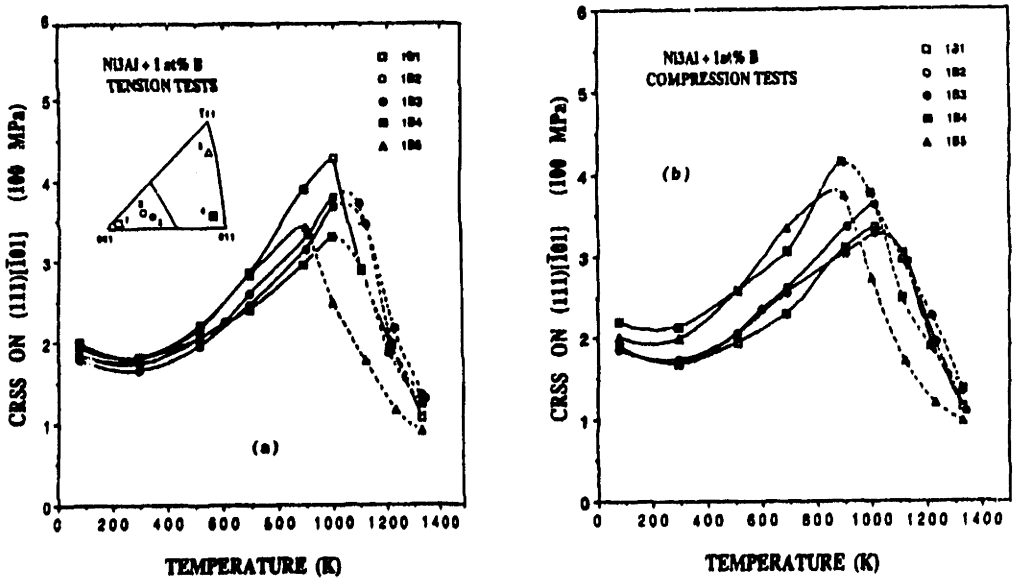

(b)

Figure C-2: Data of Heredia. (a) Binary Ni_3Al (b) Ni_3Al+1%B [Heredia, 1990]

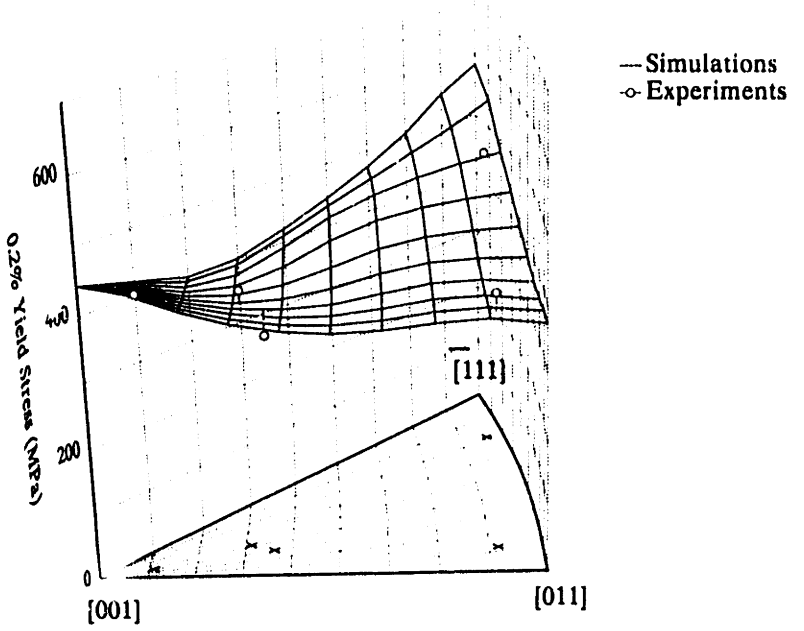

(a)

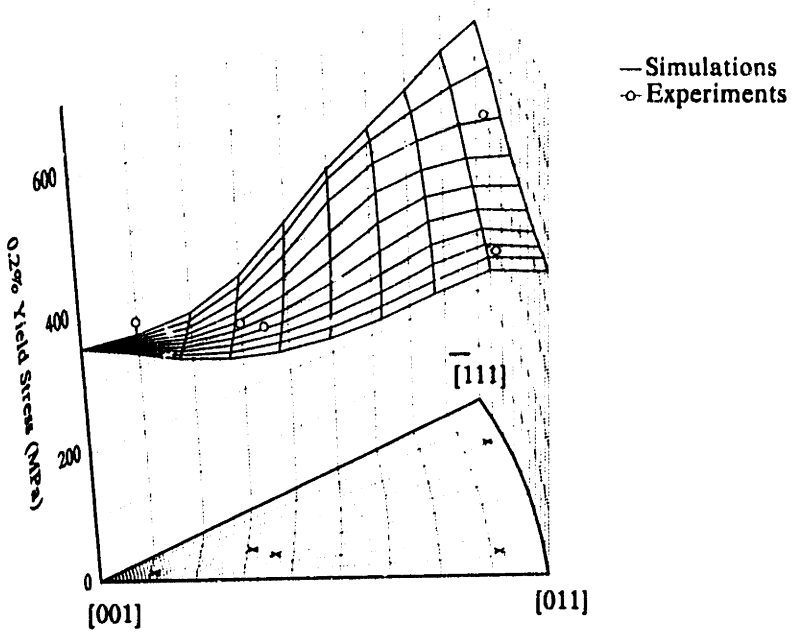

(b)

Figure C-3: Finite Element simulations of Ni_3Al+1%B yield stress vs. orientation at 295K (a) Tension (b) Compression

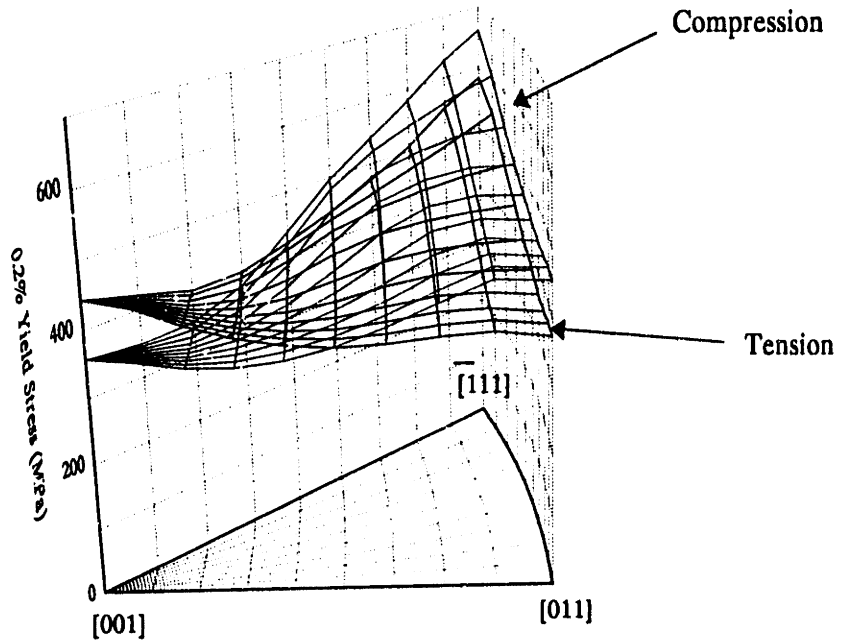

Figure C-4: Tension and compression FE simulations of Ni_3Al+1%B yield stress vs. orientation at 295K

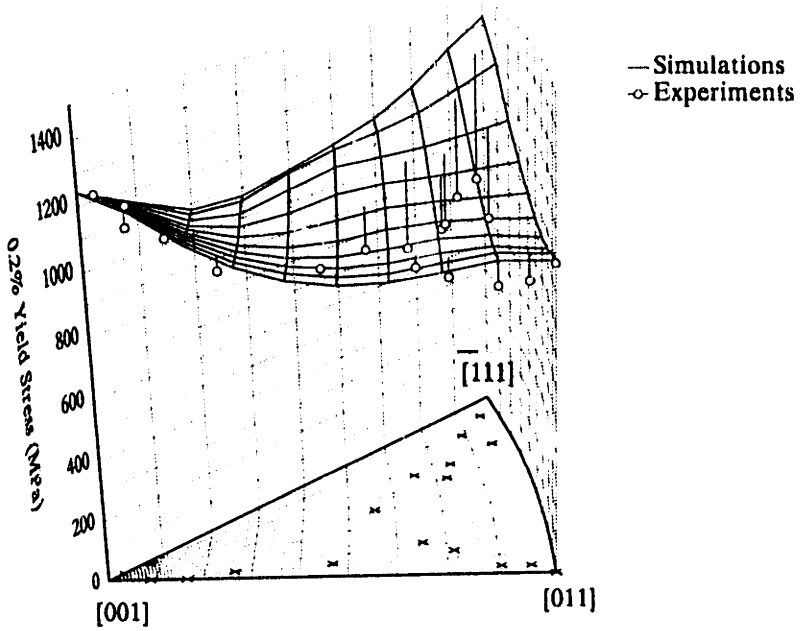

(a)

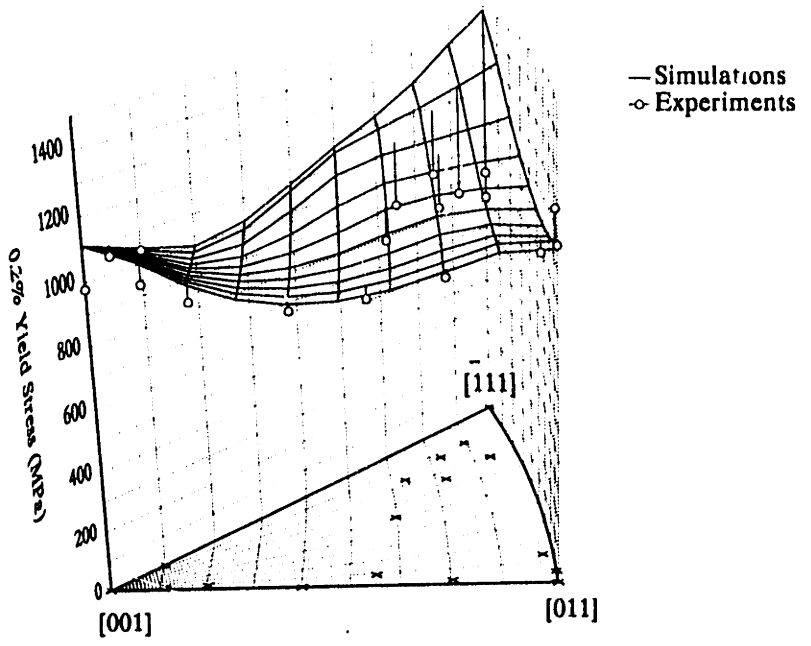

(b)

Figure C-5: Finite element simulations of PWA1480 yield stress vs. orientation at 593°C - no cube slip (a) Tension (b) Compression

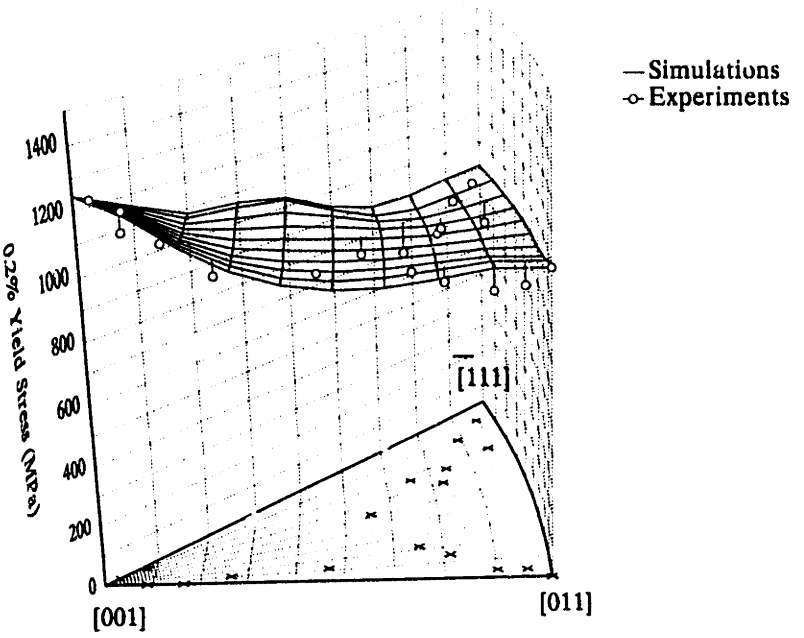

(a)

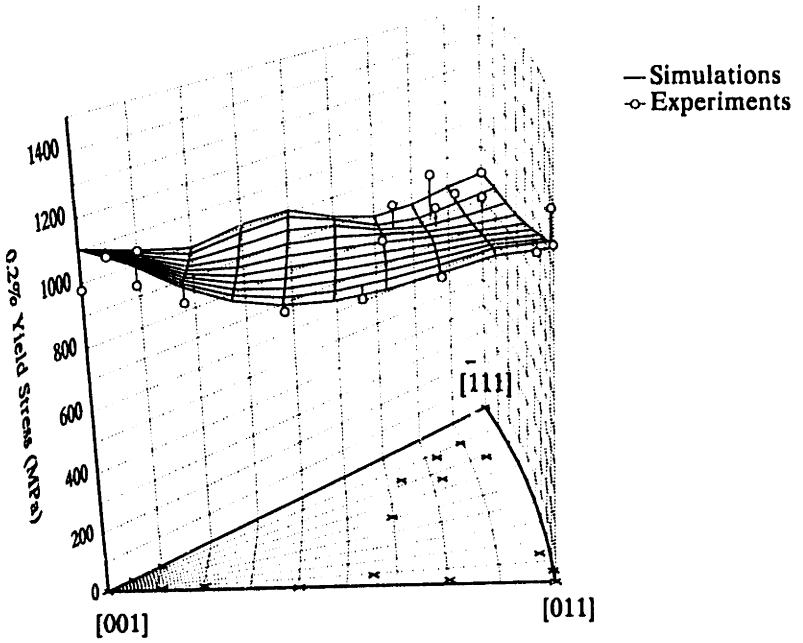

(b)

Figure C-6: Finite Element simulations of PWA1480 yield stress vs. orientation at 593°C – cube slip (a) Tension (b) Compression

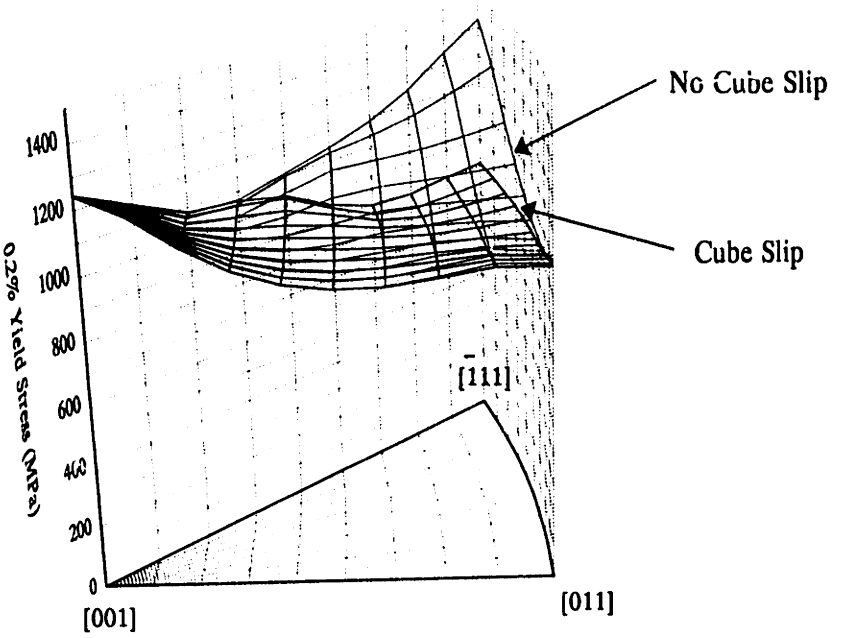

(a)

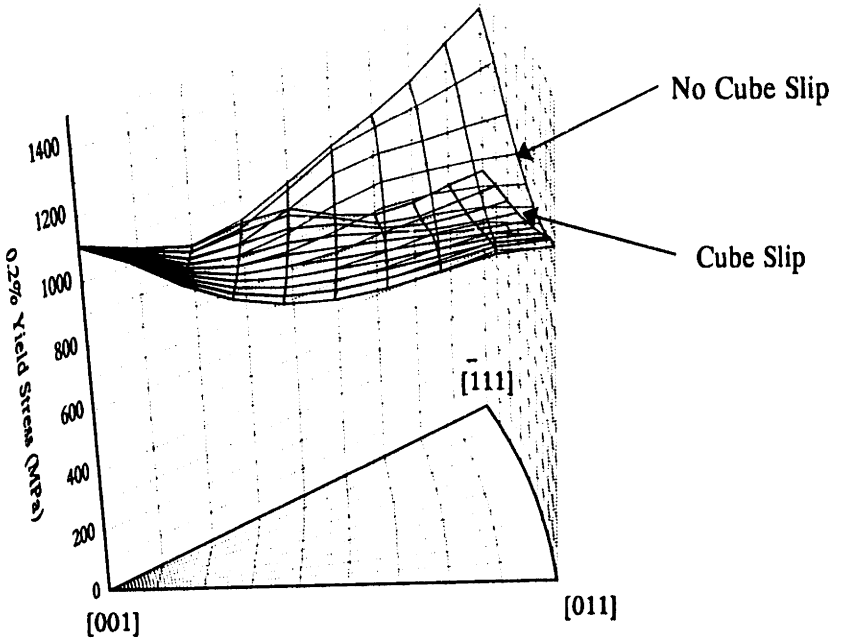

(b)

Figure C-7: Simulations of PWA1480 at 593°C with cube slip and with no cube slip (a) Tension (b) Compression

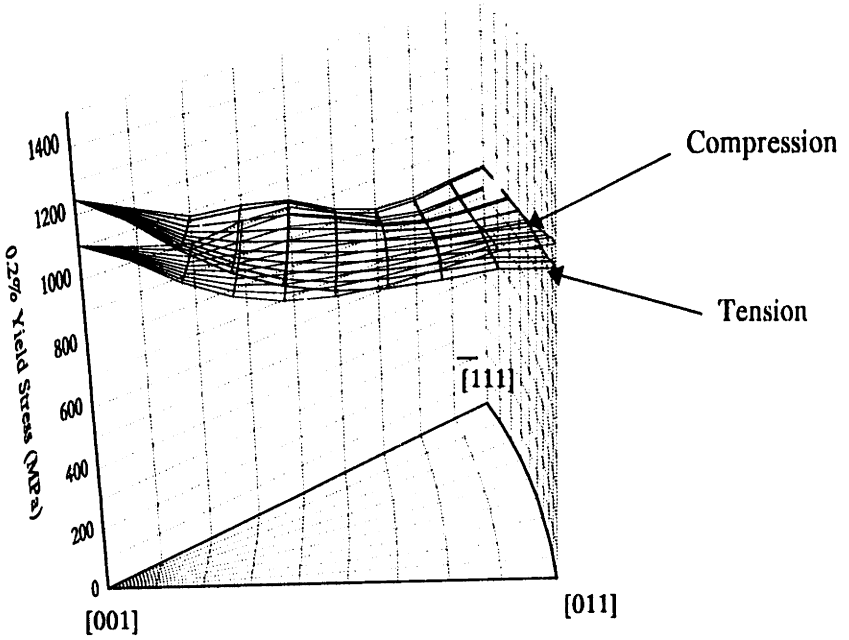

Figure C-8: Tension and compression FE simulations of PWA1480 yield stress vs. orientation at 593°C

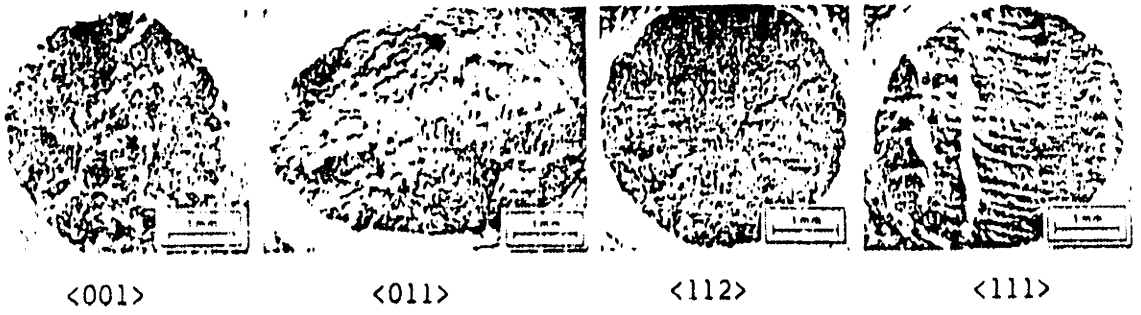

Figure C-9: Cross-sections of specimens after creep fracture [Dalal *et al.*, 1984]

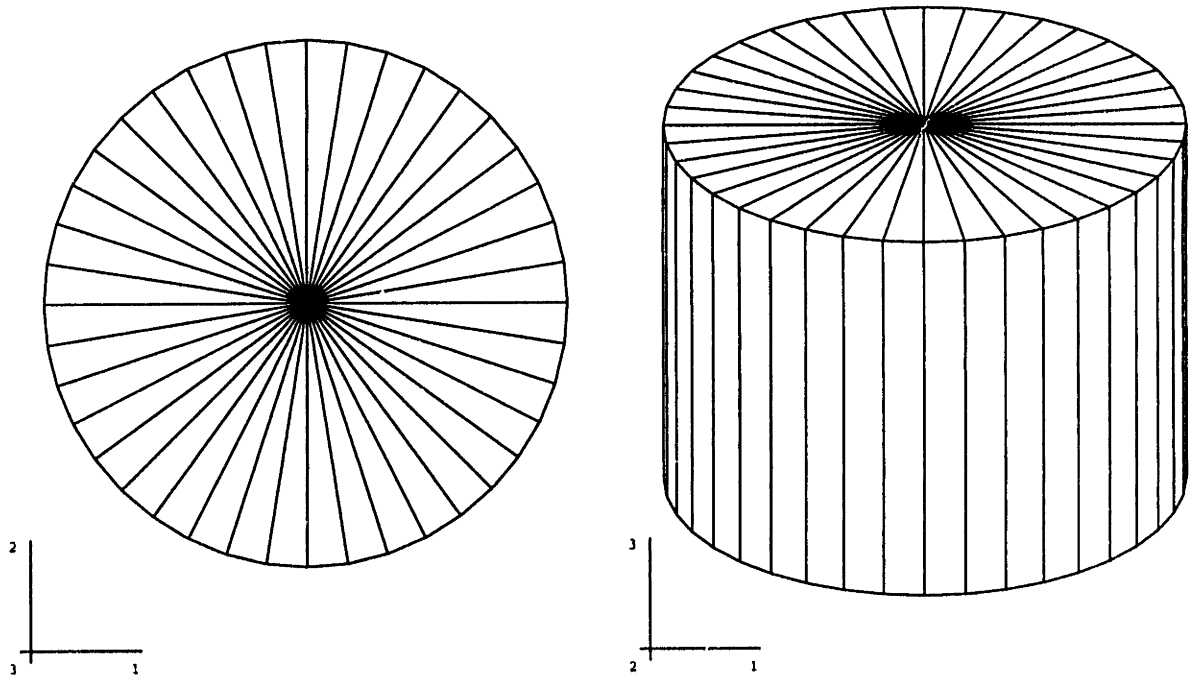

Figure C-10: Initial finite element mesh for shape change calculations

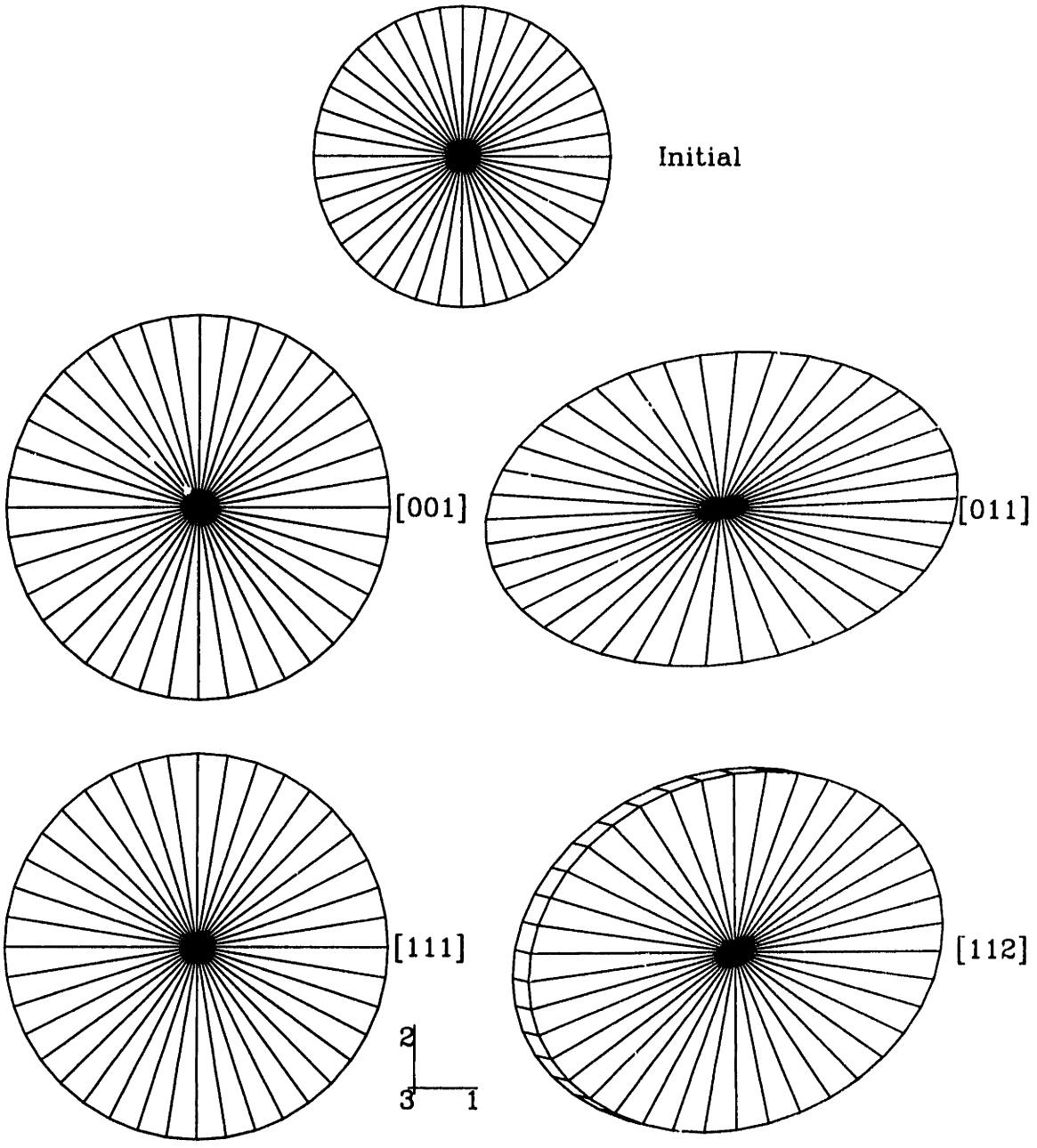

Figure C-11: Cross-sections of initial finite element mesh and final meshes for all simulations

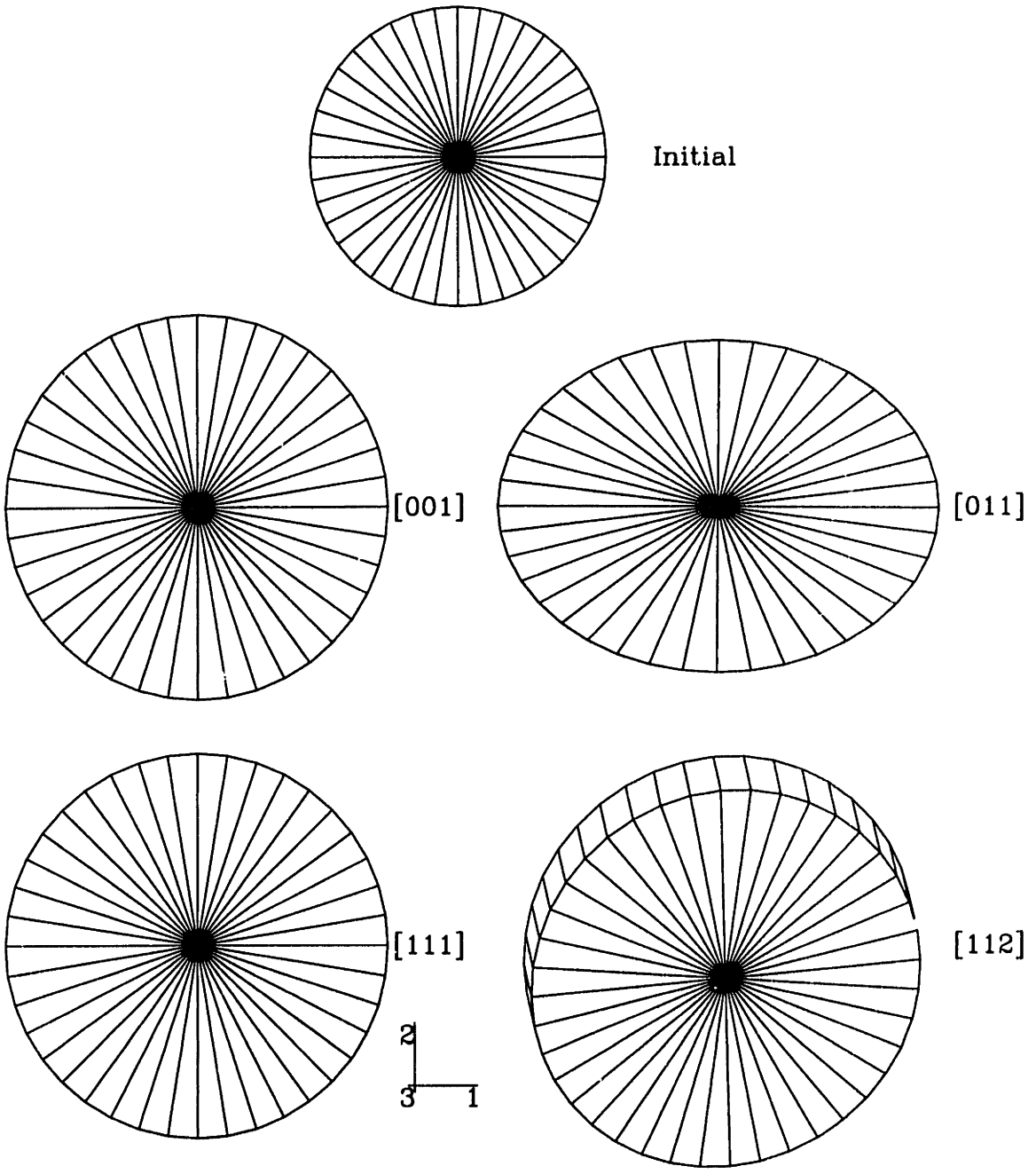

Figure C-12: Cross-sections of initial finite element mesh and final meshes for all simulations with no tension-compression asymmetry

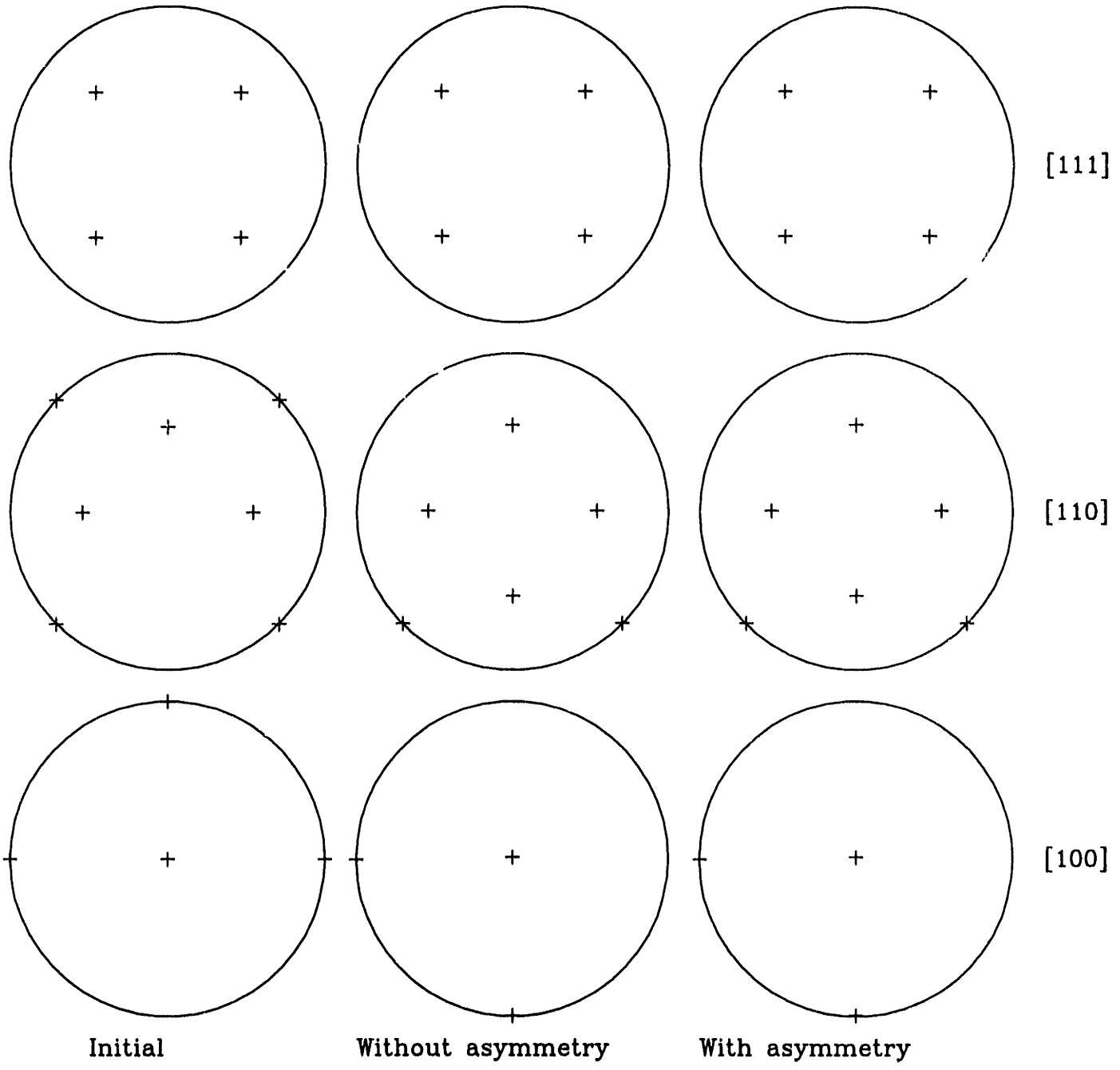

Figure C-13: (a) Initial texture (b) Final texture at 50% strain without asymmetry (c) Final texture at 50% strain with asymmetry for the ⟨001⟩ orientation

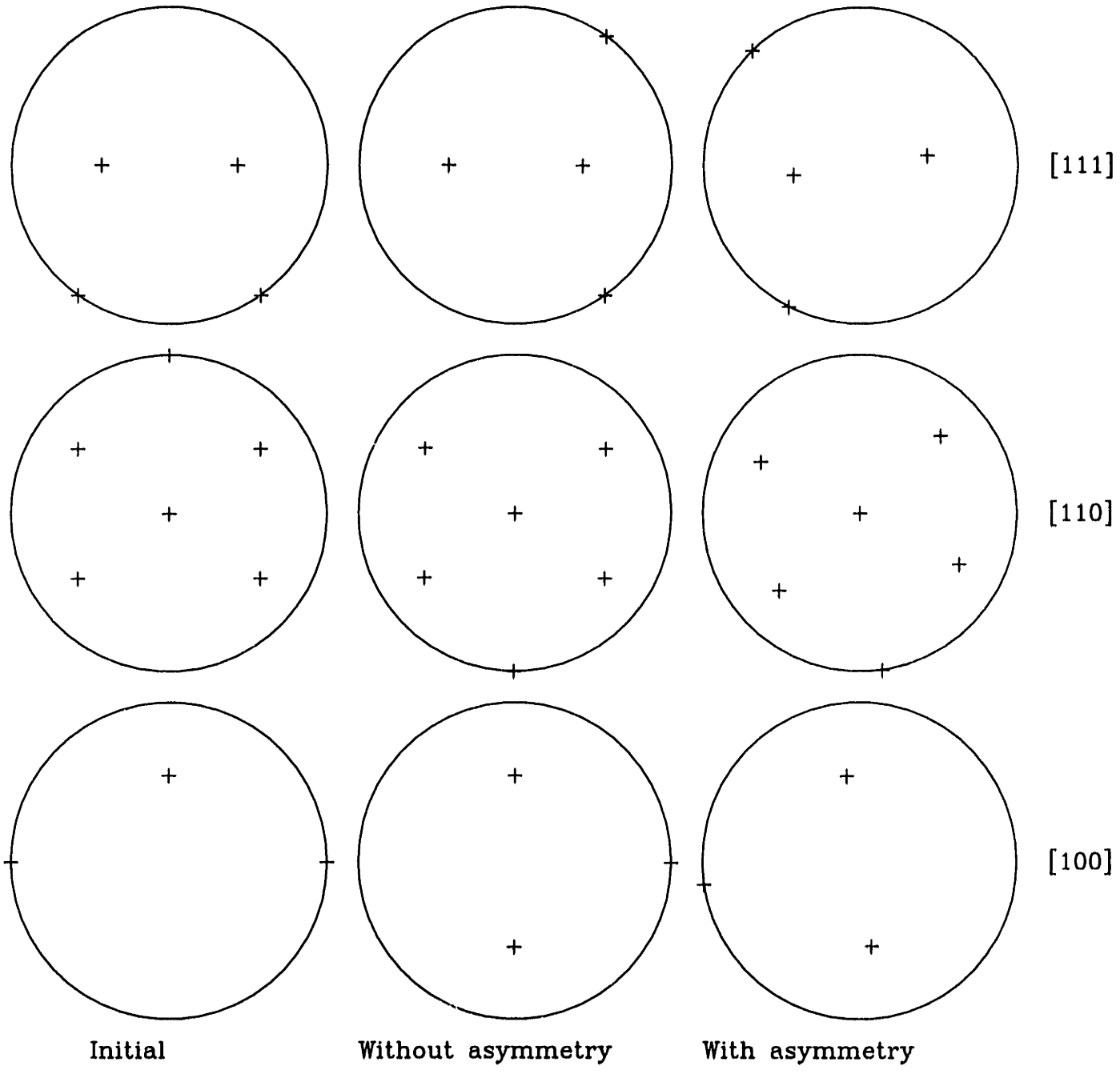

Figure C-14: (a) Initial texture (b) Final texture at 50% strain without asymmetry (c) Final texture at 50% strain with asymmetry for the ⟨011⟩ orientation

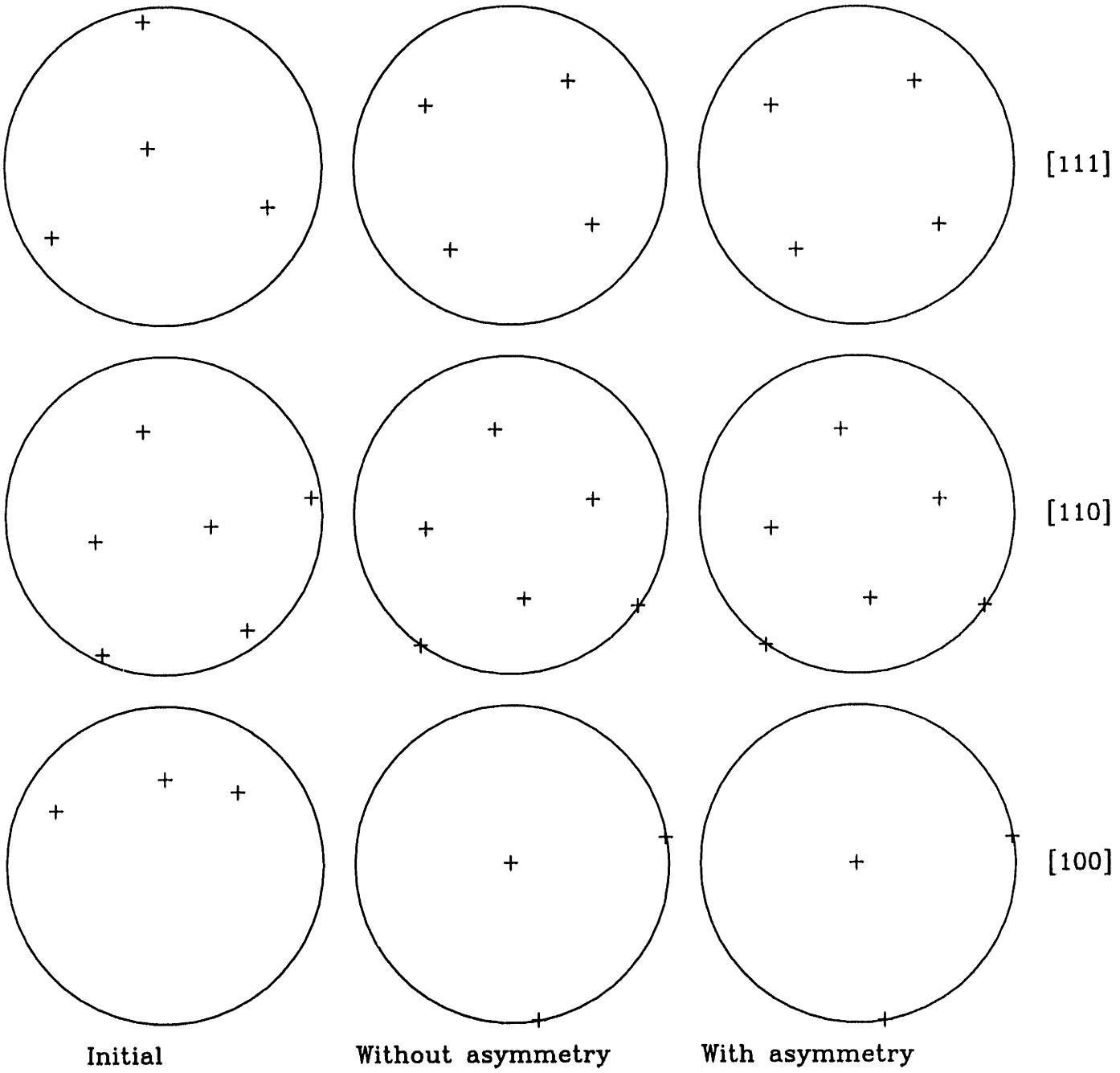

Figure C-15: (a) Initial texture (b) Final texture at 50% strain without asymmetry (c) Final texture at 50% strain with asymmetry for the ⟨111⟩ orientation

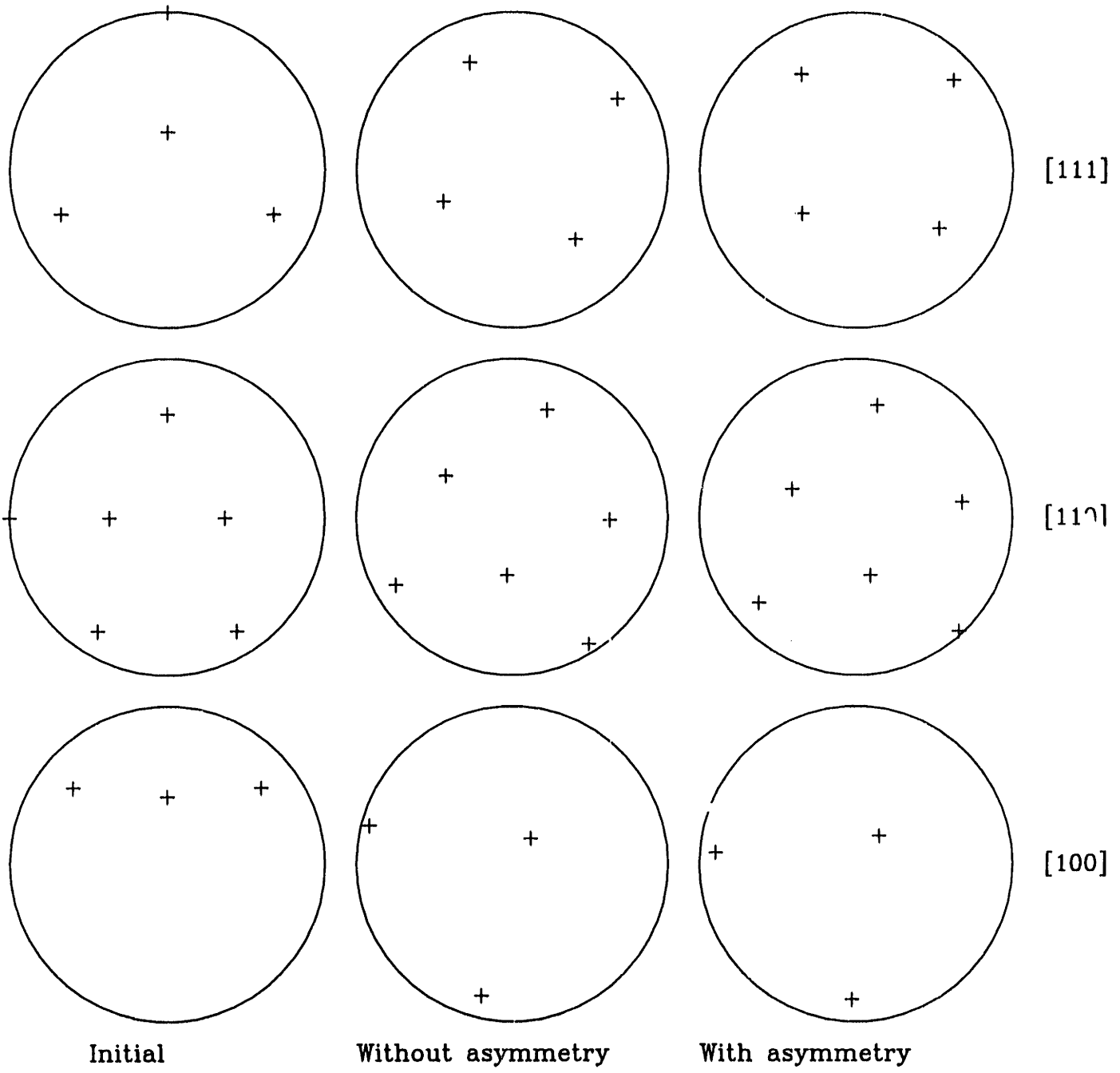

Figure C-16: (a) Initial texture (b) Final texture at 50% strain without asymmetry (c) Final texture at 50% strain with asymmetry for the ⟨112⟩ orientation

Appendix D

Experiments and Simulations on CMSX3

D.1 Experimental Program

The material was kindly provided by the Allison Gas Turbine Division of GM in 0.5in diameter bars of about 6in length in the ⟨001⟩ orientation. The alloys are received in the solution treated state - 1293°C 3 hours, gas fan cool in vacuum. Additionally, an aging heat treatment is required - 1080°C 4 hours, rapid cool, 870°C 20 hours, furnace cool for CMSX3. This aging reprecipitates the γ', giving a regular cubic array for the maximum creep strength.

Two types of experiments were performed on CMSX3: (*i*) Small strain axial cycling under strain control of the single crystals with the ⟨001⟩ direction aligned with the axis of deformation. In practice the ⟨001⟩ is the orientation most commonly used because of its high creep resistance. (*ii*) Moderate strain monotonic axial compression experiments with specimens whose ⟨001⟩, ⟨011⟩ and ⟨111⟩ axes are aligned with the compression axis. [1]

For the axial cyclic straining experiments, each bar was cut into three pieces, electron-beam welded between two lengths of Inconel 718 and machined into ASTM standard low cycle fatigue specimens. Compression specimens were 0.333in diameter and 0.5in long, Figures D-1 and D-2.

[1]The ⟨011⟩ and ⟨111⟩ orientations were tested only in compression since it is not possible to fabricate fatigue specimens from the material available.

All the experiments were performed on an Instron hydraulic biaxial testing machine. The fatigue experiments were performed in strain control using an MTS high temperature axial extensometer with gage length 0.5in. The compression experiments were performed under stroke control and correction was made for load train compliance. Heating was via induction using a 5KW generator and temperature control and measurement performed remotely with an optical pyrometer for the cyclic experiments. A thermocouple was used for the compression experiments since the specimens are too small to accommodate the pyrometer spot (0.25 inch minimum diameter).

Experiments were performed at selected temperatures in the range 750 to 950°C and constant strain rates $\dot{\epsilon} = 10^{-2}, 10^{-3}, 10^{-4}$/sec. The cyclic experiments were performed to $\pm$ 1% strain, while the compression experiments were done to 10% strain. Additional experiments include strain rate jump experiments for determining strain rate sensitivity parameters, unsymmetric strain cycling, unsymmetric stress cycling and nonisothermal experiments for checking the temperature dependence. Extensive transmission electron microscopy studies follow.

D.2 Results

The model was implemented using the finite element program ABAQUS [HKS Inc., 1991], allowing the modeling of the γ and γ' phases by different areas of the material, accurately representing the dimensions and volume fractions, and assigning separate material properties. Preliminary calculations were performed using a 3D unit cell for the $\langle 001 \rangle$ orientation. Figure D-3 shows the derivation of the $\langle 001 \rangle$ unit cell from the full two-phase material. The high degree of symmetry of this orientation allows us to represent the specimen by one-eighth of a cubic precipitate surrounded on three surfaces by one-half a channel width of matrix material, as illustrated. The origin is fixed, all the edges are constrained to remain planar, and no slip is allowed at the interface. The actual mesh is shown in Figure D-4. The γ' portion is made up of a cube of $2 \times 2 \times 2$ elements while the γ is a one-element layer surrounding the γ' on three faces. The other three faces are planes of symmetry, and so each is constrained to move only in its own plane.

Figures D-5 and D-6 show the match between experiment and initial FE simulations on the $\langle 001 \rangle$ orientation at 850°C for CMSX3 with no hardening of the slip systems. At lower

strains and stresses the deformation is expected to be restricted to the weaker matrix phase with dislocations bowing between the precipitates while at higher strains and stresses the precipitates are expected to be sheared. Due to the very high volume fraction of precipitate, the precipitate properties dominate in the high strain regime. Consequently, the cyclic experiments were used to evaluate the matrix material properties while the compression experiments give those for the precipitate. Values used in our preliminary ⟨001⟩ calculations (in both the cyclic and compression simulations) for the 12 octahedral slip systems are summarized in Table D.1.

Table D.1: Elastic constants for CMSX3 and parameter values for octahedral slip systems

$\dot{\gamma}_0 = 0.01/\text{sec}$

Phase	C_{11}(MPa)	C_{12}(MPa)	C_{44}(MPa)	m	s_o(MPa)
γ	210105	142071	102051	0.05	650.0
γ'	188094	125097	95082	0.12	350.0

D.3 Discussion

It is attractive to consider the two phases of the material separately and assign different properties, since this get closer to the actual structure of the material. However, there are a few drawbacks to this approach. Firstly, It may be difficult to obtain separate material properties, such as elastic constants, for the individual phases. Secondly, simulating orientations other than ⟨001⟩ raises some questions on the geometry and the boundary conditions which are necessary when creating a unit cell. For the simple geometry and loading considered above, however, we are able to obtain quickly a reasonable solution.

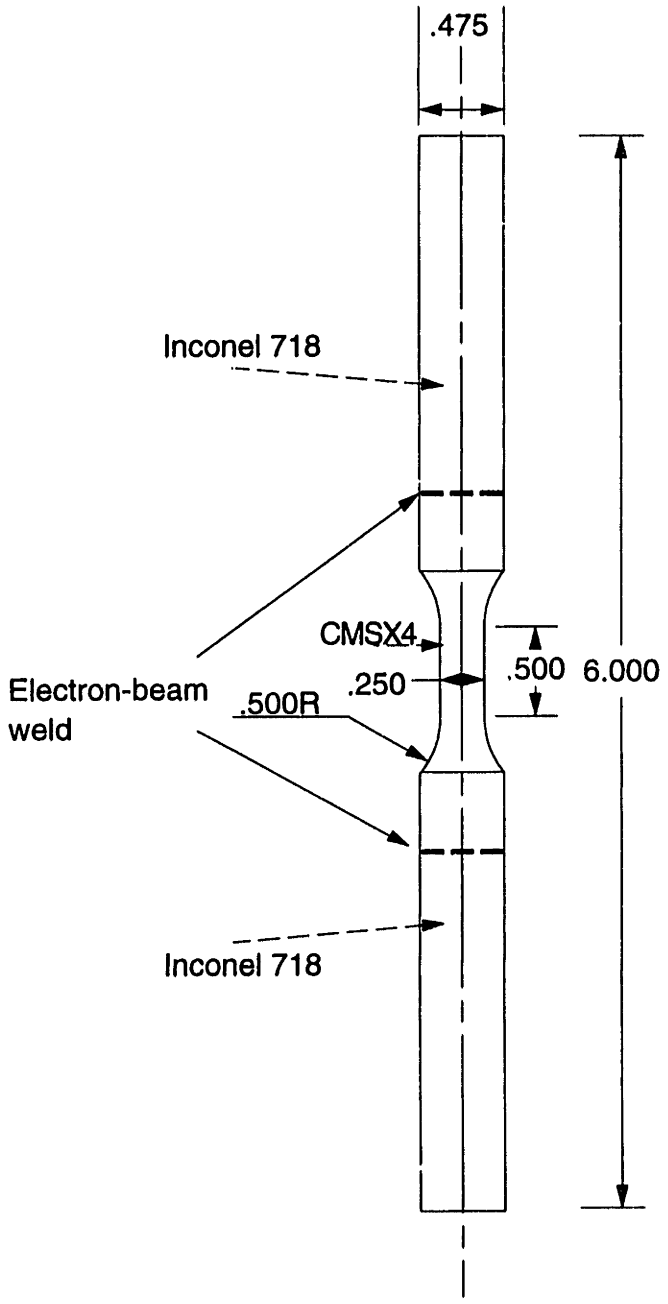

Dimensions in inches

Figure D-1: Low cycle fatigue specimen geometry

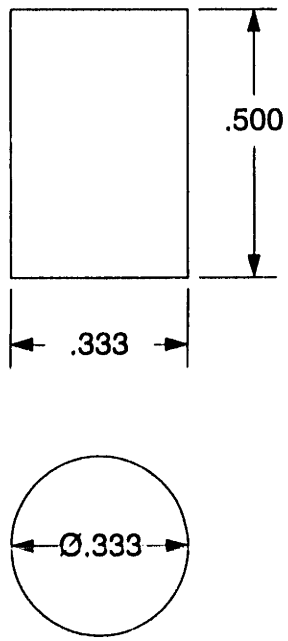

Dimensions in inches

Figure D-2: Compression specimen geometry

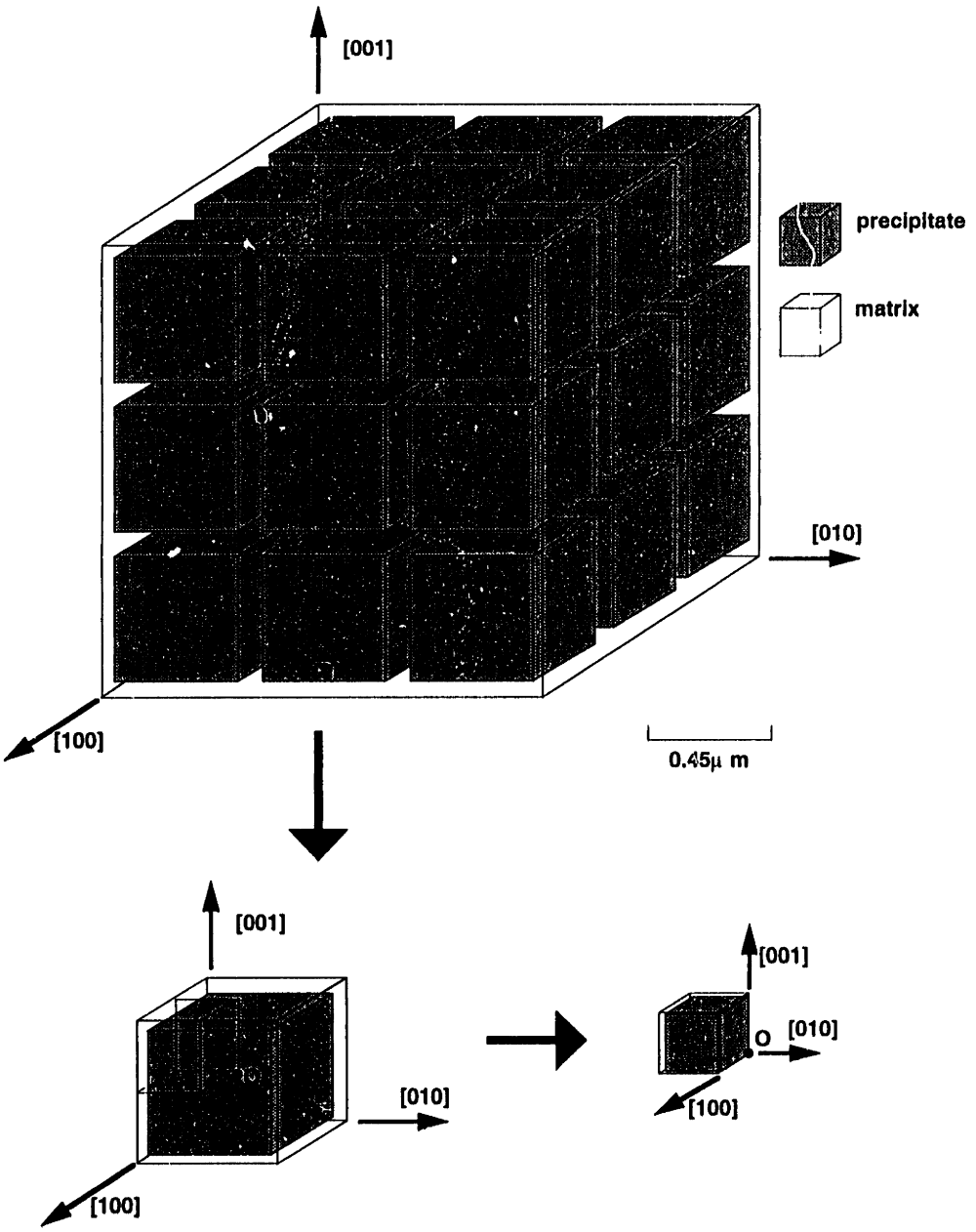

Figure D-3: Derivation of ⟨001⟩ finite element mesh

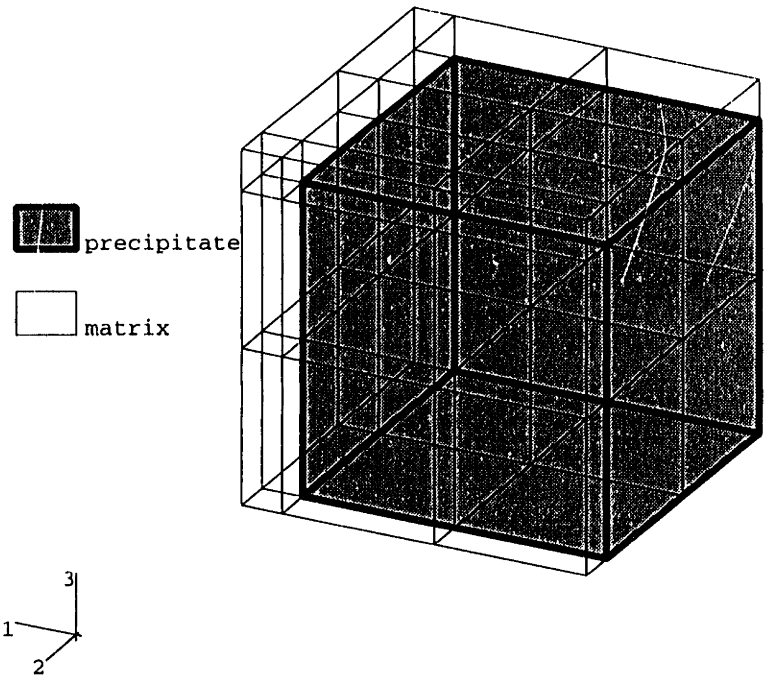

Figure D-4: ⟨001⟩ ABAQUS finite element mesh

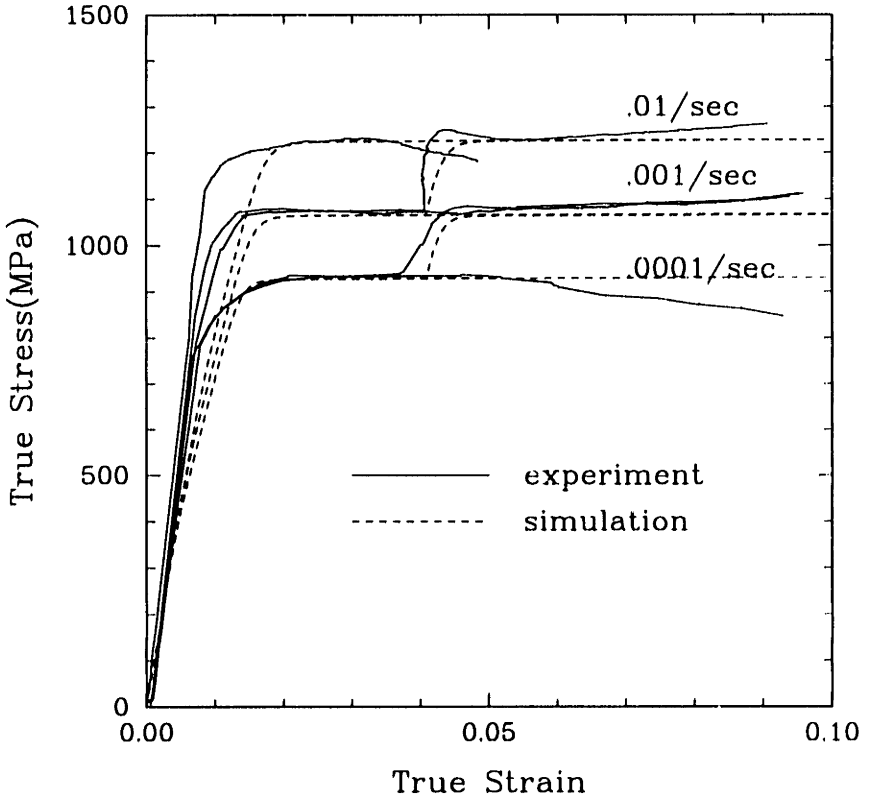

Figure D-5: Experiments and finite element simulations: compression at 850°C

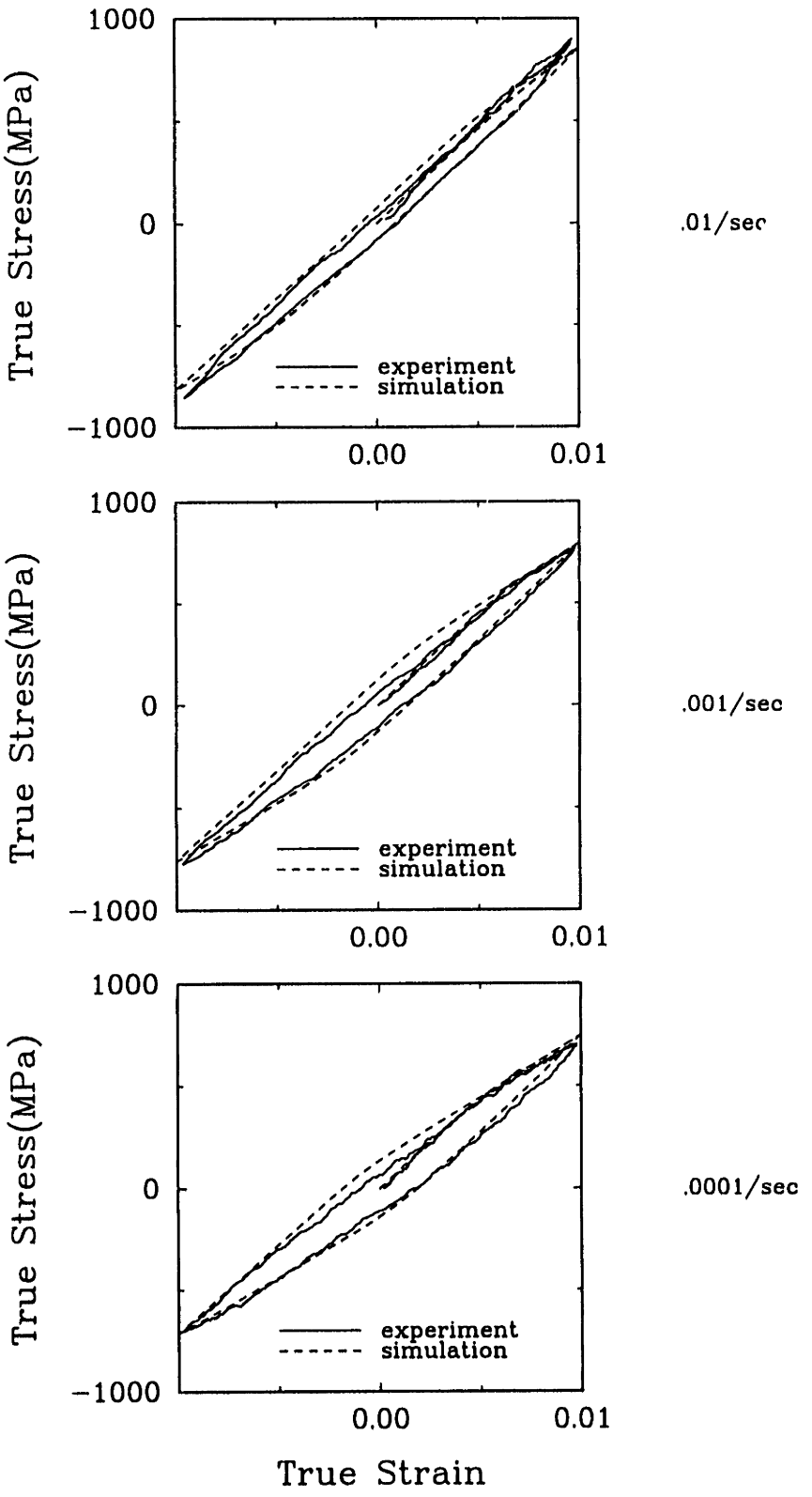

Figure D-6: Experiments and finite element simulations: cyclic at 850°C